INSTYTUT FIZYKI JĄDROWEJ
IM. HENRYKA NIEWODNICZAŃSKIEGO
POLSKIEJ AKADEMII NAUK

Praca Doktorska

Instytut Fizyki Jądrowej im. Henryka Niewodniczańskiego
Polskiej Akademii Nauk

Międzynarodowe Studium Doktoranckie IFJ PAN

Specjalność : **Plazma Termojądrowa**

Dynamika szybkich elektronów w plazmie tokamakowej z domieszkami o wysokiej liczbie atomowej Z

Przedstawiona przez:

Krzysztofa Króla

Dr hab. Marek Scholz	Promotor IFJ
Dr hab. Didier Mazon	Kopromotor CEA
Dr hab. Yves Peysson	Opiekun CEA
Dr Axel Jardin	Promotor pomocniczy IFJ

Instytut Fizyki Jądrowej im. Henryka Niewodniczańskiego
Polskiej Akademii Nauk
Zakład Fizyki Transportu Promieniowania NZ61
ul. Radzikowskiego 152
31-342 Kraków, Polska

THE HENRYK NIEWODNICZAŃSKI
INSTITUTE OF NUCLEAR PHYSICS
POLISH ACADEMY OF SCIENCES

Doctoral thesis

The Henryk Niewodniczański Institute of Nuclear Physics
Polish Academy of Sciences

International PhD Studies

Speciality : **Thermonuclear Plasma**

Fast electron dynamics in tokamak plasmas with high-Z impurities

---

Presented by:

Krzysztof Król

Dr hab. Marek Scholz	IFJ PhD Director
Dr hab. Didier Mazon	CEA PhD Co-Director
Dr hab. Yves Peysson	CEA Supervisor
Dr Axel Jardin	IFJ Auxiliary Supervisor

Institute of Nuclear Physics
Polish Academy of Sciences
Department of Radiation Transport Physics NZ61
ul. Radzikowskiego 152
31-342 Kraków, Poland

Nikomu z nas życie, zdaje się,
bardzo łatwo nie idzie, ale cóż robić,
trzeba mieć odwagę i głównie wiarę
w siebie, w to, że się jest do czegoś
zdolnym i że do tego czegoś dojść
potrzeba. A czasem wszystko się
pokieruje dobrze, wtedy kiedy
najmniej się człowiek tego spodziewa.

It seems that life
is not easy for any of us, but what to do,
you need to have courage
and mainly faith in yourself,
in the fact that you are capable of something
and that you need to reach it.
And sometimes, everything goes right
when you least expect it.

Maria Skłodowska-Curie

Acknowledgements

This work has been partially funded by the National Science Centre, Poland (NCN) grant HARMONIA 10 no. 2018/30/M/ST2/00799. We thank the PLGrid project for computational resources on the Prometheus cluster. This work has been carried out within the framework of the EUROfusion Consortium and has received funding from the Euratom research and training programme 2014-2018 and 2019-2020 under grant agreement No 633053. The views and opinions expressed herein do not necessarily reflect those of the European Commission.
The author would like to thank the members of the HARMONIA project: Didier Mazon, Yves Peysson, Marek Scholz, Jakub Bielecki, Axel Jardin, Dominik Dworak and Jędrzej Walkowiak, for the possibility of taking part in the project, help and many inspiring discussions. The author would also like to thank the members of the NZ61 department of IFJ PAN as well as the WEST team.

List of Acronyms

- **ASDEX** : Axially Symmetric Divertor Experiment (tokamak)
- **BWCD** : Bernstein Waves Current Drive
- **C3** : The old symbol for the LH1 WEST antenna
- **C4** : The old symbol for the LH2 WEST antenna
- **CFC** : Carbon Fibre Composite
- **CS** : Full (complete) screening
- **DEMO** : Demonstration (Thermonuclear) Power Plant
- **DFT** : Density Functional Theory
- **DKE** : Drift Kinetic Equation
- **EC** : Electron Cyclotron
- **ECE** : Electron Cyclotron Emission
- **ECCD** : Electron Cyclotron Current Drive
- **ECRH** : Electron Cyclotron Resonance Heating
- **ELM** : Edge-Localised Mode
- **EM** : Electromagnetic
- **ETB** : Edge Transport Barrier
- **EXP** : Experimental
- **F-P** : Fokker-Planck
- **FAM** : Full Active Multijunction
- **FW** : Fast Wave
- **FWCD** : Fast Waves Current Drive
- **HFS** : High Field Side
- **HXR** : Hard X-ray
- **IBW** : Ion Bernstein Waves
- **IC** : Ion Cyclotron
- **ICCD** : Ion Cyclotron Current Drive
- **ICRH** : Ion Cyclotron Resonance Heating
- **IO** : ITER Organization

- **ITB** : Internal Transport Barrier
- **ITER** : International Thermonuclear Experimental Reactor
- **JET** : Joint European Torus
- **LBO** : Laser Blow-Off
- **LCFS** : Last Closed Magnetic Flux Surface
- **LFS** : Low Field Side
- **LH** : Lower Hybrid
- **LH1** : Full Active Mutijunction Lower Hybrid Antenna on WEST tokamak
- **LH2** : Passive Active Mutijunction Lower Hybrid Antenna on WEST tokamak
- **LHCD** : Lower Hybrid Current Drive
- **LHRH** : Lower Hybrid Resonance Heating
- **MHD** : Magnetohydrodynamics
- **NBI** : Neutral Beam Injection
- **NBCD** : Neutral Beam Current Drive
- **NIF** : National Ignition Facility
- **PAM** : Passive Active Multijunction
- **PFC** : Plasma Facing Component
- **PT** : Pratt-Tseng model
- **RAD** : Radiation Power
- **RE** : Runaway Electrons
- **RF** : Radio Frequency
- **RP** : Rosenbluth-Putvinski model
- **SXR** : Soft X-ray
- **TCV** : Tokamak à configuration variable
- **TF** : Thomas-Fermi model
- **TF-K** : Thomas-Fermi-Kirillov model
- **TS** : Tore Supra (tokamak)
- **TTMP** : Transit Time Magnetic Pumping
- **VDE** : Vertical Displacement Event
- **WEST** : Tungsten (W) Environment in Steady-state Tokamak
- **WKB** : Wentzel-Kramers-Brillouin

Contents

Streszczenie w języku polskim

Niewielkie stężenia domieszek jonów o dużej liczbie atomowej w plazmie tokamaka mogą znacząco wpłynąć na pracę tego urządzenia [Pütterich 2010], a nawet prowadzić do zakończenia wyładowania plazmowego, jak pokazano na rysunku 1. Konieczne jest zatem opracowanie szczegółowego opisu tego wpływu, który pozwoli na prawidłową pracę przyszłych urządzeń termojądrowych.

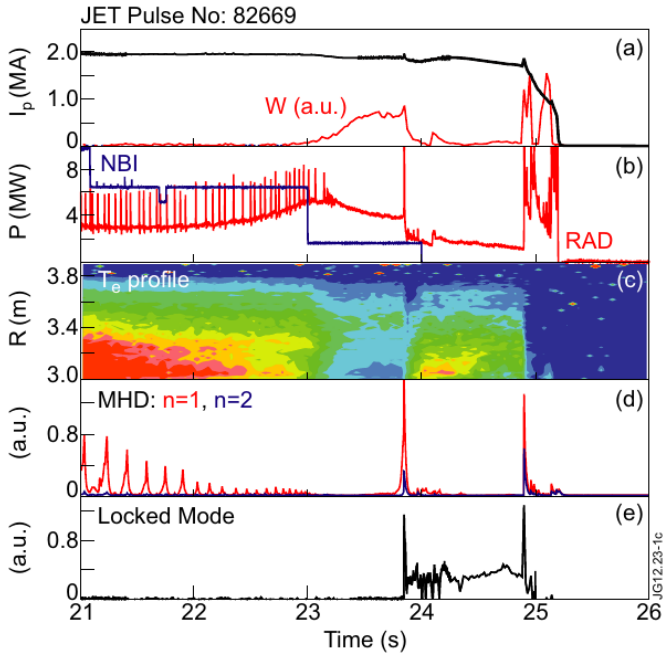

Figure 1: Przykład wyładowania plazmowego w tokamaku JET z zerwaniem sznura plazmowego w wyniku akumulacji domieszek wolframowych w rdzeniu plazmy. Prąd w plazmie I_p wyraźnie zanika około $t = 25\ s$, co widoczne jest na wykresie (a). Koncentracja wolframu (kolor czerwony) gwałtowny rośnie przed zerwaniem sznura plazmowego. (b) NBI i moc strat radiacyjnych. (c) Profil temperatury elektronowej od rdzenia plazmy ($R = 3\ m$) do brzegu plazmy ($R = 3.8\ m$). Wykres jest skalowany od 0 keV (kolor niebieski) do 2 keV (kolor czerwony). (d) Aktywność MHD dla modów $n = 1$ i $n = 2$. (e) Amplituda nierotującej wyspy magnetycznej — tzw. mod zamknięty. Rysunek zaczerpnięty z [Vries 2012].

W szczególności krytycznym zagadnieniem, które wymaga zbadania, jest wpływ domieszek o wysokiej liczbie atomowej Z na dynamikę szybkich (supratermalnych) elektronów. Opis tego wpływu związany jest z dwoma aspektami.
Po pierwsze, stabilność plazmy zależy od przepływającego przez nią prądu elektrycznego, który generuje poloidalną składową pola magnetycznego, niezbędną do eliminacji dryfów elektromagnetycznych. Ten prąd plazmowy jest częściowo generowany samoczynnie, tzw. prąd bootstrap. Prąd płynący w plazmie może być generowany na kilka sposobów: poprzez indukcję za pomocą centralnego solenoidu, przez wstrzykiwanie wiązki cząstek neutralnych (NBI) lub poprzez grzanie plazmy za pomocą fal elektromagnetycznych o różnych częstotliwościach, np. generowanie prądu za pomocą fal o częstości elektronowego rezonansu cyklotronowego (ECCD), o częstości rezonansu jonowego (ICCD) lub o częstości niższego rezonansu hybrydowego (LHCD). Jednym z głównych celów pracy jest zbadanie wpływu domieszek na profil prądowy w plazmie i intensywność promieniowania hamowania emitowanego przez szybkie elektrony. Diagnostyka twardego promieniowania rentgenowskiego (HXR) jest jednym z głównych narzędzi do badania populacji szybkich elektronów oraz do weryfikacji oszacowania udziału składowej LH prądu w całkowitym prądzie plazmy.
Po drugie, gwałtowne zmiany natężenia prądu w plazmie, np. podczas fazy ramp-up lub quench (w przypadku zerwania sznura plazmowego, Fig. 1), mogą indukować pole elektryczne zdolne do przyspieszenia szybkich elektronów do prędkości relatywistycznych, z energią kinetyczną powyżej 1 MeV. Dla tak zwanych elektronów uciekających siła tarcia pochodząca od jonów w plazmie skaluje się, jak $1/v^2$, co w rezultacie sprawia, że RE stanowią bezpośrednie zagrożenie dla komponentów komory próżniowej i systemów diagnostycznych, jak pokazano na rysunku 2. Potencjalne metody osłabiania oraz zapobiegania wiązkom RE są aktualnie intensywnie badane. W szczególności możliwe jest wstrzyknięcie do plazmy domieszek o wysokiej liczbie atomowej Z (np. kryptonu), aby spowolnić wiązkę RE przed dotarciem do ściany tokamaka.
Początkowo głównym obszarem zainteresowania były domieszki o stosunkowo niskiej liczbie atomowej Z takie jak węgiel, azot czy argon. Obecnie jednak konieczne jest rozszerzenie metod badania dynamiki szybkich elektronów na cięższe domieszki, takie jak krypton, molibden czy wolfram. W związku z tym w modelowaniu plazmy konieczne jest uwzględnienie efektu częściowego ekranowania, który występuje podczas zderzeń kulombowskich pomiędzy jonami domieszek a szybkimi elektronami. Biorąc pod uwagę, że divertor tokamaka ITER będzie wykonany z wolframu, domieszki te będą obecne w plazmie ITER-a. Stąd ich wpływ na dynamikę szybkich elektronów jest ważnym zagadnieniem badawczym.

Celem niniejszej pracy jest zbadanie nowych aspektów przedstawionych

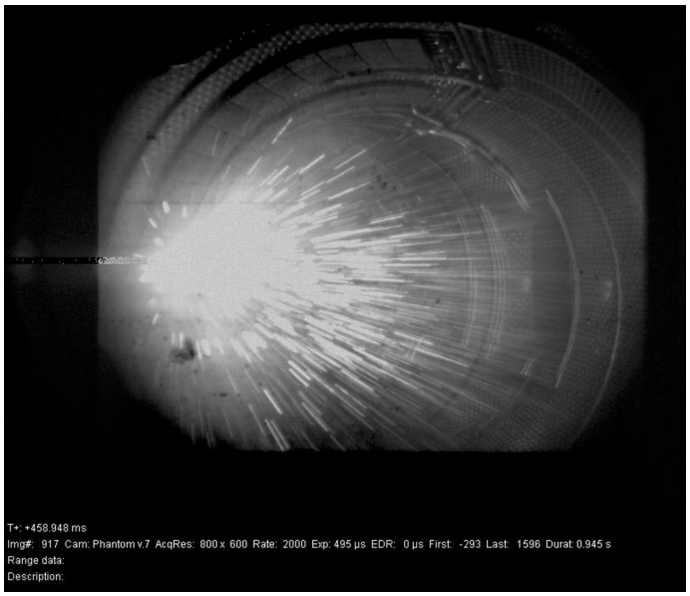

Figure 2: Iskry pyłu węglowego odpryskujące ze ściany komory tokamaka Tore Supra w wyniku uderzenia w nią wiązki elektronów uciekających podczas zerwania sznura plazmowego. Rysunek zaczerpnięty z [Loarte].

> powyżej i ich konsekwencji, a w szczególności ilościowe określenie wpływu domieszek o wysokiej liczbie atomowej Z na dynamikę szybkich elektronów. Cel ten został osiągnięty poprzez konsekwentne włączenie do obliczeń kinetycznych teorii częściowego ekranowania w przypadku domieszek o wysokiej liczbie atomowej Z.

Narzędzia numeryczne służące do tego celu to kody: METIS [Artaud 2018], ALOHA [Hillairet 2010], C3PO [Peysson 2012], LUKE [Decker 2005b] oraz R5-X2 [Peysson 2008b]. METIS pozwala na zintegrowaną symulację globalnych parametrów opisujących wyładowania plazmowe w tokamaku. LUKE umożliwia obliczenie funkcji rozkładu elektronów rozwiązując równanie Fokkera-Plancka. ALOHA oblicza widmo mocy anteny LH. Na jego podstawie możliwym jest modelowanie fal LH jako promieni przy pomocy kodu C3PO, co pozwala następnie na oszacowanie profilu depozycji mocy LH za pomocą LUKE. R5-X2 daje możliwość obliczenie nietermicznego promieniowania hamowania, emitowanego w wyniku generowania w plazmie prądu LH. Powyższe kody pozwalają na bezpośrednie ilościowe porównanie wyników teoretycznych z obserwacjami eksperymentalnymi dotyczącymi wpływu domieszek na dynamikę szybkich elektronów.
Wykorzystane w pracy dane eksperymentalne potrzebne do przeprowadzenia symulacji oraz porównania jej z eksperymentem pochodzą z bazy danych tokamaka Tore Supra i WEST. Tokamak WEST jest jednym z pierwszych urządzeń termojądrowych umożliwiających badanie plazmy z domieszkami wolframowymi, grzanej falami LH. Wyko-

rzystywana infrastruktura składa się z klastrów obliczeniowych zintegrowanych w ramach projektu PL-Grid (Prometheus, Cyfronet Kraków), serwerów IRFM-CEA (Cadarache, Francja) oraz serwera EPFL Swiss Plasma Center (Lozanna, Szwajcaria).
Badania dla domieszek o średniej liczbie atomowej Z (takich jak argon) w zimnej plazmie, po zerwaniu sznura plazmowego, zostały zapoczątkowane stosunkowo niedawno przez Hesslow et al. w [Hesslow 2017]. Natomiast w prezentowanej rozprawie doktorskiej po raz pierwszy badany jest wpływ domieszek o wysokiej liczbie atomowej Z na dynamikę szybkich elektronów w reżimie plazmy tokamakowej w stanie ustalonym, z uwzględnieniem efektu częściowego ekranowania. Szczególny nacisk został położony na konsekwencje tego wpływu na profil prądu plazmy i intensywność promieniowania hamowania. LUKE jest obecnie jedynym dostępnym solverem równania Fokkera-Plancka, który umożliwia badanie tych specyficznych problemów w plazmie tokamakowej.
Prezentowana praca doktorska ma następującą strukturę:

- W rozdziale 1 przedstawiono ogólne pojęcia związane z energią termojądrową, tokamakami, szybkimi elektronami i domieszkami o wysokim Z oraz zdefiniowano problematykę niniejszej rozprawy.
- Rozdział 2 zawiera przegląd obecnie dostępnych metod nieindukcyjnego generowania prądu w plazmie tokamakowej.
- W rozdziale 3 opisano założenia fizyczne pozwalające na symulację zjawisk fizycznych zachodzących podczas generowania przepływu prądu w tokamaku za pomocą fal LH. Opisano również łańcuch kodów umożliwiających tę symulację — METIS/ALOHA/C3PO/LUKE/R5-X2.
- W rozdziale 4 przedstawiono teorię efektu częściowego ekranowania oraz jego numeryczną implementację z wykorzystaniem różnych modeli.
- W rozdziale 5 przedstawiono wyniki symulacji z wykorzystaniem łańcucha kodów uaktualnionych o efekt częściowego ekranowania oraz porównanie uzyskanych wyników z danymi eksperymentalnymi.
- W rozdziale 6 przedstawiono wnioski i perspektywy przyszłej pracy.

Summary in English

In tokamak plasmas, small concentrations of heavy impurities are sufficient to affect the tokamak plasma performance significantly [Pütterich 2010] or can even lead to disruption, as shown in Fig. 3. An accurate description of this impact is, therefore, an absolute necessity for future fusion devices.

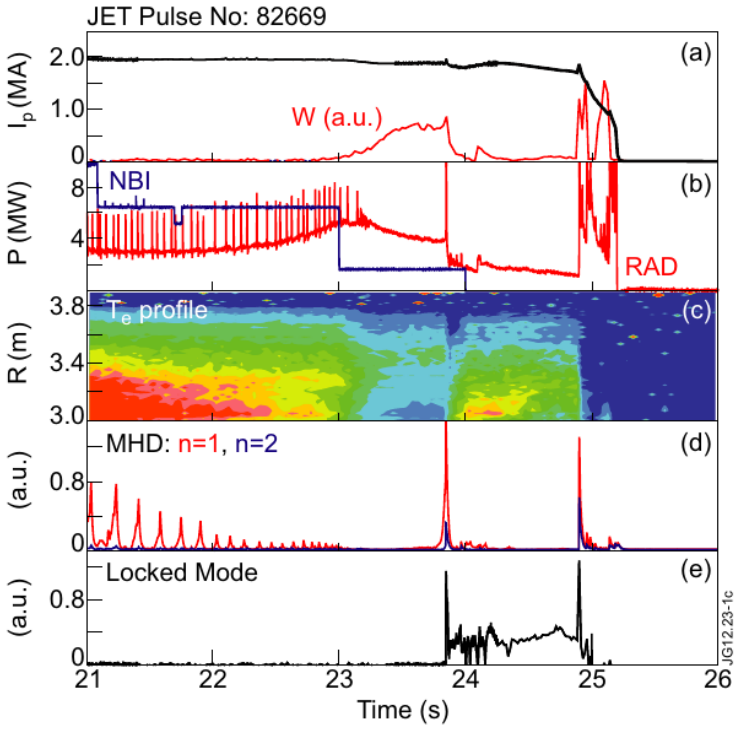

Figure 3: Example of a JET discharge with a disruption caused by tungsten impurity accumulation in the plasma core. The plasma current I_p quench is clearly visible around $t = 25\ s$ in the subplot (a), while the W concentration (in red) presents a sharp increase prior to the disruption. (b) NBI and radiation power. (c) Electron temperature profile from plasma core ($R = 3\ m$) to plasma edge ($R = 3.8\ m$). The colorbar scales from 0 keV (in blue) up to 2 keV (in red). (d) MHD activity with toroidal mode numbers $n = 1$ and $n = 2$. (e) Amplitude of non-rotating magnetic island - locked mode. Figure reproduced from [Vries 2012].

In particular, an important issue that needs to be studied is the influence of high-Z

impurities on the dynamics of fast (suprathermal) electrons. The description of this influence is related to two aspects.

First, the plasma stability depends on the electric current flowing through it, which generates the poloidal component of the magnetic field necessary to eliminate electromagnetic drifts. This plasma current is partly self-generated, so-called bootstrap current. The current flowing in the plasma can be generated in several ways: by induction with the central solenoid, by Neutral Beam Injection (NBI) or by heating with the use of electromagnetic waves of different frequencies, e.g. Electron Cyclotron Current Drive (ECCD), Ion Cyclotron Current Drive (ICCD) or Lower Hybrid Current Drive (LHCD). One of the thesis's main goals is to investigate the influence of impurities on the plasma current profile and the fast electron bremsstrahlung intensity. The hard X-ray (HXR) diagnostic is one of the leading tools to study the fast electron population and to validate the estimate of the LHCD contribution to the total plasma current.

Second, rapid changes in plasma current, e.g. during the ramp-up or quench phase (plasma disruption case as depicted in Fig. 3), can induce an electric field capable of accelerating fast electrons to relativistic speeds, with kinetic energies typically above 1 MeV. For so-called runaway electrons (RE), the friction force from the bulk plasma ions scales as $1/v^2$, consequently making REs a direct threat to vacuum chamber components and diagnostic systems, as shown in Fig. 4. The possibility of mitigating RE must

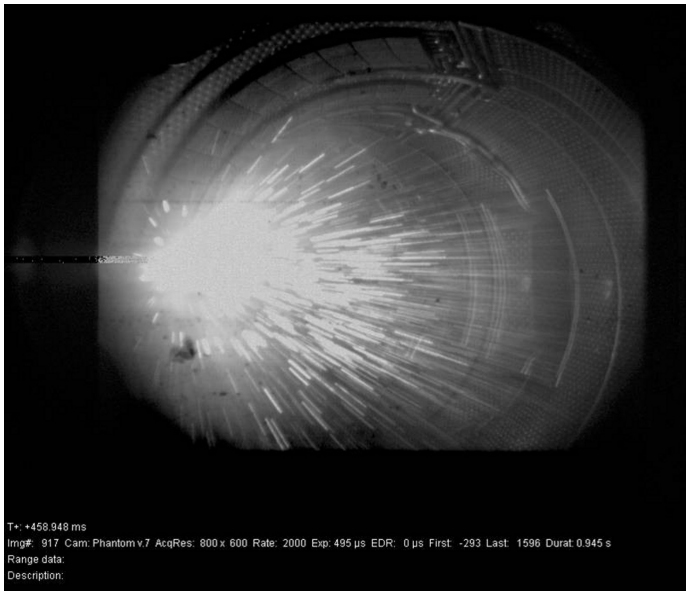

Figure 4: Sparks of carbon dust sputtered from the Tore Supra tokamak chamber wall due to impact by runaway electron beam during a disruption. Figure reproduced from [Loarte].

be investigated for the case where prevention of their formation is impossible. For this

purpose, it is possible to inject into the plasma high-Z impurities (e.g. krypton) to slow down the RE beam before reaching the tokamak wall.
Researchers were initially focused mainly on relatively low-Z impurities such as carbon, nitrogen or argon. However, nowadays, it is necessary to extend methods of investigating the fast electron dynamics to heavier impurities such as krypton, molybdenum or tungsten. As a result, in plasma modelling, it is necessary to consider the effect of partial screening during Coulomb collisions between impurity ions and fast electrons. Furthermore, considering that the ITER divertor will be made of tungsten, these impurities will be present in ITER plasma. Hence, their impact on fast electron dynamics is of great interest.

> The thesis aims to investigate the new aspects presented above and their consequences and, in particular, to quantify the impact of impurities with a high atomic number on fast electron dynamics. This goal has been achieved by consistently including the partial screening theory applied to high-Z impurities in kinetic calculations.

The numerical tools for this purpose are METIS [Artaud 2018], ALOHA [Hillairet 2010], C3PO [Peysson 2012], LUKE [Decker 2005b, Peysson 2014] and R5-X2 [Peysson 2008b] codes. METIS allows for integrated simulation of global parameters describing plasma discharges in a tokamak. LUKE provides the ability to calculate the electron distribution function by solving the Fokker-Planck equation. ALOHA can calculate the power spectrum of the LH antenna. Based on it, C3PO allows performing LH waves ray-tracing calculations that LUKE will use to estimate the LH power deposition profile. Finally, R5-X2 can calculate the non-thermal braking radiation emitted due to the generation of LH current in the plasma. The above codes allow direct quantitative comparison of theoretical results with experimental observations concerning the influence of impurities on the dynamics of fast electrons.
The data needed to perform simulations, and to compare simulation results with experiments, are provided by the Tore Supra and WEST tokamak databases. The WEST tokamak is one of the first thermonuclear devices to study plasma with tungsten impurities and heated by LH waves. The used infrastructure consists of computing clusters integrated under the PL-Grid project (Prometheus, Cyfronet Kraków), IRFM-CEA servers (Cadarache, France) and EPFL Swiss Plasma Center server (Lausanne, Switzerland).
Studies for medium-Z impurities (such as argon) in the cold post-disruptive plasmas have been initiated relatively recently by Hesslow et al. in [Hesslow 2017]. However, in the presented doctoral dissertation, the influence of high-Z impurities on the fast electron dynamics in the steady-state regime of a tokamak plasma, including the partial screening

effect, is investigated for the first time. A particular focus is put on the consequences of this influence on plasma current profile and braking radiation intensity. LUKE is currently the only available solver of the Fokker-Planck equation to investigate these specific problems in a steady-state tokamak plasma.
In the next chapters, the manuscript is structured as follows:

- In Chapter 1, the general concepts related to fusion energy, tokamaks, fast electrons and high-Z impurities are introduced, and the problem of this thesis is defined.
- Chapter 2 reviews the currently available methods for the non-inductive current drive in tokamaks.
- In Chapter 3, physical assumptions allowing simulation of non-inductive LHCD and the numerical chain of codes METIS/ALOHA/C3PO/LUKE/R5-X2 are described.
- In Chapter 4, the theory of partial screening effect and its numerical implementation using different models is presented.
- Chapter 5 presents results of LHCD simulation using the chain of codes upgraded with partial screening effect and comparison with WEST experimental data.
- In Chapter 6, conclusions and perspectives for future work are given.

Chapter 1

Introduction

Contents

1.1 Global energy issue

1.1.1 Energy production and demand

Energy is the basis for the functioning of modern civilisation. Energy is used for a variety of purposes, which can be divided into the following five categories:

1. **The transport sector** - transporting people and goods.
2. **The households sector** - houses and apartments, where energy is used, i.e. for heating (mainly), lighting, cooking.
3. **The industrial sector** - i.e. operation of factories, mines.
4. **The services sector** - i.e. operation of schools, hospitals, offices, other public places.
5. **The Agriculture sector** - cultivating plants and livestock farming.

An example of the share of energy consumption is shown in Fig. 1.1:

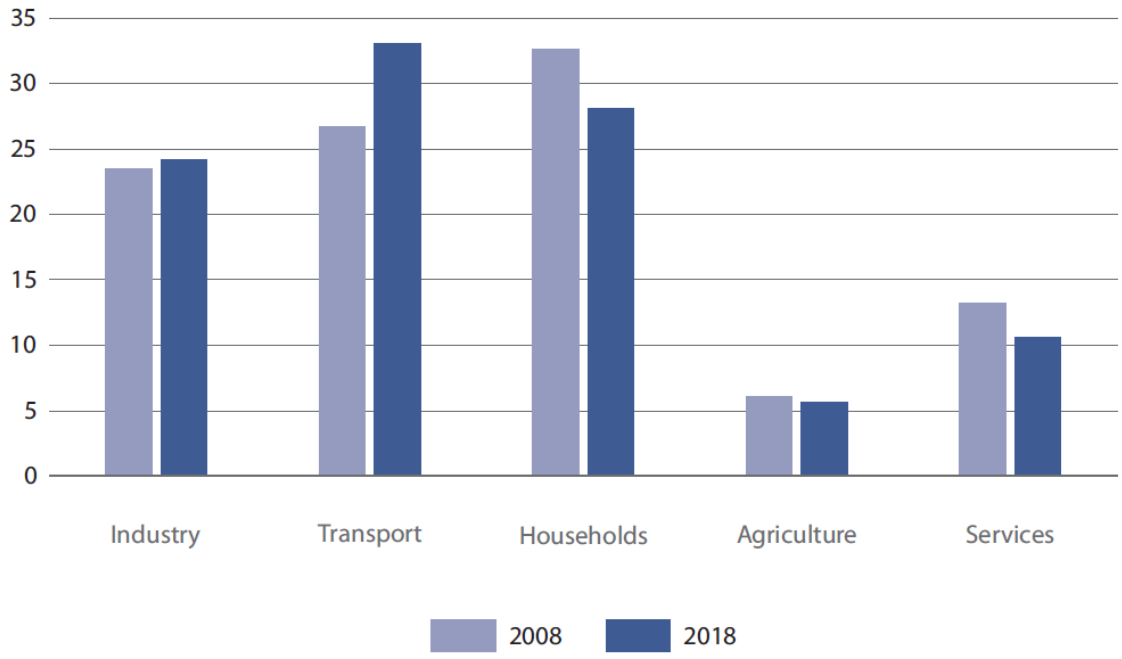

Figure 1.1: Percentage share of total energy consumption in Poland by end-use sectors in 2008 and 2018. Figure reproduced from [GUS 2020, p. 14].

Energy allows for maintaining a high quality of life. Due to the continued growth of the Earth's population, the already sizeable global demand for energy is expected to

increase. Besides, the population is becoming more and more affluent, implying that the average energy consumption per person on Earth is increasing. As a result, global energy production has increased by 17.7% from 116 214 to 136 761 TWh over ten years between 2009-2019 [Ritchie 1].

1.1.2 Energy sources and associated limitations

Because of the increase in energy demand and production, the global amount of fuel decreases drastically. The energy resources used today are primarily fossil fuels such as coal, oil and natural gas, as it can be seen in Fig. 1.2. These are so-called non-renewable sources of energy since their creation requires or involves natural processes lasting on a much larger time-scale than human civilisation.

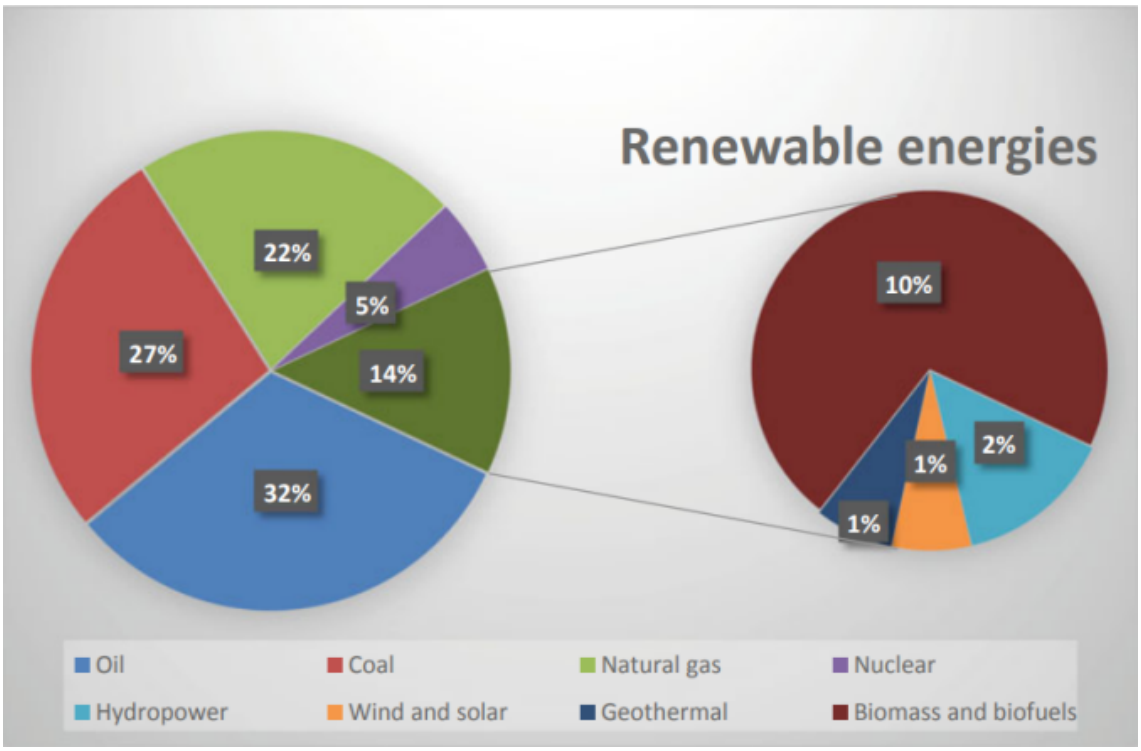

Figure 1.2: Breakdown of the world energy consumption in 2016. Non-renewable energy sources are in the first row of legend. Renewable energy sources are in the second row of legend. Figure reproduced from [Claessens 2020].

The known reserves of oil and natural gas would practically end by the end of the 21st century at the current consumption rate, and their widespread use as it is today would no longer be possible [Ritchie 2, BP]. The first to suffer will be the transport sector, which relies heavily on these resources and where energy consumption accounts for approximately 30% of total consumption. Such an enormous gap in energy resources would have

drastic economic consequences for all people. The situation regarding coal or uranium 235 is relatively similar, as it is estimated that these resources will also practically run out in about 100 - 300 years.
Using coal as the primary fuel for generating electricity also has other limitations. Many scientific studies now suggest that the observed climate change all over the globe is caused by human activity - mainly the use of coal to produce electricity or in industry. Burning coal produces carbon dioxide, which can contribute to the greenhouse effect. Also, harmful substances are emitted into the air, especially dust, which forms smog because of this process. The World Health Organization estimates that 1/8 of deaths are caused by air pollution, to which coal burning contributes up to around 5 million deaths each year. Alternatives to non-renewable energy sources include renewable sources such as solar, wind, hydro, geothermal energy or even wood fuel. However, these sources cannot currently provide a sufficient amount of power. Indeed, the energy of the Sun or wind is intermittent due to weather fluctuations. Furthermore, the major problem of renewable energies is the lack of existing technology for adequate energy storage at the scale of a city or a country, so these sources cannot currently meet the population's growing energy needs. All mentioned above energy sources are burdened with drawbacks that prevent their use to cover the population's energy needs completely. Therefore, it is necessary to find an alternative energy source, both abundant and non-intermittent, to meet the daily energy grid load.

1.1.3 The role of fusion energy

The Sun is a natural fusion reactor and is the primary source of energy reaching the Earth. It provides to the Earth's atmosphere an average power of $10^5\ TW$. In one hour, the amount of energy that the Earth obtains from the Sun is higher than the yearly energy consumption of the entire world. The Sun is mainly composed of hydrogen, which acts as the fuel for the fusion reaction process. Because of its enormous mass and gravitational force, the Sun's interior is under high pressure and has a relatively high temperature of $T = 1 - 2 \cdot 10^7\ K$. At this range of temperatures ($\sim keV$), the matter is in the plasma state. The reactants must have considerable kinetic energies to overcome the Coulomb barrier and reach a non-negligible probability of fusion reaction. As a result, fusion can occur, and the so-called proton-proton cycle is possible - a series of reactions that result in the nuclear fusion of hydrogen to helium-4. This process causes the release of kinetic energy. The reaction of deuterium and tritium is the most straightforward fusion reaction to achieve on Earth, although researchers also investigate alternative reactions such as proton-boron reaction [Scholz 2019]. The scheme of fusion of deuterium and tritium is

shown in Fig. 1.3.

The efficient extraction of fusion energy is the primary goal of future fusion power plants. However, this is not easy as the fuel temperature in the case of the fusion reaction is enormous. Gravitational confinement cannot be achieved on Earth due to the enormous mass at stake, necessary to confine the plasma. Therefore, we must look for other methods of carrying out this process on Earth. Currently, the two principal ways we know of are magnetic and inertial confinement.

The magnetic method uses a magnetic field to confine the plasma in a torus-shaped vacuum chamber (in the case of a tokamak device). An excellent example of this type of device is the International Thermonuclear Experimental Reactor (ITER), currently under construction in France [ITER Organization 2018]. In the inertial method, powerful lasers are used to fastly heat (nanosecond time scale) the surface of a spherical target containing the solid D-T fuel, leading to its implosion by ablation. The core of the target can therefore reach sufficient energy and density for the reaction to occur. An example of this type of system is the NIF - National Ignition Facility in the USA.

However, the mentioned above devices are experimental, and different fusion technologies are still in the development phase. The research aimed at constructing the first fusion power plant in humanity's history has continued since the middle of the 20th century. The possibility to extract energy efficiently from a fusion reactor has still to be demonstrated. It is the goal of ITER. Nevertheless, let us suppose that research will be successful. In that case, it will be possible to obtain energy from the D-T fuel. The extractable amount on the Earth is practically unlimited - namely deuterium (D) extracted from seawater and tritium (T) obtained from lithium. The fuel energy density is exceptionally high, as the quantity of deuterium present in one glass of water would allow getting the same energy as burning a petroleum barrel.

Also, fusion compared to conventional energy sources is a highly ecological process. During daily operation, the thermonuclear power plant will not release harmful substances or greenhouse gases from the fusion reaction products (only helium is released) into the atmosphere as it is, e.g. with power plants based on coal. However, there are still potential dangers:

1. **Tritium** will be used for fusion, a radioactive isotope of hydrogen (although mainly produced and consumed in situ).

2. **Fast neutrons** produced in fusion reactions are ionizing radiation and can activate tokamak structure elements.

3. **Beryllium** will be used as an armour material in the first wall of ITER tokamak

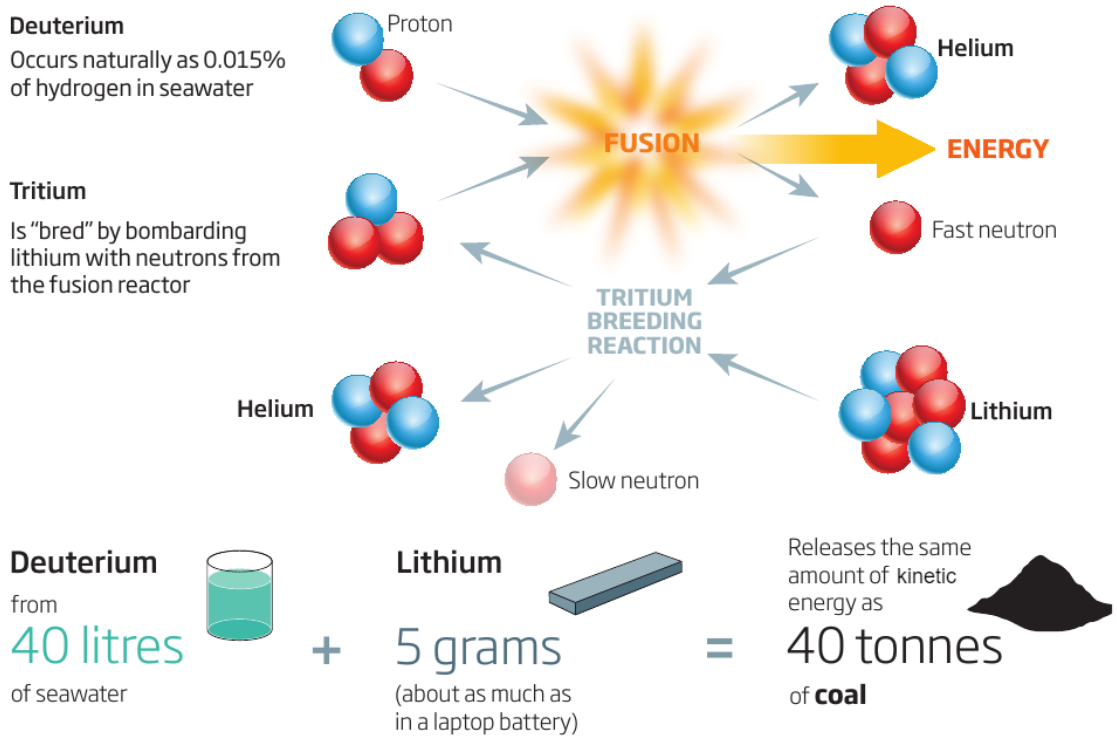

Figure 1.3: Fusion of Deuterium and Tritium, Tritium breeding and fuel equivalent. Figure adapted from [Hambling 2016].

and is potentially harmful since it is toxic and causes berylliosis.

Tritium practically does not occur naturally on Earth due to its short half-time of about 12.3 years. However, it can be produced from Lithium by neutron bombardment, using the so-called breeding blanket.

Safety is one of the most significant advantages of a fusion power plant. First, a fusion power plant differs significantly from classical nuclear fission power plants. A fusion power plant is intrinsically not affected by the risk management inherent to nuclear fission power plants. For instance, less than 1g of fuel is present at a given time in the vacuum chamber, eliminating the possibility of an overcritical state and loss of control of the reaction process. Besides, if the control of the fusion plasma is lost, the plasma will be quickly disrupted, putting an end to the fusion reaction process. Another concern could be related to the radioactive tritium that will carry out the reaction. Tritium can react with oxygen in the air to form radioactive water, which is dangerous to humans, but this does not make up a significant danger with fusion power plants since the amount of tritium used is only less than 1g at a given time in the fusion plasma. In the unlikely case, this amount of tritium would escape into the atmosphere, it would be diluted, and the damage to the population from such a leak would be negligible.

To sum up the advantages of fusion energy, first, the following aspects should be emphasized: practically unlimited fuel and harmlessness to the environment. The cost of energy produced in this way, on the other hand, is a matter of concern. At present, it is not known whether fusion energy will be competitive compared to other energy sources or, in an optimistic scenario, cheaper than them.

1.2 Generation of fusion energy

1.2.1 Thermonuclear fusion reactions

Thermonuclear reactions are nuclear reactions where light nuclei fuse into heavier ones because of the medium high temperature. As shown in Fig 1.4, ^{56}Fe is the most stable nucleus. It implies, in particular, that fusion of nuclei much lighter than iron is an exothermic process [RICE].

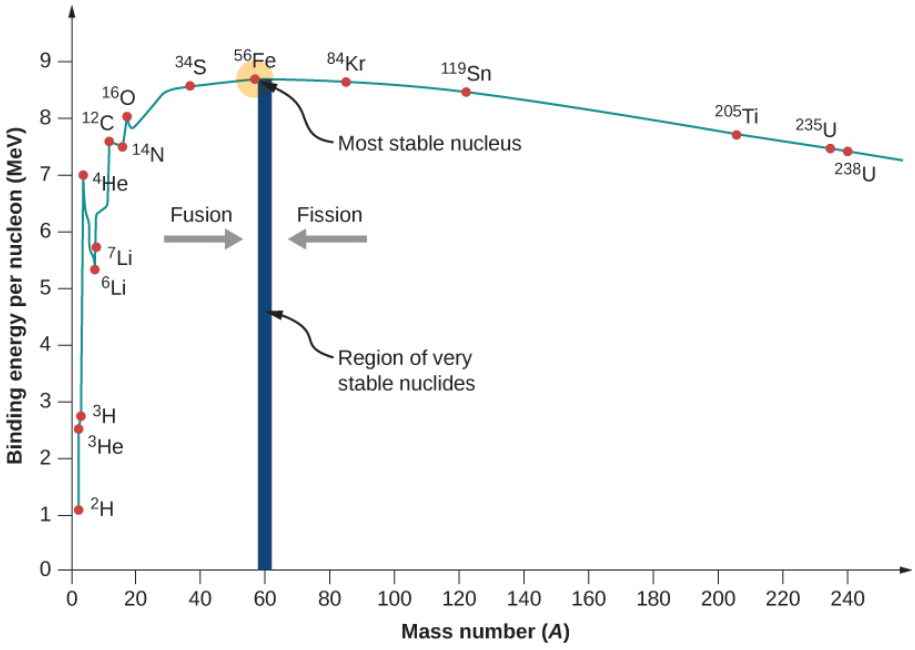

Figure 1.4: Binding energy per nucleon, as a function of the mass number of the atomic nucleus. Figure reproduced from [RICE].

The reaction energy E_r (in Joules) of the nuclear reaction is defined as:

$$E_r = (m_A + m_a - m_B - m_b)c^2, \tag{1.1}$$

where $c \approx 3 \cdot 10^8\ m/s$ is the speed of light and m_A, m_a, m_B, m_b (in kg) are the masses

of the particles participating in the nuclear reaction, which can be written

$$A + a \rightarrow B + b \Longleftrightarrow A(a,b)B. \tag{1.2}$$

The principle of energy conservation for this reaction can be written as follows:

$$E_{ks} + E_{0s} = E_{kp} + E_{0p}, \tag{1.3}$$

where E_{ks}, E_{kp} denote the total kinetic energy of the substrates and products, respectively and E_{0s}, E_{0p} the total rest energy of the substrates and products, respectively.
In order to successfully fuse two positively charged nuclei, it is necessary to overcome the Coulomb repulsion force of these nuclei. It means that there is minimum kinetic energy that an incident particle should have to overcome electrostatic repulsion and approach another particle within the range of nuclear forces. This repulsive effect can be described by a potential barrier:

$$V = \frac{Z_1 Z_2 e^2}{R_1 + R_2}, \tag{1.4}$$

where Z_1, Z_2 - are atomic numbers, R_1, R_2 - are nuclei radii and $e \approx 1.6 \cdot 10^{-19}$ is the elementary charge. The radius of a nucleus is related to its mass number A as follows:

$$R \approx e^2 \sqrt[3]{A}. \tag{1.5}$$

The above formula for the potential barrier can be written as:

$$V = \frac{Z_1 Z_2}{\sqrt[3]{A_1} + \sqrt[3]{A_2}} \ (MeV), \tag{1.6}$$

where A_1 and A_2 - are mass numbers. In a classical description, it would appear from Eq. (1.6) alone that a fusion reaction is not possible if the kinetic energy of the substrate particle is less than the above potential. However, quantum tunnelling allows the nuclear fusion reaction to occur, with a certain probability, at much larger distances than allowed by classical physics.

1.2.2 Ignition conditions and confinement of fusion plasmas

An important conclusion of the Lawson criterion [Lawson 1957] is that a suitable confinement method should allow obtaining high plasma confinement time, high plasma density, or both parameters, as shown in Fig. 1.5. For this reason, it is possible to distinguish the following main confinement methods:

- **Gravitational confinement** - Occurring in stars. Because a star has an enormous mass, plasma pressure is high enough to allow fusion reactions to occur in its core due to gravity.
- **Inertial confinement** - Allows for obtaining high plasma density but short plasma confinement time. In this method, the used fuel - a deuterium-tritium mixture is closed in a solid-state capsule. Powerful laser beams hit the target simultaneously, causing the implosion phenomenon and reaching a sufficient plasma pressure for the fusion reactions.
- **Magnetic confinement** - Allows for obtaining high plasma confinement time. In this method, plasma is not so dense as in the case of inertial confinement. Since the fusion fuel heated to high temperatures is in the plasma state, it is possible to confine the electrically charged particles using a magnetic field.

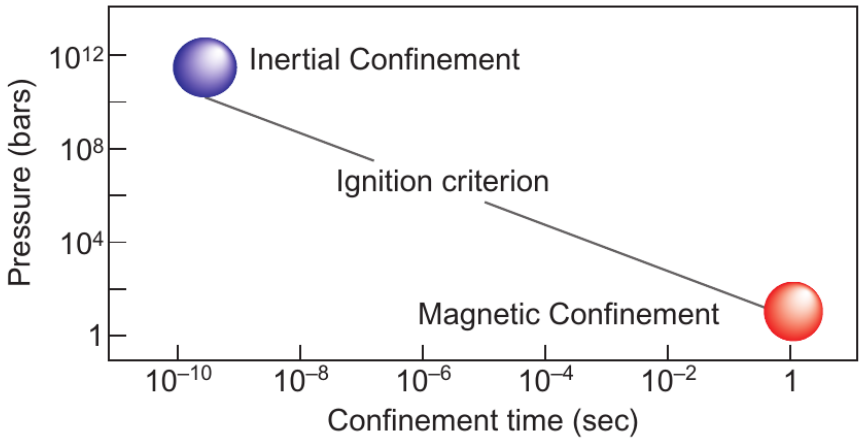

Figure 1.5: The plasma conditions, required for the generation of fusion energy in the case of magnetic and inertial confinement. A temperature of 10-20 keV (100 - 200 million degrees Celsius) is needed in both cases. Figure adapted from [McCracken 2012, p.42].

Fusion reactions may occur naturally, mainly through gravitational confinement. However, unfortunately, this method is not possible on Earth because it requires a vast mass. Hence, for the purpose of energy production, researchers are mainly focused on the magnetic confinement method.

1.2.3 Magnetic Confinement and Tokamaks

In the 1920s, Eddington found that it is highly probable that the Sun energy source is the fusion of its hydrogen. Fusion reactions were reproduced for the first time in a laboratory

by Mark Oliphant, Paul Harteck and Ernest Rutherford, as described in their article from 1934. Their experiment used an accelerated beam of deuterons hitting a metal foil containing deuterium or other atoms [Oliphant 1934]. Unfortunately, this method can not be used for energy production purposes as most particles in such a situation scatter off the fuel target instead of fusing with its nuclei [McCracken 2012, pp. 36-38]. It was then understood that obtaining a net energy gain from nuclear fusion requires providing high thermal energy to the fuel. The same year, Willard Harrison Bennett introduced a potential solution to the plasma confinement problem [Bennett 1934]. The flow of electrical current through the ionized gas creates a magnetic field. As a result, an inward force is generated perpendicular to the current direction and acts on the ionized gas, pulling it together, as depicted in Fig. 1.6. In 1937, Lewi Tonks called this phenomenon the pinch effect.

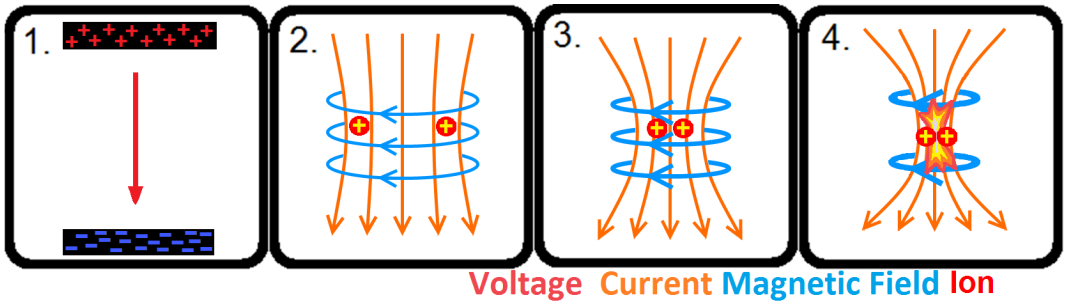

Figure 1.6: Schematic overview of pinch phenomenon. (1) A huge voltage is created, high enough to ionize the gas. (2) Current flow is created, generating a magnetic field perpendicular to it, (3) perpendicular compression of the ionized gas, and (4) nuclear fusion reactions due to the pinch effect. Figure reproduced from [Moynihan 2015].

For such a pinch, the magnetohydrodynamic (MHD) equilibrium condition is expressed as follows:

$$\vec{j} \times \vec{B} = \vec{\nabla} p, \tag{1.7}$$

where $\vec{j}$ is the plasma current density, $\vec{B}$ is the magnetic field, and p is the plasma pressure. In 1948, George Paget Thomson accomplished the construction of a fusion machine based on the pinch concept, although he could not obtain experimental proof that the machine achieved fusion reactions.

In 1950, the Soviet soldier Oleg Lavrentiev, interested in physics, proposed two ideas: obtaining ignition using a hydrogen bomb and obtaining energy from nuclear fusion using electrostatic confinement. The proposition was forwarded to Andrei Sakharov, who commented on it in the following way: "the author formulates a very important and not necessarily hopeless problem". Sakharov answered Lavrentiev that, unfortunately, there is no possibility to build a successful reactor using his idea of electrostatic confinement.

Inspired by Lavrentiev's ideas, Sakharov developed the idea of using magnetic confinement instead of an electrostatic one. An electrically charged particle of mass m and charge q moving in a magnetic field $\vec{B}$ and electric field $\vec{E}$ at the velocity $\vec{v}$ is subject to the Lorentz force:

$$m\frac{d\vec{v}}{dt} = q(\vec{E} + \vec{v} \times \vec{B}). \tag{1.8}$$

Particles in a uniform magnetic field move in a helical path along the magnetic field line, as depicted in Fig. 1.7 [Wesson 2004, pp. 42-44]. It gives the possibility that even hot

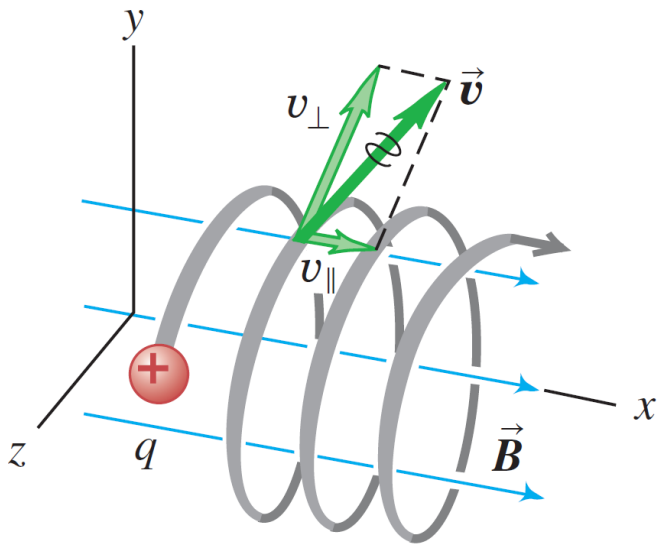

Figure 1.7: Charged particle in a uniform magnetic field. The velocity of a particle can be decomposed into $\vec{v}_\perp$ and $\vec{v}_\parallel$ - perpendicular and parallel to magnetic field components. Figure reproduced from [Young 2020, p. 916].

thermonuclear plasma with a temperature of 150 million degrees Celsius ($T \approx 13\ keV$) can be confined inside a vacuum chamber away from its walls.

On the left of Fig. 1.8, the concept of a straight solenoid is presented. It can be treated as the most straightforward magnetic confinement system in which plasma can only move towards the solenoid ends, causing particle loss. Hence, researchers started investigating systems in which the ends of the solenoid are bent, giving a torus shape [Bromberg 1982, p. 16].

In 1951, Richard F. Post started working on the first machine based on the magnetic bottle concept. A magnetic bottle consists of two cylindrical coils spaced a certain distance apart, as shown in Fig. 1.9. These coils act as mirrors - they repel charged particles approaching them towards the centre of the bottle. A particle moving at the right speed and angle can follow a spiral path and be repeatedly repelled from one coil to another. Unfortunately, this bottle is not entirely sealed. It is only possible to trap particles

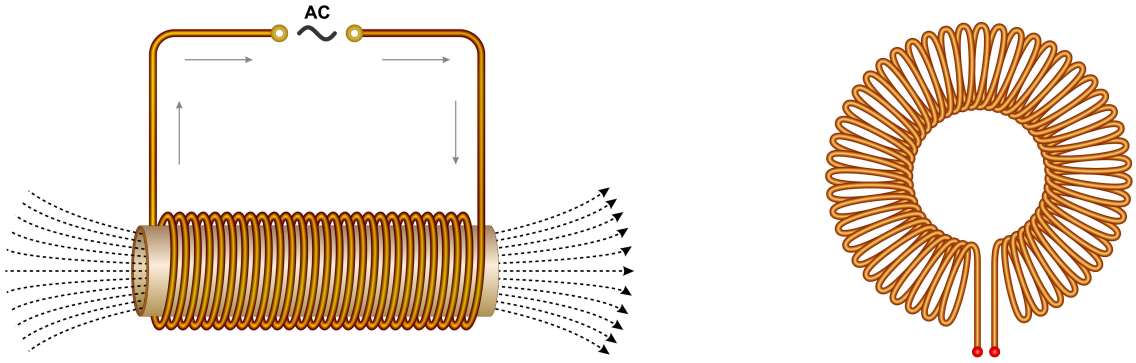

Figure 1.8: The left subfigure presents a linear configuration. It gives the possibility of evenly spaced coil windings and obtaining a uniform magnetic field. The right subfigure presents a toroidal configuration. In this case, the magnetic winding is denser on the inner side than in the outer region. Figure adapted from [Shutterstock].

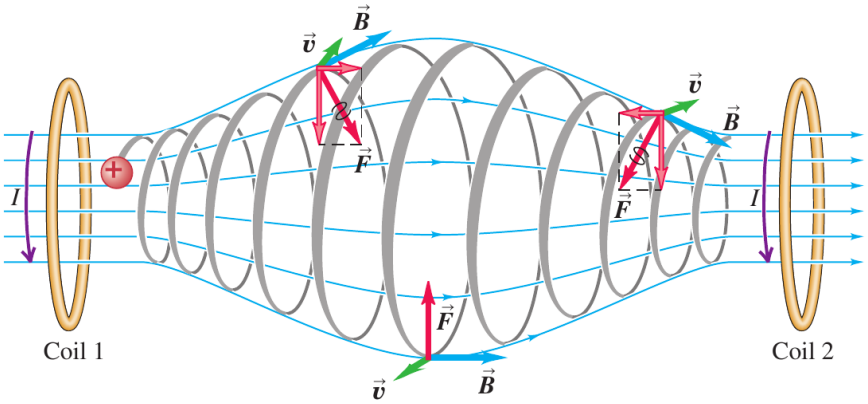

Figure 1.9: Electrically charged particles trapped in a magnetic bottle. Figure reproduced from [Young 2020, p. 917].

within a specific range of speeds and angles (pitch angle). This method is, therefore, not sufficiently effective. It can be used to confine plasma at a temperature of 1 million K ($T \approx 100\ eV$) [Young 2020, p. 917].

By the end of the year 1950, Sakharov and Igor Tamm prepared a detailed proposal for a torus-shaped device using a strong magnetic field to confine the plasma. However, the project had one big drawback. It is possible to obtain evenly spaced magnets in the simple straight solenoid. However, it is not possible in a torus geometry since coils are denser on the inner side of the torus, as shown in Fig. 1.8, leading to electromagnetic drifts that are catastrophic for plasma confinement.

Sakharov then proposed a solution to this problem – the current drive in plasma. Investigating this idea, Soviet scientists concluded that instead of toroidal configuration, a more simple linear one could be used but with a strong electric current driven into

the plasma. Thus, Sakharov and his colleagues stopped working on more complicated toroidal configurations and focused on constructing a device based on the pinch concept. They developed it independently from the previously mentioned research of British scientist George Paget Thomson.

In 1952, the Soviet physicist Nikolai Filippov with his group conducted experiments with a linear pinch machine. An example of linear pinch is presented in Fig. 1.10. At

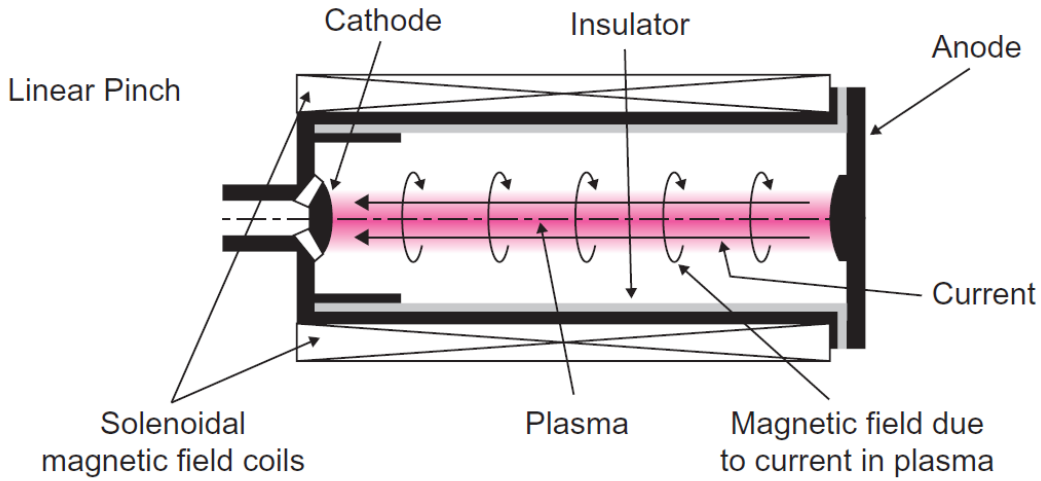

Figure 1.10: Concept of a linear plasma pinch. Figure reproduced from [McCracken 2012, p. 53].

that moment, researchers discovered plasma instabilities, which can eventually lead to plasma discharge termination. Two standard instabilities were discovered: the sausage instability (so-called $m = 0$ mode), for which inhomogeneity of the plasma compression appears along the plasma column, and the kink instability ($m = 1$ mode), where local transverse displacements are created, as presented in Fig. 1.11.

After the first failures with plasma stability, Sakharov created a new concept of the toroidal device. He concluded that the toroidal machine should work in some sense in reverse to pinch-based machines. For devices based on the pinch phenomenon, the strong current in plasma confined it through a generated magnetic field. A relatively low external magnetic field was applied to provide stabilization. Sakharov concluded that the toroidal device should be constructed to obtain the reverse effect. External magnets should provide a toroidal magnetic field responsible for confining plasma, and a relatively low current in plasma should be responsible for plasma stabilization.

Based on that, in 1955, the first toroidal pinch based machine called TMP was built in USSR, but it turned out that the plasma was not confined very well and was hitting vacuum chamber walls. After the TMP machine, Natan Yavlinsky and Igor Golovin started working on a new toroidal machine, considering an idea known today as the safety factor.

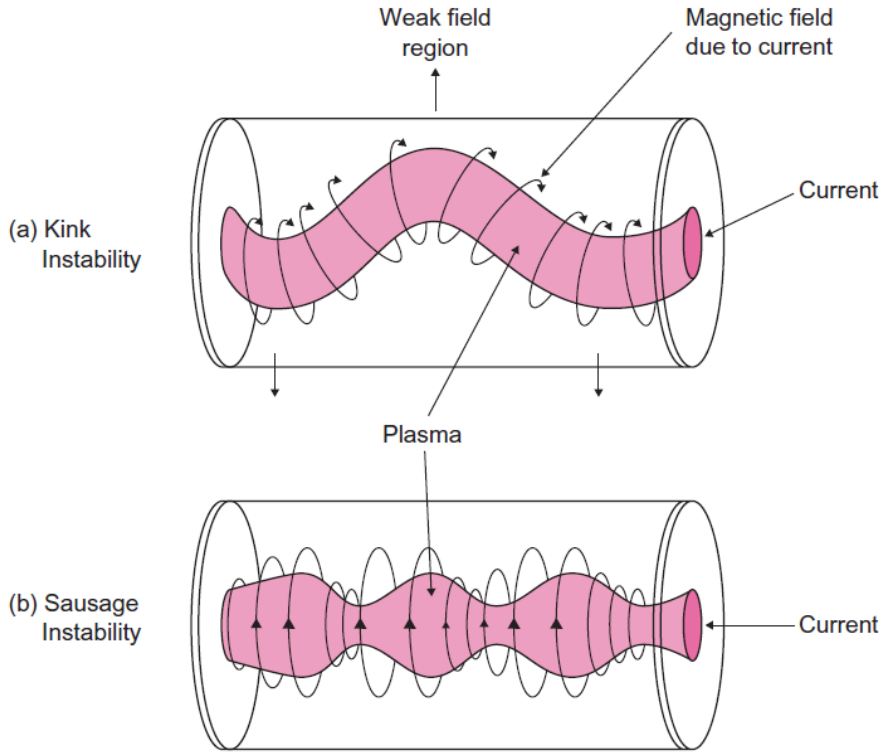

Figure 1.11: Sketch of the (a) – Kink instability, (b) – Sausage instability. Figure reproduced from [McCracken 2012, p. 49].

Plasma instabilities are common phenomena in both linear and toroidal configurations, but the kink instability is especially characteristic of the toroidal configuration. Kruskal and Shafranov found a solution to deal with kink instability ($m = 1$ mode) in the toroidal configuration. So-called passing particles make two motions in the toroidal configuration: they circulate inside the torus in the toroidal (axial) direction, and at the same time, circulate around the toroidal axis (motion in the poloidal direction). Overcoming the kink instability means that the particles must do at least one lap in the toroidal (blue arrow) direction before doing a lap in the poloidal (red arrow) direction, as shown in Fig. 1.12.

A small group of physicists and engineers led by Yavlinsky and Golovin under Lev Artsimovich, the Soviet Fusion Power Programme director, worked on a new toroidal device. In 1957 Igor Golovin proposed a name for the device – tokamak, an acronym of either Toroidal'naya Kamera s Magnitnymi Katushkami (toroidal chamber with magnetic coils) or Toroidal'naya Kamera s Aksial'nym Magnitnym Polem (toroidal chamber with an axial magnetic field). This work led eventually to the construction in 1958 of the first tokamak in history, in a research centre in Moscow known today as the "Kurchatov Institute" [Shafranov 2001].

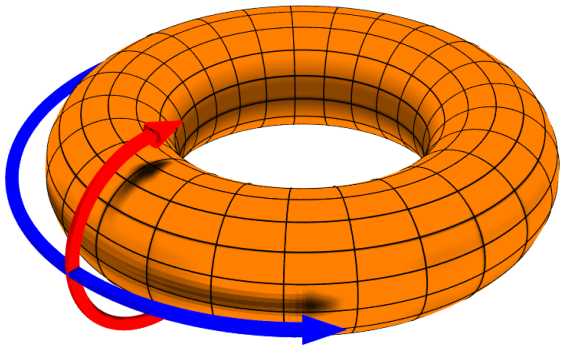

Figure 1.12: Toroidal (blue arrow) and poloidal (red arrow) directions. Figure reproduced from [Burke 2021].

The same year, the Atoms for Peace conference took place in Geneva. The most crucial device was not the tokamak or pinch-based devices but the stellarator of Lyman Spitzer. This device generates the required trajectories of particles without driving a current in the plasma, but only by using specially shaped external magnets, allowing to obtain the appropriate magnetic field configuration. The lack of necessity of the current drive means that the machine can work in a steady-state (continuous in time) way without any applied induction system like in tokamaks. Soviet researchers were first interested in this concept but eventually concluded that the current drive has one enormous advantage: plasma heating. Further investigations showed that both pinch-based machines and stellarators did not show a high enough energy confinement time. After that conference, tokamaks progressed through the years and became the most promising fusion reactor candidate.
The plasma inside a tokamak vacuum chamber can be confined thanks to a set of magnetic coils generating an appropriate magnetic field, as presented in Fig. 1.13. The toroidal field coils create the toroidal component of the magnetic field. Nevertheless, a poloidal component of the magnetic field is necessary to compensate for drifts resulting from the non-uniformity of the toroidal magnetic field. This non-uniformity is generated because the magnetic winding is denser on the torus inner side than in the outer region, as shown in Fig. 1.8. As a result, the total magnetic field generated inside the torus is also not uniform - on the inner side, the so-called high-field side (HFS), the magnetic field is higher, and on the outer side - the low-field side (LFS), the field is lower.
Any force $\vec{F}$ acting on plasma particles is associated with the following drift velocity:

$$\vec{v}_F = \frac{1}{q}\frac{\vec{F} \times \vec{B}}{B^2}. \tag{1.9}$$

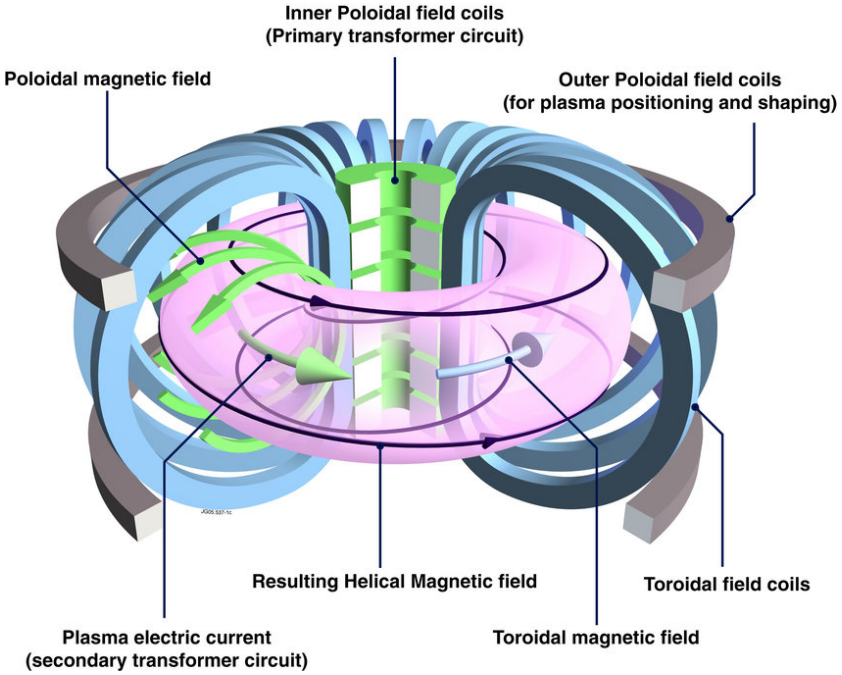

Figure 1.13: Tokamak scheme. Figure reproduced from [Pitts 2006].

Therefore, the nonuniformity of the magnetic field causes the following grad-B drift:

$$\vec{v}_{\nabla B} = \frac{\frac{1}{2}mv_{\perp}^2}{qB}\frac{\vec{B}\times\nabla\vec{B}}{B^2}. \tag{1.10}$$

This drift separates ions and electrons, resulting in a local electric field. The electric field, in turn, generates the so-called $\vec{E}\times\vec{B}$ drift:

$$\vec{v_E} = \frac{\vec{E}\times\vec{B}}{B^2}. \tag{1.11}$$

The above situation is depicted in Fig. 1.14. As a result, this combination of drifts pushes the plasma outwards toward the vacuum chamber walls. Therefore, it is necessary to average the effect of these drifts over a poloidal turn and because of that, magnetic confinement would be impossible without a poloidal magnetic field. The poloidal field coils do not generate the poloidal magnetic field component, as the name could suggest. Instead, they are responsible for plasma positioning and shaping. The current drive generates the proper poloidal component of the magnetic field.

Today, most tokamaks operate in pulsed mode, for which a single experiment represents a plasma discharge lasting not more than a few seconds. In the initial phase of a tokamak plasma discharge, the current is generated inductively based on the transformer principle. The primary winding is the central solenoid of the tokamak, and the secondary winding

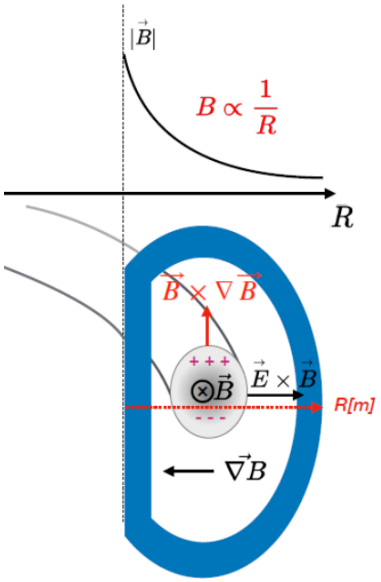

Figure 1.14: Schematic view of grad-B and $\vec{E} \times \vec{B}$ drifts in a tokamak poloidal cross-section. Figure reproduced from [Bielecki 2020].

is the plasma itself. In a tokamak using only the induction method, the discharge time is limited due to two aspects. First, driving a plasma current requires a time derivative of the current in the primary transformer, limited by the current saturation of the central solenoid. Second, the plasma resistance decreases with temperature. Thus, plasma heating by induction is unfortunately only effective for low-temperature plasmas. Any constraint on the plasma duration is undesirable for a fusion power plant due to interruptions in the generated electrical energy [Wesson 2004, p. 136, 718] [Freidberg 2007, p. 119]. Besides the use of superconducting coils, an extended steady-state discharge can only be achieved if the inductive method is used in the initial phase of the discharge and, in a second phase, replaced by other non-inductive heating systems. The auxiliary heating methods are introduced in the next section, and the non-inductive methods of the current drive will be reviewed in Chapter 2.

1.2.4 Tokamak plasma heating

A thermonuclear reactor can be compared to a furnace where the fuel must first be ignited to $T \approx 10\ keV$ before it burns. There are three main, commonly used methods of tokamak plasma heating. However, using one of these methods alone is often not sufficient to obtain the desired plasma conditions. Therefore, it is necessary to use a combination of different methods simultaneously. These plasma heating methods include:

- **Ohmic heating** - This heating method relies on a current flow generated in the

plasma by electromagnetic induction, using a central solenoid. However, as mentioned in the previous section, this system can only be used transiently due to its duration and temperature limitations.

- **Heating with radiofrequency waves** - In this case, electromagnetic waves of specific frequencies can be used to heat the plasma. However, the plasma can efficiently absorb waves only at specific frequencies, for example, the ion cyclotron resonance heating (ICRH) and the electron cyclotron resonance heating (ECRH):

$$w_c = \frac{qB}{m}, \tag{1.12}$$

where m and q are the electron/ion mass and charge, respectively, for ECRH/ICRH. The cyclotron frequencies are in the range of tens of MHz for ICRH and tens of GHz for ECRH. It is also possible to use the Lower Hybrid (LH) frequency in the intermediate range of the GHz.

- **NBI heating** - There is the possibility to inject a beam of fast deuterium atoms into the plasma. The method involves first creating deuterium ions and accelerating them to high speeds. These ions must then be neutralized before entering the plasma since the magnetic field prevents charged particles from reaching the plasma core, as indicated in Fig. 1.15.

1.2.5 Key challenges

The tokamak is currently the leading candidate for becoming a thermonuclear reactor and generating electricity [Xue 2020]. Tokamaks achieved better performance in terms of triple product $p\tau_E T$ at high temperature - where p is the plasma pressure, τ_E - the energy confinement time and T the plasma temperature - than other fusion concepts. This resulted in the construction of many tokamaks around the world [Freidberg 2007, p. 380]. The biggest tokamak currently operating is the Joint European Torus (JET) in Culham, United Kingdom [Woods 2006, p. 4]. However, even in this tokamak and any other in the world, ignition or breakeven have never been achieved. The current record for energy gain factor is held by JET – $P_{fus} = 16$ MW of obtained fusion power by using $P_{heat} = 24$ MW of heating power, thus an amplification factor $Q = P_{fus}/P_{heat} = 0.67$ [ITER].
The largest planned fusion reactor is the International Thermonuclear Experimental Reactor (ITER), currently under construction in Cadarache, France. ITER should be the

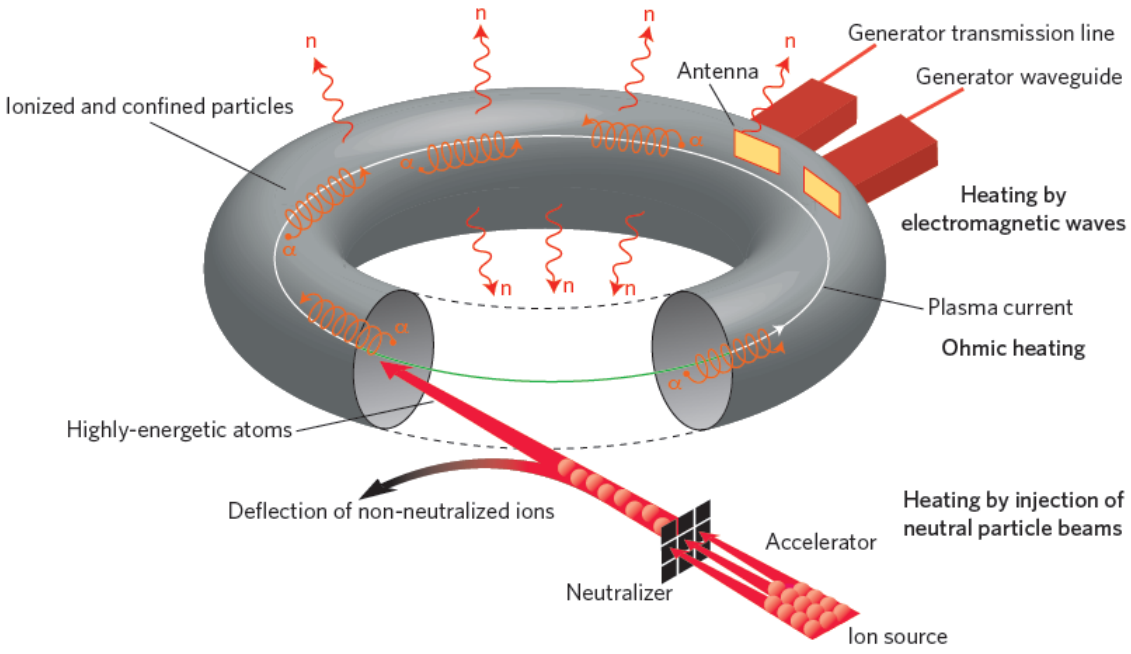

Figure 1.15: Different methods of heating a tokamak plasma. Figure reproduced from [Mazon 2016].

first tokamak capable of obtaining a net fusion energy gain $Q > 1$ from the deuterium-tritium reaction. However, ITER will face several technological and physical challenges, such as fusion power generation and tritium retention. The challenges to the successful design of a fusion reactor can be divided into the following four areas: confinement, disruptions, exhaust and technology [Wesson 2004, pp. 708-711].

- **Confinement** - The generated magnetic field allows obtaining equilibrium with plasma pressure. As a result, nested magnetic flux surfaces are created. The last closed surface of the magnetic field is called the separatrix. Fig. 1.16 shows two possible configurations - limiter and divertor configuration. The divertor allows improving the plasma confinement and plays the role of exhaust pipe extracting from plasma helium and other impurities. In 1982 on the ASDEX tokamak, the divertor configuration allowed obtaining the so-called H-mode (for high confinement mode), characterized by a pressure pedestal at the plasma edge [Wagner 1982]. However, there can be a conflict between high confinement time and alpha particles or impurity exhaust. Methods of proper control of alpha particles and impurity transport in tokamak plasma are still under development and will be crucial for future fusion reactors performance.

- **Disruptions and runaway electrons** - A disruption is an event in which the

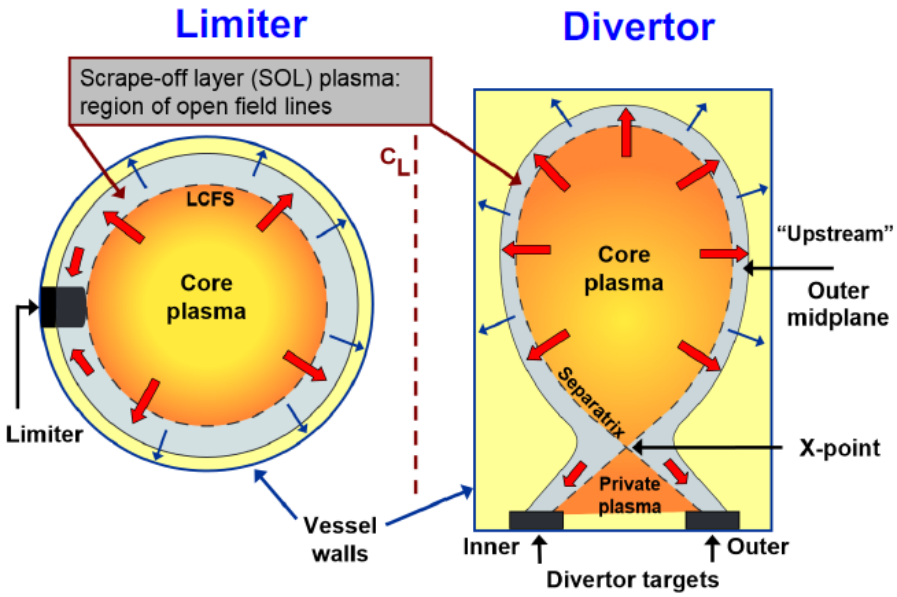

Figure 1.16: Limiter and divertor configuration. Figure reproduced from [Pitts 2007].

plasma discharge is rapidly terminated. Usually, it is a consequence of plasma instabilities. Disruptions cause high forces which can act on elements of the tokamak vacuum chamber. Besides, the current quench phase can lead to the generation of a beam of high-speed electrons, so-called runaways (typically in the MeV range), that can be harmful to some parts of the vacuum chamber and diagnostic systems. Therefore, developing methods for prediction, avoidance and mitigation of disruptions and their consequences is currently one of the most active topics in tokamak research.

- **Exhaust** - 20% of the D-T fusion power goes to the kinetic energy of alpha particles. This energy must be taken from plasma through the surfaces close to the primary plasma or divertor. It means these elements should be resistant to enormous heat flux (typically $10 - 20\ MW/m^2$ in steady-state). However, due to the sputtering and evaporation of these surfaces, they can also be subject to erosion.

- **Technology** - The thermonuclear reactor first wall will be heated to 600 degrees Celsius and must stand high neutrons flux. A tokamak blanket should give the possibility of tritium breeding. Toroidal coils must be superconducting to provide the requested high magnetic field and resistant to sizeable magnetic stress and forces acting on them, e.g. during disruptions. A highly efficient current drive must be applied to allow the reactor to remain efficient over long pulses.

1.2.6 The WEST tokamak

WEST, which stands for Tungsten (**W**) **E**nvironment in **S**teady-state **T**okamak (formerly Tore Supra), is currently the primary French magnetic confinement device, located in the south of France in Cadarache, in the vicinity of the construction site of ITER. A sketch of the WEST poloidal cross-section and its main parameters are presented in Fig. 1.17.

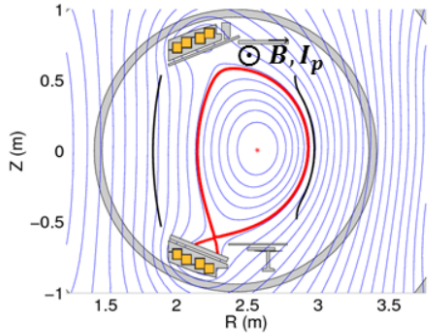

Main WEST parameters	
Plasma current	1 MA (q_{95}~2.5)
Toroidal field	3.7 T @ R=2.5m
Major radius	2.5 m
Minor radius	0.5 m
Aspect ratio	~ 5-6
Elongation	1.35
Triangularity	0.5
Plasma volume	15 m^3
ICRH heating power	9 MW
LHCD heating power	7 MW
Flat-top duration	up to 1000 s

Figure 1.17: Poloidal cross-section (left) and main parameters of the WEST tokamak (right). Figure reproduced from [CEA].

An especially noteworthy feature of WEST is its plasma-facing components (PFCs) which are presented in Fig. 1.18 and consist of the six following elements:

- "The lower divertor target, where the ITER divertor technology is tested,
- The upper divertor target, allowing upper single null operation,
- The baffle, channeling neutrals towards the pumping systems in the lower vertical ports,
- A set of inner bumpers and a movable outer limiter, protecting the vessel,
- The ripple/VDE protections, located on upper vertical port,
- The antennas protections" [CEA]

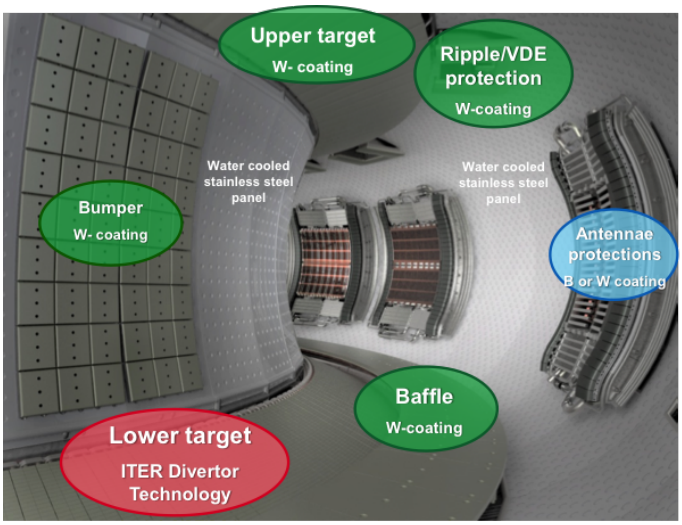

Figure 1.18: Overview of the WEST plasma-facing components. Figure reproduced from [CEA].

From an experimental point of view, in WEST, the most critical component is the ITER-like lower divertor target marked in red in Fig. 1.18. This component is entirely made of W monoblocks. The rest of the PFCs are only tungsten coated. In ITER, PFCs will have to be resistant to high fluxes of heat and particles. Therefore, the primary goal of WEST is to investigate tokamak operation with ITER-like PFCs, focusing mainly on ITER-like divertor. Investigating such kind of operation is essential from a technical, operational and physics point of view.
Furthermore, W impurities are released during plasma operation due to erosion of WEST PFCs caused by the edge plasma. Therefore on WEST, proper methods of controlling W impurities during long tokamak discharges are also essential to investigate [Ghendrih 2015].
The West Research Plan is therefore organized around the two following issues:

1. Testing ITER-like W PFCs with active cooling in a tokamak environment.

2. Operating a tokamak plasma in long-pulse H-mode and steady-state discharges.

1.3 Generation of fast electrons in tokamaks

The presence of fast electrons in tokamak plasma is related to two aspects:

1. **Current drive** - suprathermal electrons can be carriers of the current driven in the plasma.

2. **Runaway electrons** - fast electrons can accelerate further and form an undesirable beam of runaway electrons.

The above two aspects will be discussed in the two following subsections.

1.3.1 Fast electrons and current drive

Ions, slow electrons (thermal) and fast electrons (suprathermal) can be used for the current drive. The present section describes the possibility of using fast electrons for the current drive from a theoretical perspective. Therefore, the following considerations will concern the current drive based on transferring parallel momentum to electrons, but this is not an obligatory condition for all current drive methods - the ECCD method does not use this mechanism.
Let us introduce the following reasoning carried out by J.N. Fisch [Fisch 1987, pp. 178-179]. Let us consider an electron with mass m and charge q. The problem concerns driving current into the direction parallel to the magnetic field. In plasma, electrons collide with other particles with an average collision frequency ν. Let us consider the time $\Delta t = \frac{1}{\nu} = t_2 - t_1$, where t_1 - is the initial time, t_2 is the ending time after which collision happens. During Δt time, the electron does not collide with any particle. The initial electron velocity can be decomposed into parallel and perpendicular to magnetic field components:

$$\vec{v}_1 = \vec{v}_{1\parallel} + \vec{v}_{1\perp}. \tag{1.13}$$

In order to drive a current, the electron is accelerated into a direction parallel to the magnetic field such that, after the time Δt, it has the velocity:

$$\vec{v}_2 = \vec{v}_1 + \Delta\vec{v}_{\parallel}. \tag{1.14}$$

As a result, an incremental current is created, which can be written in the following non-vectorial form:

$$\Delta j = q\Delta v_{\parallel}. \tag{1.15}$$

The considered electron will gain kinetic energy, which can be expressed as:

$$\Delta E_k = \frac{mv_{2\parallel}^2}{2} - \frac{mv_{1\parallel}^2}{2} = \frac{m}{2}(2v_{1\parallel}\Delta v_{\parallel} + (\Delta v_{\parallel})^2) \approx \frac{m}{2}(2v_{1\parallel}\Delta v_{\parallel}) = mv_{1\parallel}\Delta v_{\parallel}. \tag{1.16}$$

Let us consider now how much energy is necessary to obtain a unit of current. This consideration can be done by dividing the energy in Eq. (1.16) by the incremental

current in Eq. (1.15):

$$\frac{\Delta E_k}{\Delta j} = \frac{m v_{1\parallel} \Delta v_\parallel}{q \Delta v_\parallel} = \frac{m v_{1\parallel}}{q}. \tag{1.17}$$

It could be noticed that the ratio in Eq. (1.17) depends on the initial speed of the electron. It means that it is easier to accelerate slow electrons than fast ones. Based on this result, Ohkawa, in 1970, proposed a neutral beam current drive (NBCD) [Ohkawa 1970]. In 1971, Wort proposed a current drive with slow electrons using Alfvén waves [Wort 1971]. However, the current flow must not only be initiated but also maintained. After the initial acceleration, the electron will lose energy to collisions with other particles met on its way. Therefore, the following power must be provided to the electron to maintain current:

$$P = \nu \Delta E_k, \tag{1.18}$$

where ν is the frequency of the electron collisions with other particles. In the most simple picture, the electron after each collision must be accelerated once again to maintain its motion in the magnetic field direction. The collision frequency is high for slow electrons and low for fast electrons. Using Eq. (1.17), it is possible to derive the current:

$$J = \Delta j = \frac{\Delta E_k q}{m v_\parallel}. \tag{1.19}$$

Dividing the current in Eq. (1.19) by the power in Eq. (1.18), it is possible to obtain current drive efficiency:

$$\frac{J}{P} = \frac{q}{m v_\parallel \nu(v)}. \tag{1.20}$$

From Eq. (1.20), one can see that an extremum will be reached when the quantity $v_\parallel \nu(v)$ has a minimum value. It can happen in two cases:

1. $v_\parallel \to 0$ and $v_\perp \approx v_T$, where v_T is thermal speed. It means that the considered electron must be slow, and in this limit, $\nu \approx const$.

2. $v_\parallel >> v_T$ resulting in $\nu \sim \frac{1}{v_\parallel^3}$. It means that the accelerated electron must be fast.

Case 1 cannot be realised in practice because an electron with $v_\parallel \to 0$ and $v_\perp \approx v_T$ is trapped, as shown in Fig. 1.19. Case 2 involves giving parallel momentum to fast electrons. It is the case for lower hybrid waves, which have a high parallel phase velocity, necessary to accelerate fast electrons. However, high phase velocity does not mean high parallel momentum. Alfvén waves have higher parallel momentum than lower hybrid waves. In turn, electron cyclotron waves have almost no parallel momentum. For this reason, the current drive efficiency of these three methods is presented in Fig. 1.20.

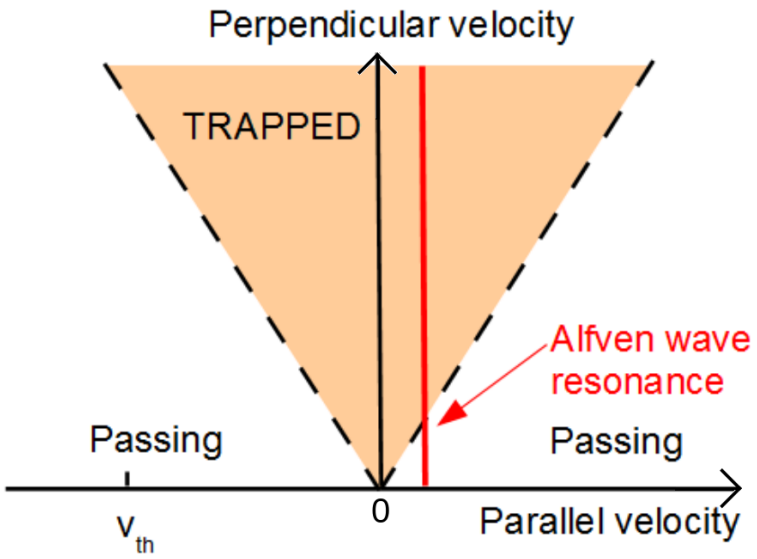

Figure 1.19: Electron velocity space. It is possible to distinguish the region of trapped electrons (the light orange one) for electrons having a relatively small parallel velocity component than the perpendicular one. The red line shows that only a few electrons with Alfvén waves resonant speed are passing electrons. Figure adapted from [Peeters 2013].

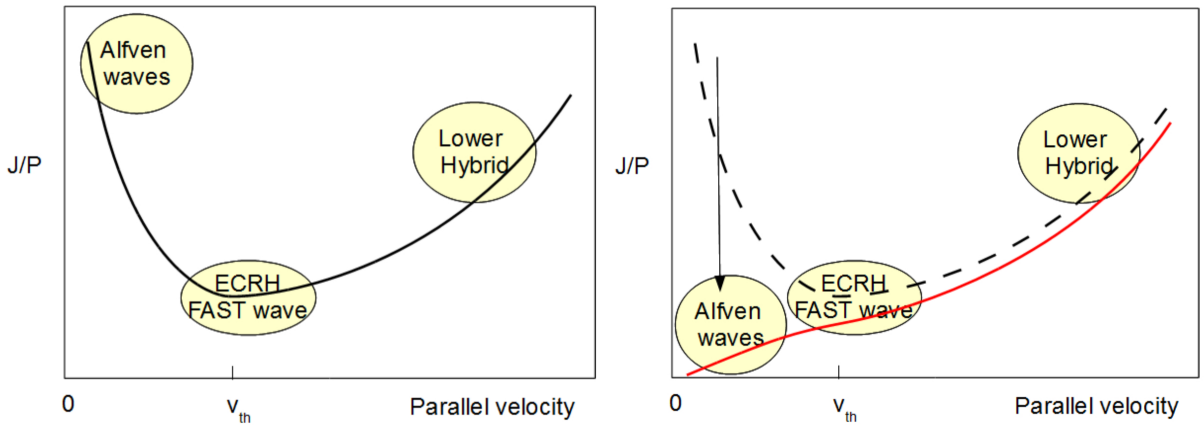

Figure 1.20: Comparison of current drive efficiency for four methods using plasma waves: Alfvén waves, electron cyclotron waves, fast ion cyclotron waves and lower hybrid waves. Figures show current drive efficiency for Alfvén waves before (left figure) and after (red curve on the right figure), considering the trapped nature of accelerated electrons. Figure adapted from [Peeters 2013].

The use of LH waves to drive current was proposed by J.N. Fisch in 1978 [Fisch 1978]. LH waves are currently the most efficient off-axis current drive method, as depicted in Fig. 1.21, and will be described in more detail in Chapter 2.

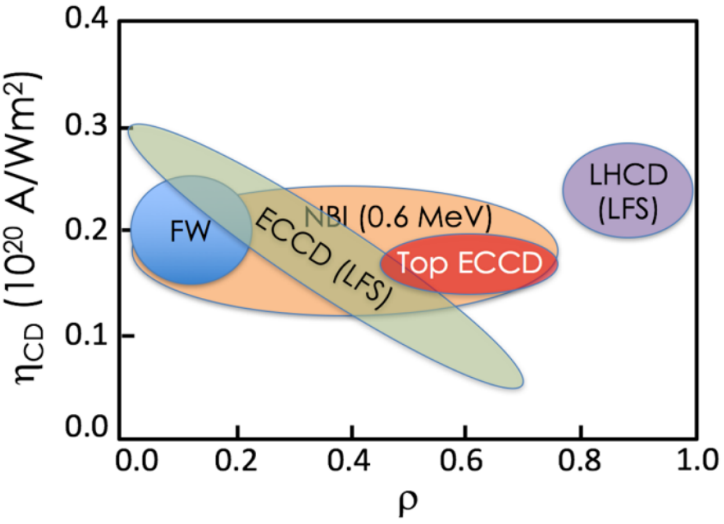

Figure 1.21: The non-inductive current drive efficiency for different methods as a function of the minor radius. Figure reproduced from [Chen 2019].

1.3.2 Runaway electrons

The collision frequency ν of fast electrons with the bulk plasma is expressed as follows [Nilsson 2015, p. 8]:

$$\nu = \frac{e^4 n_e \ln \Lambda}{4\pi\varepsilon_0^2 m_e^2 v^3} \sim \frac{1}{v^3}, \tag{1.21}$$

where m_e, e - are the electron mass and charge, n_e - is the electron density, ε_0 - is the vacuum permittivity, $\ln \Lambda$ - is the Coulomb logarithm and v - is the electron speed. Fast electrons are more collisionless than slow electrons since the collision frequency decreases with the velocity, as shown in Eq. (1.21). It means that even a relatively low electric field can effectively accelerate fast electrons up to relativistic speeds in tokamaks. Such fast electrons are called runaway electrons (RE). A beam of RE can significantly damage the first wall of the tokamak vacuum chamber. RE are a critical research topic, and the development of methods to predict, avoid or mitigate them is intensively pursued [Reux 2015].

Let us consider how this type of RE beam can be generated. Plasma can be considered as a fluid in which a friction force acts on electrons moving in it. This force is depicted in Fig. 1.22 as a function of electron kinetic energy. Two regions can describe the friction force for electrons in the plasma. For electrons slower than thermal velocity, the friction force behaves similarly to classical gas - it increases almost linearly with velocity. For electrons with a velocity higher than thermal velocity, this force can be expressed by the

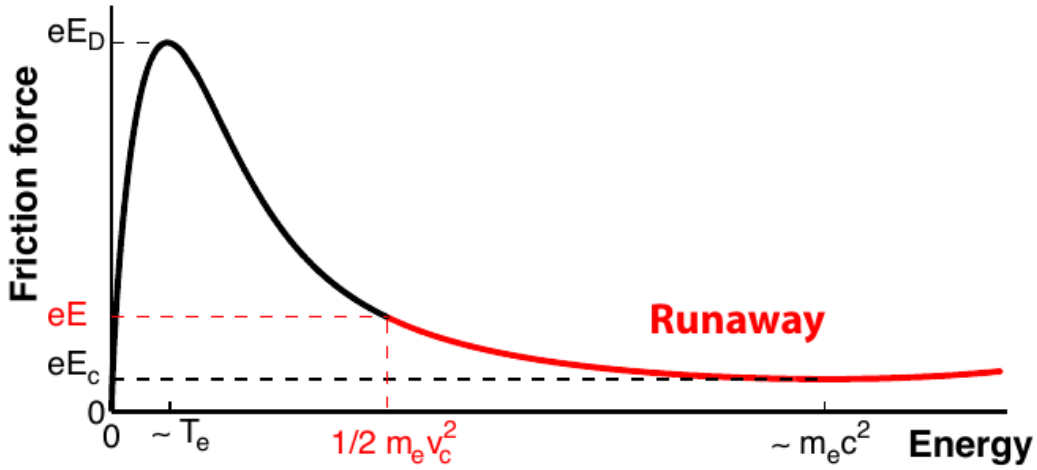

Figure 1.22: Friction force acting on an electron in plasma as a function of the electron kinetic energy. Figure reproduced from [Nilsson 2015].

following formula [Nilsson 2015, p. 11]:

$$F_f(v) = mv\nu \approx m_e v \frac{n_e e^4 \ln \Lambda}{4\pi\varepsilon_0^2 m_e^2 v^3} \sim \frac{1}{v^2}. \tag{1.22}$$

For the case where only the electric force and the friction force act on the electron, it is then possible to write the equation of motion for an electron moving in an electric field in the following form:

$$m_e a = eE - F_f. \tag{1.23}$$

The electron will be accelerated only if:

$$E > \frac{F_f}{e}. \tag{1.24}$$

So, it turns out that the generation of an RE beam can take place only if the electric field is higher than the particular critical electric field E_c value:

$$E_c = \frac{F_f}{e} = \frac{m_e v\nu}{e} = \frac{n_e e^3 \ln \Lambda}{4\pi\varepsilon_0^2 m_e c^2}. \tag{1.25}$$

The condition in Eq. (1.24) shows that the main parameter governing runaway electrons production is the tokamak electric field. Moreover, if the electric field is higher than the so-called Dreicer field, then all electrons in plasma become RE:

$$E_D = \frac{1}{4\pi\varepsilon_0^2} \frac{n_e e^3 \ln \Lambda}{m_e v_{T_e}^2}, \tag{1.26}$$

where v_{T_e} - is the electron thermal speed. The maximum friction force occurs for electrons with thermal speed. If an electron has a low enough velocity, its acceleration by the electric field is compensated by the friction force. However, it follows from the Fokker-Planck equation that there are two ways in which such kind of electron can go into the so-called runaway mode:

1. Increasing the electric field over the Dreicer field value.
2. Increasing the electron velocity over the so-called critical velocity.

Depending on the value of the electric field, three different cases can be distinguished:

1. If $E > E_D$, then all electrons of the plasma become runaway electrons.
2. If $E < E_c$, none of the electrons can become a runaway electron.
3. For $E_c < E < E_D$, two types of electrons exist. Electrons from the region where the curve is black are electrons in the so-called ohmic mode. They have a velocity smaller than the critical velocity v_c. Electrons from the region where the curve is red have a velocity higher than critical velocity v_c and are in the runaway mode.

Based on Eq. (1.25), it is possible to notice that $E_c \sim n_e$. So simply saying the tokamak should be safe from runaway electrons at high plasma densities. The number of runaway electrons is significantly reduced for densities $n = 10^{19} - 10^{20}\ m^{-3}$ and higher, typical in tokamak plasmas. However, RE can appear in the ramp-up phase of a discharge or later when plasma stability is lost and its density decreases drastically (for example, during disruptions).
However, conducted experiments [Martín-Solís 2010, Paz-Soldan 2014, Granetz 2014] showed that this simple formula derived in 1959 by Dreicer does not match the experimental results obtained for tokamak plasmas. In reality, the critical electric field above which all plasma electrons become runaway electrons is far higher than the one predicted by the Dreicer formula. Models giving a good matching with experiments were proposed in [Stahl 2015] and [Ismailov 2016]. One of the proposed solutions to deal with the RE problem is to develop a system capable of predicting RE and mitigating them using an injection of noble gases like neon or krypton [Reux 2015].

1.4 Impact of impurities

Two different criteria can categorise impurities in a tokamak plasma [Ivanova-Stanik 2020].

1. Classification based on the origin of impurities:

   - **Internal impurities** - impurities that appear in the plasma due to tokamak operation, such as:
     - Helium-4 nuclei as products of DT reaction,
     - Ions of other elements due to an erosion of the first wall plasma-facing components (PFCs).
   - **External impurities** - injected voluntarily into the plasma for plasma control or impurity transport studies, either by gas puffing, Laser Blow-Off (LBO) or pellet injection. In the first method, examples of such gases are nitrogen and noble gasses like neon, argon or krypton, particularly for disruption mitigation purposes.

2. Classification based on the atomic number Z:

   - **Low-Z impurities** for $Z < 10$, easily fully ionized in a tokamak plasma, such as Be, N, O.
   - **Middle-Z impurities** for $10 \leq Z \leq 40$, usually fully ionized in the plasma core but not fully ionized in the plasma edge, such as Ar, Ni, Fe and Cu.
   - **High-Z impurities** for $Z > 40$, for which multiple ionization states coexist in the plasma core, for example, W, Mo.

1.4.1 The transition from carbon to tungsten components

ITER will not use carbon composites as structural elements of the so-called first wall, like previous tokamaks. This decision is motivated by restrictions on the amount of tritium that the vacuum chamber walls can trap. Instead, ITER will have to use high atomic number Z elements for components in direct contact with the plasma, such as tungsten (W) or molybdenum (Mo). ITER, in particular, will work with a tungsten divertor [Pitts 2019] which is presented in Fig. 1.23. W has a low retention rate of tritium. Moreover, its high thermal conductivity and melting point make this material resistant to high heat streams from the plasma under steady-state conditions, up to $10 - 20$ MW/m^2. However, W impurities in the plasma are the major disadvantage of this solution. W impurities enter the plasma because of the erosion of divertor plates by physical sputtering. In addition, non-fully ionized impurities increase plasma energy loss by electromagnetic radiation (EM) due to collisions with free electrons in the plasma. For example, the average ionization level of tungsten is between W^{20+} and W^{50+} for typical tokamak plasma core temperatures of $T = 1 - 10$ keV.

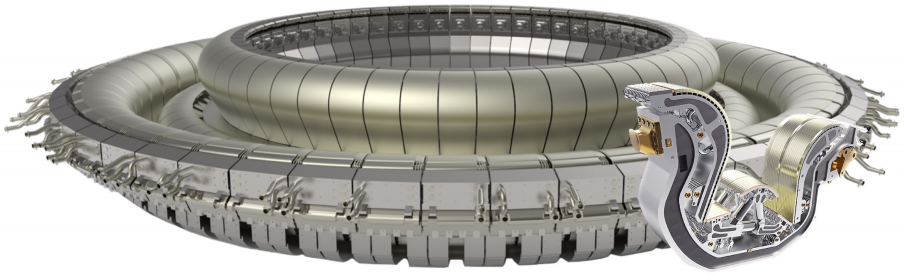

Figure 1.23: ITER tungsten divertor. Figure created by ITER Organization and reproduced from [IAEA].

1.4.2 Wall erosion and impurity transport

Impurities can harm the tokamak operation for two reasons: plasma dilution and increase of the radiation losses. The cross-field transport of impurity ions leads to their radial diffusion and convection in the plasma. In particular, impurities may travel towards the plasma core and accumulate there, which is very unfavourable and may even lead to termination of the plasma discharge in the tokamak.
Erosion of PFCs can happen through many mechanisms. The most critical processes are physical sputtering, chemical sputtering, erosion by arcs, and blistering [Ivanova-Stanik 2020]. For example, Fig. 1.24 shows that PFCs erosion can be caused by sputtering with deuterium bombardment.
Such kind of sputtering for carbon components is higher than for tungsten. For carbon, this sputtering occurs for energies $>$ 10 eV so that it will occur in standard tokamak operation. In the case of W, minimal deuteron energy of around 200 eV is needed. The temperature in the scrape-off layer region is usually $T_e < 100$ eV. It means that tungsten components should a priori be safe from such sputtering. However, because of ELMs and sputtering by other impurities in plasma, W components are also subject to erosion. Impurity ions move in the plasma along magnetic field lines, but three transport mechanisms can perturb this trajectory:

- **Magnetohydrodynamic (MHD) activity** - The appearance of magnetic islands can lead to the local short-circuit of the plasma between core and edge and dramatically increase the radial particle and heat transport, sometimes leading to global disruption of the plasma [Chapman 2010, Ahn 2016].

- **Turbulent transport** - caused by fluctuations of the electromagnetic field in the

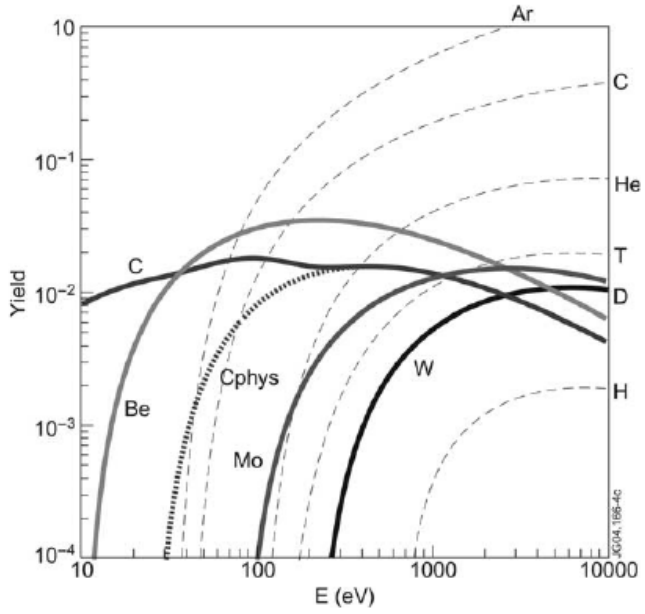

Figure 1.24: Sputtering yield for various materials due to bombardment by deuterium. Figure reproduced from [Matthews 2005].

spatial scale much greater than Debye length.

- **Neoclassical transport** - caused by particles collisions that lead to diffusion in the velocity space, including the electromagnetic drifts inherent to the tokamak geometry, which lead to a net radial transport.

For heavy impurities like W, which are mainly considered in this thesis, neoclassical transport is dominant [Donnel 2018]. In contrast, in the case of light impurities, turbulence can play a dominant role. For heavy impurities, the neoclassical transport theory implies that the inward impurities flux is created because of the electron density gradient. Conversely, the temperature gradient is linked with an outward impurity flux, referred to as temperature screening. However, poloidal asymmetry of the impurity density [Angioni 2014] and poloidal asymmetry of the electric potential [Donnel 2019] can complicate this picture. These asymmetries can be caused by heating systems, plasma turbulence, and friction forces [Angioni 2012, Angioni 2017, Jardin 2021]. Because heavy impurities are mainly governed by neoclassical transport, this transport will be described in more detail.

Classical transport of particles and energy in tokamak plasma, in particular, happens thanks to Coulomb collisions, as depicted in Fig. 1.25. In this framework, the diffusion coefficient has the form:

$$D \sim \frac{\rho^2}{\tau_c}, \tag{1.27}$$

where ρ - is Larmor radius, τ_c - is the characteristic time between collisions. Due to plasma quasineutrality, the electrons and ions must diffuse radially at the same speed. This is the simplest picture and corresponds to ambipolar diffusion.

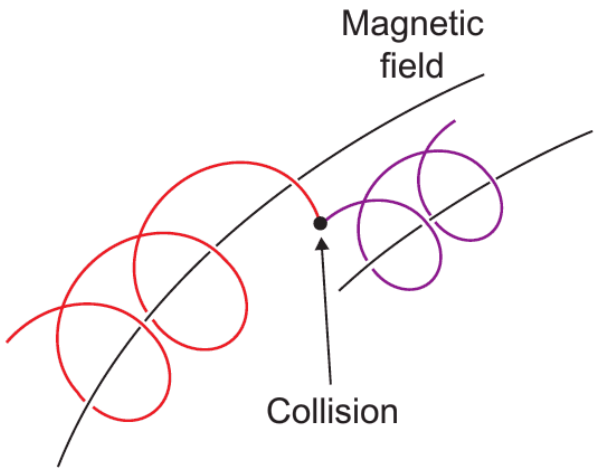

Figure 1.25: Schematic changing of guiding magnetic field line of a charged particle after collision with another particle. Figure reproduced from [McCracken 2012, p. 47].

However, in the case of a toroidal configuration, the situation is more complicated, and the theory describing diffusion, in this case, is the neoclassical theory. The total radial flux of impurities is usually expressed as the result of two processes, diffusion and convection, in the following way:

$$\vec{\Gamma_Z}(r) = -D_z \vec{\nabla}_r n_Z + n_Z \vec{V_z}, \tag{1.28}$$

where Z - is the index for particular particles species and D_Z, V_Z - are diffusion and convection coefficients of particles species Z. However, even neoclassical theory does not always give results matching experimental ones, giving sometimes smaller diffusion coefficient values than experiments. This experimentally observed increased transport is called anomalous transport. Up to now, there is no theory explaining this discrepancy fully satisfactorily. It is believed that fine-scale turbulent fluctuations could cause this difference [McCracken 2012, p. 116].

In the case of neoclassical transport, it is possible to distinguish different transport regimes for different plasma collisionality, as shown in Fig. 1.26. If the plasma has a low temperature, it can be in a highly collisional regime called the Pfirsch-Schlüter regime. Plasma with low collisionality allows particles to make full poloidal turns along magnetic field lines. The particle's poloidal cross-section trajectory has a banana shape for particles with a high pitch angle (trapped particles) and a circular shape for those with a low pitch angle (passing particles). This poloidal trajectory of trapped particles is

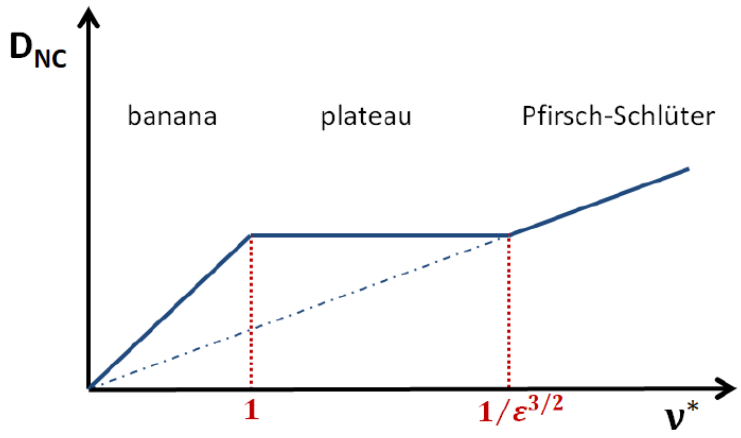

Figure 1.26: A simplified picture of the neoclassical diffusion coefficient D_{NC} as a function of the collisionality ν^* (ε - is inverse tokamak aspect ratio), showing different transport regimes: banana, plateau and Pfirsch-Schlüter. Figure reproduced from [Jardin 2017].

called the banana orbit. Trapped particles and passing particles trajectories are described more in detail in Appendix A.1.

For an estimated range of possible diffusion coefficients, neoclassical transport gives the bottom border of this limit - real values of diffusion coefficients are not smaller than predicted by neoclassical transport. Neoclassical ion thermal conductivity has an order of magnitude of $\chi_i \approx 0.1\ m^2/s$. However, in the case of tokamak discharges in L-mode, values of ion or electron heat conductivities are from the range of $1 - 10\ m^2/s$. Experimentally measured heat conductivity for ions is one order of magnitude higher, and for electrons, it is two orders of magnitude higher [Wolf 2002, p. 9]. Also, for H-mode discharges, experimental values of diffusion are higher than neoclassical values.

It is possible to distinguish five different transport regions in plasma, as shown in Fig. 1.27 [Parail 2002].

1. The first one is the Scrape-off Layer region located outside the separatrix. In this region, transport occurs through open magnetic field lines. It is also noteworthy that the particles emitted from the first wall enter this region first.

2. The second region, close to the separatrix, is Edge Transport Barrier (ETB) region. Here the transport is very close to the neoclassical, and a high-pressure gradient is formed in H-mode discharges. Due to this pressure gradient, so-called Edge Localised Modes (ELMs) can form, which are a type of MHD instabilities.

3. The third region is located between edge plasma and core plasma. Transport is governed here by ELMs, turbulence and charge exchange with neutral particles.

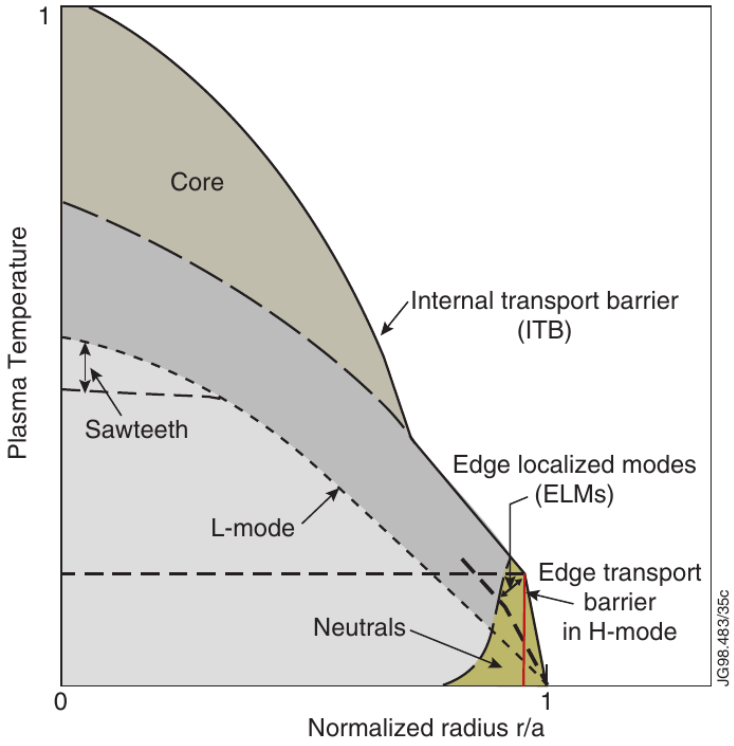

Figure 1.27: Regions of different transport in a tokamak plasma. Figure reproduced from [Parail 2002].

4. The fourth region is in the range of $0.4 < r/a < 0.8$. Here, anomalous transport occurs mainly. There are no intensive MHD instabilities. It is important that here, a so-called Internal Transport Barrier (ITB) can be created, reducing anomalous transport.

5. The fifth region is in the range of $r/a \leq 0.4$. The very core of the plasma can see the appearance of an MHD called sawteeth, corresponding to a periodic relaxation (flattening) of the pressure profile.

1.4.3 Radiation losses

Three different processes can contribute to impurity radiation in tokamak plasmas:

- **Bremsstrahlung radiation** - charged impurity ions can emit electromagnetic radiation in a continuous spectrum due to their velocity change during Coulomb collisions with other charged particles in the plasma.

- **Radiative Recombination** - an inverse process to ionization in which a free electron can recombine to an impurity ion. The process occurs with the emission of electromagnetic radiation in a semi-continuous spectrum.

- **Line emission** - in this process, free electrons of plasma can collide with bound electrons of impurity ions. Therefore, such bound electrons can be excited to higher energy levels and then spontaneously decay to a lower state, emitting photons of specific energies and leading to a discrete emission spectrum.

Due to energy loss by radiation, impurities narrow the operational domain in which reaching the break-even or ignition is possible, as shown in Fig. 1.28. For W concentrations above $c_W = 1.9 \cdot 10^{-4}$ ignition is impossible. However, it is for hypothetical DT plasma with only helium ashes and tungsten impurities. In a real reactor, other impurities will also be present. Based on that, the maximum tolerable W concentration in tokamak core plasma is estimated to be of the order of several 10^{-5} [Pütterich 2010].

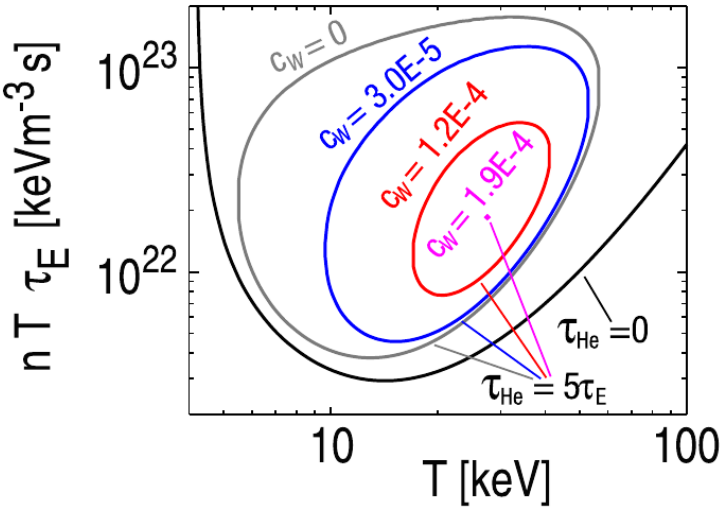

Figure 1.28: Shrinking domain of ignition in DT plasma with helium ashes and tungsten impurities. Figure reproduced from [Pütterich 2010].

The radiated power $P_{r,Z}$ of an impurity species Z can be expressed in the following way:

$$P_{r,Z} = n_e^2 c_Z L_Z(T_e), \tag{1.29}$$

where $c_Z = \frac{n_Z}{n_e}$ - is impurity concentration, L_Z - is the cooling factor of species Z. The cooling factors for different elements are depicted in Fig. 1.29.

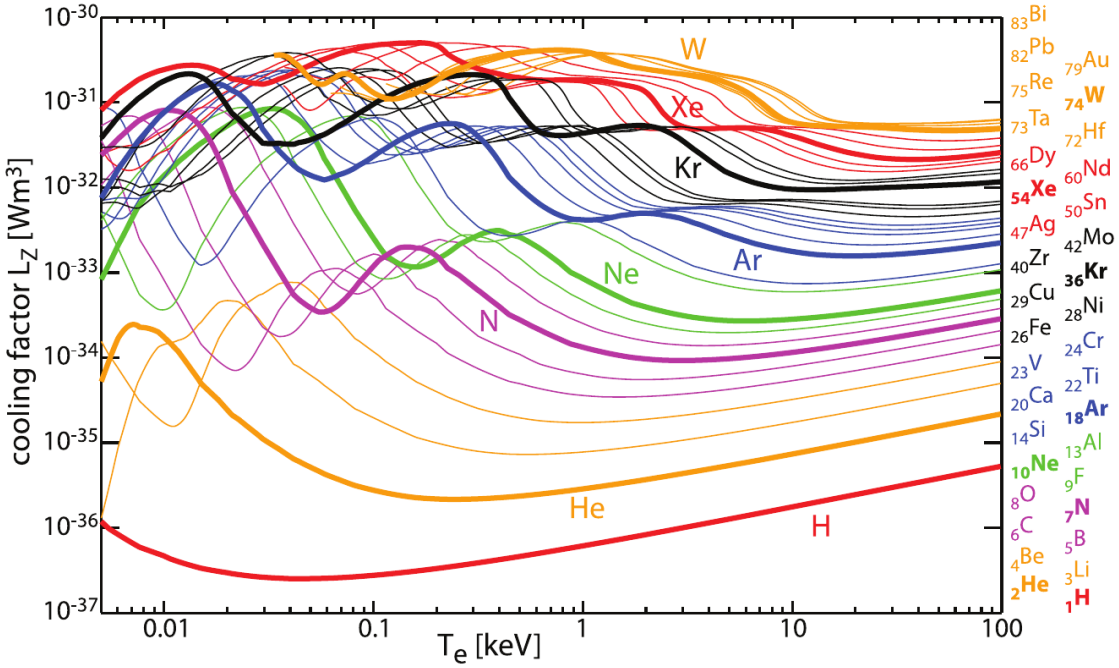

Figure 1.29: Cooling factors for chosen elements in the range $1 \leq Z \leq 83$. Figure reproduced from [Pütterich 2019].

It is noticeable that the cooling factor is increasing with the atomic number. In particular, the W cooling factor (in orange) is several orders of magnitude higher than the one of carbon (in purple).

Chapter 2

Non-inductive current drive

Contents

2.1 Introduction

Non-inductive methods of current drive in tokamaks can be categorized by particles that are the current carriers:

- **Ions methods** - i.e. Neutral Beam Current Drive (NBCD), Ion Cyclotron Current Drive (ICCD) with ion minority species,
- **Electrons methods** - i.e. Electron Cyclotron Current Drive (ECCD), Lower Hybrid Current Drive (LHCD), Alfvén waves.

The case of methods with electrons as carriers of current can be divided into two groups regarding the initial energy of electrons in which energy will be deposited:

- **Slow electrons methods** (thermal electrons), i.e. using Alfvén waves,
- **Fast electrons methods** (suprathermal electrons), i.e. using Lower Hybrid or Electron Cyclotron waves.

Electron methods can also be divided by the mechanism of the current generation:

- **Parallel momentum transfer** to electrons (LHCD, Alfvén waves).
- **Without parallel momentum transfer** to electrons (ECCD).

There are five primary methods of generating current non-inductively in tokamaks: neutral beam injection, lower hybrid current drive, fast wave electron current drive, electron cyclotron current drive and fast wave minority ion current drive [Wesson 2004, p. 136-146]. All of them have different limitations and can be used for different current drive purposes. Therefore, in this chapter, different non-inductive current drive methods will be introduced, with a focus on the LHCD method.
The possibility of employing plasma waves to generate current in a torus was discovered in 1952 by Thonemann [Fisch 1987, p. 177]. Thonemann used a small toroidal glass tube containing plasma in which he generated current using waves. In the 1960s, it was discovered that the tokamak performance improves if the toroidal current is continuous. At that time, the current drive was achieved by NBI [Ohkawa 1970] or Alfvén waves [Wort 1971].
After many years of research, it occurred that the most efficient method in terms of the current-to-power ratio is LHCD [Westerhof 2010, Peysson 1999, Hillairet 2015]. However, LH waves have low penetration ability and eventually - according to the 2018 ITER Organization report - chances that LH waves will be ever used in ITER are meagre

[ITER Organization 2018, p. 377-378]. Instead, ITER will be using three other methods: NBI, ICCD and ECCD [ITER Organization 2018, p. 356]. Even though ITER will likely not be using an LHCD system, the ECCD method will drive the current of fast electrons, and plasma will contain tungsten impurities. Despite the above concerns, the LHCD method is still an essential topic for investigation regarding possible applications for the first thermonuclear power plant DEMO and future fusion reactors.
Non-inductive methods of current drive give the possibility of steady-state (continuous) operation of the tokamak, which is very desirable because of the following advantages [Fisch 1987, p. 181]:

1. One of the most significant issues for future thermonuclear reactors working in pulsed mode would be heat stresses on the wall due to critical temporal fluctuations of the surface temperature. In such a case, the lifetime of tokamak components would be significantly lower than in steady-state operation, where much smaller temperature fluctuations are present.

2. One of the threats to large tokamaks is disruptions. Disruption is a sudden loss of confinement resulting in termination of the plasma discharge. In steady-state operation, it is possible to choose a regime of tokamak operation with a low probability of disruption. However, in pulsed operation, the tokamak would be going through a spectrum of different regimes, with changes in many parameters, thus with a higher probability of disruption. Disruption can damage some essential plasma-facing components, other structural elements or diagnostics irreversibly, forcing the shutdown of tokamak operation.

3. Not using a central solenoid could provide more free space, which could be used for shielding material or energy extraction.

4. In a pulsed reactor, superconducting coils generating a toroidal field need better refrigeration than in the case of a steady-state (continuously working) reactor. Changing the magnetic field can generate inductive losses in the coils.

5. Downtime in the continuous operation is shorter than in the case of pulsed tokamaks. In a pulsed tokamak, during downtime, it is necessary to reset the transformer coils. It is possible to reduce this time, but this needs expensive power supplies and some temporary storage of the plasma thermal energy.

These reasons make the continuous operation of tokamak one of the main goals of fusion research. However, non-inductive current drive methods also have another significant

advantage: they allow obtaining a current density profile independent of the plasma temperature and provide the possibility of controlling plasma stability [Westerhof 2010, p. 323].

All of the methods of current drive can also be used for plasma heating. However, it does not mean that a particular method can be used efficiently at the same time for both purposes. For example, efficient LHCD needs asymmetric power spectrum, and efficient LHRH needs symmetric power spectrum - two different scenarios of the LH method that can not be realised simultaneously [Freidberg 2007]. This difference can be seen in Fig. 2.1.

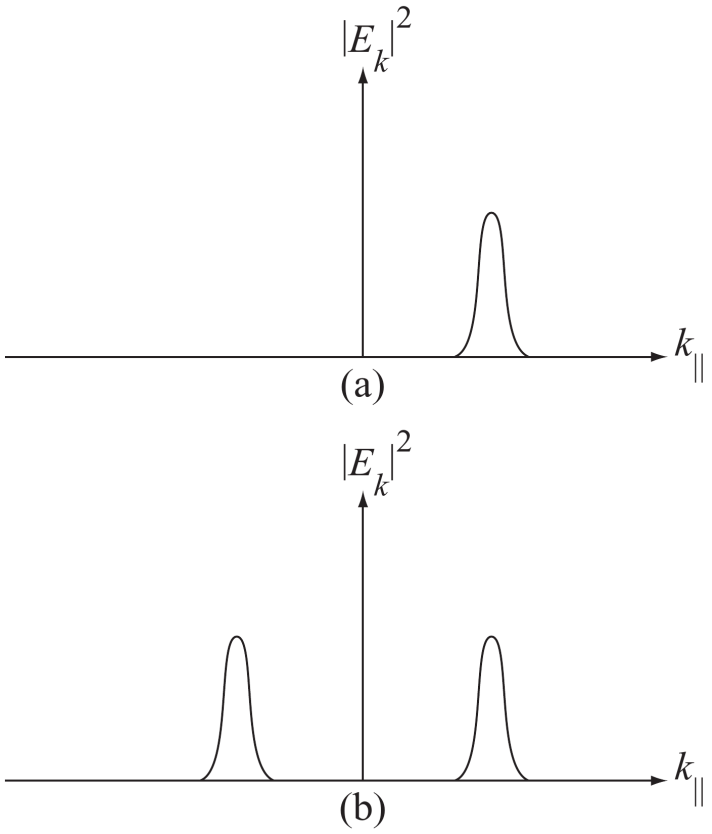

Figure 2.1: Spectra of LH electric energy for the cases: (a) of current drive (asymmetric) and (b) heating (symmetric). Figure reproduced from [Freidberg 2007, p. 610].

The existing heating methods already allow obtaining the needed high temperature of a tokamak plasma. The main difficulty is that current drive is not as efficient as plasma heating. Furthermore, none of the existing methods is efficient enough by itself - each of them needs too much power to generate current at the required level.

A crucial quantity to compare different current drive methods is the current drive efficiency, defined as the ratio of current density over the power density used to drive

current. However, to compare current drive between different methods used on different present and future machines (for example, extrapolation for ITER), it is more convenient to define the current drive efficiency η_{CD} in the following way [Westerhof 2010, p. 323]:

$$\eta_{CD} = n_e R I_{CD}/P, \tag{2.1}$$

where n_e - is the electron density, R - is the major radius of the tokamak, I_{CD} - is the total driven current and P - is the total power used to drive current. The total power P scales as $P \sim 2\pi R \pi a^2 p$, where a - is the tokamak minor radius and p - is the power density used to drive current. The total driven current I_{CD} scales as:

$$I_{CD} \sim \pi a^2 j, \tag{2.2}$$

where j - is the current density. The current density j is inversely proportional to the electron density:

$$j \sim 1/n_e. \tag{2.3}$$

It means that the current drive efficiency defined in such a way is independent of plasma density for a specific machine and heating method.

2.2 Bootstrap current

Using any combination of the presently known current drive methods is a priori not allowing to obtain the necessary level of plasma current in a fusion reactor, with an energy cost that would make the reactor economically profitable [Freidberg 2007, p. 490]. However, this problem can be solved in the following way. Instead of increasing the externally imposed non-inductive current, it is possible to use the so-called bootstrap current. Its most significant advantage is the fact that it is self-generated in the plasma. The bootstrap current is a consequence of the coexistence of a plasma pressure gradient and a poloidal magnetic field. Plasma particles are subject to plasma pressure which pushes them outwards. This direction of motion is perpendicular to the poloidal field generated by the toroidal current. As a result, a magnetic force acts on such particles, changing the direction of this radial motion into the toroidal direction, as depicted in Fig. 2.2. The whole process of the bootstrap current generation is more complicated than in the simple picture presented here, which is, however, sufficient to understand the nature of this phenomenon. Using bootstrap current instead of an externally imposed current allows minimizing the cost of current drive in a tokamak plasma. Furthermore, research on TCV tokamak has shown that it is possible even to perform a tokamak

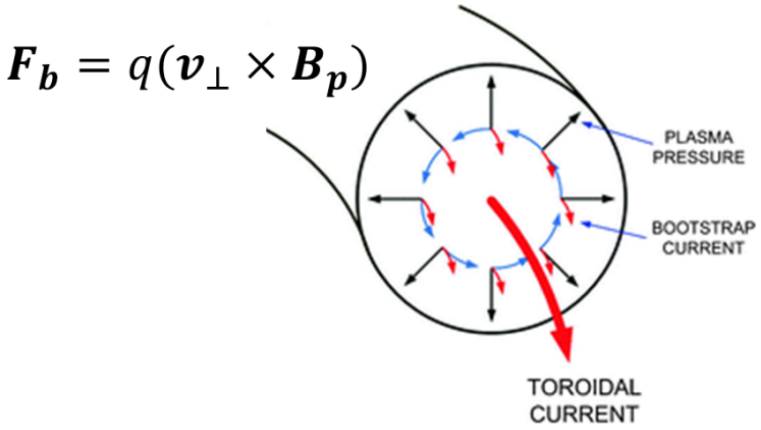

Figure 2.2: Bootstrap current. Figure adapted from [Chen 2011, p. 257].

discharge without current drive - with bootstrap current as of the only component of the current [Coda 2008, p. 3]. Such an advanced tokamak scenario in which the bootstrap current represents the major part of the plasma current is the most promising scenario for tokamak operation and, particularly, for ITER.

2.3 Neutral Beam Current Drive (NBCD)

One of the main ways to generate an electric current in a tokamak plasma is to inject fast beams of neutral particles. The principle of this method can be seen in Fig. 2.3. The injected neutral particles become ionized by collisions with plasma particles. As a

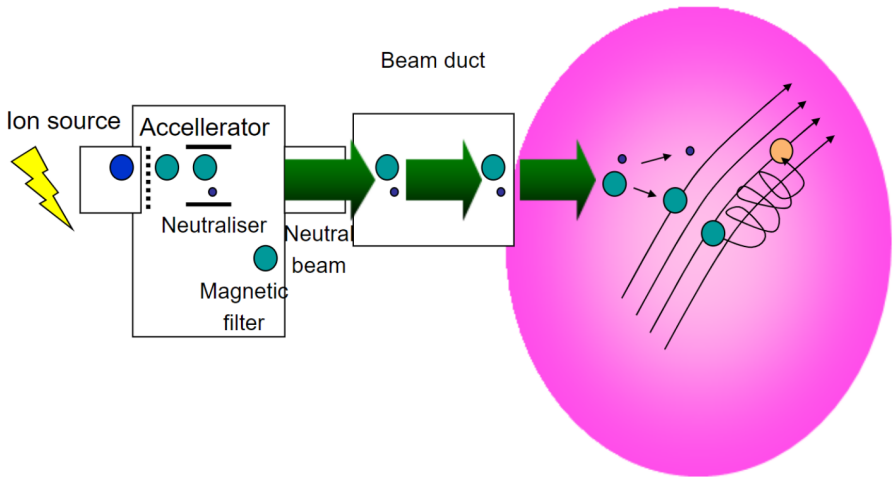

Figure 2.3: Principle of NBI. Figure reproduced from [Mlynář 2016].

result, the injected beam becomes a beam of fast ions circulating around the tokamak. These ions are carriers of a net electric current, which makes this method classified as the

fast ions current method [Wesson 2004, p. 137]. The biggest drawback is that such ions circulating around the torus give momentum to electrons. These electrons, moving in the same direction as the fast ions, constitute an electric current in the direction opposite to the current generated by fast ions, thus reducing it.
To understand what can be done to deal with this problem, Fisch proposed considering this problem in the zero ion current frame of reference [Fisch 1987, pp. 205-207]. Such kind of reasoning leads to two possible schemes of NBCD, which are depicted in Fig. 2.4. The total ion current consists of two components: fast ions generated by NBI (marked by a red ball in Fig. 2.4) and thermal ions of the bulk plasma (marked by a blue ball in Fig. 2.4).

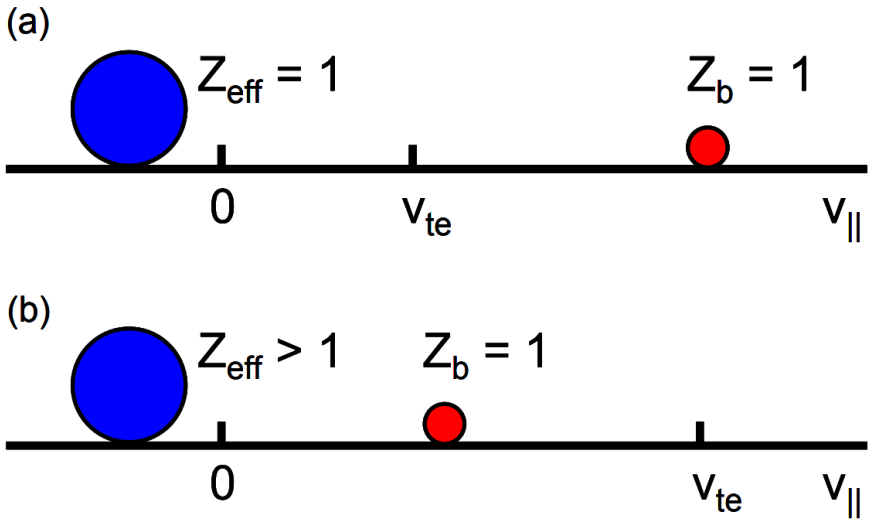

Figure 2.4: Two different ways of NBCD: (a) thanks to velocity of injected particles far higher than electron thermal velocity and (b) thanks to the difference between charge state of bulk ions Z_{eff} and the atomic number Z_b of injected particles. Figure reproduced from [Westerhof 2010, p. 327].

In the first scheme, we inject neutral particles with velocities far higher than the thermal velocity of electrons, i.e. $v_{||} >> v_{te}$. Let us assume that, when tokamak is viewed from the top, bulk ions go in the clockwise direction along magnetic field lines, which means that they constitute an ion current in this direction. Let us consider that the second current - fast ion current corresponding to the injected neutral particles - goes into the anticlockwise direction. Let us choose the reference frame in which the total current of the above mentioned two kinds of ions equals zero. What is needed is that the population of bulk ions moving in the clockwise direction will collide more efficiently with electrons than the population of fast ions moving in the anticlockwise direction. In such a case, electrons would obtain momentum in the clockwise direction, constituting current in the

anticlockwise direction. However, this is not a practical approach because of the high power which has to be provided to the injected beam.

The second scheme allows injecting neutral particles with relatively low energies, lower than the thermal energy of electrons, i.e. $v_{||} < v_{te}$. In this scheme, we also need to obtain the current of electrons in a zero ion current frame of reference. To do this, we consider a plasma with an effective charge state Z_{eff} of bulk ions satisfying the condition $Z_{eff} > Z_b$, where Z_b is the atomic number of ions injected by NBI [Fisch 1987, p. 205]. Once again, like in the first scheme, fast ions moving in the anticlockwise direction will interact through Coulomb collisions weaker, because of their lower charge, with electrons than bulk ions moving in the clockwise direction. So, electrons will be pushed in the clockwise direction, constituting a current in the anticlockwise direction. This second scheme is most often used for NBCD in tokamak plasmas.

Neglecting the trapped electron effect, the formula for NBCD current density has the following form:

$$J = (1 - \frac{Z_b}{Z_{eff}})J_b, \tag{2.4}$$

where Z_b - is the atomic number of ions in the ion beam generated by NBI, Z_{eff} - is the effective charge of bulk ions and J_b - is the current carried by the ion beam generated by NBI. The effect of reducing the NBI current by the electron current decreases if the impact of trapped electrons is taken into account. In the case of tokamaks with a large aspect ratio, the formula for current density takes the form:

$$J = (1 - \frac{Z_b}{Z_{eff}}(1 - 1.46\sqrt{\varepsilon}A(Z_{eff})))J_b, \tag{2.5}$$

where $\varepsilon = \frac{r}{R}$ - is the inverse aspect ratio and $A(Z_{eff})$ - is some function of the charge state of bulk ions. To calculate J, one must calculate the beam current J_b, which requires solving the Fokker-Planck equation to obtain the velocity distribution function of the ion beam.

The model presented above gives results that are in good agreement with experiments. The energy of applied neutral beams ranges from 10 to 350 keV. However, for ITER, the beam will have to penetrate the plasma more efficiently, and thus the energy of the beam must be in the range of 500 - 1000 keV. It constitutes one of the challenges to overcome for ITER. These required high energies mean that it is only possible to use negative ion sources. The NBCD method is mainly dedicated to driving current in the plasma core [Westerhof 2010, p. 328].

2.4 Current drive with plasma waves

2.4.1 Generalities

In addition to the current drive based on injection of neutral particles, an essential group of current drive methods are those using electromagnetic waves. Many years of research on controlled thermonuclear fusion proved that plasma waves are critical for tokamak operation, giving a chance that the realization of a thermonuclear power plant will be successful. Electric and magnetic fields in plasma can be decomposed in the following way [Swanson 2003, p. 22]:

$$\vec{E} = \vec{E}_1 e^{i(\vec{k}\vec{r}-\omega t)}, \tag{2.6}$$

$$\vec{B} = \vec{B}_0 + \vec{B}_1 e^{i(\vec{k}\vec{r}-\omega t)}, \tag{2.7}$$

where $\vec{k}$ - is the wave vector and ω - is the wave frequency. Index 0 denotes the undisturbed static component of a particular field, and index 1 denotes the oscillating wave component of a particular field. Plasma waves, on account of their properties, can be categorized in many different manners (e.g. parallel/perpendicular, longitudinal/transverse) [Chen 2016, p. 96] [Meneghini 2012, pp. 32-34]. Three main kinds of plasma waves are commonly used in tokamaks for non-inductive current drive: electron cyclotron, ion cyclotron and lower hybrid waves as follows:

1. **Electron cyclotron wave** - an electromagnetic wave with dispersion relation:

$$\omega = n|\Omega_{ce}|/\gamma + k_{\parallel} v_{\parallel}, \tag{2.8}$$

   where n - is the index of a particular harmonic, Ω_{ce} - is the electron cyclotron frequency, γ - is the Lorentz factor, $k_{\parallel}$ - is the component of the wave vector parallel to the magnetic field direction and $v_{\parallel}$ - is the parallel component of the wave phase velocity.

2. **Electrostatic ion cyclotron wave** - Longitudinal wave propagating nearly perpendicular to the magnetic field. Its dispersion relation is given by the formula:

$$\omega^2 = \Omega_{ci}^2 + k^2 v_s^2, \tag{2.9}$$

   where Ω_{ci} - is the ion cyclotron frequency and v_s - is the speed of sound in plasma.

3. **Lower hybrid wave** - Longitudinal wave propagating perpendicularly to the mag-

netic field ($\vec{k} \parallel \vec{B}_0$). Its resonance frequency is given by the formula:

$$\frac{1}{\omega_{LH}^2} = \frac{1}{\Omega_{ce}\Omega_{ci}} + \frac{1}{\Omega_p^2}, \tag{2.10}$$

where Ω_{ce} - is the electron cyclotron frequency, Ω_{ci} - is the ion cyclotron frequency and Ω_p - is the ion plasma frequency.

Now we will discuss how radio-frequency energy is transmitted from an RF power source to the plasma edge, as depicted in Fig. 2.5. Depending on how the energy of the wave

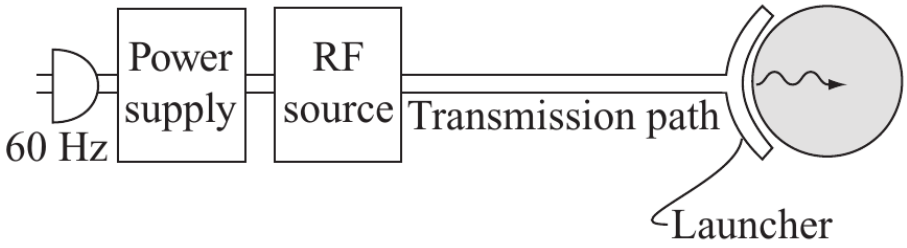

Figure 2.5: Scheme of RF power system. Figure reproduced from [Freidberg 2007, p. 553]

is deposited, we distinguish reflection, transmission, absorption and mode conversion. These phenomena are represented in Fig. 2.6. Let us consider, for example, the usage of

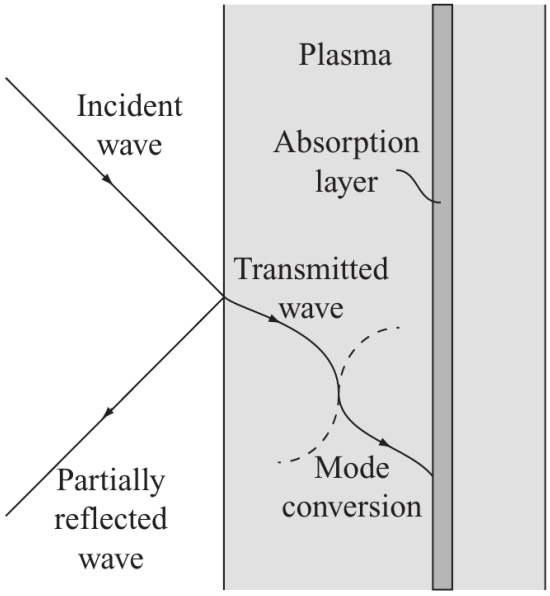

Figure 2.6: Reflection, transmission, absorption and mode conversion. Figure reproduced from [Freidberg 2007, p. 565].

LH waves for current drive. Generated by an RF power source, electromagnetic waves

(microwaves) go along waveguides (transmission path) and then into the plasma edge. These microwaves are partially reflected from the plasma edge with some reflection coefficient. In the plasma, the energy of the electromagnetic wave can be transferred to plasma particles, causing their oscillation and creating a so-called evanescent wave, for example, the LH wave. The process of transformation of microwaves power into LH waves power is called lower hybrid waves coupling. However, if the plasma edge density is too low, the coupling can be very poor, and the LH wave can not be excited in the plasma. Instead, the microwave is reflected into the antenna, heating it. Thus, if the reflection coefficient is too high, the antenna must be turned off to avoid its melting.

An important quantity describing a plasma wave is its refractive index $n = c/v$. If the wave phase velocity v goes to infinity, this event is called cut-off, and if the velocity goes to zero, this situation is called resonance. After reaching resonance, mode conversion is happening, leading to the creation of a new wave. In the case of LHCD, this newly created type of electrostatic wave is called the Bernstein wave. It is one of the possible schemes of the LH method. Both schemes allow to heat the plasma and drive current at the same time. However, one must choose between efficiently driving current with LH waves or heating the plasma using mode conversion into Bernstein waves. A PhD thesis was dedicated to Bernstein Waves Current Drive (BWCD) and related modelling with the LUKE code [Decker 2005a].

Very effective current drive by plasma waves can be obtained by wave-particle resonance. In this case, the wave is absorbed, and the resonance has a collisionless nature. The formula for wave-particle resonance has the following form:

$$\omega = k_{\parallel} v_{\parallel} + l\omega_c, \tag{2.11}$$

where $l = 0, 1, 2, ...$ If $l = 0$, then the Landau damping resonance happens. If $l = 1$, then heating at the fundamental frequency occurs. For $l = 2$, the second harmonic heating happens, and so on.

The Landau damping was first confirmed experimentally, but a proper theoretical explanation was still missing for a long time. After more than 50 years from the Landau prediction, this problem was solved by Cedric Villani and Clemente Mouhot [Mouhot 2010, Mouhot 2011]. Cedric Villani obtained the Fields Medal for this achievement in 2010. The Landau damping is one of the most important phenomena in plasma physics, allowing heating and current drive by excited electrostatic plasma waves like ion cyclotron or lower hybrid waves. The Landau damping mechanism can be compared, in a simplified picture, to ocean waves and surfers. If the velocity of the surfer is slightly lower than the velocity of the wave, then the surfer will be accelerated. Conversely, the

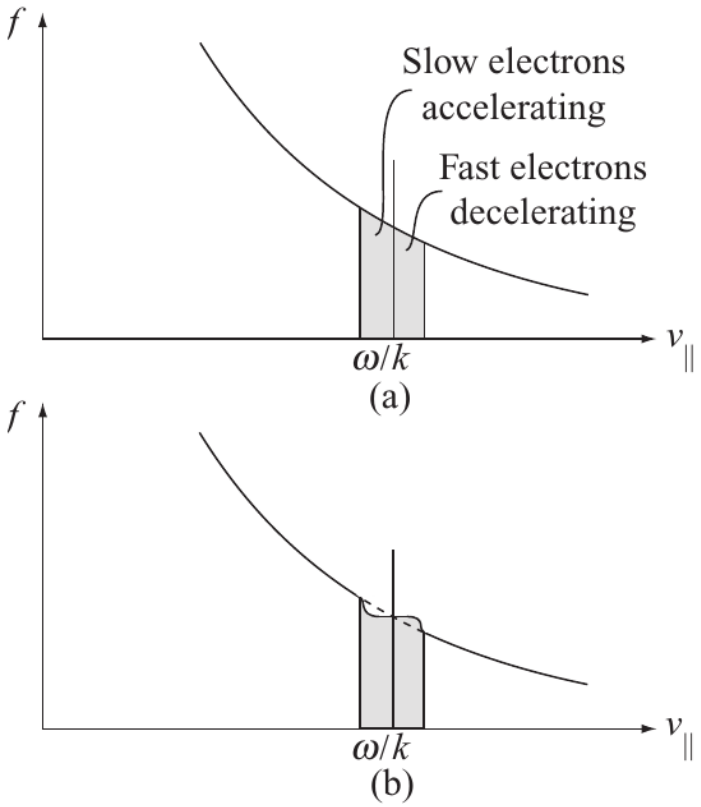

Figure 2.7: Representation of the Landau damping for a wave of frequency ω and wave number k acting on the velocity distribution function $f(v_{||})$. Figure reproduced from [Freidberg 2007, p. 574].

surfer will be decelerated if its velocity is slightly higher than the one of the wave.
By analogy, if a plasma particle has a lower velocity than the wave, then the particle can be accelerated. However, this simplified explanation is not fully true for Landau damping. It can also happen that a particle with a higher velocity than the wave is accelerated. To understand better this process, let us consider the 1D case of the motion of a single charged particle interacting with an electrostatic wave described by the following formula:

$$E = E_1 e^{i(kx-\omega t)}. \tag{2.12}$$

Then, the equation of motion for the particle can be written in the following form:

$$\frac{d^2x}{dt^2} = \frac{e}{m} E_1 e^{i(kx-\omega t)}. \tag{2.13}$$

We will mark the initial velocity of the particle as v_0 and its initial position by x_0. Since

the perturbation caused by the wave to the particle is small, $x \approx x_0 + v_0 t$, we can write:

$$\frac{dv}{dt} = \frac{e}{m} E_1 e^{i(kx_0 + kv_0 t - \omega t)}. \tag{2.14}$$

This allows to derive the velocity:

$$v - v_0 = \frac{e}{m} E_1 \frac{e^{i(kx_0 + kv_0 t - \omega t)} - e^{ikx_0}}{i(kv_0 - \omega)}. \tag{2.15}$$

Let us consider particles for which $(kv_0 - \omega) \longrightarrow 0$. Then the velocity can be expressed in a simpler form:

$$v - v_0 = \frac{e}{m} E_1 t e^{ikx_0}. \tag{2.16}$$

This result is obtained for a particle having an initial velocity v_0 close to the wave phase velocity ω/k. Such particles are called resonant particles, and they can gain energy from the wave, which is responsible for wave damping.

2.4.2 Electron Cyclotron Resonance Current Drive (ECCD)

EC waves provide to electrons in plasma no or minimal amount of momentum. Momentum transfer is not a mechanism responsible for EC current drive. In this case, the so-called Fisch-Boozer mechanism takes place. EC waves can heat electrons selectively. In order to obtain it, it is necessary to use the resonance condition:

$$\omega = n|\Omega_{ce}|/\gamma + k_{\|} v_{\|}, \tag{2.17}$$

where n - is the index of a particular harmonic, Ω_{ce} - is the electron cyclotron angular frequency,γ - is the Lorentz factor, $k_{\|}$ - is the component of wave vector parallel to the magnetic field and $v_{\|}$ - is the parallel component of the wave phase velocity. The applied wave should have a parallel refractive index $N_{\|}$ as follows:

$$N_{\|} = k_{\|} c/\omega, \tag{2.18}$$

where c - is the speed of light. In the case of EC waves, it is possible to distinguish between downshifted (lower than EC frequency) and upshifted frequencies (higher than EC frequency). To obtain downshifted ECCD, one can inject slow X-mode waves at the fundamental resonance from the high field side. However, most experiments use upshifted frequencies. To obtain upshifted ECCD, one can inject fundamental O-mode or second harmonic fast X-mode waves from the low field side.

Because the electron distribution becomes significantly different from a particular threshold level of power [Harvey 1989], for the proper description of ECCD, the quasilinear theory must be applied. This threshold power is given by the condition:

$$p_{ECCD}[MW/m^3]/n_e^2[10^{19}/m^3] > 0.5. \tag{2.19}$$

In this situation, the EC current can be calculated only by using codes solving bounce averaged quasi-linear Fokker-Planck equation in 2D velocity space. Results from ECCD experiments are in good agreement with the results of simulations based on ray-tracing and Fokker-Planck codes [Petty 2002]. The TCV tokamak demonstrated that full non-inductive EC current is possible [Sauter 2000]. The most significant advantage of ECCD is that one can deposit the EC wave anywhere in the plasma - which is not valid, for example, for LH waves. This feature means that ECCD can be used to change the current density profile to control sawteeth and neoclassical tearing modes [Février 2016].
Simulations showed that in the case of ITER [Ramponi 2007], the current efficiency of ECCD in the core plasma will be high, but not in the off-axis part. It means that it should be possible to use EC waves for driving current in the core and LH waves to drive current in the off-axis part of the plasma. The low ECCD efficiency at the plasma edge results from the trapped particles effect and too low temperature in this part of the plasma. Therefore, the control of sawteeth and tearing modes remains the most crucial goal of the ECRH system.

2.4.3 Ion Cyclotron Current Drive (ICCD)

The ion cyclotron wave is a fast magnetosonic wave. Such kind of wave has a perpendicular electric field polarization. In order to lead to effective absorption of IC waves, one must avoid two processes: damping on the ions and mode conversion to ion Bernstein waves. Power from IC waves is accelerating electrons. Two processes are responsible for it: multi-pass absorption by electron Landau-damping and transit time magnetic pumping (TTMP).
One of the main features of ICCD is that if the injected wave has an asymmetric spectrum, then this results in a so-called fast wave current drive - FWCD. Like in the case of ECCD, ICCD generates current mainly in the plasma core. It happens because of the central peaking of the power deposition and trapped particle effect. A simulated extrapolation to ITER gives a similar result as in the case of other tokamaks - centrally peaked current density profile [ITER Organization 1999, Petty 2001].
In the case of ICCD, an important issue is ion minority current drive. One can use

ion minority species to drive current. It is an alternative approach, and here instead of electron current, ions constitute the current. One can calculate this current J using the Fisch-Boozer efficiency formula [Westerhof 2010, pp. 324, 327]:

$$\frac{J}{P_{RF}} = -e\frac{\hat{s}\nabla_p(v_\parallel/v)}{\hat{s}\nabla_p(p^2/2m_e)}, \tag{2.20}$$

where P_{RF} - denotes the radiofrequency power and $\hat{s}$ - is the versor in the direction of RF caused momentum displacement. Like in the case of the NBI method, ions collide with electrons which start travelling in the same direction as ions. As a result, an electron current is generated, which is partly cancelling the ion current. It is possible to write the net plasma current in the following way:

$$J = J_m(1 - Z_m/Z_i), \tag{2.21}$$

where J_m - is the minority ion current, Z_m - is the minority ion charge and Z_i - is the majority ion charge. After taking into account the cancelling electron current, it is possible to express the ion minority current drive efficiency in the following way:

$$\frac{J}{P_{ICCD}} = eZ_m(1 - Z_m/Z_i)\frac{\hat{s}\nabla_p(v_\parallel/v)}{\hat{s}\nabla_p(p^2/2m_e)}. \tag{2.22}$$

Additionally, in the case of ICCD, there is another type of possible generated ion current. The presence of trapped resonant ions can be another source of ion current. This current has a diamagnetic origin and bipolar shape. As a result, it is suitable for MHD instability control, especially sawteeth.

2.4.4 Lower Hybrid Current Drive (LHCD)

LHCD is the most efficient method of current drive. LH waves are in the frequency range of 0.8 - 8 GHz. In order to generate them, a phased waveguide array antenna can be used [Wesson 2004, pp. 139-142]. An LH antenna deposits power to waves propagating into the toroidal direction, which can resonate with high energy electrons. LH waves have a phase velocity parallel to the magnetic field.

In the case of driving current with LH waves, so-called slow waves are used, which are in the range of frequencies between ion and electron cyclotron frequencies. It is possible to express LH resonance in the following way [Freidberg 2007, p. 613]:

$$\omega_{LH}^2 = \frac{\omega_{pi}^2}{1 + \omega_{pe}^2/\Omega_{ce}^2} = \frac{|\Omega_{ci}\Omega_{ce}|}{1 + \Omega_{ce}^2/\omega_{pe}^2}, \tag{2.23}$$

where ω_{pi} - is the plasma ion frequency, ω_{pe} - is the plasma electron frequency, Ω_{ci} - is the ion cyclotron frequency and Ω_{ce} - is the electron cyclotron frequency. In this case, the parallel refractive index $N_{||}$ must satisfy the accessibility condition:

$$N_{\|} > N_c \equiv \frac{1}{1 - \omega^2/|\Omega_{ci}\Omega_{ce}|}. \tag{2.24}$$

Coupling LH waves to the plasma requires the LH antenna to be installed close to the plasma edge.

An essential quality of LH waves is that their group velocity is perpendicular to the wave vector. Furthermore, the perpendicular component of the wave vector is far higher than the parallel one. As a result, the group velocity is almost parallel to the magnetic field. It means that the LH wave propagates in the toroidal direction.

For efficient LHCD, it is necessary to apply waves with high phase velocity, which means a low parallel refractive index. Historically, the theory was predicting that LH waves with high phase velocity will not be well absorbed. However, in tokamak plasmas, there are not many electrons with such high velocities. Surprisingly, it was proved experimentally that LH waves with high phase velocity are very well absorbed in tokamak plasmas [Westerhof 2010]. This apparent paradox is known as the so-called spectral gap problem and remains not fully understood. Some proposed explanations are spectral broadening due to density fluctuations at the plasma edge, wave diffraction, magnetic ripple and instabilities in the scrape-off layer in front of the antenna. In the work presented here, LH spectral broadening is implemented thanks to the so-called spectral tail model [Decker 2014, Peysson 2020], which is described more in detail in section 3.4.

The mechanism of driving current by LH waves is as follows. The main goal of applying LH waves is to accelerate electrons. Let us consider one electron having a parallel velocity $v_{||}$ and gaining additional velocity $\Delta v_{||}$. The amount of energy ΔE which electrons in unit volume have to obtain from LH wave to increase their velocity by $\Delta v_{||}$ can be expressed in the following way:

$$\Delta E = n_e m_e v_{\|} \Delta v_{\|}, \tag{2.25}$$

where n_e - is the plasma density and m_e - is the electron mass. As a result, a current density j is generated:

$$j = n_e e \Delta v_{\|} = \frac{\Delta E e}{m_e v_{\|}}. \tag{2.26}$$

The corresponding current drive efficiency is expressed in the following way:

$$\frac{j}{p_d} = \frac{e}{m_e v_{\|} \nu}, \tag{2.27}$$

where $p_d = \nu \Delta E$ - is the power density and ν - is the collision frequency. The assumption that the parallel electron velocity is far higher than the thermal electron velocity ($v_\parallel \gg v_{Te}$) implies that the collision frequency is inversely proportional to the parallel velocity to the third power ($\nu \propto \frac{1}{v_\parallel^3}$). It means that the current drive efficiency is proportional to the parallel velocity to the second power ($\frac{j}{p_d} \propto v_\parallel^2$). This proportionality is a very important result and means that the dependency of current drive efficiency on collisionality leads to a dependency on the phase velocity of the wave.

In order to calculate precisely the current drive efficiency, it is necessary to use a two-dimensional treatment of velocity space dynamics. The result of such calculation is the following formula:

$$\frac{j}{p_d} = \frac{e}{\nu_0 m_e v_{Te}^3} \frac{2}{(5 + Z_{eff})} \frac{\hat{s}(\partial/\partial v)(v_\parallel v^3)}{\hat{s}(\partial/\partial v) v^2}, \tag{2.28}$$

where ν_0 - is a characteristic electron-ion collision frequency given by

$$\nu_0 = \frac{\omega_{pe}^4 ln\Lambda}{4\pi n_e v_{Te}^3}. \tag{2.29}$$

In the case of LH waves, the versor $\hat{s}$ which is in the direction of the RF caused momentum displacement, is parallel to the magnetic field, and it is possible to write the following proportionality:

$$\frac{j}{p_d} \propto v_\parallel^{-1}(v_\parallel^2 + v_\perp^2)^{3/2} + 3v_\parallel(v_\parallel^2 + v_\perp^2)^{1/2}. \tag{2.30}$$

Electrons that resonate with LH waves have a perpendicular velocity which is much lower than the parallel one. In the above proportionality in Eq. (2.30), the first term is momentum, while the second is energy. It can be noticed that the energy term is three times bigger than the momentum term. It means that asymmetric resistivity provides three-quarters of the current. In this phenomenon, there is no transfer of momentum from wave to electrons. It is because the parallel momentum of ions balances the parallel momentum of electrons. However, the current of electrons is not balanced by the current of ions because they have higher mass and low velocity, so the ion current is negligible.

After introducing the following normalized parameters

$$u = \frac{v}{v_{Te}}, \tag{2.31}$$

$$J = \frac{j}{n_e e v_{Te}}, \tag{2.32}$$

$$P_d = \frac{p_d}{n_e m_e v_0 v_{Te}^2}, \tag{2.33}$$

the current efficiency can be expressed in the following way:

$$\frac{J}{P_d} = \frac{2}{(5+Z_{eff})} \frac{\hat{s}(\partial/\partial u)(u_{\parallel}u^3)}{\hat{s}(\partial/\partial u)u^2}. \tag{2.34}$$

For the case of LH waves and high-velocity limit $u_{\parallel} \gg u_{\perp}$, this gives:

$$\frac{J}{P_d} \propto u_{\parallel}^2 \propto \frac{(\omega/k_{\parallel})^2}{v_{Te}^2}. \tag{2.35}$$

The efficiency of a particular current drive method for a specific machine can be expressed as

$$\frac{I}{P} = \frac{Aj}{2\pi RAp_d}, \tag{2.36}$$

where I - is the driven current, P - is the power used to drive the current, A - is the surface area of the plasma cross-section, j - is the (not normalized) current density, R - is the major radius and p_d - is the (not normalized) power density. It is possible to use these normalized parameters to express the current drive efficiency in the following way:

$$\frac{I}{P} = 0.061 \frac{T_e}{R(n_e/10^{20})ln\Lambda} (\frac{J}{P_d}) AW^{-1}. \tag{2.37}$$

This formula is valid only by making two assumptions. The first assumption is that electrons are suprathermal. The second assumption is that they do not move with relativistic speeds. Then, the LHCD efficiency is proportional to the second power of the wave phase velocity. It is also inversely proportional to the major radius R and electron density n_e. There is also a weak dependency on the effective plasma charge Z_{eff}. It is worth noticing that there is no dependency on the temperature in this particular case. However, the current drive efficiency depends on the temperature in situations with no generated suprathermal electrons [Wesson 2004, p. 141].

Generally, to calculate LHCD efficiency, it is necessary to calculate the response of the electron velocity distribution function to the power spectrum of the launched wave. To do this, one must solve the two-dimensional Fokker-Planck equation, including electron trapping and relativistic effects. Experiments showed that in many tokamaks, it was possible to drive the whole current using LHCD only. It is possible also to use LHCD instead of the inductive current drive at the beginning of the discharge.

One of the issues with LH waves is that they travel in the toroidal direction many times before their absorption. Despite this disadvantage, experiments clearly show that LHCD is useful for controlling the radial profile of plasma current [Wesson 2004, p. 142]. The most significant disadvantage of LH waves is a low plasma penetration capacity. It would

be ideal to use high phase velocity LH waves since these waves provide the highest current drive efficiency among any other waves. Unfortunately, high phase velocity means also poor penetration due to mode conversion.
In the case of ITER, because of the high temperature around 10 keV, firm Landau damping occurs, and LH waves could propagate only in the outer part of the plasma. Therefore, the predicted LHCD efficiency for ITER is around $\eta_{LHCD} = 0.2 \times 10^{20} A/Wm^2$. The ITER Organization was considering LHCD for ITER because of the following goals: achieving and sustaining reversed shear or hybrid scenarios and achieving discharges with fully non-inductive current drive.

2.5 LH antennas of Tore Supra/WEST

LHCD on Tore Supra and then on WEST has been used for many years. Two LH antennas are in operation on WEST: Full Active Multijunction (FAM) and Passive Active Multijunction (PAM) antennas. FAM antenna is currently marked as LH1 (previously C3), whereas PAM antenna is marked as LH2 (previously C4). These antennas, depicted in Fig. 2.8, were also in operation in the ending period of the Tore Supra tokamak. The PAM antenna consists of passive and active waveguides compared to the FAM antenna, which only consists of active waveguides. The difference between them can be seen in Fig. 2.9.
Passive waveguides allow the PAM antenna to work with a low reflection coefficient for plasma edge densities near the cut-off density $n_c = 1.7 \cdot 10^{17} m^{-3}$. In the case of the FAM antenna, the optimal plasma edge density is around $n_e \approx 3n_c$. The PAM antenna is an upgraded version of the FAM antenna, and it was dedicated to ITER. In the case of the PAM antenna, cooling channels can be installed behind passive waveguides. It allows operating the antenna with high power, making it possible to use it for bigger tokamaks like ITER. During the first experimental campaign with the PAM antenna on Tore Supra in 2009-2010, it was possible to couple 2.7 MW of power to the plasma during 78 s. The reflection coefficients for cut-off plasma edge densities were in the range of 1-4%. A picture of the WEST PAM antenna is shown in Fig. 2.10.

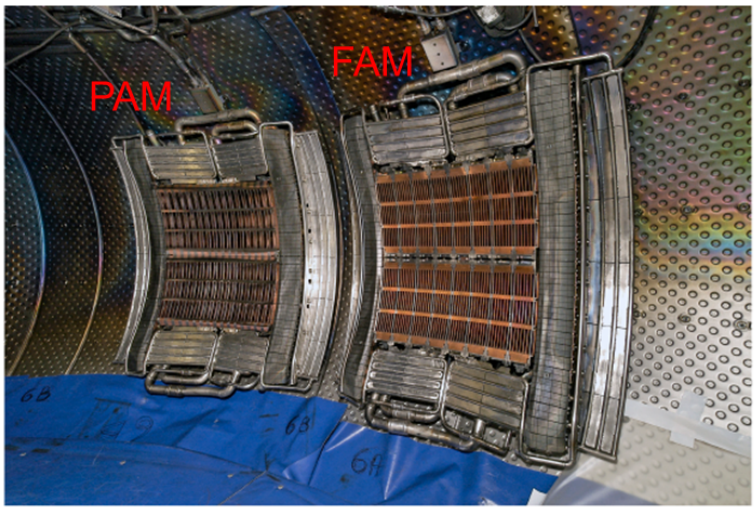

Figure 2.8: LH1 FAM (C3) antenna and LH2 PAM (C4) antenna inside Tore Supra. The same LH antennas are used in WEST. Figure adapted from [Nilsson 2012, p. 12].

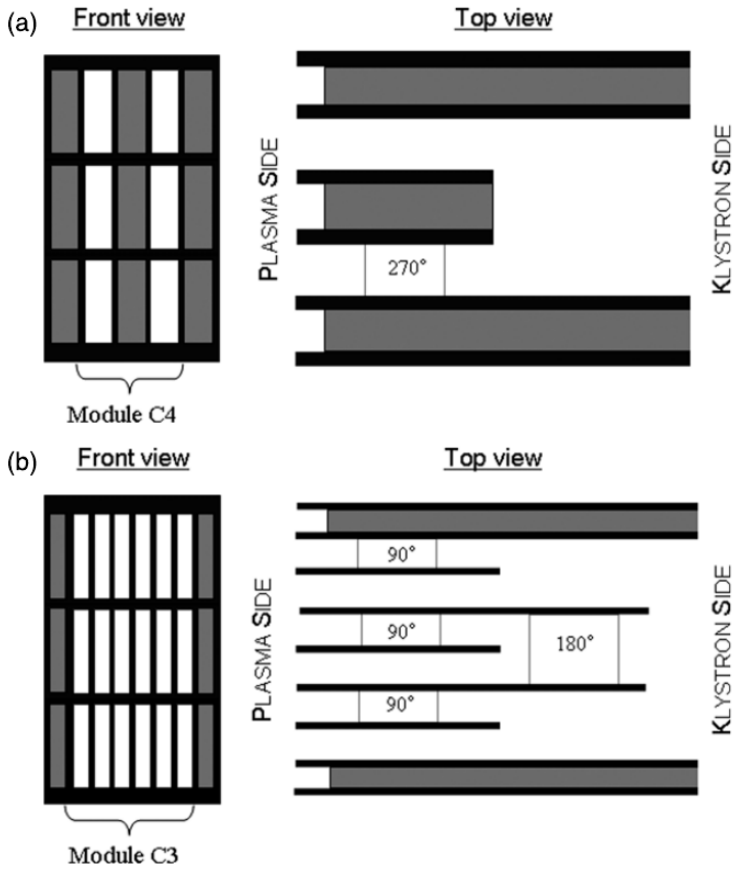

Figure 2.9: Scheme of PAM (a) and FAM (b) LH antennas. Grey rectangles correspond to passive waveguides and white to active waveguides. Figure reproduced from [Preynas 2011].

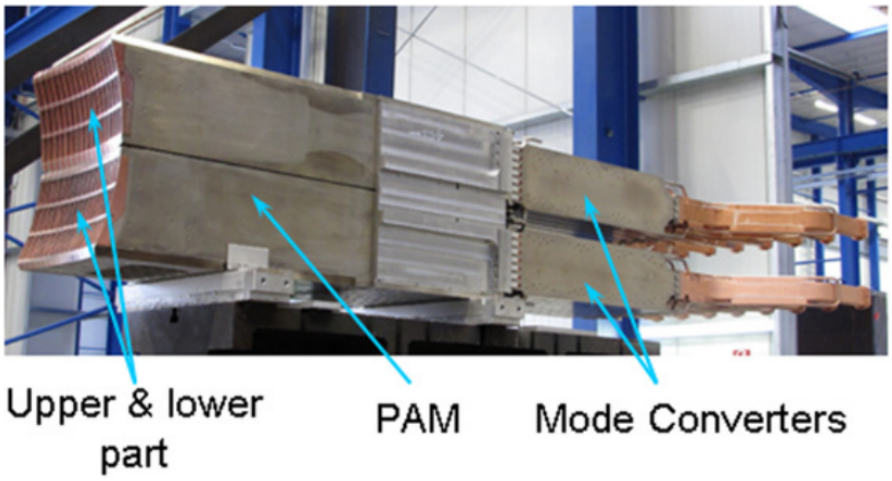

Figure 2.10: PAM antenna before installation in Tore Supra tokamak. The PAM launcher weighs 8 tonnes. Figure reproduced from [Preynas 2011].

2.6 LHCD and ITER

This section aims at presenting the status of the current drive strategy of ITER and at showing that, although the chances that ITER will be using LHCD are meagre, it remains an important topic that must be investigated. Initially, LHCD was not in the so-called ITER construction baseline, but ITER Organization (IO) considered it as a possible additional upgrade and reserved some ports for LHCD. The system would be responsible for providing off-axis current and also additional heating. It could provide to the ITER plasma 20 MW of power and even 40 MW in some advanced scenarios. The planned frequency of LH waves is in the range of 3.7 - 5 GHz, with 5 GHz as a default frequency. The planned ITER LHCD system would be composed of three elements: wave launcher, transmission lines and power sources. However, the development of a klystron at 5 GHz for the LHCD ITER system failed. The main technical difficulty was that the klystron must operate efficiently despite a very high reflected power. Therefore, IO was considering a backup plan with 3.7 GHz LH waves. This backup solution would use the existing PAM antenna with klystron and transmission line from WEST and transport it to ITER. For this scenario, all of these components are currently in full operation on WEST (the distance between WEST and ITER tokamaks is around 3 km).
However, it is mentioned in the ITER 2018 report that there is currently no free port available for LHCD [ITER Organization 2018, p. 376-377]. Regarding the budget, such kind of upgrade would cost around 82 - 87 million euros. However, even if the funding of the system were provided, still human access would be necessary to install the LHCD system, which means that the installation can happen only in the prenuclear assembly

phase. Because of that, the final decision of IO will be irreversible, and in the case of rejection now, the upgrade of ITER with the LHCD system will not be possible also in future. Despite this, several tokamaks operate with LHCD and propositions of taking into account this system for the DEMO project are being investigated.
Because none of the existing methods provides enough current alone, the bootstrap current will be used in ITER as the main component of the total plasma current. Bootstrap current is characterised by a hollow profile. Therefore in ITER, NBCD and ECCD will also be used to perform steady-state, continuous plasma discharges.
According to the ITER 2018 report, it is possible to achieve $Q \geq 5$ with NBI, ICRH and ECRH without LHCD. In 2006, METIS simulations showed that it is possible to achieve $Q = 5$ on ITER with the stable non-inductive operation, using, among other methods, 20 MW of LHCD [Litaudon 2006]. The simulation was performed with 33 MW of NBI, 20 MW of ICRH and 20 MW of LHCD, giving in total 73 MW of heating power.
Many simulation tools available to perform simulations of ITER discharge were compared by investigating different combinations of possible heating and current drive systems [Kessel 2007]. Using the TSC/TRANSP and CRONOS codes, $Q = 5$ could be obtained with LHCD. A CRONOS simulation allowed to obtain $Q = 6.5$ with only RF heating [Garcia 2008]. The simulated discharge included 13 MW of LHCD. Wagner et al. performed a simulation in which they applied 27 MW ECRH, 33 MW NBI and 20 MW ICRH and obtained Q = 4.4 - 5.2 [Wagner 2010]. Different heating schemes were also investigated with the TRANSP code, for which $Q = 5$ was obtained with different schemes, including 20-40 MW of LHCD [Poli 2012].
The main conclusion is that it is possible to obtain similar results with or without LHCD, in other words, achieve a similar Q using 20 MW of LHCD or instead of LHCD: 16.5 MW NBI or 16.5 MW NBI + 20 MW ECRH.
Nevertheless, Cardinali et al. performed an investigation regarding LHCD and high plasma density and temperature for future fusion reactors. As a result, it was reported that, with the currently available knowledge, the LHCD option should be reconsidered once again for ITER as a priority. Furthermore, the possibility of applying LHCD for DEMO reactor was also investigated [Cardinali 2018].

2.7 Synergy of primary current drive methods

A significant conclusion from the previous sections is that none of the existing current drive methods is efficient enough to generate alone the plasma current required for a thermonuclear reactor. Because of that, it is necessary to use many methods simultane-

ously to reach the desired current and obtain a proper radial current profile. It occurred during experiments that, luckily, there is a synergy between the different current drive methods. Thus, it is possible to generate more current using, for example, LHCD and ECCD together than the sum of independent currents from both methods.
Indeed, in this case, LHCD produces a tail of energetic electrons, which then can absorb additional energy from ECCD. Another example of synergy is the synergy between LHCD and ion Bernstein waves (IBW). It occurs that IBW can generate a broad electron velocity distribution, increasing the efficiency of LHCD [Paoletti 1999]. NBI can also go into synergy with ICCD. Ion cyclotron waves can increase the perpendicular velocity of the ion beam and, in this way, increase the beam current. Therefore, establishing a reliable heating and current drive scenario for tokamak plasmas requires considering the synergetic effect between the different current drive methods at play.

Chapter 3

Modelling of Lower Hybrid Current Drive

Contents

3.1 Simulation workflow

For modelling the dynamics of fast electrons, appropriate numerical tools have been developed. This work is dedicated to LHCD modelling on the WEST tokamak, and thus the default suite of codes used for this purpose will be described now. Among many tokamaks, LHCD was intensively investigated on Alcator C-Mode tokamak, and interesting examples of both simulation and experimental work can be found in: [Schultz 1999], [Meneghini 2012], [Schmidt 2011], [Liptac 2006], [Wallace 2010], [Faust 2016], [Baek 2014], [Mumgaard 2015] and [Lau 2013]. The results of the works mentioned here were obtained in particular with the Genray ray-tracing code and CQL3D Fokker-Planck solver. CQL3D has a synthetic diagnostic module of hard X-ray (HXR) bremsstrahlung, making the Genray/CQL3D suite of codes a competitor to the chain of codes used in this work C3PO/LUKE/R5-X2 [Schmidt 2011, p. 92]. Some results comparing Genray/CQL3D with C3PO/LUKE can be found in [Peysson 2007]. Both suites of codes can be used for modelling the fast electron current drive. However, the Genray/CQL3D suite of codes extensively used for LHCD modelling on Alcator C-Mode does not take into account the partial screening effect described in Chapter 4 of this PhD thesis. C3P0/LUKE/R5-X2 is the first suite of codes that accurately describes collisions of fast electrons with partially ionized impurities in the plasma and the corresponding non-thermal bremsstrahlung. The present thesis describes this novelty in LHCD modelling and validation of the obtained first results by comparison with WEST experimental data, as presented in Chapter 5.
A general description of the C3PO/LUKE/R5-X2 suite of codes can be found in [Nilsson 2012] and [Nilsson 2014]. The main code is the LUKE solver used to solve the Fokker-Planck equation [Decker 2005b, Peysson 2014]. The workflow of these simulation tools is depicted in Fig. 3.1. The primary input for simulation is provided by the METIS (Minute Embedded Tokamak Integrated Simulator) code [Artaud 2018]. The used suite of codes describes the following physical processes [Nilsson 2012, pp. 21-26]:

- **LH power coupling** - is a transformation of electromagnetic wave with microwave frequency, injected by the antenna, into LH wave in the plasma. The coupling is described by the ALOHA – Advanced Lower Hybrid Antenna code. From the WEST database, ALOHA takes as input the incident powers, phases and reflection coefficients of each module of the LHCD antenna. Based on that, ALOHA can calculate the LH power spectrum at the front of the antenna, which is then an input for C3PO. Alternatively, the METIS code can provide a simplified LH power spectrum, meaning that using ALOHA is not strictly necessary to perform an LHCD simulation.

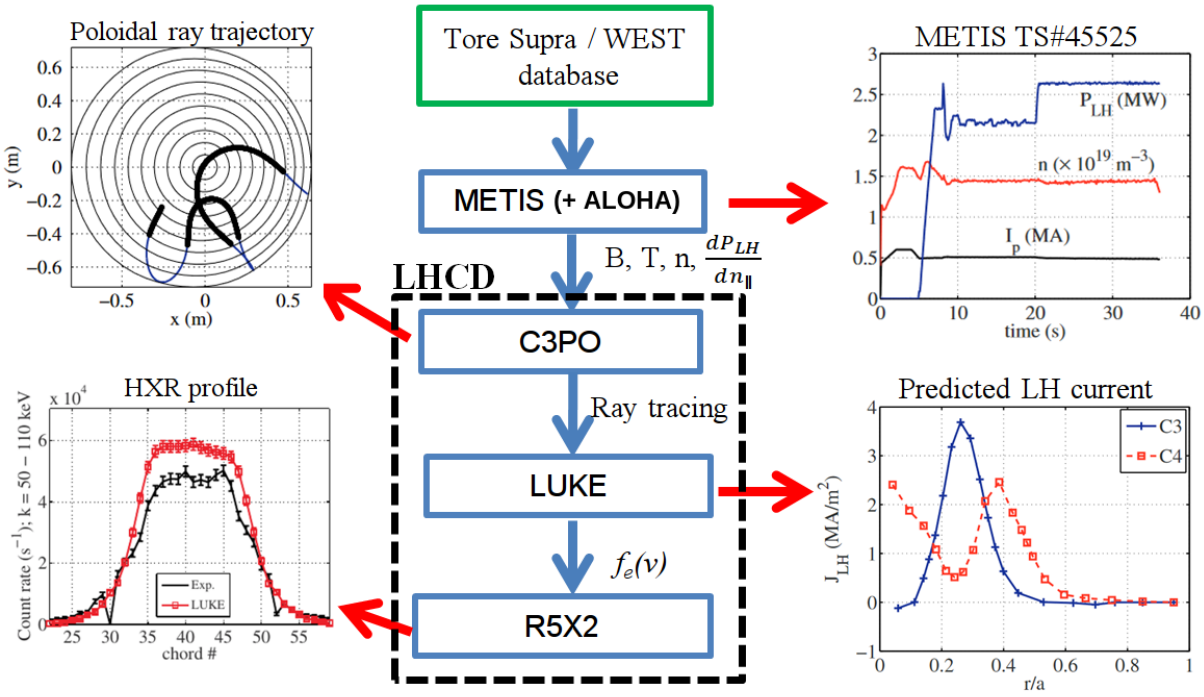

Figure 3.1: LHCD simulation workflow for Tore Supra/WEST. Figure based on [Nilsson 2013].

- **LH wave propagation** - The LH waves propagate in the plasma and its phase velocity decreases up to a certain value determined by the Landau damping condition (full absorption). Propagation of LH wave is described by the C3PO ray-tracing code.

- **LH power absorption** - The electron velocity distribution function is modified due to the LH wave absorption, inducing suprathermal electrons, which constitute the LH current. The LUKE code describes this in particular. Based on the calculated electron distribution function, LUKE can further estimate the current density.

- **Fast electron bremsstrahlung** - The electron distribution function can also be used to estimate the HXR radiation. It is described by the R5-X2 synthetic diagnostic of bremsstrahlung emitted by electrons in the HXR range from 20 keV to 200 keV, allowing a direct comparison of simulation results with experimental data [Peysson 2008b].

3.2 LH wave coupling between antenna and plasma edge

There are two types of lower hybrid waves: slow wave and fast wave. ALOHA is an upgrade of the SWAN code which could model only the slow wave [Hillairet 2010, p. 1]. ALOHA can model both the slow and the fast LH wave. The main output of ALOHA code is the derivative of the LH power with respect to the parallel refractive index, so-called LH power spectrum. ALOHA can be launched in two variants: ALOHA 1-D calculates the LH power spectrum for the slow wave only, while ALOHA 2-D calculates it, taking into account both slow and fast waves. In the usual ranges of Tore Supra or WEST plasma edge densities, the fast wave is cut-off and only the slow wave propagates in the plasma. The difference for usual plasma discharge between ALOHA 1-D and ALOHA 2-D power spectrum is most often negligible, as shown in Fig. 3.2 for Tore Supra.

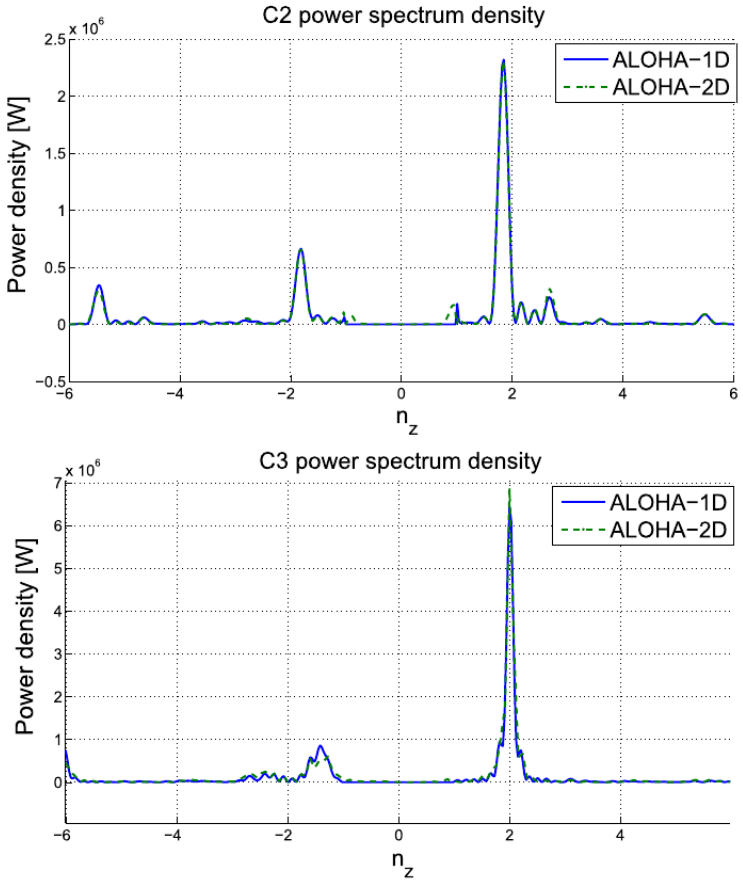

Figure 3.2: LH power spectrum obtained by ALOHA-1D and ALOHA-2D for Tore Supra C2 FAM and C3 FAM antennas. Figure reproduced from [Hillairet 2010].

One of the most important inputs for ALOHA is the density of plasma edge. Unfor-

tunately, this parameter is not easy to measure precisely, while the resulting LH power spectrum is sensitive on its value, as it can be noticed in Fig. 3.3. Changing the plasma edge density results in different heights of the power spectrum peaks, without changing their location.

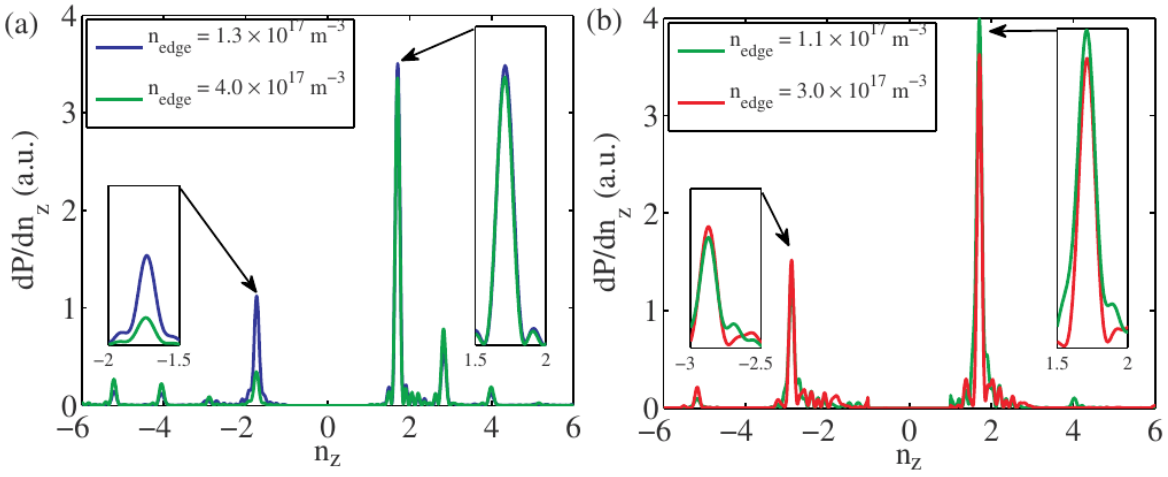

Figure 3.3: Coupled LH spectrum with two different values of edge density at the antenna mouth for (a) TS shot 31527 (C3 launcher), and (b) TS shot 45525 (C4 launcher). Figure reproduced from [Nilsson 2013].

ALOHA can be launched for one antenna at the same time - the user has to choose for which antenna the simulation should be performed. Because of that, there are two possible solutions:

1. Use the plasma density at the edge measured by Langmuir probes and perform one iteration of the ALOHA simulation based on this input. This option leads to a good agreement between the current calculated by LUKE and the experimental one in the case of the LH2 (C4) PAM antenna.

2. In the case of the LH2 (C4) antenna, it gives better results to calculate the plasma edge density based on the reflection coefficients. Firstly, it is necessary to give to ALOHA a first initial guess of the plasma edge density as an input. After one launch of ALOHA, the code is returning the reflection coefficients as an output. These ALOHA reflection coefficients can be compared with the ones measured experimentally. Based on that, the plasma edge density can be estimated by adjusting it iteratively in order to find the best fit of the experimental reflection coefficients. A comparison of both methods of plasma edge density determination was performed in [Nilsson 2013, p. 6-8].

3.3 LH wave propagation

In the case of waves in ion cyclotron range of frequencies like, for example, ion cyclotron wave or fast wave (magnetosonic wave), the order of magnitude of wavelength is the same as the magnetic equilibrium variation scale length [Peysson 2012, p. 1]. It means that the description of such kinds of waves needs so-called full-wave techniques. However, for the waves with wavelengths much smaller than the equilibrium variation length, like lower-hybrid (LH) and electron cyclotron (EC) waves or ion Bernstein waves (IBW), ray-tracing techniques are appropriate. One can use these techniques if the Wentzel-Kramers-Brillouin (WKB) approximation is valid [Weinberg 1961, p. 1899]. The standard ray-tracing code used to model LH wave propagation on Tore Supra and WEST is C3PO. The most detailed description of C3PO can be found in its documentation [Peysson 2008a] and the corresponding description of wave kinetic equation in [Peysson 2010], [Peysson 2012] and [Peysson 2014].

Although many ray-tracing codes use the toroidal coordinate system (R, Z, ϕ), the C3PO code uses magnetic flux coordinates (ψ, θ, ϕ). The advantages of this choice are that the flux functions need only 1D interpolations and the angular coordinate θ can be described using Fourier series. Besides, the LUKE code also uses magnetic flux coordinates, which allows coupling C3PO to LUKE more easily. C3PO can calculate ray trajectories and properties of the wave, like wave polarization, energy flow, and linear power absorption. The core numerical method is the Runge-Kutta-Fehlberg method. An example of LH power spectrum used as an input of C3PO and the corresponding ray tracing can be seen in Fig. 3.4. Six peaks were choosen from the ALOHA power spectrum. Both antennas FAM and PAM consists of 6 rows. In C3PO, each power spectrum peak of each antenna row is represented by one ray, thus here 36 rays = 6 rows $\times$ 6 peaks as depicted in Fig. 3.4 (bottom right). Red curves corresponds to waves from the 3 upper rows of the PAM antenna and blue curves correspond to the 3 bottom rows. The black color along ray trajectories corresponds to regions of strong LH wave absorption. An LH ray is defined as the curve which is tangent in each point to the direction of wave propagation. In ray-tracing techniques, we model the wave as a ray by solving ray-tracing equations which allows obtaining the position of wave and its wave vector [Meneghini 2012, p. 39]. To perform such kind of ray-tracing, we need to know the initial refractive index of the LH wave, which is one of the main parameters determining the ray trajectory [Liptac 2006, p. 46]. In the case of C3PO, this information is given as an input to the code in the form of LH power spectrum obtained from METIS (by default) or ALOHA.

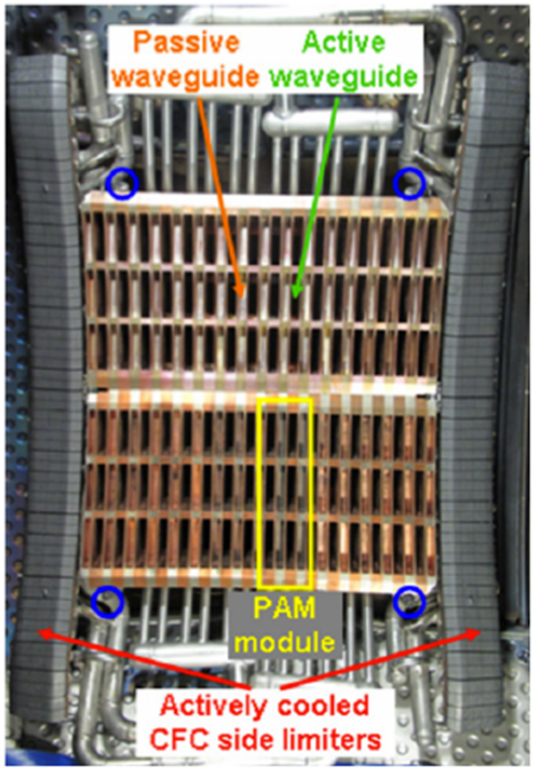

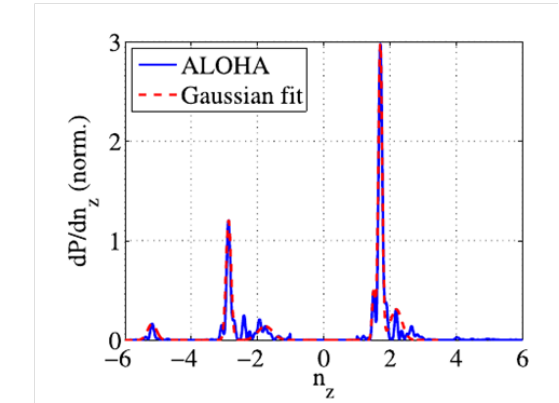

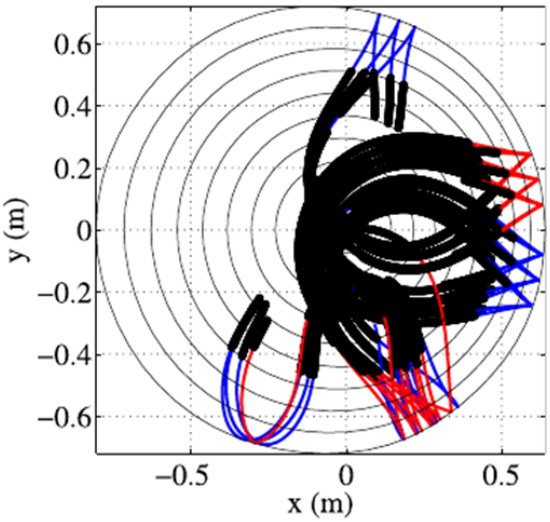

Figure 3.4: On the left: WEST PAM antenna with Langmuir probes marked by blue circles. Figure reproduced from [Ekedahl 2010]. On the right: example of C3PO simulation for Tore Supra shot #45525. Figures reproduced from [Decker 2014].

To derive the wave equation, the starting point is the two following Maxwell equations:

$$\vec{\nabla} \times \vec{E} = -\frac{\partial \vec{B}}{\partial t}, \tag{3.1}$$

$$\vec{\nabla} \times \vec{B} = \mu_0 \vec{J} + \frac{1}{c^2}\frac{\partial \vec{E}}{\partial t}, \tag{3.2}$$

where $\vec{E}, \vec{B}$ - are the electric and magnetic fields of the considered plasma wave, μ_0 - is the vacuum permeability, $\vec{J}$ - is the electric current density and c - is the speed of light. The wave equation can be written in the following form:

$$\vec{k} \times \vec{k} \times \vec{E} + i\omega\mu_0 \bar{\bar{\sigma}} \cdot \vec{E} + \frac{\omega^2}{c^2}\vec{E} = 0, \tag{3.3}$$

where $\vec{k}$ - is the wave vector, ω - is the wave angular frequency and $\bar{\bar{\sigma}}$ - is the conductivity tensor. Eq. (3.3) is valid for plasmas with a constant density in space and time in the considered plasma volume. Such kind of situation is an idealization which in laboratory is rarely achieved. In tokamak plasmas, the magnetic field and plasma density are changing in space. This causes that the phase velocity of the excited LH wave is changing during its propagation. In C3PO, it is assumed that plasma density is not changing fast in space and time [Peysson 2008a, p. 6]. This allows to obtain the so-called ray tracing equations [Weinberg 1961, p. 1908]:

$$\frac{d\vec{x}}{d\tau} = \frac{\partial D}{\partial \vec{k}}, \tag{3.4}$$

$$\frac{d\vec{k}}{d\tau} = -\frac{\partial D}{\partial \vec{x}}, \tag{3.5}$$

$$\frac{dt}{d\tau} = -\frac{\partial D}{\partial \omega}, \tag{3.6}$$

$$\frac{d\omega}{d\tau} = \frac{\partial D}{\partial t}, \tag{3.7}$$

where $\vec{x} = (x_1, x_2, x_3)$ - is the euclidean position vector, τ - is a variable measuring the ray trajectory length, D - is the wave dispersion function. We will consider a small time period in which plasma properties are not changing, so we can assume that: $\frac{\partial D}{\partial t} = 0$. This means that the above system of equations can be simplified into the following equations:

$$\frac{\partial \vec{x}}{\partial t} = -\frac{\frac{\partial D}{\partial \vec{k}}}{\frac{\partial D}{\partial \omega}}, \tag{3.8}$$

$$\frac{\partial \vec{k}}{\partial t} = \frac{\frac{\partial D}{\partial \vec{x}}}{\frac{\partial D}{\partial \omega}}. \tag{3.9}$$

The LH wave propagates in the tokamak plasma by circulating many times around the torus as depicted in Fig. 3.5, where black regions correspond to strong absorption of LH wave. In the presented figure, the wave trajectory is cut when 99% of the wave energy has been absorbed.

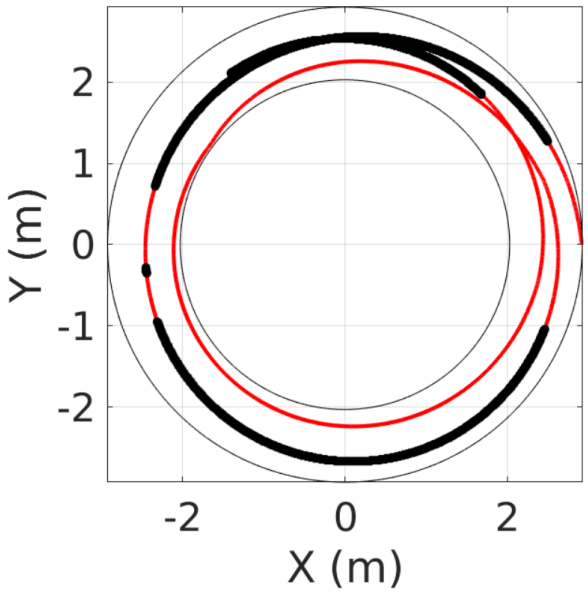

Figure 3.5: Toroidal trajectory of one chosen LH ray viewing from top of tokamak, for WEST discharge #55193, t = 4.5 s.

The LH wave presented here propagates in the anti-clockwise direction, pushing electrons also in this direction, causing LH current in the clockwise direction. During this propagation, the parallel refractive index of the wave $n_{\parallel} = \frac{c}{v_{\parallel}}$ is changing, where $v_{\parallel}$ is the component of the wave phase velocity parallel to the magnetic field, as seen in Fig. 3.6.

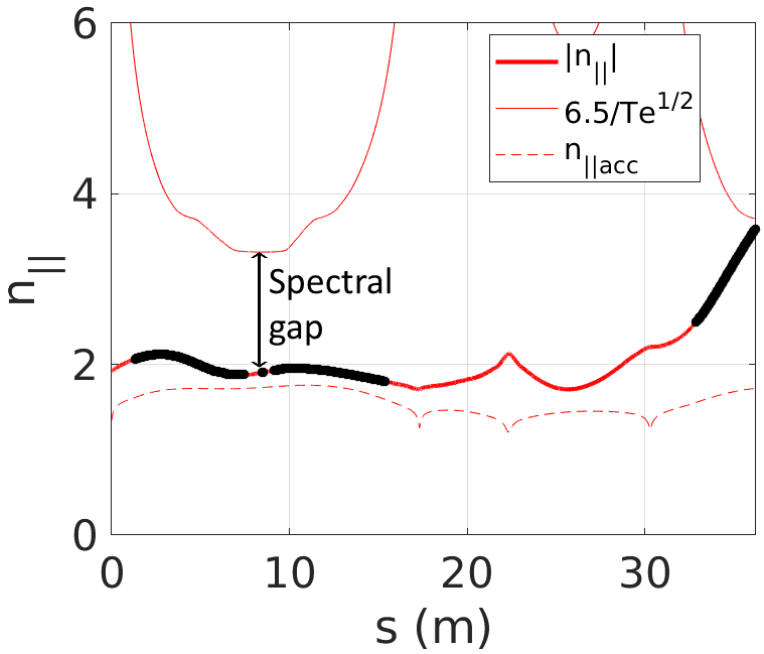

Figure 3.6: Evolution of $n_{\parallel}$ of one chosen LH ray as a function of the trajectory length s, for WEST discharge #55193, t = 4.5 s.

It is possible to see that the gap between the parallel refractive index of the LH wave and the one of the wave-particle Landau resonance ($n_{||LD} = 6.5/T_e^{1/2}$) decreases along the trajectory length. The peaks of $n_{||LD}$ correspond to moments when the wave is going into the core region of the plasma. An increase in temperature allows lowering the Landau condition. It can be seen in the poloidal view of the ray trajectory presented in Fig. 3.7. This figure shows that LH wave was two times in the plasma core before reaching $n_{||}$ very close to $n_{||LD}$, and this corresponds to two peaks of $n_{||LD}$ in Fig. 3.6.

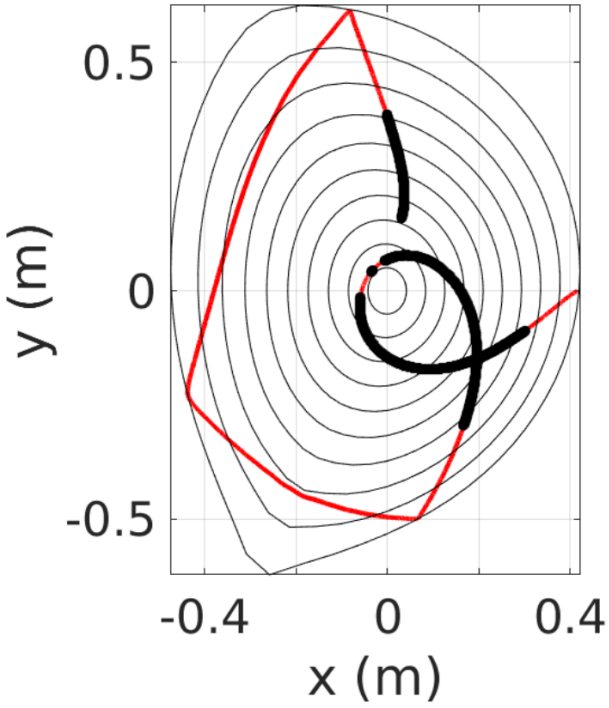

Figure 3.7: Poloidal view of the trajectory of one chosen LH ray, for WEST discharge #55193, t = 4.5 s.

3.4 Spectral gap problem and tail model

Despite that the LHCD method has been used throughout many years of fusion research to drive current efficiently, the mechanism responsible for current drive in the case of this method is still not fully explained. During standard LHCD experiments in tokamaks, LH waves are excited with an initial parallel velocity that is too high compared to the required one, determined by the Landau resonance condition, as depicted in Fig. 3.6. LH waves with such high phase velocity can not be damped via Landau damping, thus no current should be driven. Despite this, an LH curent is observed experimentally. This paradox is referred to as the spectral gap problem. This can be seen in Fig. 3.6, where the wave is excited with a roughly twice higher phase velocity (two times lower $n_{||}$) than

the one needed to satisfy Landau resonance. Some suggested explanations to solve this paradox include spectral broadening due to density fluctuations at the plasma edge, wave diffraction, magnetic ripple and plasma instabilities in the scrape-off layer in front of the LH antenna [Westerhof 2010, p. 325]. To deal with the spectral gap problem, the spectral tail model was developed and implemented in the suite of codes [Decker 2014]. Recent investigations of the spectral gap problem on TRIAM-1M, WEST and HL-2A tokamaks can also be found in [Peysson 2020]. An example of LH power spectrum modified with the spectral tail model to bridge the spectral gap is presented for WEST shot #55193 in Fig. 3.8. The initial LH power spectrum (blue curve in Fig. 3.8) obtained from METIS consists of two main peaks, where the blue peak around $n_{||} = 6$ is graphically covered by the red one. The negative peak around $n_{||} = -2$ corresponds to the LH wave launched

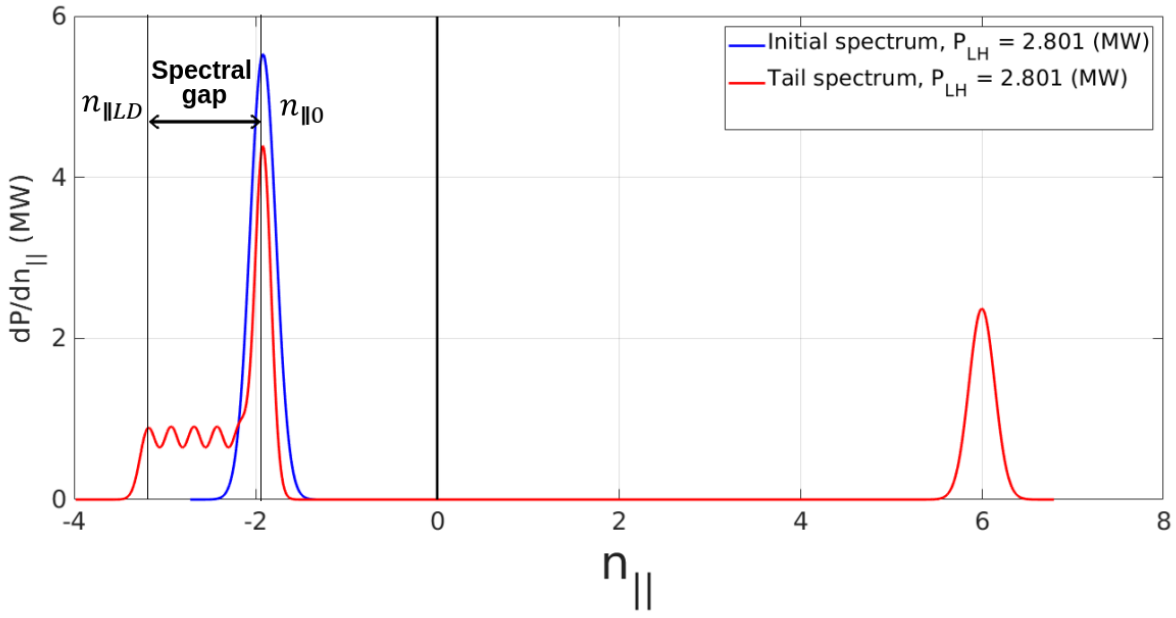

Figure 3.8: LH power spectrum calculated by METIS, for WEST discharge #55193, t = 4.5 s. The red curve is modified by the tail model.

in the direction opposite to the magnetic field, pushing electrons in the same direction and driving LH current (so-called co-current) in the same direction as the magnetic field. However the LH power spectrum has always a second main peak on the opposite side of the power spectrum. This positive peak is responsible for the generation of a so-called LH counter-current. In this case, the total LH current is thus the current of the main peak reduced by the opposite LH current of the second peak.

The peak located at $n_{||} = 6$ is not changed by the spectral tail model (the red curve covers the blue one). However, the main peak located at $n_{||} = -1.9195$ is transformed

into six peaks - a main one and five smaller peaks constituting a spectral tail (one small peak is located around the point where the red curve intersects the blue curve). The last peak of the spectral tail is located at the position:

$$n_{\parallel LD} = \frac{c}{4v_T}, \tag{3.10}$$

where $n_{\parallel LD}$ - is the parallel refractive index of Landau damping, c - is the speed of light and v_T - is the thermal velocity of electrons. Eq. (3.10) corresponds to the condition $6.5/T_e^{1/2}$ with T_e in keV in Fig. 3.6 by considering that the thermal velocity $v_T \sim T_e^{1/2}$ [Decker 2014, p. 1].

3.5 LH power absorption

In this thesis, the absorption of LH wave power and its impact on the electron dynamics is modelled with the Fokker-Planck solver LUKE. Descriptions of the physics implemented in the LUKE code can be found in [Schultz 1999], [Decker 2002], [Peysson 2004], [Decker 2005a], [Decker 2005b] and [Peysson 2014]. The C3PO/LUKE codes in particular can be used to model two technics of current drive: Lower Hybrid Current Drive (LHCD) and Electron Cyclotron Current Drive (ECCD) [Nilsson 2012, p. 24]. LUKE can calculate the three following components of plasma current: inductive current, electron current driven by particular plasma waves and bootstrap current.

Two competing effects are essential when considering the generation of electron current. First of all, electrons collide with the rest of the particles in the plasma. Collisions take electrons closer to thermal equilibrium, i.e. to a Maxwellian distribution. Secondly, the injected waves have an impact on electrons. The critical issue related to waves is that they generate asymmetry in the electron velocity distribution function $f(v)$, which is crucial in generating current. The central equation describing the dynamics of $f(v)$ in the presence of these two effects is the Fokker-Planck equation, which describes the evolution in time of the distribution function:

$$\frac{df}{dt} = C(f,f) + C(f,f_i) - \frac{\partial}{\partial v} S_w, \tag{3.11}$$

$$S_w = -D_{QL}\frac{\partial f}{\partial v}, \tag{3.12}$$

where f and f_i - are the distribution functions of the electrons and the ions respectively, $C(f,f_i)$ - is a collision operator, S_w - is the wave-induced flux and D_{QL} - is the quasilinear diffusion coefficient [Montgomery 1964]. In 1936, Landau derived a collision operator for

two particle species a and b [Landau 1936]:

$$C(f_a, f_b) = -\frac{\partial}{\partial v} S^{a/b} \quad , \tag{3.13}$$

where

$$S^{a/b} = \frac{q_a^2 q_b^2}{8\pi\varepsilon_0^2 m_a} ln\Lambda^{a/b} \int U(y)(\frac{f_a(v)}{m_b}\frac{\partial}{\partial v'} f_b(v') - \frac{f_b(v')}{m_a}\frac{\partial}{\partial v} f_a(v))d^3v', \tag{3.14}$$

$$U(y) \equiv \frac{y^2 I - yy}{y^3}, y \equiv v - v'. \tag{3.15}$$

If one species, for example species b, has a Maxwellian distribution, then the Coulomb operator can be written in the following form [Hesslow 2017, p. 2]:

$$C^{ab}(f_a) = \nu_D^{ab}\mathcal{L}(f_a) + \frac{1}{p^2}\frac{\partial}{\partial p}[p^3(\nu_S^{ab} f_a + \frac{1}{2}\nu_{||}^{ab} p\frac{\partial f_a}{\partial p})], \tag{3.16}$$

where ν_D^{ab} - is the (elastic) deflection frequency, ν_S^{ab} - is the (inelastic) slowing-down frequency, $\nu_{||}^{ab}$ - is the parallel-diffusion frequency, $\mathcal{L}$ - is the so-called Lorentz scattering operator, p - is the normalized momentum and f_a - is the velocity distribution function of particles of species "a". The above operator in Eq. (3.16) consists of three parts:

1. Elastic collisions part: $\nu_D^{ab}\mathcal{L}(f_a)$.
2. Inelastic collisions part: $\frac{1}{p^2}\frac{\partial}{\partial p}(p^3\nu_S^{ab} f_a)$.
3. Parallel diffusion part: $\frac{1}{p^2}\frac{\partial}{\partial p}(\frac{1}{2}\nu_{||}^{ab} p\frac{\partial f_a}{\partial p})$.

Research on the efficient current drive in fusion plasmas started from the investigation of the transfer of momentum from electromagnetic waves to electrons [Wort 1971, Klima 1973]. Since the Fokker-Planck equation has an analytical solution only for a few simple cases, the first obtained solutions were simple one-dimensional approximations [Fisch 1978, Klima 1979]. Despite the simplicity of this approach, it occurred that even one-dimensional approximations were giving results in agreement with numerical solutions [Harvey 1981]. The one-dimensional approximation is described in Appendix A.2.

A common method to simplify the Fokker-Planck equation is the linearization to obtain Green's functions [Karney 1986]. Linearized Fokker-Planck equation is described more in detail in Appendix A.3. The approach with Green's functions allows obtaining individual cases in which the Fokker-Planck equation has analytical solutions. It can be done using Langevin or adjoint equations instead of solving the Fokker-Planck equation

directly. Another important simplification of the Fokker-Planck equation in the case of fast electrons is the so-called high-velocity limit described in Appendix A.4.
The wave-induced flux S_ω depends on both effects: wave-particle interaction and collisions of electrons with the rest of the particles. Diffusion depends on the wave energy density and the gradient of the distribution function. Nonlinearities come from collision terms. The interaction of electrons with waves can be described as the diffusion of electrons, such as written in Eq. (3.12). This approach gives similar results to more complicated approaches [Gell 1984, Gell 1985].
On the left-hand side of the previously written Fokker-Planck equation, see Eq. (3.11), there is a total time derivative of the electron distribution function. Considering f as a function of 3 variables: magnetic momentum μ, kinetic energy ε and position r of the electron, it is possible to write a total time derivative in the following way:

$$\frac{d}{dt} = \frac{\partial}{\partial t} + (v_{dr} + v_\parallel \hat{b})\frac{\partial}{\partial r} + \frac{\partial \varepsilon}{\partial t}\frac{\partial}{\partial \varepsilon}, \tag{3.17}$$

where v_{dr} - is the drift velocity perpendicular to the magnetic field, $v_\parallel$ - is the parallel electron velocity, $\hat{b}$ - is the versor in the direction of magnetic field and ε - is the electron kinetic energy.
Now let us consider a homogenous plasma. This assumption allows writing f as a function of parallel and perpendicular components of electron velocity. Then, the total time derivative of f can be written as follows:

$$\frac{d}{dt} = \frac{\partial}{\partial t} + \frac{qE_\parallel}{m}\frac{\partial}{\partial v_\parallel}. \tag{3.18}$$

The approximation of homogenous plasma allows describing most of the current drive methods precisely. The most notable exception is the trapped-electron effect. In this case, such an approximation can not be made [Fisch 1987].
The Fokker-Planck equation can be written in expanded form based on the so-called small drift approximation, namely [Schultz 1999, pp. 45-47]:

$$\delta = \frac{\tau_b}{\tau_c} << 1, \tag{3.19}$$

where τ_b – is bounce time, τ_c – is collision time, see Appendix A.1. This assumption allows writing the electron velocity distribution function in the form of the following power series:

$$f = f_0 + \delta f_1 + \frac{1}{2}\delta^2 f_2 + ... \tag{3.20}$$

In order to calculate the ohmic + LH current, it is enough to consider only f_0 in

the electron distribution function. We obtain zeroth-order Fokker-Planck equation [Peysson 2004, p. 6]:

$$v_s \frac{\partial f_0}{\partial s} = \mathcal{C}(f_0) + \mathcal{Q}(f_0) + \mathcal{E}(f_0), \tag{3.21}$$

where v_s – is the electron speed along the magnetic line, s – is a curvilinear coordinate, $\mathcal{C}(f_0)$ - is a Coulomb collisions operator, $\mathcal{E}(f_0)$ – is an ohmic electric field operator responsible for taking into account ohmic current, $\mathcal{Q}(f_0)$ – is a quasilinear operator of electrons diffusion caused by RF waves. An example of an electron velocity distribution function calculated with LUKE for an LH-heated WEST plasma is depicted in Fig. 3.9. In this figure, it is clear that the electron distribution is close to a Maxwellian for the thermal part $p_{//}/p_{Te} < 1$, while for higher energies (suprathermal electrons), there is a significant deviation from a Maxwellian distribution due to the LH wave - electrons interaction.

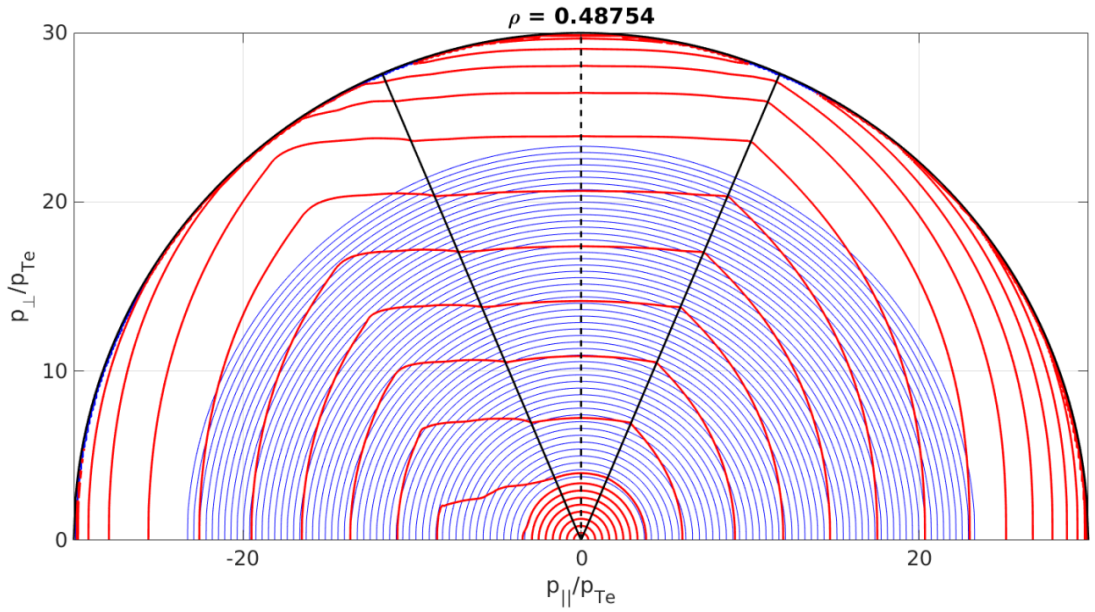

Figure 3.9: Electron velocity distribution function calculated for WEST discharge #55193, t = 4.5 s, $\rho_G = 0.48754$. The distribution function has a constant value on each blue or red curve in the momentum space. Blue curves denote the Maxwellian distribution. Red curves denote the electron distribution calculated by LUKE.

Solving Eq. (3.21) allows us to obtain the ohmic + LH current:

$$\vec{J}(\vec{x}, t) = q_e \int d^3 p \vec{v} f_0, \tag{3.22}$$

where $\vec{J}$ - is the current density, $\vec{x}$ - is a 3D position vector, t - is time, q_e - is the elementary electron charge, p - is the electron momentum, $\vec{v}$ - is the electron velocity and f_0 - is the first term in the power series expansion of f in Eq. (3.20).

In order to calculate the bootstrap current component, it is necessary to consider the two first terms of the electron distribution function in the power series of Eq. (3.20), namely: $f_0 + \delta f_1$. This gives the first order Fokker-Planck equation which is called Drift Kinetic Equation (DKE):

$$v_s \frac{\partial(\delta f_1)}{\partial s} + \frac{v_\parallel}{\Omega_e} I(\psi) \frac{|\nabla\psi|}{R} \frac{\partial}{\partial s}\left(\frac{v_\parallel}{B}\right) \frac{\partial f_0}{\partial \psi} = \mathcal{C}(\delta f_1) + \mathcal{Q}(\delta f_1) + \mathcal{E}(\delta f_1), \tag{3.23}$$

where Ω_e - is the electron cyclotron frequency, $I(\psi)$ - is some flux function, ψ - is the poloidal flux, R - is the distance from the central vertical axis of the tokamak to a particular point, B - is the magnetic field intensity. The electron bootstrap current averaged over a flux surface can be written in the following way:

$$J_b = \int_{-\pi}^{\pi} \frac{d\theta}{2\pi} q_e \int d^3p v_\parallel \delta f_1. \tag{3.24}$$

The zeroth and first-order Fokker-Planck equations are a kind of starting point for LUKE simulation, and they reflect the possible two working modes of LUKE, with or without bootstrap current.

3.6 Fast electron bremsstrahlung

In this thesis, the R5-X2 code - synthetic diagnostic of non-thermal bremsstrahlung emitted by fast electrons, in the hard X-ray (HXR) energy range 20 keV $<$ hν $<$ 200 keV, is used. Another example of such kind of code, not considered in this thesis, is a synthetic diagnostic module of the CQL3D code [Schmidt 2011, p. 92]. A detailed description of R5-X2 can be found in [Peysson 2008b]. A more detailed description of fast electron bremsstrahlung emission can be found in Chapter 3 of the following PhD thesis [Arslanbekov 1995].

In this section, by HXR pulse profile, we will mean the HXR count rate measured by the detectors as a function of their chord numbers. In the case of Tore Supra, the HXR diagnostic was composed of one horizontal and one vertical camera, while for WEST, the HXR diagnostic consists of the horizontal camera only. The main functionality of R5-X2 is to calculate the HXR pulse profile based on the electron distribution function, which can be obtained with the LUKE code. Then, the predicted HXR pulse profile can be directly compared with the one measured experimentally. An example of such kind of comparison can be seen in Fig. 3.10 for Tore Supra.

The HXR count rate pulse spectrum $\frac{dN_E(t,E)}{dtdE}$ recorded by a detector along one line of

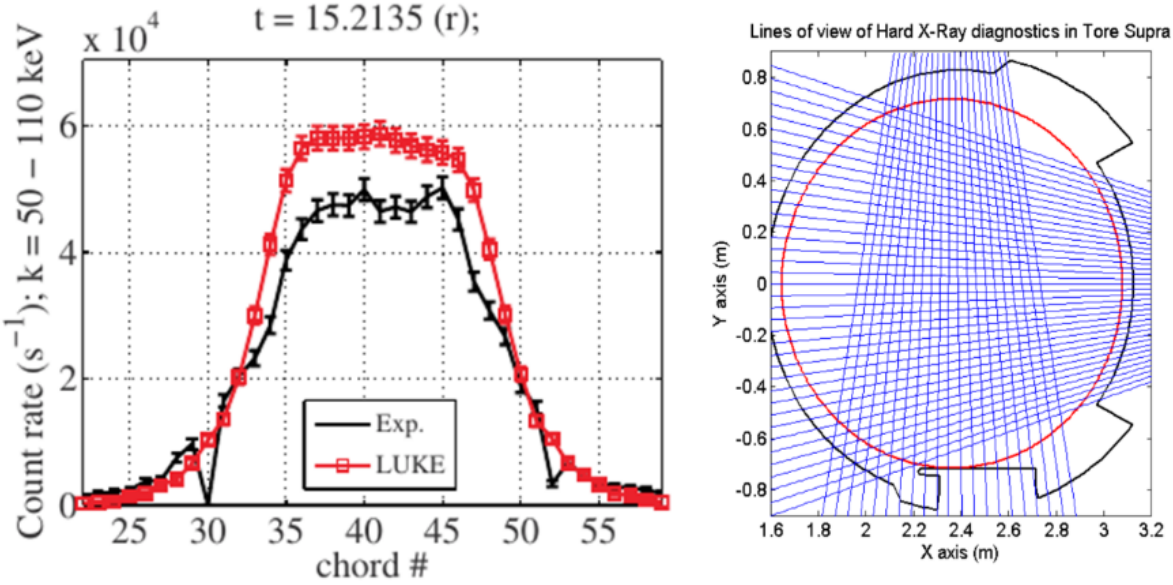

Figure 3.10: On the left, comparison of HXR pulse profiles - experimental and calculated by R5-X2, for Tore Supra shot #45525, t = 15.2 s (figure reproduced from [Nilsson 2013]). On the right, line of sight of vertical and horizontal HXR cameras of Tore Supra (figure reproduced from [Nilsson 2012, p. 18]).

sight as a function of time t and of pulse energy E can be expressed by the following formula [Peysson 2008b, p. 2]:

$$\frac{dN_E(t,E)}{dtdE} = \int_0^\infty \eta_T(k)(1-\eta_D(k))G(k,E)\frac{dN_k(t,k)}{dtdk}dk, \tag{3.25}$$

where $\frac{dN_k(t,k)}{dtdk}$ - is the HXR plasma spectrum emitted by the plasma along the line of sight, as a function of the photon energy k. Only the fraction η_T of incident photons along a particular line of sight can be transmitted to the detector, as some of them do not reach the detector. Then, only part of the remaining photons, namely $1-\eta_D$, is effectively absorbed by the active detection volume of the detector. The detector response function G is a consequence of different physical phenomena like, for example, Compton scattering. Two kinds of HXR photons can contribute to the emitted spectrum, [Peysson 2008b, p. 3]:

$$\frac{dN_k(t,k)}{dtdk} = \frac{dN_{kV}(t,k)}{dtdk} + \frac{dN_{kS}(t,k)}{dtdk}, \tag{3.26}$$

where $\frac{dN_{kV}(t,k)}{dtdk}$ - is a direct contribution from the plasma, i.e. non-thermal bremsstrahlung due to Landau resonance LH wave-particle interaction, and $\frac{dN_{kS}(t,k)}{dtdk}$ - is the radiation scattered from the inside of the tokamak chamber. This scattered radiation is not calculated

by R5-X2. Such kind of radiation scattering from the inner part of the tokamak vessel is described in [Peysson 1993]. It is important to emphasize that the non-thermal bremsstrahlung component of the radiation is negligible with respect to the scattered component for some particular lines of sight looking at the plasma edge. For the WEST HXR camera, especially the eight first chords and last chords measure mainly the scattered radiation contribution. The presence of a tungsten divertor in WEST particularly increases this effect in comparison with Tore Supra, as can be seen in Fig. 3.11. It is also

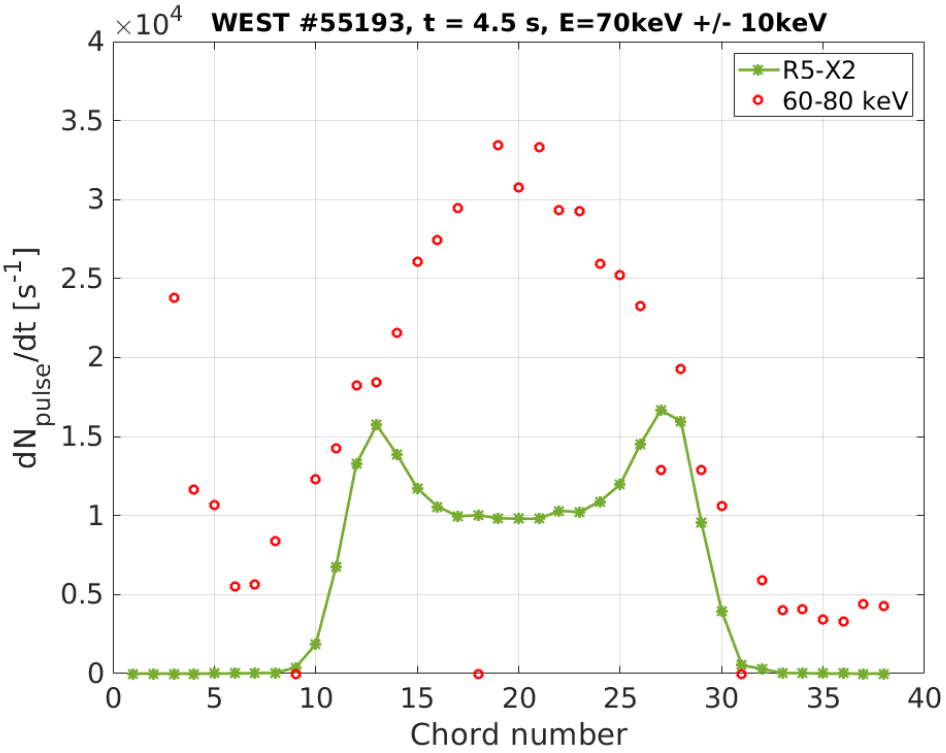

Figure 3.11: Comparison of HXR pulse profiles - experimental and calculated by R5-X2 - for WEST shot #55193, t = 4.5 s, in the energy range k = 60 - 80 keV. For the edge chords, the measured HXR signal corresponds mostly to scattered radiation from tokamak inner components.

noticeable that the HXR experimental profile is largely underestimated by a factor 2 - 3, with respect to the R5-X2 prediction, for the central HXR chords. The origin of this discrepancy is investigated in Chapters 4 and 5.

To calculate $\frac{dN_{kV}(t,k)}{dtdk}$ in R5-X2, we have to integrate each contribution over the plasma volume and solid angle associated with a particular line of sight. This is expressed by the following formula:

$$\frac{dN_{kV}(t,k)}{dtdk} = \int_{\Delta V(k)} dV \int_{\Delta\Omega(k)} \frac{dN_k(t,k,\mathbf{X},\hat{b}\cdot\hat{d})}{dtdkdVd\Omega} d\Omega, \tag{3.27}$$

where k - is the photon energy, $N_{kV}(t,k)$ - is the number of non-thermal bremsstrahlung photons with energy k emitted at time t along the direction of the considered line of sight, $\Delta V(k)$ and $\Delta\Omega(k)$ - are the volume and solid angle associated with a considered line of sight, $\mathbf{X}$ - is a particular position in the position space, $\hat{b}$ - is the versor in the magnetic field direction, $\hat{d}$ - is the versor in the direction along a particular line of sight. In the limit of small-diaphragm aperture, the formula for non-thermal bremsstrahlung part of plasma spectrum can be approximated in the following way:

$$\frac{dN_{kV}(t,k)}{dtdk} \simeq \int_{l_c^{min}}^{l_c^{max}} \mathcal{G}_{\mathcal{D}} \frac{dn_k(t,k,\mathbf{X},\hat{b}\cdot\hat{d})}{dtdkd\Omega} dl, \tag{3.28}$$

where l_c is the length of the line of sight in the plasma, $\mathcal{G}_{\mathcal{D}}$ – is some geometrical factor, $n_k = dN_k/dV$ - is the photon density. For weakly collisional plasmas, photon density can be decomposed into two contributions from electron-ion collisions and electron-electron collisions, respectively:

$$\frac{dn_k(t,k,\mathbf{X},\hat{b}\cdot\hat{d})}{dtdkd\Omega} = \sum_s \frac{dn_k^{ei}(t,k,\mathbf{X},\hat{b}\cdot\hat{d},Z_s)}{dtdkd\Omega} + \frac{dn_k^{ee}(t,k,\mathbf{X},\hat{b}\cdot\hat{d})}{dtdkd\Omega}, \tag{3.29}$$

where Z_s - is the atomic number of ions of species s. The corresponding two differential collision cross-sections are introduced as follows:

$$\frac{dn_k^{ei}(t,k,\mathbf{X},\hat{b}\cdot\hat{d},Z_s)}{dtdkd\Omega} = n_s(t,\psi) \iiint d^3\mathbf{p} \frac{d\sigma_{ei}(k,p,\hat{k}\cdot\hat{p},Z_s)}{dtdkd\Omega} v f(t,\mathbf{X},\mathbf{p}), \tag{3.30}$$

$$\frac{dn_k^{ee}(t,k,\mathbf{X},\hat{b}\cdot\hat{d})}{dtdkd\Omega} = n_e(t,\psi) \iiint d^3\mathbf{p} \frac{d\sigma_{ee}(k,p,\hat{k}\cdot\hat{p})}{dtdkd\Omega} v f(t,\mathbf{X},\mathbf{p}). \tag{3.31}$$

From a numerical point of view, high accuracy of calculations together with relative small calculation time can be obtained using Legendre polynomials. Then total bremsstrahlung photon density from electron-ion and electron-electron collisions can be expressed in the following way [Peysson 1993, p. 5]:

$$\frac{dn_k(t,k,\mathbf{X},\hat{b}\cdot\hat{d})}{dtdkd\Omega} = \sum_{m=0}^{\infty} (m+\frac{1}{2}) I_B^{(m)}(t,\mathbf{X},p,k) P_m(cos\theta_d), \tag{3.32}$$

where P_m - are Legendre polynomials. The function I depends on the electron distribution function calculated by the LUKE code.

The HXR pulse profile can be used for reconstructing the current profile based on Abel inversion [Nilsson 2012, pp. 37-39]. For many years, this approach was used as a standard

method to measure the LH current profile obtained with the C3 FAM antenna on Tore Supra. However, the Abel inverted current profile and the current profile calculated by LUKE are slightly different, as can be seen in Fig. 3.12.

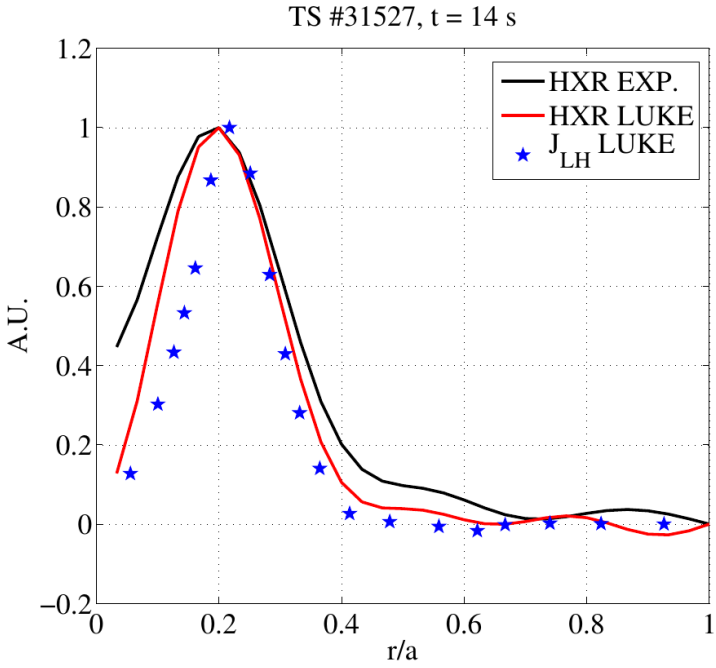

Figure 3.12: Comparison of: Abel inverted current based on experimental HXR profile (marked as HXR EXP) with Abel inverted current based on calculated by R5-X2 HXR profile (marked as HXR LUKE) and current calculated by LUKE (marked as J_{LH} LUKE). Figure reproduced from [Nilsson 2012, p. 39].

Although it is possible to obtain an estimate of the current profile based on the measured HXR profile, it is impossible to step further and obtain an electron distribution function based on the HXR profile.

Chapter 4

Theory of partial screening effect

Contents

The implementation of the partial screening effect in the LUKE and R5-X2 codes has been performed in the framework of this thesis and of the Harmonia (NCN) collaboration between IFJ PAN and IRFM research teams [Peysson 2019, Jardin 2020a, Król 2020]. The goal of the present chapter is to summarize the results obtained on this topic. More specifically, this thesis contributed to the analytical derivation of the screening integrals using the Pratt-Tseng atomic model (see Appendix B). It allows to fastly compute, in a semi-analytical way, the updated fast electron bremsstrahlung differential cross-sections in R5-X2.

4.1 Partial screening effect

The central point of this research is the single Coulomb collision of a fast electron with a high-Z impurity ion, such as a tungsten ion, as shown in Fig. 4.1. For such collision,

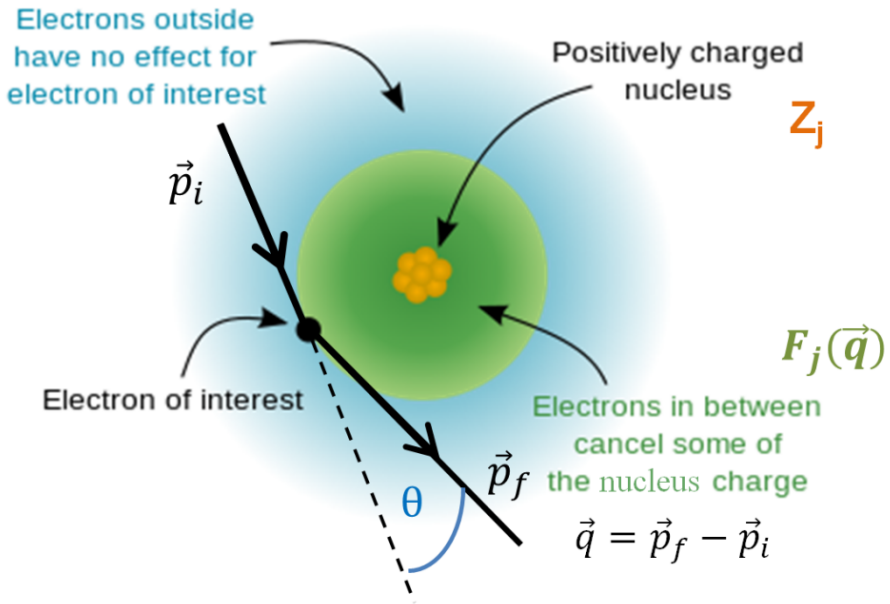

Figure 4.1: Sketch of the partial screening effect occurring during a collision between a non-fully ionized atom and an incident electron.

it is essential to take into account that the incident fast electron can partially probe into the electron cloud of the non-fully ionized impurity atom. In such a case, only part of the electron cloud (the green region in Fig. 4.1) screens the ion nucleus. This partial screening results in a higher effective charge Z of the impurity ion, namely:

$$Z = Z_j - F_j(\vec{q}), \tag{4.1}$$

where Z_j - is the charge of the nucleus, $\vec{q} = \vec{p}_f - \vec{p}_i$ - is the transferred momentum between the initial $\vec{p}_i$ and final $\vec{p}_f$ (after collision) electron momentum, $F_j(\vec{q})$ - is the so-called atomic form factor. The atomic form factor can be defined as the Fourier transform of the electron density $\rho_j(\vec{r})$ around the nucleus in the following way:

$$F_j(\vec{q}) = \int \rho_j(\vec{r}) e^{-i\vec{q}\vec{r}/a_0} d^3\vec{r}, \tag{4.2}$$

where $\vec{r}$ - is the position vector and a_0 - is the Bohr radius. In this work, to obtain the needed form factors, the spherically averaged electron density was used:

$$\widetilde{\rho}_j(r) = \frac{1}{4\pi} \int_0^{\pi} \int_0^{2\pi} \rho_j(\vec{r}) sin\theta d\theta d\phi. \tag{4.3}$$

The spherically averaged electron density allows calculating the form factor using the following formula:

$$F_j(q) = 4\pi \int_0^{+\infty} \widetilde{\rho}_j(r) \frac{r a_0}{q} sin(\frac{qr}{a_0}) dr, \tag{4.4}$$

where the transferred momentum q is given by [Rosenbluth 1956, p. 3]:

$$q = |\vec{p}_f - \vec{p}_i| = \frac{2p_i}{\alpha} \sin(\frac{\theta}{2}), \tag{4.5}$$

where θ - is deflection angle and α - is fine-structure constant.

The form factor can be understood as a measure of the effective number of electrons screening the nucleus. Therefore, its value is a real number in the range: $0 \leq F_j(q) \leq N_{e,j}$, where $N_{e,j}$ - is the total number of bound electrons of the considered ion. Here, it is important to emphasize that the case $F_j(\vec{q}) = N_{e,j}$ means that all bound electrons screen the nucleus and is referred to as the full screening case. Conversely, if $F_j(q) = 0$, none of the bound electrons screens the nucleus from the incident fast electron (like if the atom was fully ionized), which is referred to as the no screening case.

From Eq. (4.4), we see that the main quantity necessary to calculate the form factor is the electron density $\widetilde{\rho}_j(r)$. In this work, three different approaches to calculate $\widetilde{\rho}_j(r)$ were studied: the Thomas-Fermi (TF) approximation, the Pratt-Tseng (PT) approximation and the Density Functional Theory (DFT). The main goal was to upgrade the existing suite of codes with the physics of tungsten impurities and the partial screening effect. This included, in particular, the upgrade of the LUKE and R5-X2 codes. One of the most crucial points was implementing the atomic form factor into the Coulomb collisions

and non-thermal bremsstrahlung cross-sections.
In standard hot tokamak plasmas in ITER, we will have to deal with tungsten impurities with ionization levels like, for example, W^{40+}. Therefore, one of the goals of this work was to understand which model between TF and PT would give more accurate results for such kind of partially ionized high-Z impurities. In order to achieve it, DFT was used as a reference.

4.2 Atomic form factor approximations

4.2.1 Thomas-Fermi approximation

The Thomas-Fermi model gives a theoretical description of many-electrons systems like atoms or ions. It was developed as an alternative approach to the Schrödinger equation. In this approach, we do not use the wave function but instead focus on the electron density as the primary function to develop the model [Fermi 1928]. To do so, we start by writing the formula for the total energy of the system - atom or ion:

$$E = E_k + E_{pn} + E_{pe}, \tag{4.6}$$

where E_k - is the total kinetic energy of the system, E_{pn} - is the potential energy of interaction of electrons with the nucleus, E_{pe} - is the potential energy of mutual interaction of electrons. To derive E_k, we consider first the momentum space. The energy of the highest occupied single-particle state is called Fermi energy, and the corresponding momentum of this particle is Fermi momentum. In the momentum space, a ball with a radius of Fermi momentum p_F has the volume:

$$V_F = \frac{4}{3}\pi p_F^3(\vec{r}). \tag{4.7}$$

Despite that we will not be using the Schrödinger equation, two following points from quantum mechanics will be assumed: 1. The Fermi statistics. All the states up to those with maximum energy and hence momentum p_F – that may vary over space – are occupied. 2. The exclusion principle. Every cell in the phase space of volume h^3 may host up to 2 electrons with opposite spin directions.
This allows to obtain the electron density in terms of Fermi momentum:

$$\rho(\vec{r}) = \frac{8\pi}{3h^3} p_F^3(\vec{r}). \tag{4.8}$$

The considered phase space consists of points with six coordinates (x, y, z, p_x, p_y, p_z).

Knowing Eq. (4.8), it is possible to write the total kinetic energy of the system per unit volume of the position space:

$$E_{ku} = C\rho^{5/3}(\vec{r}), \tag{4.9}$$

where C - is a constant. Integrating over $\vec{r}$ allows obtaining the kinetic energy of the system:

$$E_k = C\int(\rho(\vec{r}))^{5/3}d\vec{r}. \tag{4.10}$$

Now let us consider the potential energy. The total potential energy of interaction between electrons and nucleus is given by the formula:

$$E_{pn} = \int \rho(\vec{r})V_N(\vec{r})d\vec{r}, \tag{4.11}$$

where $V_N(\vec{r})$ - is the electric potential of the nucleus. The potential energy of electrons mutual interaction is given by the formula:

$$E_{pe} = \frac{1}{2}e^2\int\frac{\rho(\vec{r})\rho(\vec{r'})}{|\vec{r}-\vec{r'}|}d\vec{r}d\vec{r'}. \tag{4.12}$$

Taking expressions (4.10), (4.11) and (4.12) together, we obtain the total energy of the system:

$$E(\rho(\vec{r})) = C\int(\rho(\vec{r}))^{5/3}d\vec{r} + \int\rho(\vec{r})V_N(\vec{r})d\vec{r} + \frac{1}{2}e^2\int\frac{\rho(\vec{r})\rho(\vec{r'})}{|\vec{r}-\vec{r'}|}d\vec{r}d\vec{r'}. \tag{4.13}$$

The above derived total energy will allow us to derive the electron density using the Lagrange multipliers technique. The goal is to find the electron density for which energy is minimal - which means that the atom (ion) is in the ground state. We introduce the F function defined in the following way:

$$F[\rho(\vec{r})] = E[\rho(\vec{r})] - \mu\int(\rho(\vec{r}) - N)d\vec{r}, \tag{4.14}$$

where μ - is the Lagrange multiplier, N - is the total number of electrons of the system, and the partial derivative of F with respect to ρ satisfies the following condition:

$$\frac{\partial F}{\partial\rho} = 0. \tag{4.15}$$

Then, it is possible to obtain the following equation:

$$\mu = \frac{5}{3}C\rho^{2/3}(\vec{r}) + V_N(\vec{r}) + \int \frac{\rho(\vec{r'})}{|\vec{r} - \vec{r'}|}d\vec{r'}. \tag{4.16}$$

The last term is induced by electrons potential, which we can mark as:

$$\widetilde{V}(\vec{r}) = \int \frac{\rho(\vec{r'})}{|\vec{r} - \vec{r'}|}d\vec{r'}. \tag{4.17}$$

Then, the last two terms on the right-hand side of the Eq. (4.16), being the total potential, can be written in the following way:

$$V(\vec{r}) = V_N(\vec{r}) + \widetilde{V}(\vec{r}). \tag{4.18}$$

Further transformations lead to the following equation:

$$\frac{1}{r}\frac{d^2}{dr^2}rV(\vec{r}) = 4\pi(\frac{3}{5C})^{\frac{3}{2}}V^{3/2}(\vec{r}). \tag{4.19}$$

The total potential can be written in terms of the so-called Thomas-Fermi function χ:

$$V(r) = -\frac{Z}{r}\chi(x)\alpha, \tag{4.20}$$

where Z - is the atomic number, $\alpha \approx 1.129Z^{1/3}$ and $x = \alpha r$. To obtain $V(r)$, we need to find $\chi(x)$, which can be done by solving the following equation [Lundqvist 1983]:

$$\frac{d^2\chi}{dx^2} = \frac{\chi^{3/2}}{\sqrt{x}}. \tag{4.21}$$

The above equation is called the Thomas-Fermi equation, and it allows obtaining the electron density of a particular atom or ion using the following analytical formula:

$$\rho(x) = C_s\frac{\chi^{3/2}(x)}{x^{3/2}}, \tag{4.22}$$

where C_s - is a constant which depends on the considered element. For neutral atoms: $\chi = 1$ for $x = 0$ and $\chi = 0$ at $+\infty$. In turn, for ions: $\chi = 1$ for $x = 0$ and $\chi = 0$ for $x = x_0$, which corresponds to the ion radius. More detailed results for numerical calculations of the above solutions can be found in [Jardin 2020a, Peysson 2019]. The above Eq. (4.22) allowed us to obtain the electron density averaged over solid angle of Eq. (4.3) for every ionization state of several elements such as argon or tungsten, as

depicted in Fig. 4.2 and Fig. 4.3. The accuracy of the Thomas-Fermi model increases with the increased number of electrons.

It is worth mentioning that in the framework of the Thomas-Fermi model, Kirillov proposed an approximation (which will be noted TF-K in the following) of the atomic form factor by interpolating between the two limit cases of very low or very high electron momentum [Kirillov 1975], allowing to obtain the following analytical expression:

$$F_j(q) = \frac{N_{e,j}}{1 + (qa_j)^{3/2}}. \tag{4.23}$$

The effective ion radius a_j is expressed by the formula:

$$a_j = \frac{N_e^{2/3}}{Z} \frac{(9\pi)^{1/3}}{8} a_0 \tag{4.24}$$

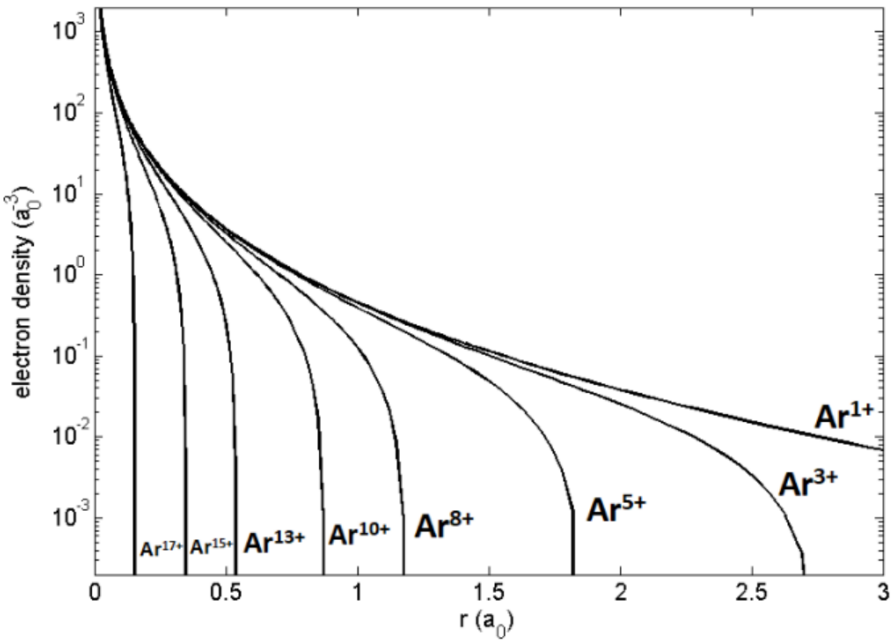

Figure 4.2: Spherically averaged density of bound electrons as a function of radius for selected ionization states of argon using the Thomas-Fermi model. The length scale is given in units of the Bohr radius a_0. Figure reproduced from [Jardin 2020a].

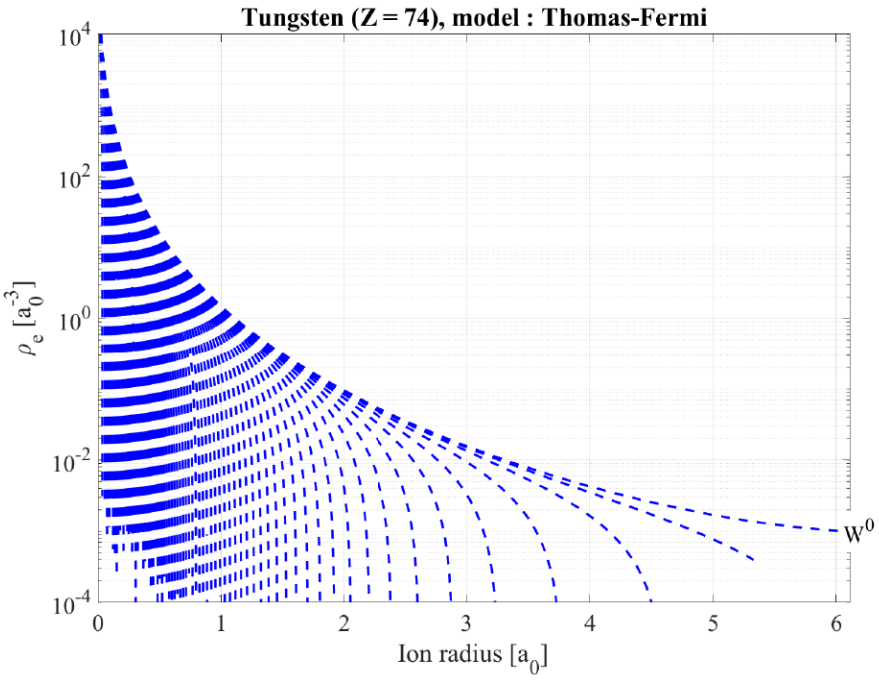

Figure 4.3: Spherically averaged density of bound electrons as a function of radius for all ionization states of tungsten using the Thomas-Fermi model. The length scale is given in units of the Bohr radius a_0. Figure reproduced from [Peysson 2021b].

4.2.2 Pratt-Tseng approximation

The previous model considered the total potential in Eq. (4.18) as a sum of parts associated with the nucleus and with electrons. We consider once again such kind of sum. However, in this model, we use the so-called Yukawa potential, and we can write the total potential in the following form [Pratt 1972]:

$$V(r) = \frac{1}{4\pi\varepsilon_0 r}[Z + (Z - Z_0)e^{-\lambda_0 r}], \tag{4.25}$$

where Z_0 - is the ionization level, Z - is the atomic number and λ_0^{-1} - is the radius of the considered atom or ion. We can see in the above formula that the considered potential consists of two parts. The first one is the classical Coulomb potential of the nucleus and the second one is Yukawa potential describing the potential associated with electrons. The Pratt-Tseng model gives more accurate results than the Thomas-Fermi model for systems with a small number of electrons.

In the case of the Pratt-Tseng potential, it is crucial to calculate the inverse radius parameter λ_0. One of the ways of calculating it is by solving Hartree-Fock-Slater equations,

which has been done, among others, by [Botto 1978]. Botto gave the following formula:

$$\lambda_0^B \approx 0.9 Z^{0.42} a_0^{-1}. \tag{4.26}$$

Lamoureux and Avdonina gave another formula in [Lamoureux 1997]. Their analytical formula for the square inverse atomic radius has the form:

$$(\lambda_0^{LA})^2 = 0.798 Z \frac{1 - (\frac{Z_0}{Z})^{n+1}}{1 - \frac{Z_0}{Z}} a_0^{-2}, \tag{4.27}$$

where $n = Z(\frac{1}{3} - 0.002Z)$. Examples of $\lambda_{0,s}^{LA}$ values for argon are depicted in Fig. 4.4. The approximate Lamoureux-Avdonina formula for inverse atomic radius is given by:

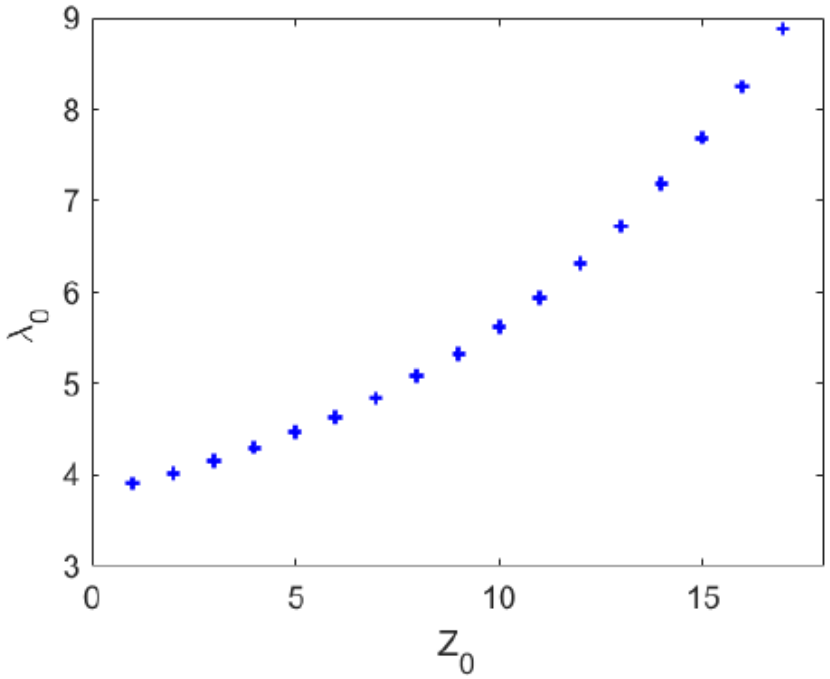

Figure 4.4: Lamoureux-Avdonina inverse ion radius for different argon ionization levels, obtained using Eq. (4.27). Figure adapted from [Jardin 2020a].

$$\lambda_0^{LA} \approx 0.8932 Z^{0.5} a_0^{-1}. \tag{4.28}$$

In the case of the Thomas-Fermi model, we have in turn the following formula [Peysson 2019, p. 31]:

$$\lambda_0^{TF} \approx 1.13 Z^{1/3} a_0^{-1}. \tag{4.29}$$

Both above models allow for obtaining very precise values of the radius of a particular atom or ion.

The spherically averaged electron density $\rho(r)$, in the case of the Pratt-Tseng model, can be obtained thanks to the Poisson equation applied for the potential in Eq. (4.25). We can write:

$$\nabla^2 V = -\frac{\rho(r)}{\varepsilon_0}. \tag{4.30}$$

Writing the nabla operator in spherical coordinates allows writing the above equation in the following form:

$$\frac{1}{r^2}\frac{\partial}{\partial r}(r^2\frac{\partial V}{\partial r}) = -\frac{\rho(r)}{\varepsilon_0}. \tag{4.31}$$

Calculating the partial derivative with respect to radius r, we can write:

$$r^2\frac{\partial V}{\partial r} = -Vr - \lambda_0\frac{r}{4\pi\varepsilon_0}(Z - Z_0)e^{-\lambda_0 r}. \tag{4.32}$$

It is then possible to calculate:

$$\begin{aligned}\frac{1}{r^2}\frac{\partial}{\partial r}(r^2\frac{\partial V}{\partial r}) &= -\frac{1}{r^2}(V + r\frac{\partial V}{\partial r}) - \lambda_0\frac{1}{4\pi\varepsilon_0 r^2}(Z - Z_0)(1 - \lambda_0 r)e^{-\lambda_0 r} \\ &= \frac{1}{r^3}(\lambda_0\frac{r}{4\pi\varepsilon_0}(Z - Z_0)e^{-\lambda_0 r}) - \lambda_0\frac{1}{4\pi\varepsilon_0 r^2}(Z - Z_0)(1 - \lambda_0 r)e^{-\lambda_0 r}.\end{aligned} \tag{4.33}$$

This allows to obtain an analytical formula for the electron density:

$$\rho(r) = \frac{\lambda_0^2}{4\pi r}(Z - Z_0)e^{-\lambda_0 r}. \tag{4.34}$$

An example of electron density obtained with the Pratt-Tseng model for every ionization level of tungsten is plotted in Fig. 4.5. It occurs that the above Pratt-Tseng formula for the electron density allows also obtaining an analytical formula for the form factor. Using Eq. (4.34), we can calculate that:

$$F_j(q) = \frac{\lambda_0^2}{q}(Z - Z_0)\int_0^\infty sin(qr)e^{-\lambda_0 r}dr. \tag{4.35}$$

Calculating the above integral, we obtain the simplified expression for the Pratt-Tseng-Botto form factor:

$$F_j(q) = \frac{N_{e,j}}{1 + (qa_j^B)^2}, \tag{4.36}$$

where $a_j^B = 1/\lambda_0^B$.

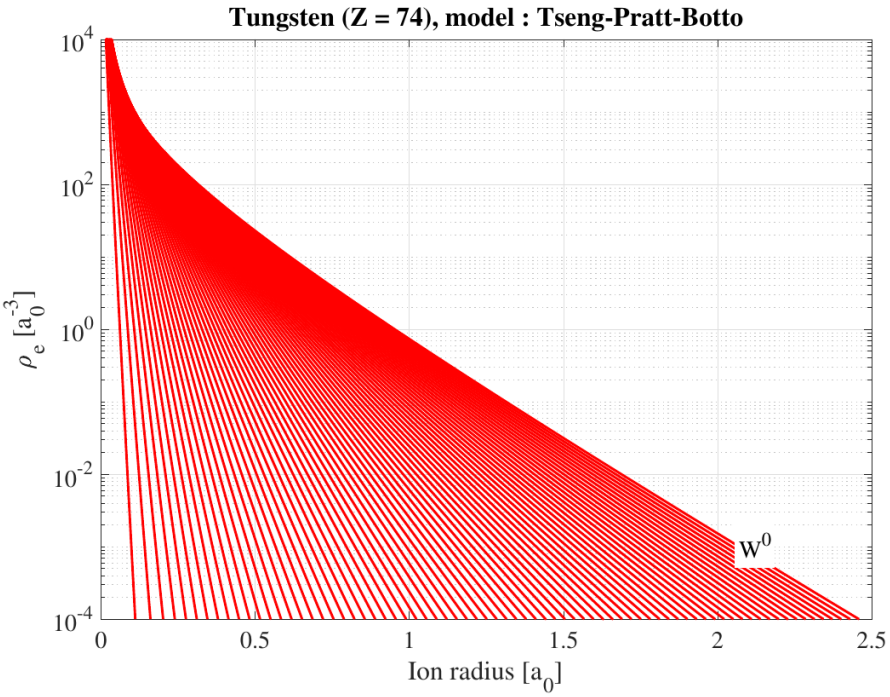

Figure 4.5: Spherically averaged electron density as a function of radius for all ionization states of Tungsten using the Pratt-Tseng model with Botto inverse atom radius. The length scale is given in units of the Bohr radius a_0. Figure reproduced from [Peysson 2021b].

4.2.3 DFT calculations

The primary source of inaccuracy of the Thomas-Fermi model comes from the inaccurate description of the total kinetic energy of electrons. This model does not take into account exchange energy and electronic correlation. However, this model gave fundaments for another method that we used as a reference in our research: the Density Functional Theory (DFT). To calculate the electron density of a many-electrons system like an atom or an ion, one should solve the time-independent Schrödinger equation:

$$\hat{H}\Psi = E\Psi, \tag{4.37}$$

where $\hat{H}$ - is the Hamiltonian, Ψ - is the wave function of the N-electrons system and E - is its total energy. The Hamiltonian consists of the following components:

$$\hat{H} = \hat{T} + \hat{V}_N + \hat{U}, \tag{4.38}$$

where $\hat{T}$ - is an operator of kinetic energy, $\hat{V}_N$ - is an operator of potential energy in the nucleus field and $\hat{U}$ - is an operator of electron-electron interaction energy. Using

formulas for each of these three operators, we can write the Schrödinger equation in the following form:

$$[\sum_{i=1}^{N}(-\frac{\hbar^2}{2m_i}\nabla_i^2) + \sum_{i=1}^{N} V_N(\vec{r_i}) + \sum_{i<j}^{N} U(\vec{r_i},\vec{r_j})]\Psi = E\Psi. \tag{4.39}$$

The electron-electron interaction causes that the above equation can not be considered equivalently in the form of many single-particle equations. In addition, in the case of atoms with a high number of electrons (for example, W with Z=74), the considered wave function is a function of $3N$ ($= 222$ for $N = 74$) variables. There are many different methods of solving the Schrödinger equation, like based on the Slater determinants or the Hartree-Fock method. However, such approaches in the case of tungsten are not efficient from a computational point of view. This was a motivation to develop an alternative method - the Density Functional Theory. In quantum mechanics, if we know the wave function, we can calculate the electron density using the following formula:

$$\rho(\vec{r}) = N \int d^3r_2 ... \int d^3r_N \Psi^*(\vec{r_1},\vec{r_2},...,\vec{r_N}). \tag{4.40}$$

However, like in the case of the Thomas-Fermi model, it is possible to treat the electron density as the central quantity to be determined. We can reverse the relation between the wave function and the electron density and write the wave function as a functional of the electron density:

$$\Psi_0 = \Psi(\rho_0), \tag{4.41}$$

where Ψ_0 - is the ground-state wave function and ρ_0 - is the electron density of the ground state. This means that for any observable $\hat{O}$, the corresponding ground-state expectation value O is a functional of the electron density ρ_0:

$$O(\rho_0) =< \Psi(\rho_0)|\hat{O}|\Psi(\rho_0) > . \tag{4.42}$$

In particular, the total energy can be written as a functional of the electron density in the following way:

$$E(n) = T(n) + U(n) + \int V_N(\vec{r})n(\vec{r})d^3\vec{r}. \tag{4.43}$$

Now, like in the case of the Thomas-Fermi model, we need to find the electron density for which the total energy is minimal. This can be done with the Lagrange multipliers method. The knowledge of the electron density allows calculating all ground-state observables based on Eq. (4.42). We used the GAUSSIAN code [Frisch 2019] to calculate

the electron density for tungsten ions, and the results are presented in Fig. 4.6. It is clear that the DFT is the most accurate approach, although numerically expensive, and is the only one able to recover the atomic shell structure in the electron density profiles as compared to the smooth radial profiles obtained with the TF and PT approaches.

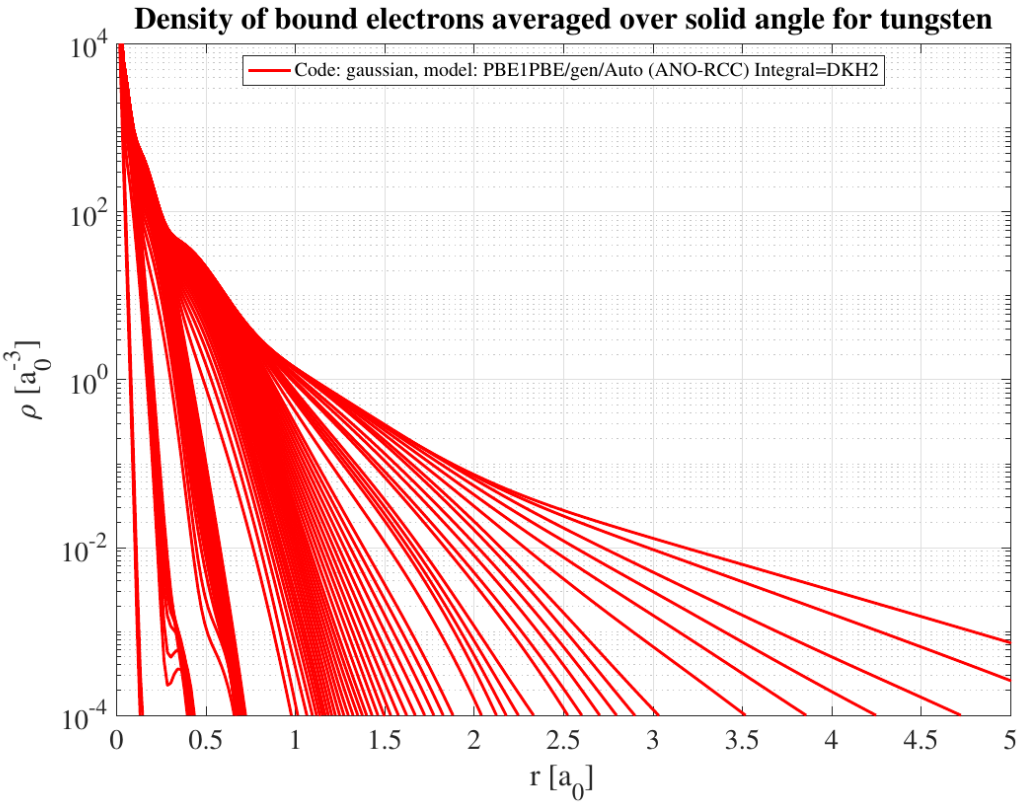

Figure 4.6: Electron density of bound electrons averaged over the solid angle as a function of the radius for all ionization states of tungsten as calculated by the Gaussian code. Figure reproduced from [Peysson 2021b].

The electron density calculated by the three different methods (TF-K, PT, DFT) allowed us to calculate the corresponding form factors and compare them, as shown in Fig. 4.7. For middle ionized heavy impurities like, for example, W^{40+}, the Pratt-Tseng-Botto approximation allows obtaining a form factor with values closer to the reference DFT result than the Thomas-Fermi-Kirillov approximation. Thus, Pratt-Tseng-Botto should be chosen among the two considered approximations for describing the hot tokamak plasma with heavy impurities with an analytical expression of the atomic form factor. Because of that, all results, which will be presented in Chapter 5, were obtained using the Pratt-Tseng-Botto approximation.

The DFT approach allows transforming the problem of the many-body interacting system into a problem of a non-interacting system with a total potential $V(\vec{r})$. In this case, the

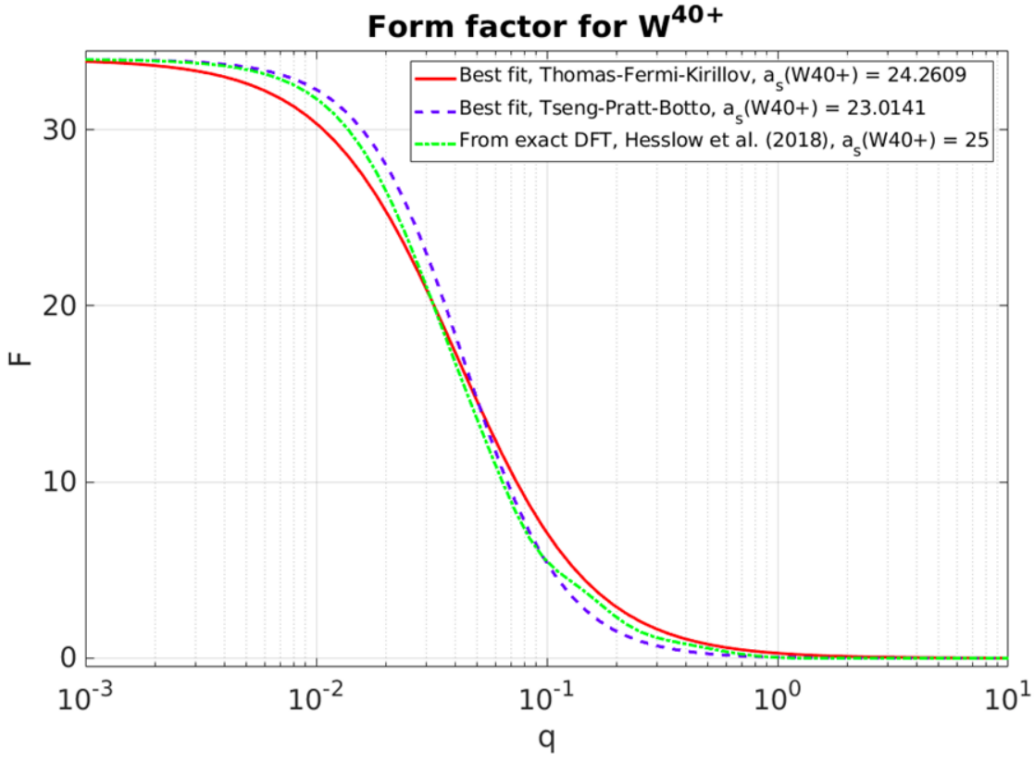

Figure 4.7: The form factor of the W^{40+} ion, calculated with three different methods. DFT is marked by a green dot-dashed line, Thomas-Fermi-Kirillov by solid red and Pratt-Tseng by dashed blue. Figure reproduced from [Peysson 2021b].

wave function can be represented by a Slater determinant of Kohn-Sham orbitals. This allows expressing the problem in the form of one-electron Schrödinger-like equations - Kohn-Sham equations. In this approach, we consider the equivalent system of non-interacting particles to the system of interacting particles in this sense that both of them are described by the same electron density. Kohn-Sahm equations have the following form:

$$(-\frac{\hbar^2}{2m}\nabla^2 + V(\vec{r}))\Phi_i(\vec{r}) = \varepsilon_i\Phi_i(\vec{r}), \tag{4.44}$$

where $\Phi_i(\vec{r})$ - are Kohn-Sham orbitals. The electron density can be then expressed in the following way:

$$\rho(\vec{r}) = \sum_{i=1}^{N} |\Phi_i(\vec{r})|^2. \tag{4.45}$$

4.3 Coulomb operator including partial screening effect

One of our main goals was to upgrade the LUKE code such that simulations will take into account the partial screening effect in the Coulomb collisions between fast electrons and tungsten ions. This means in particular that the Coulomb collision cross-sections must be expressed in the following way:

$$\frac{d\sigma_{e,j}^{coll}}{d\Omega} = \frac{r_0^2}{4p^4}\left(\frac{cos^2(\theta/2)p^2+1}{sin^4(\theta/2)}\right)|Z_j - F_j(q)|^2, \tag{4.46}$$

where Ω - is the solid angle, r_0 - is the classical electron radius, p - is the momentum of the incident fast electron, θ - is its deflection angle, Z_j - is the impurity atomic number. It is important to look closer at the term $Z_j - F_j(q)$, the effective ion charge due to partial screening. Let us consider the example of W^{40+}, for which the form factor is plotted in Fig. 4.7. When a fast incident electron probes into the W^{40+} electron cloud, the form factor has lower values than the total number of bound electrons (here 34). This results in a higher effective charge, and consequently, a higher Coulomb collisions cross-section. In order to estimate the impact of the partial screening effect on elastic collisions, the behaviour of the elastic electron-ion collision frequency can be investigated, as defined by the following formula [Hesslow 2017]:

$$\nu^{ei} = \nu_{CS}^{ei}\left(1 + \frac{1}{Z_{eff}}\sum_j \frac{n_j}{n_e}\frac{g_j(p)}{ln\Lambda}\right), \tag{4.47}$$

where ν^{ei} - is the elastic electron-ion collision frequency in the case of partial screening, ν_{CS}^{ei} - is the one in the case of full screening (complete screening), $ln\Lambda$ - is the Coulomb logarithm and p - is the momentum of incident electrons. The effective charge of plasma is defined in the following way:

$$Z_{eff} = \frac{\sum_j n_j Z_{0,j}^2}{n_e}, \tag{4.48}$$

where n_j - is the density of particles of species j, $Z_{0,j}$ - is the ionization level of particles of species j and n_e - is the density of free electrons in the plasma. The quantity $g_j(p)$ is called screening function and is defined by the following formula:

$$g_j(p) = \int_{1/\Lambda}^{1}(|Z_j - F_j(q)|^2 - Z_{0,j}^2)\frac{dx}{x}, \tag{4.49}$$

where $x = sin(\theta/2)$. In the simple approximation of a plasma consisting of one ion species at one ionization level only, we can write:

$$\frac{\nu^{ei}}{\nu^{ei}_{CS}} = 1 + \frac{g_j(p)}{Z_o ln\Lambda}. \tag{4.50}$$

In the case of the Thomas-Fermi model, $g_j(p)$ has the following form:

$$g_j(p) = \frac{2}{3}(Z_j^2 - Z_0^2) ln[(p\bar{a_j})^{3/2} + 1] - \frac{2}{3}\frac{N_e^2 (p\bar{a_j})^{3/2}}{(p\bar{a_j})^{3/2} + 1}, \tag{4.51}$$

where Z_j - is the impurity atomic number, Z_0 - is its ionization level, a_j - is the effective ion radius, $\bar{a}_j = 2a_j/\alpha$ and N_e - is the number of bound electrons. Such kind of investigation done by [Hesslow 2017] for Argon can be seen in Fig. 4.8. Even for relatively light

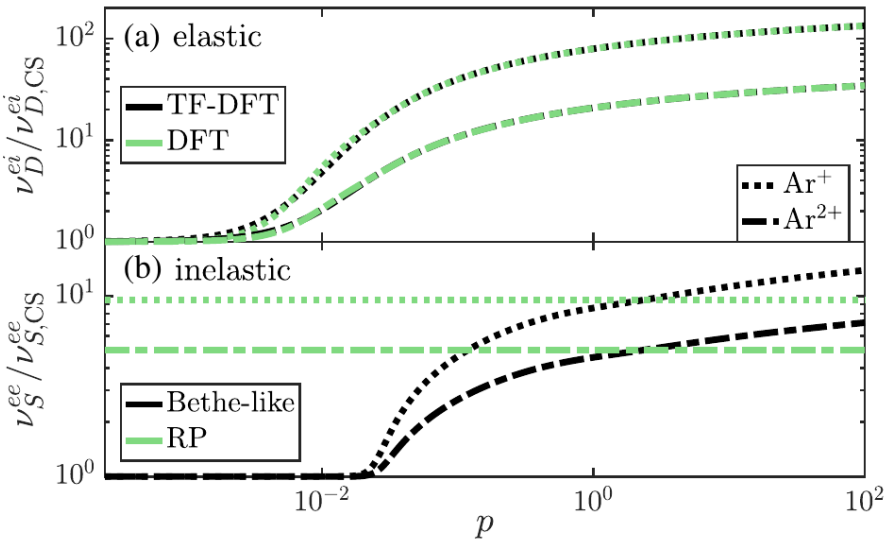

Figure 4.8: (a) The deflection frequency and (b) the slowing-down frequency as a function of the incoming electron momentum, normalized to the completely screened collision frequencies for the case of Argon. Figure reproduced from [Hesslow 2017].

impurity - Argon - the deflection frequency can be around two orders of magnitude higher in the partial screening case for highly energetic electrons. Here, p denotes the normalised momentum of an incoming electron, and the value $p = 1$ corresponds to the kinetic energy of around a few hundred keV.

4.4 Fast electron bremsstrahlung with partial screening effect

The synthetic diagnostic of fast electron bremsstrahlung R5-X2 had also to be upgraded with the physics of non-fully ionized impurities. The primary quantity to be updated is the corresponding cross-section which was given by [Koch 1959]:

$$\frac{d^5\sigma_{e,j}^{Brem}}{dkd\Omega_k d\Omega_p} = \alpha(\frac{r_e}{2\pi})^2 \frac{p_f}{kp_i q^4} B(q, \alpha_f, \varphi)|Z_j - F_j(q)|^2. \tag{4.52}$$

Here:

$$q^2 = p_f^2 + p_i^2 + k^2 - 2p_i k cos\alpha_i + 2p_f k cos\alpha_f - 2p_f p_i (cos\alpha_f cos\alpha_i + sin\alpha_f sin\alpha_i cos\varphi) \tag{4.53}$$

where $\vec{k}$ - is the wave vector of the emitted photon, $\vec{p_i}, \vec{p_f}$ - are the initial and final electron momentum, α - is the fine-structure constant, α_i, α_f - are the associated angles with respect to $\vec{k}$, φ - is the angle between the $(\vec{p_i}, \vec{k})$ plane and the $(\vec{p_f}, \vec{k})$ plane as depicted in Fig. 4.9. B is a function which is introduced to write the cross-section in the

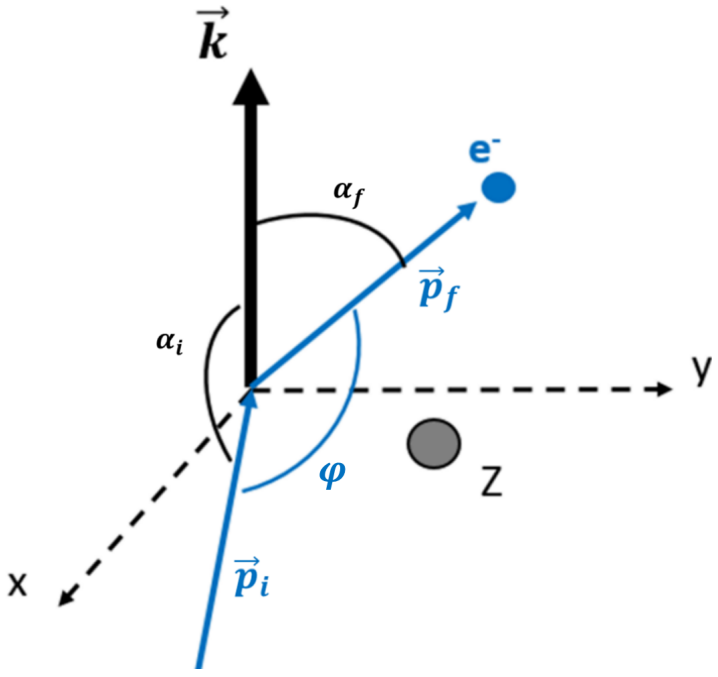

Figure 4.9: Parametrization of the fast electron - ion bremsstrahlung process. Figure adapted from [Jardin 2020a].

simple form of Eq. (4.52). The function B is decomposed as follows:

$$B(q, \alpha_f, \varphi) = \sum_{k=1}^{4} B_k. \tag{4.54}$$

The four B_k terms are expressed in the following way:

$$B_1 = \frac{p_i^2 sin^2\alpha_f}{(E_i - pcos\alpha_f)^2}(4E_i^2 - q^2), \tag{4.55}$$

$$B_2 = \frac{p_0^2 sin^2\alpha_i}{(E_i - p_i cos\alpha_i)^2}(4E_f^2 - q^2), \tag{4.56}$$

$$B_3 = \frac{2p_f p_i sin\alpha_f sin\alpha_i cos\varphi}{(E_f - p_f cos\alpha_f)(E_i - p_i cos\alpha_i)}(4E_f E_i - q^2), \tag{4.57}$$

$$B_4 = \frac{2k^2(p_f^2 sin^2\alpha_f + p_i^2 sin^2\alpha_i - 2p_f p_i sin\alpha_f sin\alpha_i cos\varphi)}{(E_f - p_f cos\theta_f)(E_i - p_i cos\theta_i)}. \tag{4.58}$$

In the following formulas for B_k terms, E_i and E_f - are initial and final total energies of electron (before and after collision) expressed in m_0c^2 units. We will integrate over $d\Omega_p = sin\alpha_f d\alpha_f d\varphi$ which is the infinitesimal element of solid angle in the direction of electron motion after collision - direction of $\vec{p_f}$:

$$\frac{d^3\sigma_{e,j}^{Brem}}{dkd\Omega_k} = \int_0^{\pi} sin\alpha_f \int_0^{2\pi} \frac{d^5\sigma_{e,j}^{Brem}}{dkd\Omega_k d\Omega_p} d\varphi d\alpha_f. \tag{4.59}$$

The crucial point here is to calculate the integral over φ. In order to do this, we will use the complicated Eq. (4.52), which includes the atomic form factor. It occurs that for the Thomas-Fermi model, the form factor cannot be integrated over φ analytically. However, it is possible in the case of the Pratt-Tseng model or the TF-Kirillov approximation. Nevertheless, the PT approach gave better accuracy (closer to the DFT) in the previous sections. Thus we will conduct the derivation with the PT model.
Firstly, the integration over φ leads to the following expression:

$$\int_0^{2\pi} \frac{d^5\sigma_{e,j}^{Brem}}{dkd\Omega_k d\Omega_p} d\varphi = \alpha(\frac{r_e}{2\pi})^2 Z_s^2 \frac{p_f}{kp_i} \sum_{k=1}^{4} \int_0^{2\pi} (1 - \frac{F_j(q)}{Z_s})^2 B_k \frac{d\varphi}{q^4}. \tag{4.60}$$

The above formula can be written in a more compact form:

$$\int_0^{2\pi} \frac{d^5\sigma_{e,j}^{Brem}}{dk d\Omega_k d\Omega_p} d\varphi = Z_s^2 \frac{p_f}{k p_i} \sum_{k=1}^{4} a_k J_k, \tag{4.61}$$

where a_k - are complicated coefficients that consist of quantities that do not depend on φ and thus could be taken out of the integral, J_k - are the resulting integrals over φ after deriving the coefficients a_k. The coefficients a_k are complicated mainly because of the complicated B_k functions and have the following form:

$$a_1 = \frac{4E_i^2 p_f^2 sin^2\alpha_f}{(E_f - p_f cos\alpha_f)^2} + \frac{4E^2 p_0^2 sin^2\alpha_i}{(E_i - p_i cos\alpha_i)^2} + \frac{2k^2(p_f^2 sin^2\alpha_f + p_i^2 sin^2\theta_i)}{(E_f - p_f cos\alpha_f)(E_i - p_i cos\alpha_i)}, \tag{4.62}$$

$$a_2 = -(\frac{p_f^2 sin^2\alpha_f}{(E_f - p_f cos\alpha_f)^2} + \frac{p_i^2 sin^2\alpha_i}{(E_i - p_i cos\alpha_i)^2}), \tag{4.63}$$

$$a_3 = -\frac{2p_f p_i sin\alpha_f sin\alpha_i (4E_i^2 + 4E_0^2)}{(E_f - p_f cos\alpha_f)(E_i - p_i cos\alpha_i)}, \tag{4.64}$$

$$a_4 = \frac{2p_f p_i sin\alpha_f sin\alpha_i}{(E_f - p_f cos\alpha_f)(E_i - p_i cos\alpha_i)}. \tag{4.65}$$

After the derivation of the above coefficients, a validation of their correctness has been performed by comparisons with equivalent formulas found in [Köhn 2014]. In turn, the integrals J_k are expressed in the following way:

$$J_1 = \int_0^{2\pi} (1 - \frac{F_j(q)}{Z_j})^2 \frac{d\varphi}{q^4}, \tag{4.66}$$

$$J_2 = \int_0^{2\pi} (1 - \frac{F_j(q)}{Z_j})^2 \frac{d\varphi}{q^2}, \tag{4.67}$$

$$J_3 = \int_0^{2\pi} (1 - \frac{F_j(q)}{Z_j})^2 cos\varphi \frac{d\varphi}{q^4}, \tag{4.68}$$

$$J_4 = \int_0^{2\pi} (1 - \frac{F_j(q)}{Z_j})^2 cos\varphi \frac{d\varphi}{q^2}. \tag{4.69}$$

The atomic form factor given by the Pratt-Tseng model has the following form:

$$F_j(q) = \frac{N_{e,j}}{1 + (qa_j)^2}, \tag{4.70}$$

where q - is the value of transferred to electron momentum vector because of collision and a_j - is effective ion radius. The expression occurring in all four integrals can be reformulated in the following way:

$$(1-\frac{F_j(q)}{Z_j})^2=(1-\frac{1-I}{1+(qa_j)^2})^2=1-\frac{2(1-I)}{1+(qa_j)^2}+\frac{(1-I)^2}{(1+(qa_j)^2)^2}. \tag{4.71}$$

We define the ionization degree as:

$$I=\frac{Z_{0,j}}{Z_j}. \tag{4.72}$$

Eq. (4.71) consists of three terms, which means that in total, 12 integrals must be calculated.
The term q^2 occurring in the integrals can be expressed in the following way:

$$q^2=acos\varphi+b, \tag{4.73}$$

where

$$b=p_f^2+p_i^2+k^2-2p_ikcos\alpha_f-2p_fp_icos\alpha_fcos\alpha_i\geq 0, \tag{4.74}$$

$$a=-2p_fp_isin\alpha_fsin\alpha_icos\varphi<0, \tag{4.75}$$

$$-b/a>1. \tag{4.76}$$

Using the introduced parameters a and b, the integrals J_k (where $k\in\{1,2,3,4\}$) can be expressed in the following general form:

$$J_k=\int_0^{2\pi}(1-\frac{1-I}{1+(acos\varphi+b)a_j^2})^2cos^p\varphi\frac{d\varphi}{(acos\varphi+b)^n}. \tag{4.77}$$

Now, thanks to the fact that we consider the Pratt-Tseng form factor, we can use Eq. (4.71) and obtain:

$$\begin{aligned}J_k=&\int_0^{2\pi}\frac{(cos\varphi)^p}{(acos\varphi+b)^n}d\varphi\\&-2(1-I)\int_0^{2\pi}\frac{(cos\varphi)^p}{(acos\varphi+b)^n(1+(acos\varphi+b)a_j^2}d\varphi\\&+(1-q_j)^2\int_0^{2\pi}\frac{(cos\varphi)^p}{(acos\varphi+b)^n(1+(acos\varphi+b)a_j^2)^2}d\varphi.\end{aligned} \tag{4.78}$$

We marked the above three integrals in the following way:

$$J_k = \hat{J}^{TP}_{k,1} - 2(1-q_j)\hat{J}^{TP}_{k,2} + (1-q_j)^2\hat{J}^{TP}_{k,3}. \tag{4.79}$$

This leads to the general formula for 12 integrals in the following form:

$$J^{TP}_{k,l} = \int_0^{2\pi} \frac{(cos\varphi)^p d\varphi}{(acos\varphi + b)^n (1 + (acos\varphi + b)c^{TP})m}, \tag{4.80}$$

where indexes have the following values $p \in \{0,1\},\ n \in \{1,2\},\ m \in \{0,1,2\}$. Among all 12 integrals, the simplest case is for $m = 0$. In this case, for four integrals $cos(\varphi + \pi) = -cos\varphi$, and we have:

$$\hat{J}^{TP}_{k,l} = \int_0^{2\pi} \frac{(cos\varphi)^p}{(acos\varphi + b)^n} d\varphi = 0. \tag{4.81}$$

More detailed calculations of the rest eight integrals can be found in Appendix B.

The upgrade of R5-X2 allowed us to obtain the necessary non-thermal bremsstrahlung cross-sections, including the partial screening effect. Comparison for different cases can be seen in Fig. 4.10, where we can see that the partial screening case is closer to the no screening case than the full screening case. However, the vertical axis is on a logarithmic scale, and there is still a significant difference between the partial screening and the no screening cases.

In this chapter, we have investigated the Thomas-Fermi model, the Pratt-Tseng model and the DFT to calculate the electron density and the atomic form factors of non-fully ionized impurity atoms. Both Thomas-Fermi-Kirillov and Pratt-Tseng models allow obtaining analytical expressions for the form factor. We could benchmark the obtained results by comparison with DFT calculations showing a better accuracy of the PT model. This allowed us to perform LHCD simulations with high-Z impurities, including the partial screening effect for chosen WEST discharge, as reported in Chapter 5, which was not possible before our work.

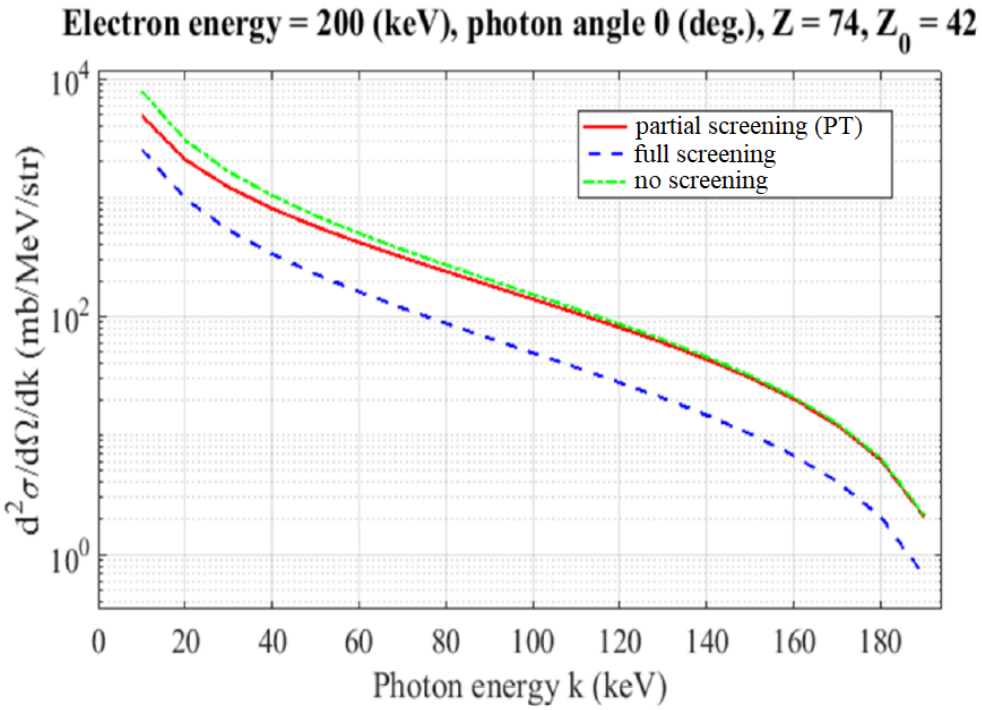

Figure 4.10: Non-thermal electron-ion bremsstrahlung cross-section for the case of electron energy of 200 keV and tungsten ion W^{42+}. Blue curve - full screening case, green one - no screening case, red one - partial screening case. Figure adapted from [Peysson 2021b].

Chapter 5

Experimental analysis of LHCD in WEST

Contents

5.1 Objectives

The main goal of this work was to investigate the impact of tungsten impurities and, in particular the impact of partial screening effect on the efficiency of the LHCD technique and emission of non-thermal bremsstrahlung from fast electrons on WEST tokamak. We will investigate now the WEST discharge #54981. A preliminary analysis of this shot has been reported in [Król 2021]. The study is reported here and extended in detail after a recent campaign of recalibration of the WEST shots database, including the correction of some diagnostics data.

5.2 Hard X-Ray diagnostic on WEST

Fast electrons constituting Lower Hybrid current emit non-thermal bremsstrahlung - photons in the hard X-ray (HXR) range with energies of 3 - 200 keV [Preynas 2012, p. 77]. In the case of Tore Supra, the HXR system consisted of 2 HXR cameras. Their description, as well as other detection systems, can be found in [Gil 2009, p. 1239]. In the case of WEST, only the horizontal camera of Tore Supra tokamak is still used. The vertical HXR camera was decommissioned. The WEST HXR camera consists of 38 horizontal lines of sight, as depicted in Fig. 5.1. The above system allows detecting photons in the range 20

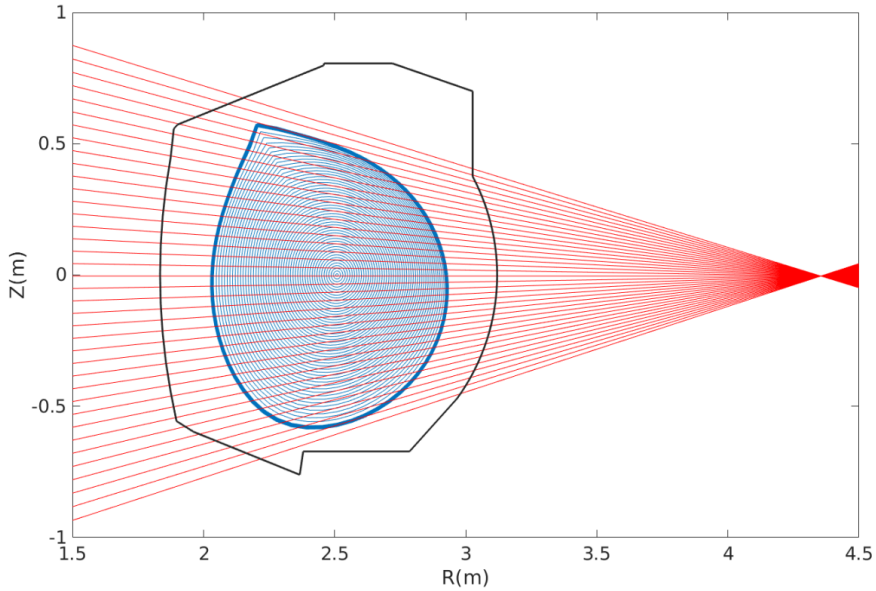

Figure 5.1: WEST HXR diagnostic system consisting of one horizontal camera.

- 200 keV emitted because of wave-particle Landau resonance interaction of fast electrons with LH waves [Nilsson 2012, p. 18]. The camera is composed of 38 cadmium telluride (CdTe) detectors and is equipped with neutron shielding [Gil 2009, p. 1239]. Each of

the 38 detectors measures the non-thermal photons emitted along the line of sight of the detector in the tokamak poloidal cross-section presented in Fig. 5.1. The particular signal from each detector is distributed into eight energy ranges, each of 20 keV width, by the proper spectrometer. In this thesis, measurements data of the energy channel 60 - 80 keV was used only. This choice is motivated by the fact that the signal-to-noise ratio is high for this energy channel characteristic of the suprathermal population induced by LHCD, and there is no thermal contribution to the signal [Preynas 2012, p. 79].

5.3 The WEST discharge #54981

For the purpose of this work, the LH-heated WEST discharge #54981 is investigated, where a plasma current $I_p = 0.4$ MA with two plateaus of LHCD power $P_{LH} = 1.5$ MW, 2.5 MW, a low loop voltage $V_{loop} \approx 50 - 300$ mV, a core electron temperature of $T_{e,0} \approx 3 - 4$ keV as measured by the Electron Cyclotron Emission (ECE) diagnostic and a core electron density of $n_{e,0} \approx 4 - 5 \times 10^{19}\ m^{-3}$ were successfully achieved, as presented in Fig. 5.2. Based on the measured total plasma radiation, the tungsten impurity concentration in the plasma was estimated to be of the order of $c_W \approx 2 \times 10^{-4}$.

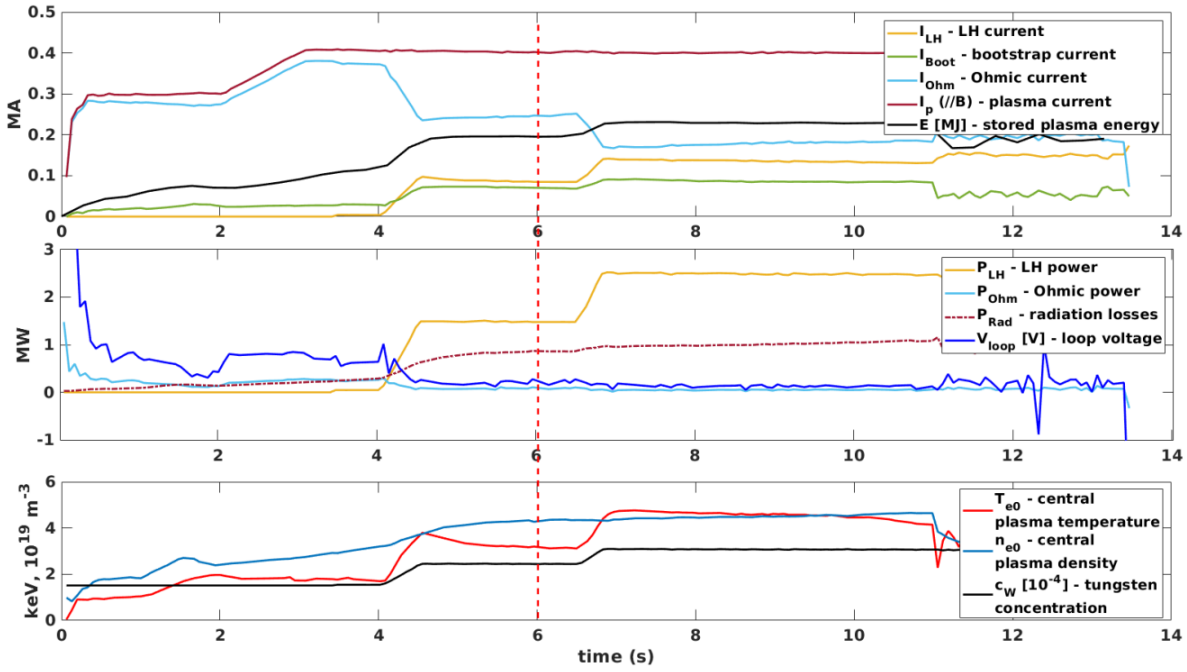

Figure 5.2: Experimental time traces, given by METIS for shot #54981. The red vertical dashed line indicates the selected time slice t = 6 s for the LHCD simulation.

The operation of the central solenoid of the tokamak causes the magnetic flux to vary with time, which induces a voltage around the tokamak, a so-called loop voltage. Non

zero loop voltage means that a toroidal electric field is present in the plasma that results in the ohmic component of plasma current.
DTOMOX (SXR range 1 - 20 keV) is the typical WEST diagnostic to observe W impurity radiation in the plasma core [Mazon 2012, Jardin 2020b], while fast electron bremsstrahlung is usually monitored in the HXR range 20 - 200 keV. Here HXR measurements in the range 60-80 keV (energy range characteristic of the suprathermal population induced by LHCD) are considered. The corresponding time traces of the SXR and HXR horizontal cameras are therefore displayed in Fig. 5.3. For example, a W central accumulation is clearly visible in SXR around t = 10 - 11 s, followed by a radiative collapse.

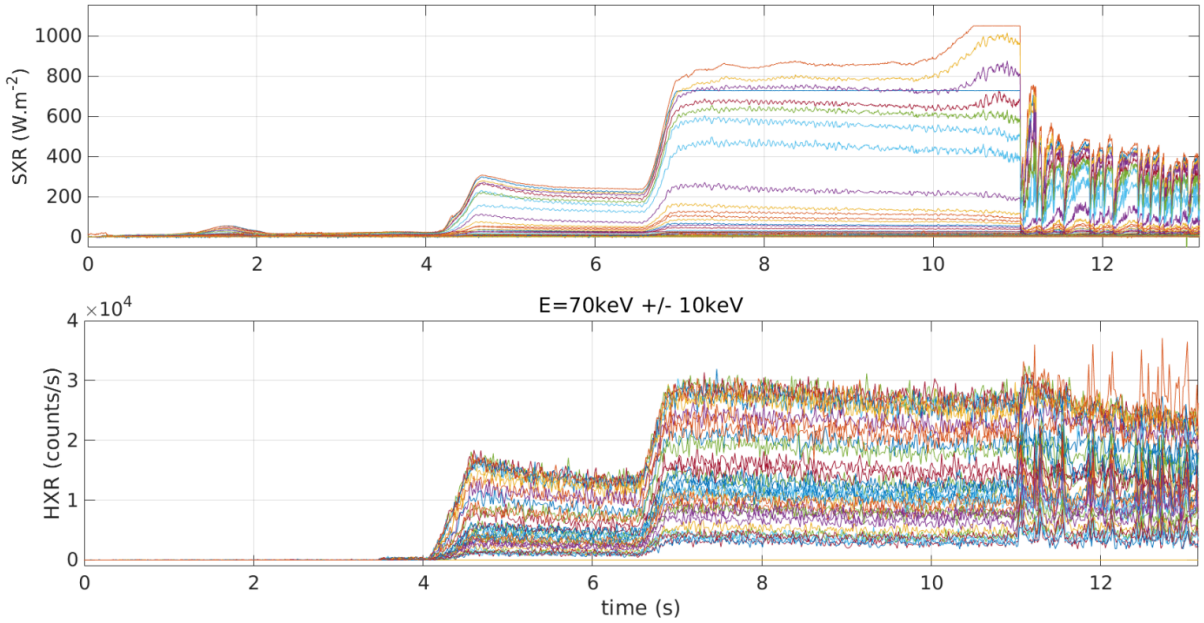

Figure 5.3: SXR (DTOMOX diagnostic) and HXR (energy channel 60 - 80 keV) time traces of the horizontal cameras channels for WEST #54981.

The METIS code provides the primary input for simulation. Among many quantities provided by METIS to LUKE, the main simulation inputs are the magnetic equilibrium, plasma temperature and plasma density. The plasma temperature and density radial profiles used in the simulation presented here for shot #54981 at t = 6 s are depicted in Fig. 5.4, where the geometric effective plasma radius was defined in Appendix A.1 by Eq. (A.6). The W impurity density profile is considered to be homothetic to the electron density profile (i.e. flat W concentration profile).

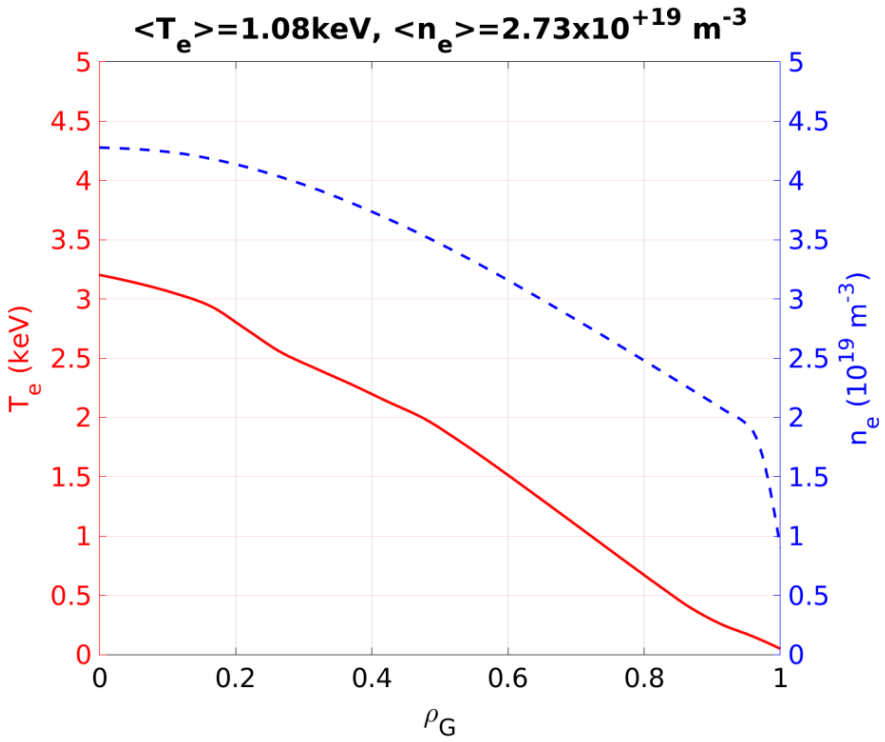

Figure 5.4: Plasma electron temperature and density profiles for the discharge #54981, time t = 6 s, as a function of the geometric effective plasma radius ρ_G.

5.4 Results and discussion

5.4.1 Ohmic simulation

As a preliminary step, the most straightforward simulation can be done by not taking into account LH power [LUKE 2019]. Therefore, launching LUKE with METIS input only (without C3PO ray-tracing) allows obtaining a current profile of the ohmic component only. The ohmic current profile and the absorbed ohmic power are depicted in Fig. 5.5. The obtained LUKE ohmic current profile can be compared with the METIS one. Such comparison allows validating the correctness of the simulation on the level before including LH power. In our case, LUKE calculates a total ohmic current of 203 kA, while METIS predicts 247 kA, thus indicating an overestimation of the ohmic current of around 40-50 kA. This result can be valuable while comparing the ohmic + LH current simulated by LUKE with the experimental one in the next sections.

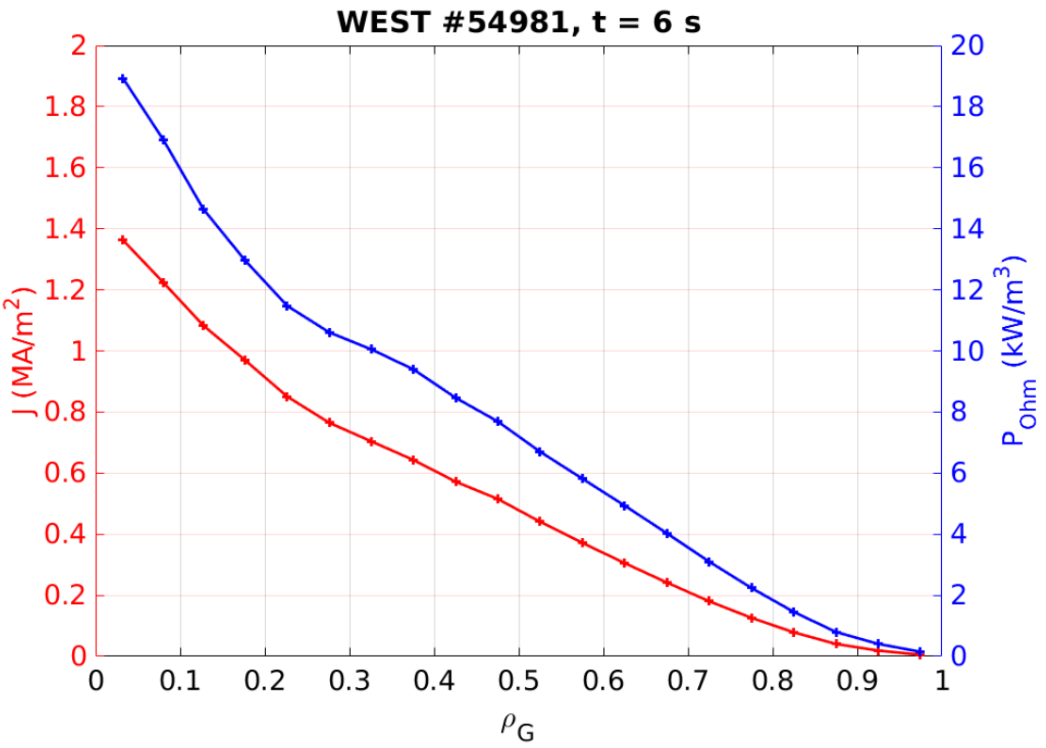

Figure 5.5: LUKE Ohmic current and absorbed Ohmic power radial profiles for discharge #54981, time t = 6 s, as functions of the geometric effective plasma radius ρ_G.

5.4.2 C3PO ray-tracing results

In the case of the C3PO/LUKE/R5-X2 suite of codes, considered here to take into account LH power, firstly, ray-tracing simulations with C3PO are conducted. The primary input for C3PO is the spectrum of coupled LH power - power successfully transferred from the LH antenna grid to the plasma edge. In particular, the spectrum of coupled LH power can be obtained by METIS (simplified spectrum) or ALOHA (more precise spectrum). In this work, for shot #54981, time t = 6 s, the METIS LH power spectrum was used, as depicted in Fig. 5.6. The use of the ALOHA power spectrum is kept as a perspective for more detailed results in future work.

The initial METIS LH power spectrum is modified with the so-called tail model, spreading the main peak in several smaller peaks [Decker 2014], which allows for a better agreement with the experiments by bridging the spectral gap [Peysson 2020]. The propagation of the LH power coupled to the plasma is modelled in a particular number of waves, each represented by one ray. The modified METIS LH power spectrum consists of seven peaks: the highest peak for $n_{\|0} \approx -2$, the second one for $n_{\|0} = 6$, and the additional tail made of five peaks (with the last one being partially merged with the main blue peak). In the case of the METIS power spectrum, each of the seven rays represents one of seven

peaks of the LH power spectrum. The poloidal and toroidal propagation of one chosen ray corresponding to $n_{||0} \approx 2$ (main peak) is presented in Fig. 5.7. The regions along the ray path where a significant absorption occurred are marked by black colour.

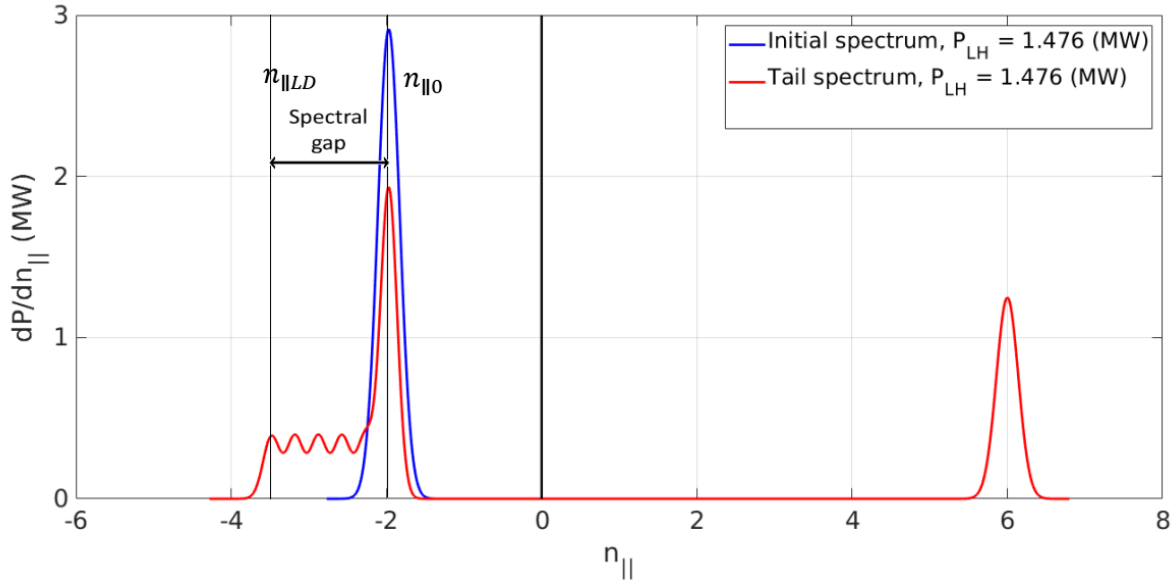

Figure 5.6: LH power spectra for discharge #54981, t = 6 s. The blue curve corresponds to the LH power spectrum calculated by METIS (initial spectrum). The red curve (tail spectrum) is obtained by modifying the blue spectrum with the tail model.

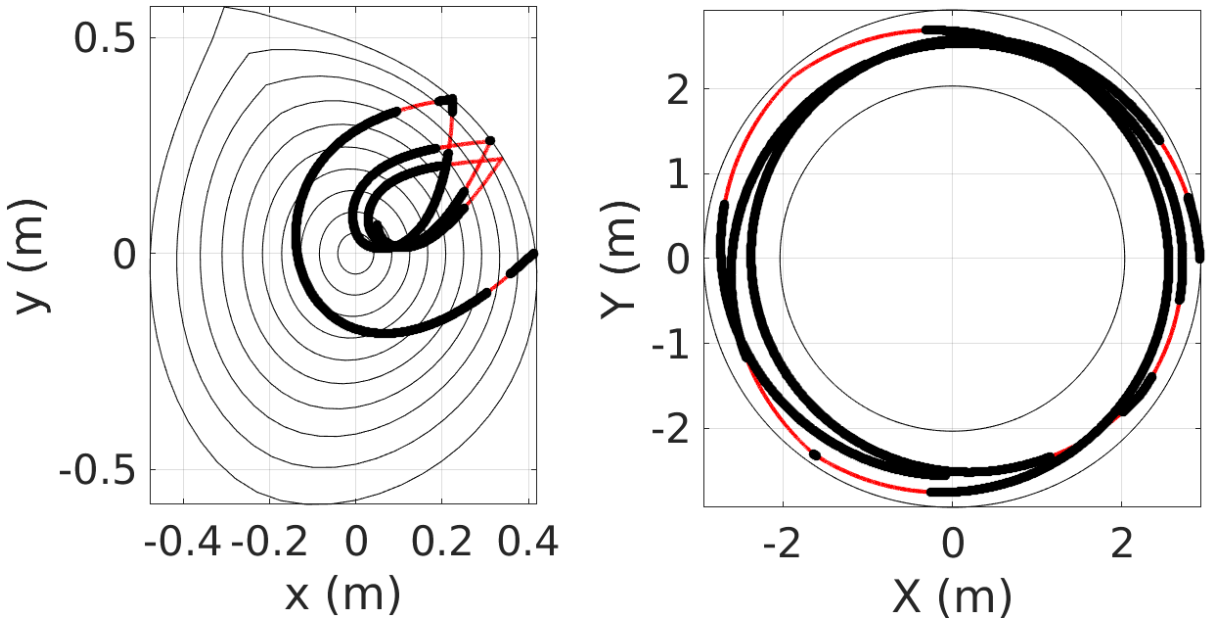

Figure 5.7: Poloidal view (left) and toroidal view (right) of trajectory for one chosen LH wave (ray), for discharge #54981, t = 6 s.

In turn, the evolution of the parallel refractive index along the ray path is depicted in Fig.

5.8. The curve is shown together with two other curves corresponding to: $n_{\parallel LD} = \frac{6.5}{\sqrt{T_e}}$ - parallel refractive index of the Landau wave-particle resonance condition and $n_{\parallel acc}$ - parallel refractive index of the LH wave accessibility condition.
LH waves can propagate in plasma only if their parallel refractive index satisfies the following condition: $n_{\parallel acc} < n_{\parallel} < n_{\parallel LD}$. The presented four peaks in the Landau resonance curve correspond to moments in which the wave was in the plasma core (high temperature), as can also be seen in the poloidal cross-section in Fig. 5.7. When the $n_{\parallel}$ curve meets the Landau resonance condition curve (one of the peaks in the top part of Fig. 5.8), the wave is fully absorbed, and its propagation is ended. The ray trajectories presented here are cut at the moment when 99% of the power of the wave was absorbed. In contrast to the results presented in Fig. 5.7 and Fig. 5.8 for one chosen ray with $n_{\parallel 0} \approx -2$, the poloidal trajectories of all seven LH rays used in the modelling of shot #54981, t = 6 s are presented in Fig. 5.9.

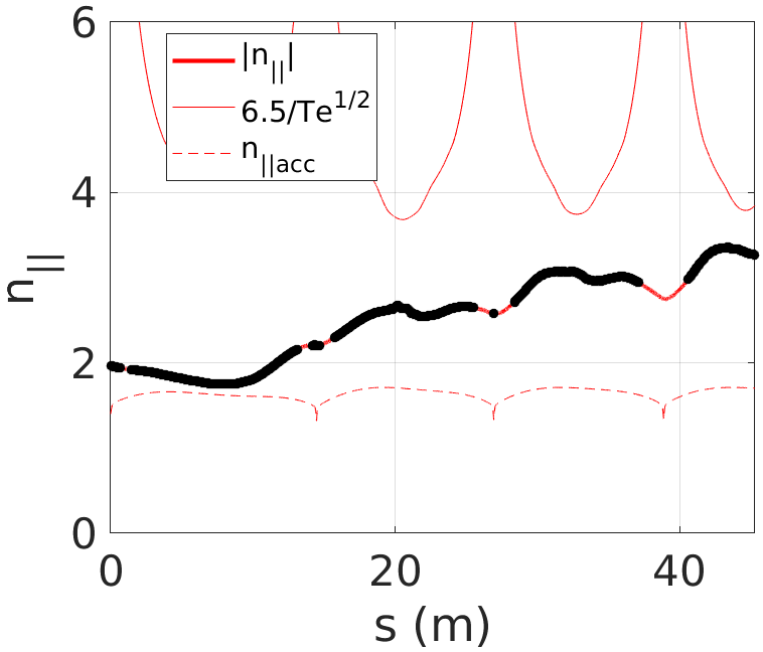

Figure 5.8: Evolution of parallel refractive index $n_{\parallel}$ of one chosen LH ray as a function of the trajectory length, for discharge #54981, t = 6 s.

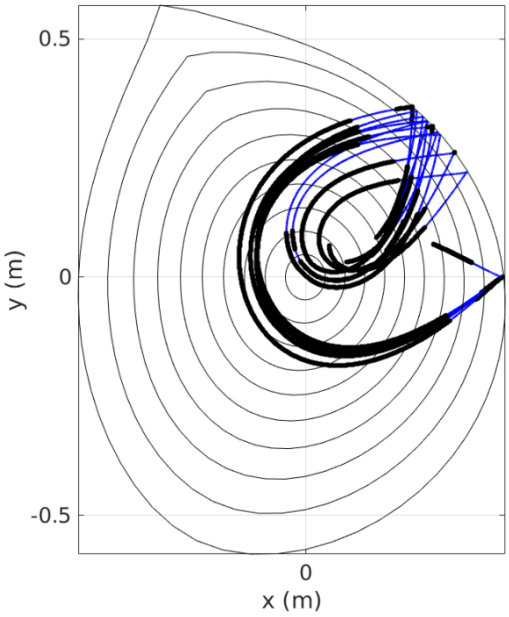

Figure 5.9: The poloidal trajectory of all seven rays for discharge #54981, time t = 6 s.

5.4.3 LH current drive and HXR profile prediction

Once the LH wave propagation and regions of absorption have been calculated by C3PO ray-tracing, the central quantity that can be obtained by the LUKE code - is the electron velocity distribution function. By default, LUKE calculates the electron distribution function in 20 points laying on the low-field side (positive part of the x-axis) of the WEST poloidal cross-section. The calculated electron distribution function for shot #54981, t = 6 s, at the first radial position in the plasma core ($\rho_G = 0.04558, \theta = 0$) is depicted in Fig. 5.10, where the deviation from the Maxwellian distribution is clearly visible with a fraction of suprathermal electrons, for $p_{||} \gg p_{Te}$.
Based on the obtained electron velocity distribution function, the ohmic + LH current radial profile can be calculated as a moment of the electron velocity distribution function. This profile, together with the LH absorbed power profile, is presented in Fig. 5.11.

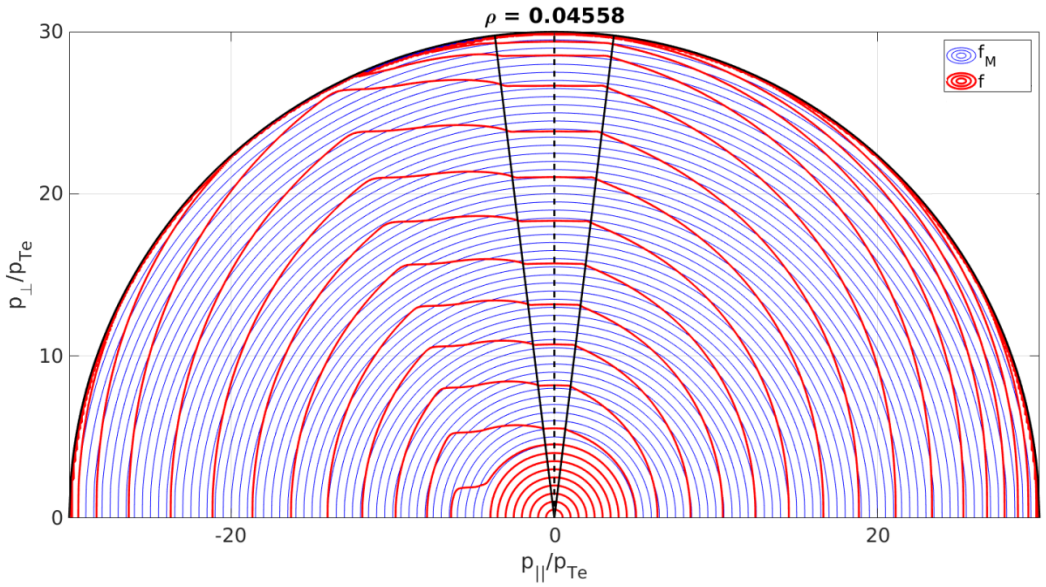

Figure 5.10: Electron distribution function for shot #54981, time t = 6 s, $\rho_G = 0.04558$ based on simulation with partial screening effect taken into account.

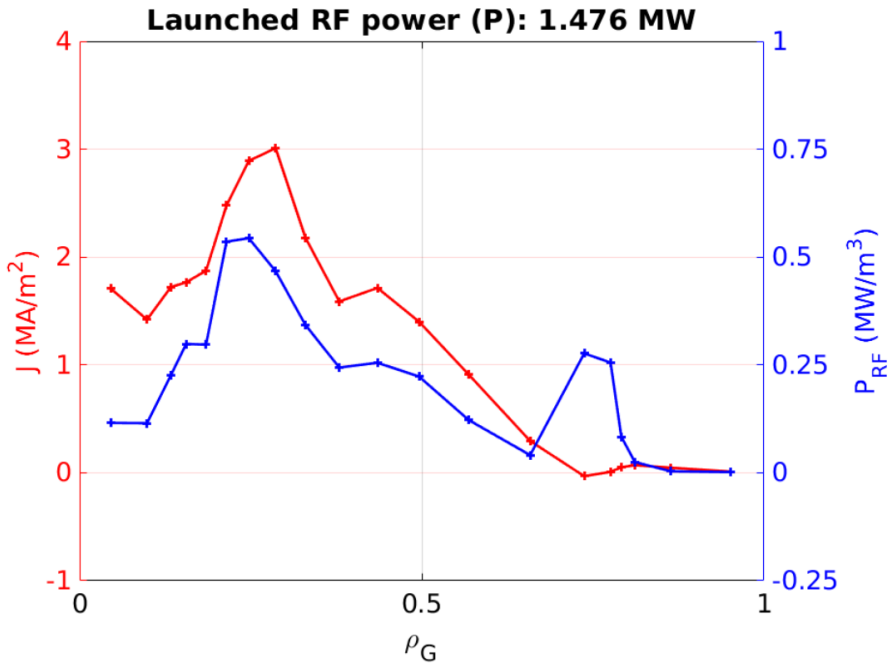

Figure 5.11: Current and absorbed power profiles for discharge #54981, time t = 6 s with partial screening effect taken into account, as functions of the geometric effective plasma radius ρ_G.

It is visible that most of the power and current are deposited in the core around $\rho_G \approx 0.2 - 0.3$. However, it is worth noting that a small part of the RF power is also deposited at the edge around $\rho_G \approx 0.7$. The fact that the initial LH power spectrum in Fig. 5.6

consists of positive and negative peaks means that co and counter-currents are generated (clockwise and anti-clockwise direction when WEST tokamak is viewed from the top). These two currents compensate each other, and despite that some power is absorbed in $\rho_G \approx 0.7$, the resulting current is almost equal to zero.

Another essential advantage of the calculated electron distribution function is that it allows the calculation, using the R5X2 code, of the fast electron bremsstrahlung as well as the prediction of the associated line-integrated measurements by the HXR horizontal camera. The predicted HXR profile (count rate in photon/sec) can then be compared with experimental measurements (red circles), as presented in Fig. 5.12.

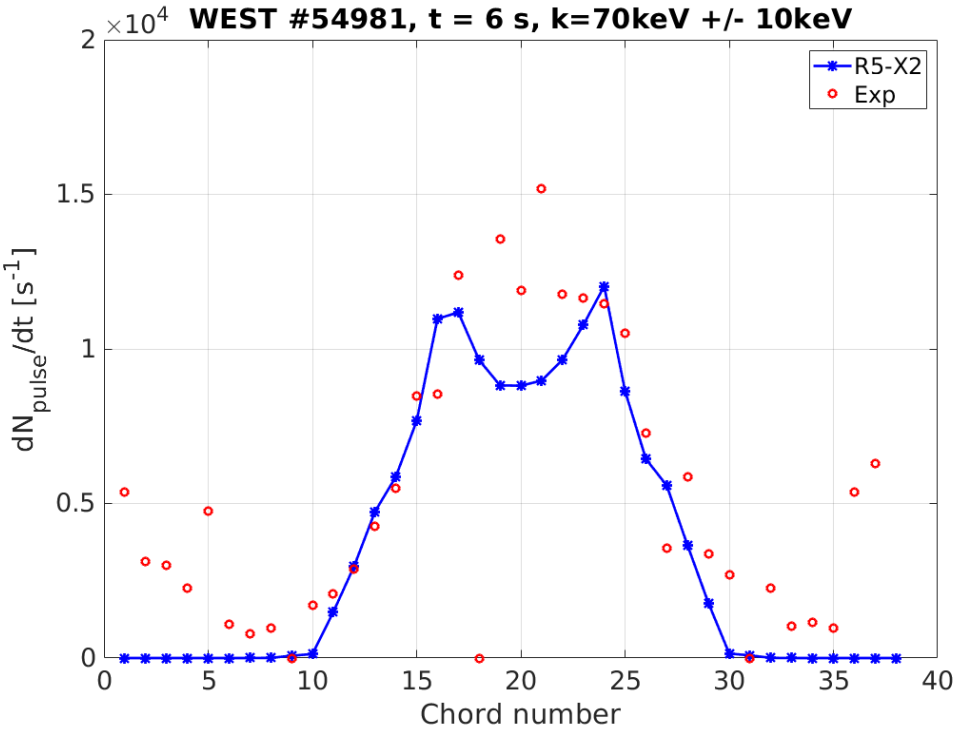

Figure 5.12: Comparison of pulse count rate HXR profiles - experimental and calculated by R5-X2 - for WEST shot #54981, t = 6 s, HXR photons energy range k = 60 - 80 keV. In the case of beginning and ending chords, the measured signal corresponds mostly to scattered radiation from tokamak inner components.

5.4.4 Impact of partial screening effect

The LHCD simulation can be performed for full screening and partial screening cases. Results presented up to now were obtained for the partial screening case, which was described in Chapter 4. A full screening simulation was also performed to present the difference between results for both cases. The full screening case is equivalent to assuming that all electrons bound to the impurity ions completely screen the atomic nuclei during

the interaction with fast electrons, which means that fast electrons cannot probe the electron cloud of impurity ions.

Activation of partial screening effect in the performed simulations does not affect the results obtained by METIS, ALOHA and C3PO with respect to the full screening case. In turn, LUKE and R5-X2 codes have to be launched independently for the cases of full and partial screening. The current profiles obtained by LUKE with partial and full screening are depicted in Fig. 5.13. A slight reduction of the predicted current is observed when including the partial screening effect. In the case of the full screening simulation, the obtained ohmic + LH current is equal to 508 kA. In turn, in the case of partial screening, the obtained ohmic + LH current equals 445 kA, which is a value closer to the experimental one - 332 kA. The comparison of HXR experimental profiles with simulated ones in three cases: without W impurities ($n_W = 0$) and with W impurities for full and partial screening cases is depicted in Fig. 5.14.

It is clearly visible that the presence of W impurities increases the HXR intensity, as expected. Besides, the partial screening effect increases the impact of W impurities on the predicted HXR measurements by a factor $\approx 2 - 3$. As a result, the predicted HXR measurements are much closer to the experimental ones. This demonstrates the importance of the partial screening effect to increase the accuracy of R5-X2 simulations.

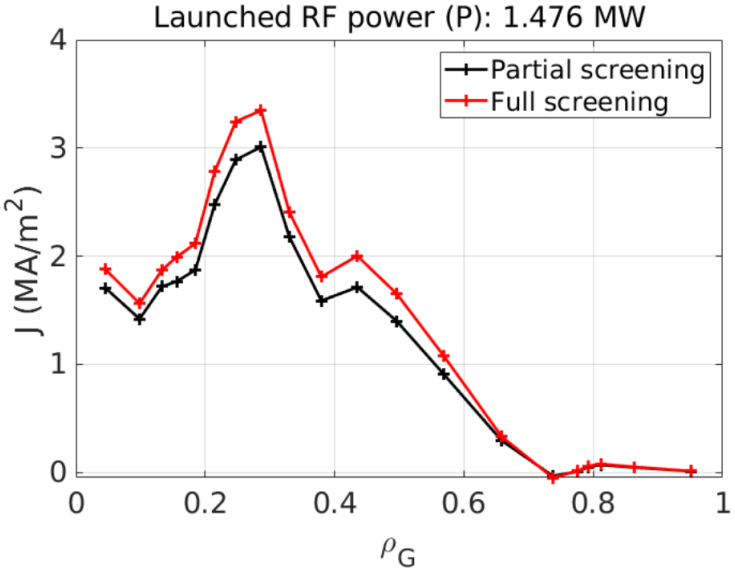

Figure 5.13: LUKE current profiles for cases of full and partial screening for shot #54981, time t = 6 s.

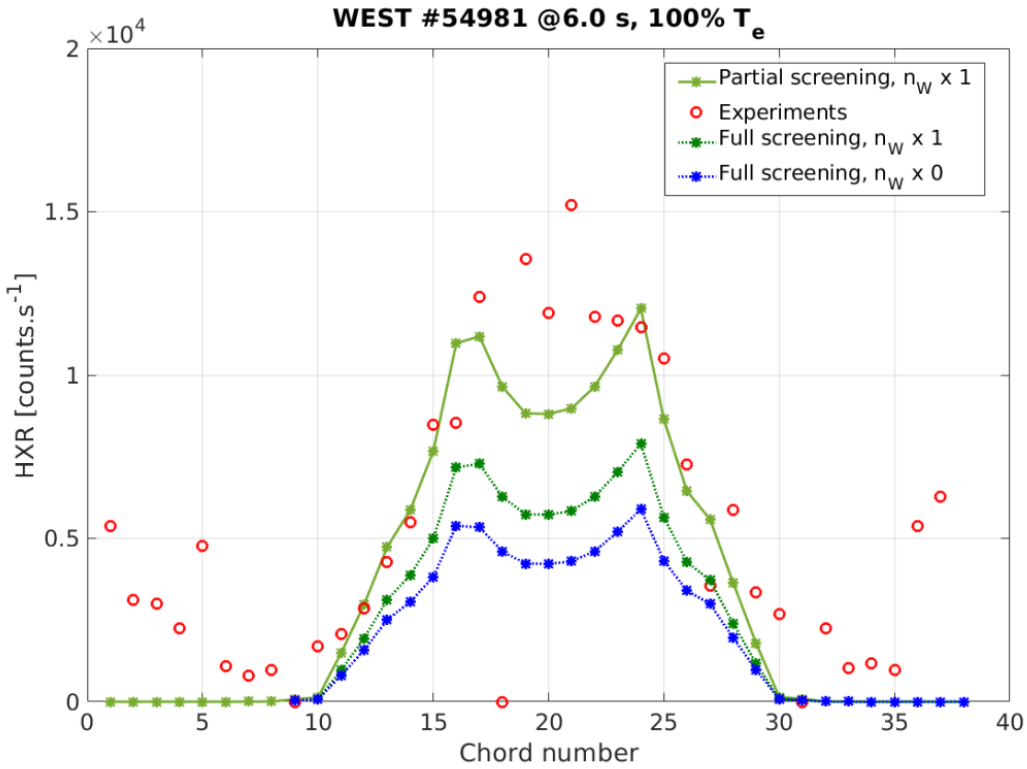

Figure 5.14: Comparison of HXR pulse profiles - experimental and calculated by R5-X2 - for WEST shot #54981, t = 6 s in the case of full and partial screening.

5.4.5 Analysis of sensitivity to c_W and T_e

Since in practice there are experimental uncertainties on the W concentration, chosen by METIS in order to match the total radiated power, and on the electron temperature from the ECE diagnostics, several scenarios with different electron temperatures and W concentrations were tested in order to match jointly experimental SXR and HXR measurements. Table 5.1 summarizes the total ohmic + LH current predicted for different scenarios of T_e and n_W, to be compared with the experimental plasma current, taking into account that the ohmic current was overestimated by 40-50 kA in the section 5.4.1.

Table 5.1: Comparison of ohmic + LH current for WEST #54981 at t = 6 s.

Tungsten amount (in %, METIS)	Experimental plasma current, [kA]	Calculated current for 100% of T_e, [kA]	Calculated current for 90% of T_e, [kA]
0%		487	
75%		452	447
100%	332	445	437
125%		435	428
150%		426	421

The total HXR experimental error (in counts/sec) for different values of T_e and n_W are displayed in Fig. 5.15.

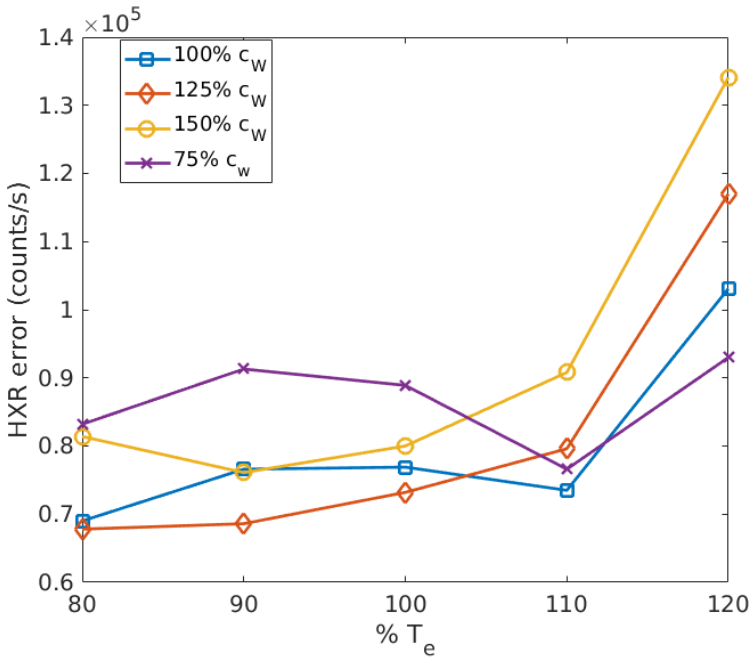

Figure 5.15: HXR errors for #54981, time t = 6 s.

As a result, a decrease of T_e by 10 - 20% while increasing W concentration by 0 - 25% allows obtaining a much better matching of HXR measurements. This result has been corroborated by the analysis of SXR measurements [Mazon 2021]. The impact of T_e on the predicted current profile and HXR measurements can be seen in Fig. 5.16 and Fig. 5.17.

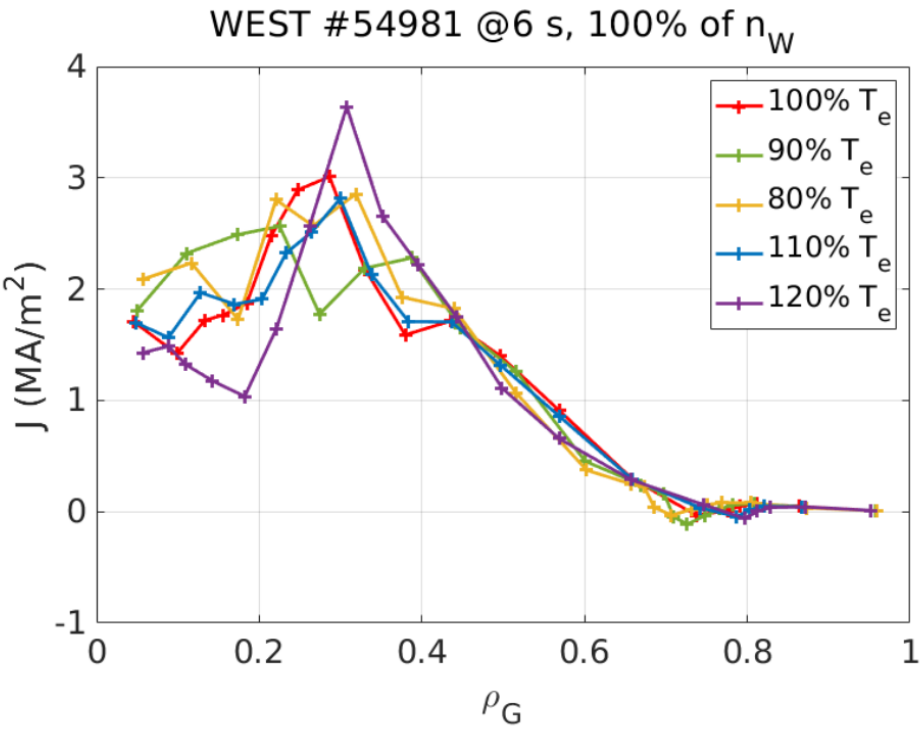

Figure 5.16: Temperature scan of the predicted current profile including partial screening for shot #54981, time t = 6 s.

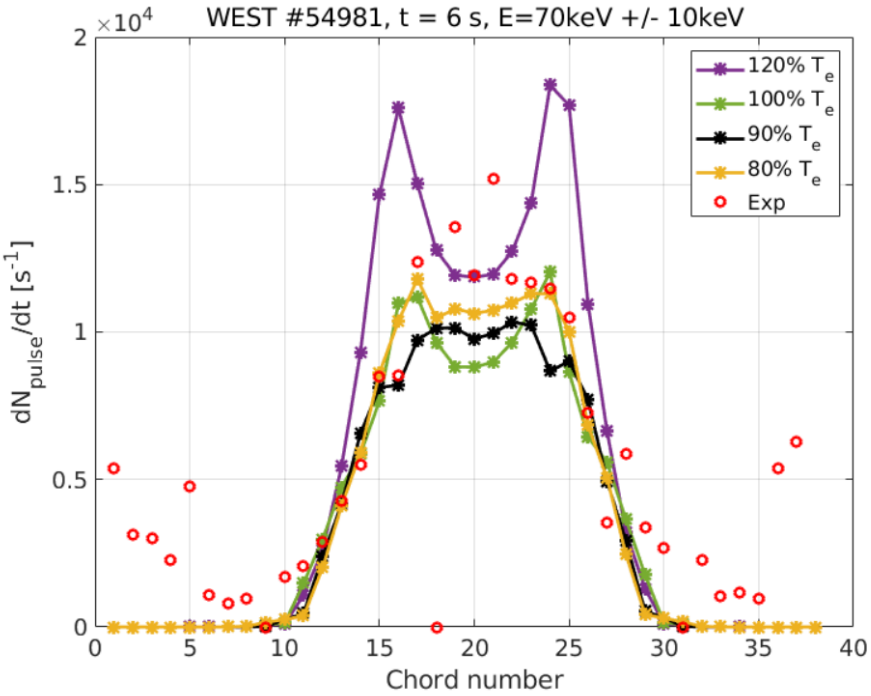

Figure 5.17: Temperature scan of the HXR pulse profile including partial screening for shot #54981, time t = 6 s.

It is visible that changing T_e is moving the radial localization of the peak of LH power deposition and the HXR pulse profile. The impact of W concentration on the predicted current profile and HXR measurements is depicted in Fig. 5.18, Fig. 5.19 and Fig. 5.20. We can see that, unlike T_e, increasing the amount of W impurities leads to a slight decrease of the current profile and a significant increase of the HXR intensity, but without affecting the global shape of the profiles.

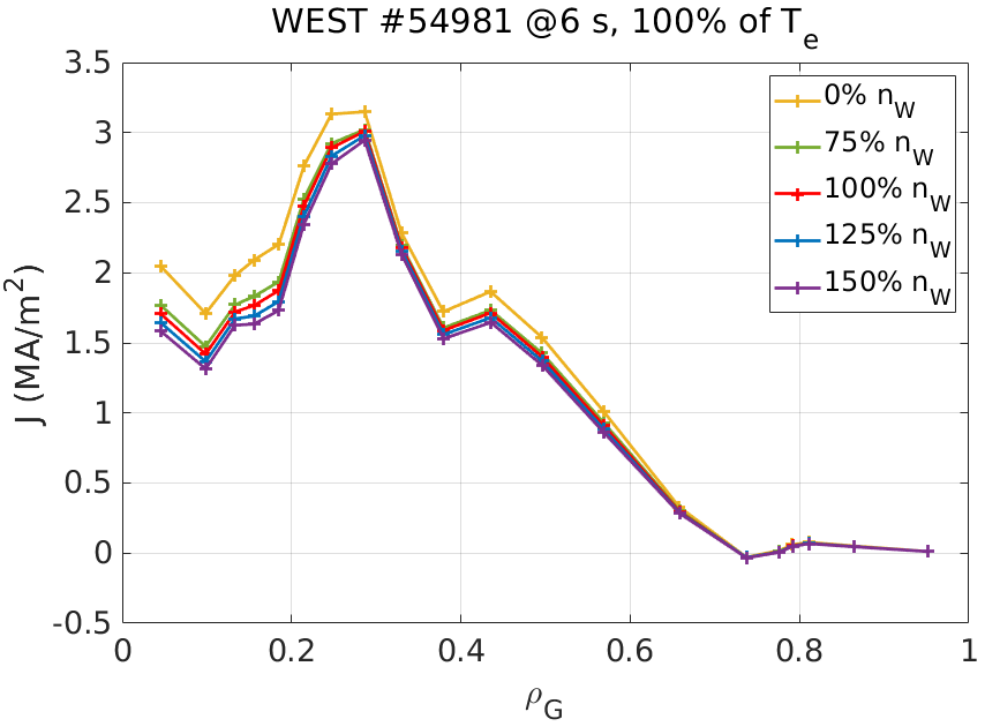

Figure 5.18: Tungsten density scan of the predicted current profile including partial screening for shot #54981, time t = 6 s.

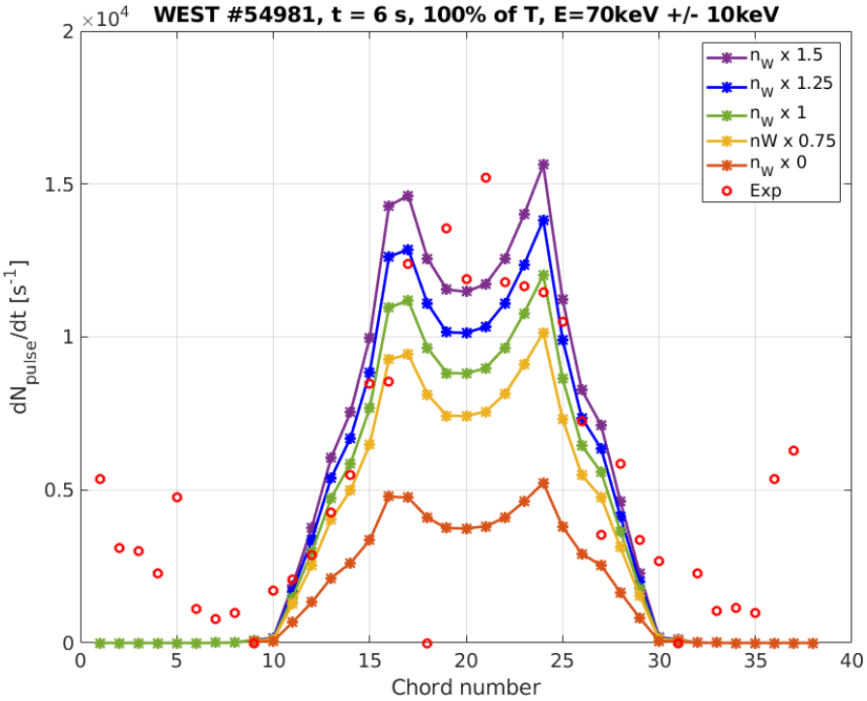

Figure 5.19: Tungsten density scan of HXR profile for the case of partial screening for shot #54981, time t = 6 s. Results for standard temperature.

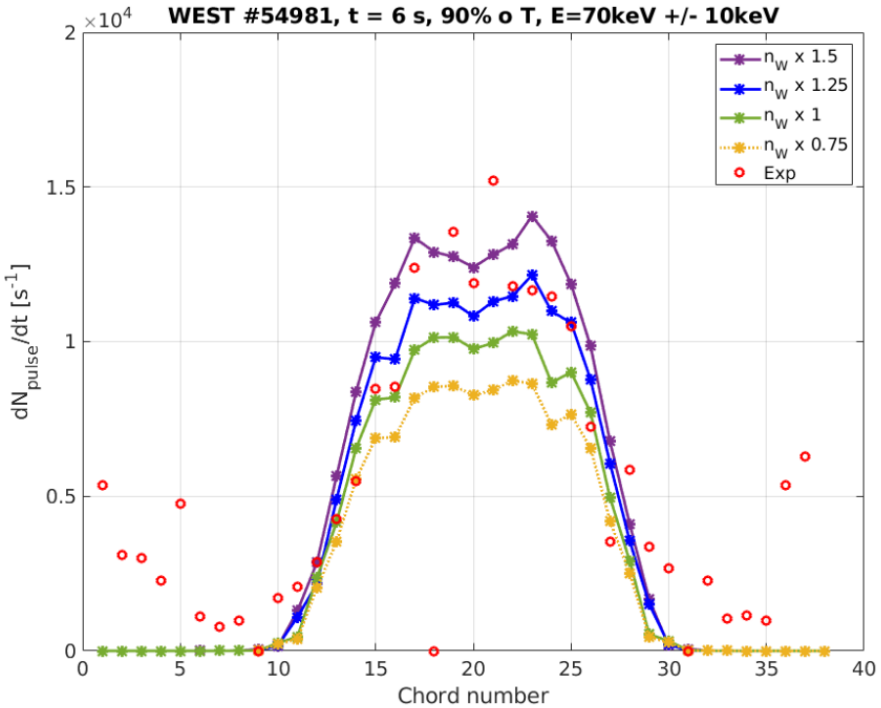

Figure 5.20: Tungsten density scan of HXR profile for the case of partial screening for shot #54981, time t = 6 s. Results for temperature decreased by 10%.

5.4.6 Stability in time of the LH simulations

In order to check the stability of the obtained results in time, LHCD simulations were performed for t = 5.9 s and t = 6.1 s together with t = 6 s. The comparison of these three times was made with standard METIS temperature and density profiles without arbitrary changes (100% of T_e and 100% of n_W). Each simulation for all three times was performed with an initial LH power spectrum modified with the tail spectral model and taking into account the partial screening effect. The temperature and density profiles for these three times are depicted in Fig. 5.21.

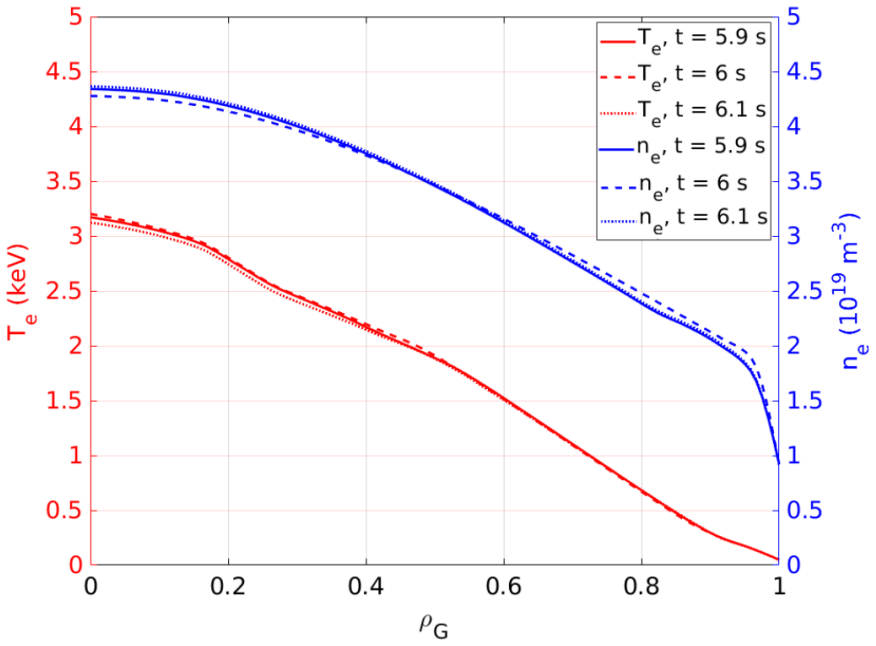

Figure 5.21: Electron temperature (in red) and density (in blue) profiles for shot #54981 at times t = 5.9 s (thick line), t = 6.0 s (dashed line) and t = 6.1 s (dotted line).

It is visible that both temperature and density profiles are not changing significantly in the time window t = [5.9 s; 6.1 s], which allows investigating the stability of LHCD simulations with respect to small perturbations of the plasma profiles. The C3PO ray-tracing calculations of LH wave at t = 5.9 s, 6.0 s, 6.1 s, for one ray corresponding to the main peak of LH power spectrum are depicted in Fig. 5.22. For visualization purposes, the ray is interrupted after 75% of the LH power has been absorbed. It is visible that for the three times, the poloidal and toroidal trajectories of the main LH ray are very similar. Although the distance between the three rays increases progressively along the ray trajectory, most of the LH power is already deposited before this distance becomes significant. This is reflected in the current profiles calculated by LUKE and depicted in Fig. 5.23, which exhibit relatively similar shapes.

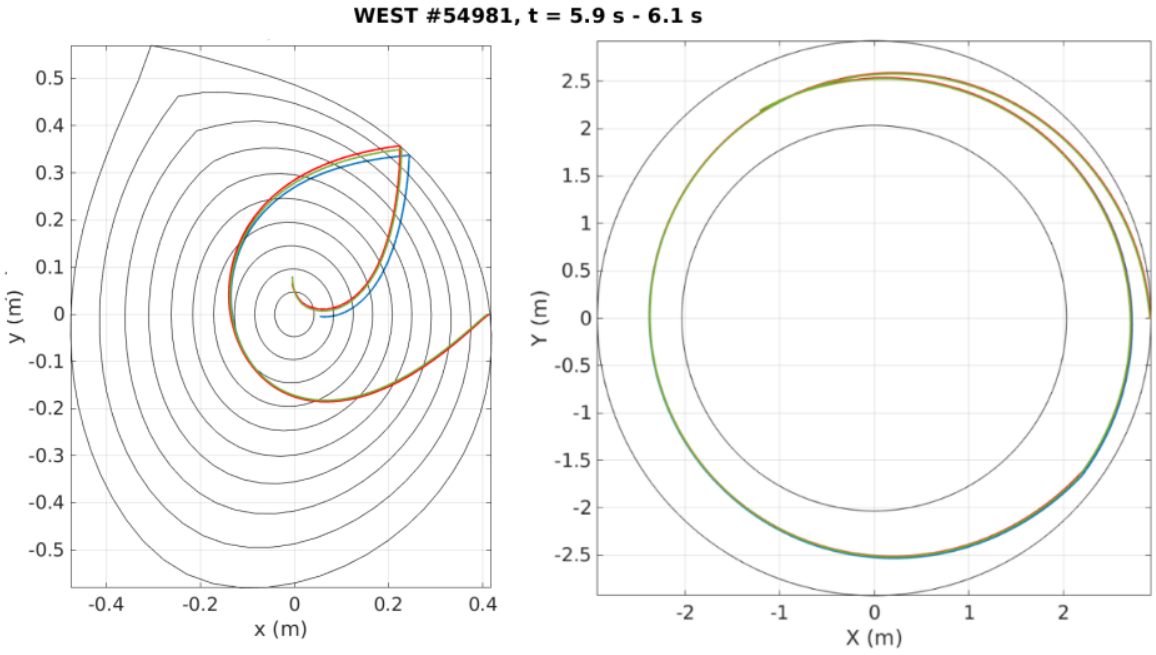

Figure 5.22: Poloidal (left) and toroidal (right) propagation of one ray corresponding to the main peak of LH power spectrum for shot #54981 at t = 5.9 s - blue curve, t = 6 s - red curve, t = 6.1 s - green curve.

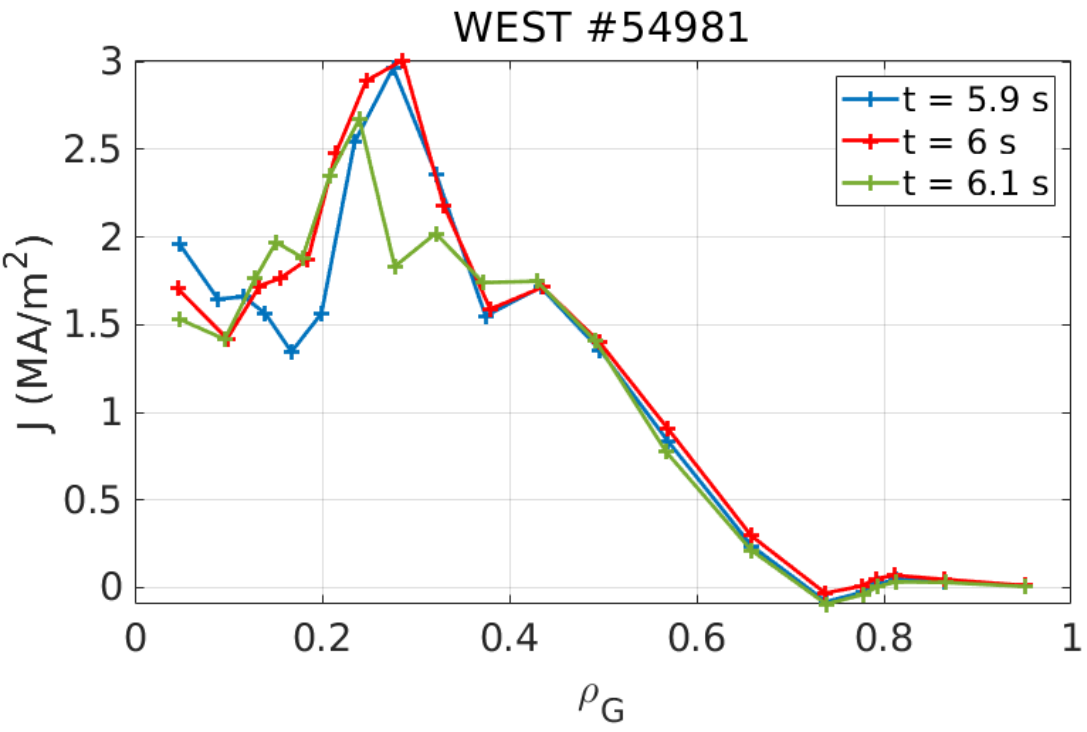

Figure 5.23: Predicted plasma current profile for shot #54981 at times t = 5.9 s (in blue), t = 6.0 s (in red) and t = 6.1 s (in green).

Starting from $\rho_G \approx 0.5$, the current profile for all three times is almost identical. However, in the core $\rho_G \leq 0.3$, the difference of current deposition is more noticeable, in particular at t = 6.1 s, for which the temperature is slightly lower in the core, see Fig. 5.21. The predicted and experimental HXR pulse profiles for each time are depicted in Fig. 5.24.

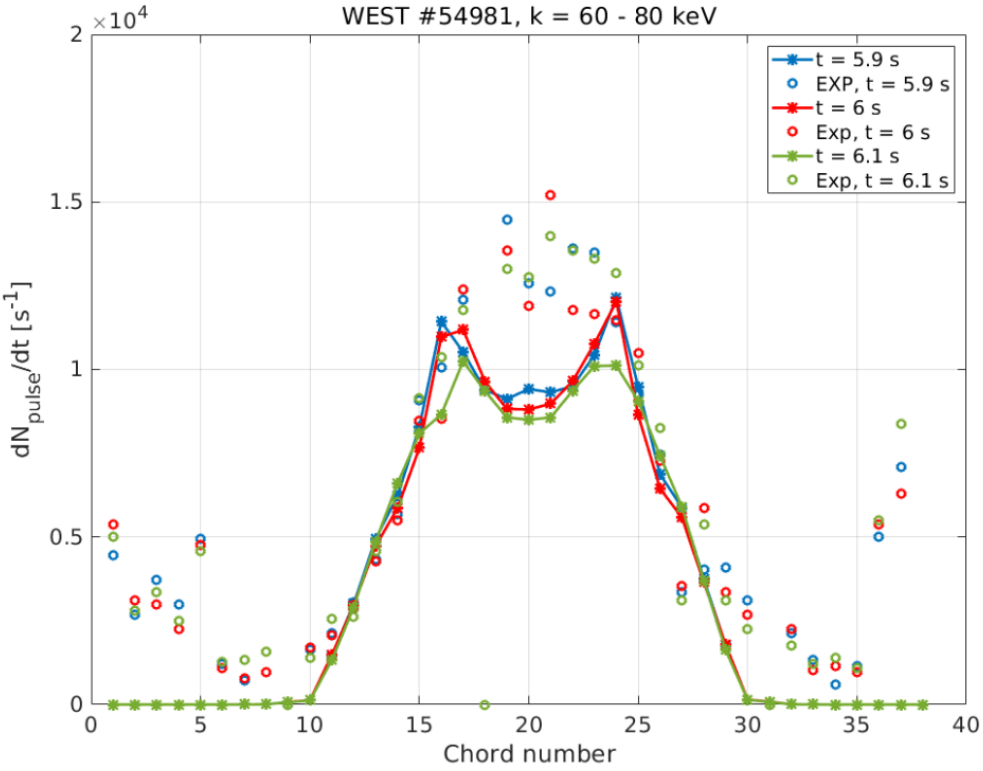

Figure 5.24: Experimental and predicted HXR pulse profiles for shot #54981 at times t = 5.9 s (in blue), t = 6.0 s (in red) and t = 6.1 s (in green).

Both experimental and calculated HXR profiles do not change significantly over this time window, consistently with the rest of the simulations. The predicted HXR intensity is slightly lower at t = 6.1 s, in correlation with the predicted current profiles in the plasma core. It can be noted that the fluctuations of the experimental HXR profile are of similar amplitude as the fluctuations of the HXR profile predicted by R5-X2, validating the impact of small perturbations of the plasma profiles on the resulting fast electron bremsstrahlung.

Chapter 6

Conclusions and Perspectives

Modern tokamaks like ITER will use metals with high atomic numbers, e.g. tungsten (W, Z=74), for their plasma-facing components. In this context, the Tore Supra tokamak was recently upgraded into WEST, with a full W environment. The presence of non-fully ionized high-Z impurities is raising new scientific issues for the dynamics of fast electrons, notably the partial screening effect, i.e. the fact that suprathermal electrons can partially probe the electron cloud of impurity ions resulting in a higher effective ion charge.
In the framework of this PhD thesis, being a part of a Harmonia (NCN) project, different analytical and numerical methods were used in order to estimate the atomic form factors of impurity ions, namely based on the Density Functional Theory (DFT), Thomas-Fermi (TF) and Pratt-Tseng (PT) approximations, allowing to calculate new cross-sections of electron-ion Coulomb collisions and fast electron bremsstrahlung. In particular, taking DFT as a reference, it was found that the most convenient way to obtain an analytical approximation of the form factor is to use the PT approximation. Indeed, the TF approach requires the use of the Kirillov approximation (TF-K), which implies a significant loss of accuracy [Jardin 2020a, Peysson 2021b]. Therefore, in this thesis, screening integrals were analytically derived based on the PT approximation, see Appendix B, to allow quick computation of the fast electron bremsstrahlung cross-sections in the upgraded R5-X2 code. Nevertheless, investigations on atomic physics are still in progress to refine the models, aiming at estimating quickly but accurately the atomic form factors, but also regarding the excitation energies for inelastic collisions or the enhanced impurity ionization by fast electrons [Walkowiak 2021]. The chain of codes C3PO/LUKE/R5-X2 has been upgraded to take into account the physics of heavy impurities with partial screening in the simulations [Peysson 2021b, Król 2020]. In this work, for the first time, LHCD simulations were made for the selected WEST discharge #54981 with these new features. In particular, it was shown that the partial screening effect reduces the plasma current

weakly while increasing the tungsten contribution to the non-thermal bremsstrahlung strongly by a factor of approximately two to three [Król 2021]. The inclusion of partial screening is, therefore, necessary to model the hard X-ray (HXR) emission accurately and to compare the experimental HXR measurements with the ones modelled by the R5-X2 code. Due to the experimental uncertainty associated with the measurements of the electron temperature T_e and tungsten concentration c_W, a sensitivity analysis was also performed by investigating the impact of these plasma parameters on the LH current drive and on the expected HXR measurements for the WEST shot #54981. It was observed that changing T_e modifies the region of wave absorption and thus the deposited current profile, shifting radially the peak of LH-driven current, as well as the expected HXR profile shape. In turn, increasing the W content progressively but weakly lowers the current profile while significantly increasing the HXR profile intensity, but without any significant change of the global shape of profiles. In practice, it was found that decreasing T_e by 10 - 20% while increasing c_W by 0 - 25% allows obtaining a much better matching of HXR measurements with R5-X2. This result was found to be in accordance with a parallel study that compared experimental and synthetic soft X-ray (SXR) measurements [Mazon 2021]. Finally, the stability of the results in time has been checked by repeating the LHCD simulations for the times t = 5.9 s, 6.0 s, 6.1 s, showing the robustness of the simulation chain against small time fluctuations of the plasma profiles.

As perspectives, the use of the ALOHA code instead of METIS is foreseen in future work to obtain a more accurate LH power spectrum at the plasma edge. ALOHA output will be used as an input for C3PO/LUKE/R5-X2 to refine the results obtained by the full simulation chain. Significant work is also ongoing to use the chain of codes in an automatized way [Peysson 2021a]. This will allow to perform numerous parallel simulations for different WEST shots and selected time slices. This statistical approach is an important step to draw robust experimental conclusions regarding the impact of high-Z impurities on the fast electron dynamics in tokamak plasmas.

The purpose of the investigations and results obtained in the framework of this thesis is to contribute to more accurate modelling of the methods of control of the plasma current profile and impurity mitigation strategies in tokamaks. These topics play an important role in the design and development of future magnetic fusion devices like ITER or DEMO.

Appendix A

Simplifications of the Fokker-Planck equation

A.1 Bounce averaging

The solution of the Fokker-Planck equation is the electron velocity distribution function of a priori 7 variables $f(x_1, x_2, x_3, v_1, v_2, v_3, t)$, where x_1, x_2, x_3 - are position variables, v_1, v_2, v_3 - are velocity variables and t - is time. However this seven dimensions problem can be reduced to a four dimensions problem with $f(\rho, v_1, v_2, v_3)$, where ρ - is the effective plasma radius, by so-called bounce averaging. It is possible if plasma particles are in the so-called banana regime, which is valid for most tokamak plasmas with usual parameters [Wallace 2010, p. 51]. Different transport regimes, including the banana regime are depicted in Fig. A.1. Let us introduce the system of toroidal coordinates (r, θ, ϕ) to

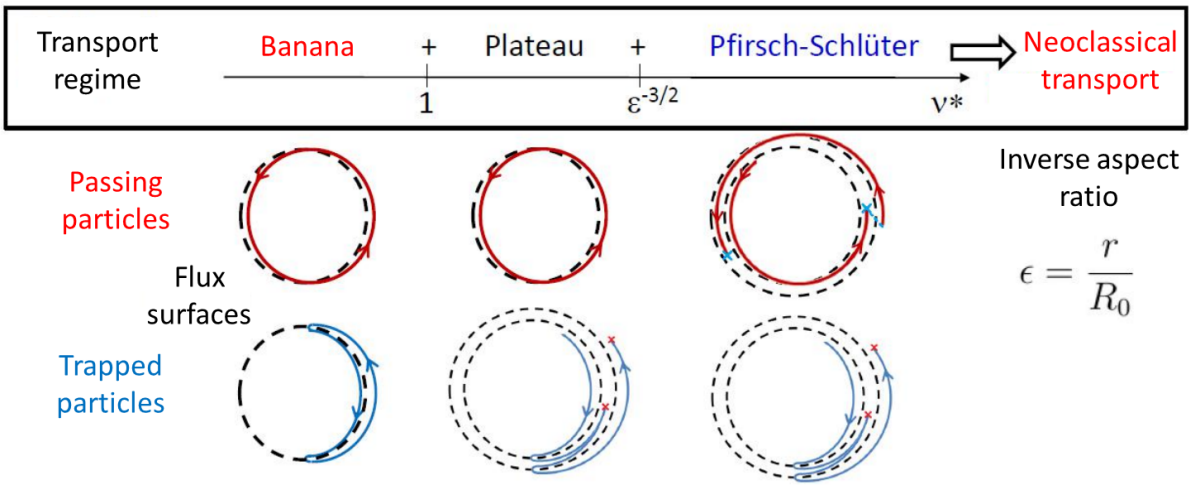

Figure A.1: Impact of increased collisionality on particles trajectories. Figure adapted from [Donnel 2018, p. 10].

describe one point in the position space, as shown in Fig. A.2, where R_0 - is called the major radius and denotes the distance from the torus vertical axis to the centre of the poloidal cross-section, R - is the distance from the vertical axis to a particular point, r, θ - are polar coordinates describing the position in the tokamak poloidal cross-section and ϕ - is the toroidal angle. In addition to the position space, we will also consider the

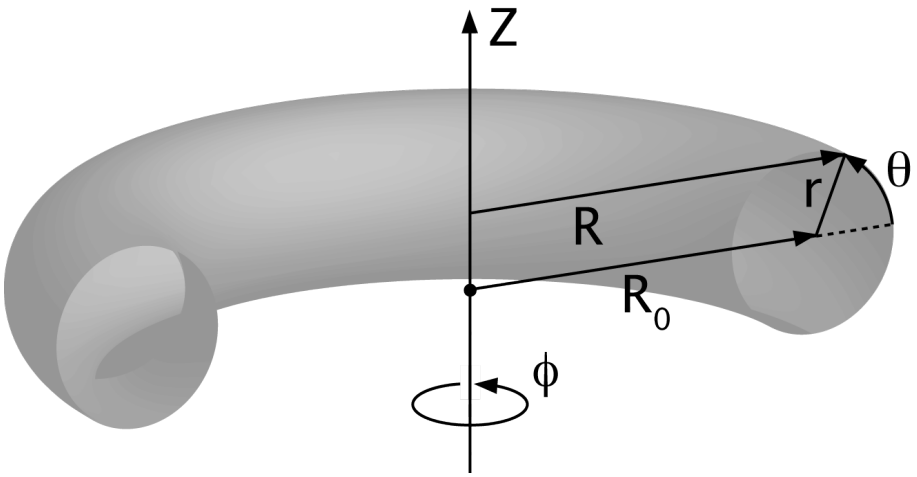

Figure A.2: Toroidal system of coordinates. Figure reproduced from [CIEMAT 2009].

momentum space which is depicted in Fig. A.3. In tokamaks, particles can be passing or

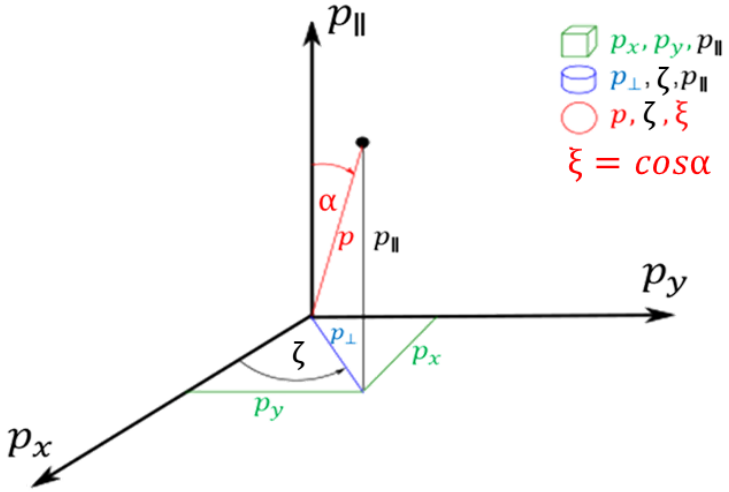

Figure A.3: Momentum space represented in different coordinate systems.

trapped due to the magnetic field gradient, depending on their parallel to perpendicular velocity ratio. Particles are trapped (i.e. with banana orbit, see Fig. A.1) if they satisfy the following condition:

$$\frac{v_{\parallel}^2}{v_{\perp}^2} < 1 - \frac{B}{B_{max}}, \tag{A.1}$$

where for a particular point of the particle trajectory, $v_{\parallel}$ - is the parallel to magnetic field velocity of particle, $v_{\perp}$ - is the perpendicular velocity, B - is the magnetic field, B_{max} - is the maximal magnetic field value on the high field side.
In the velocity space, it is possible to distinguish regions of trapped particles and passing particles as presented in Fig. A.4, where ξ is defined as:

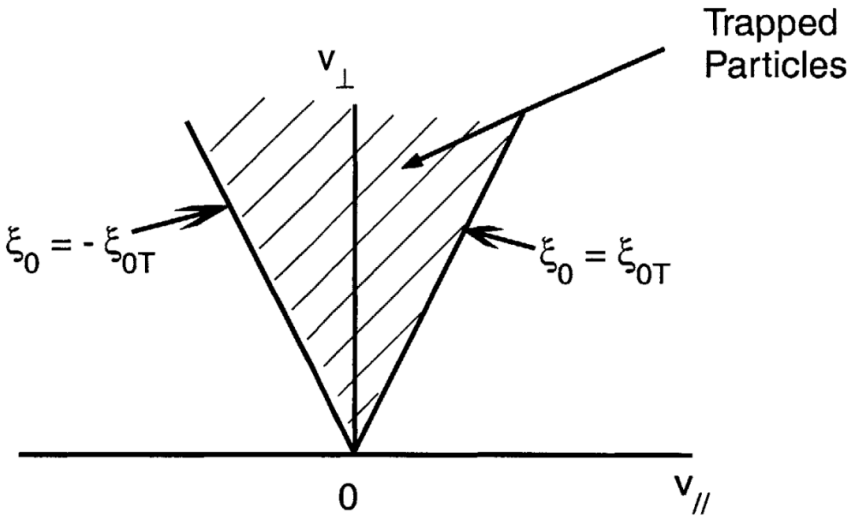

Figure A.4: Trapped electrons and passing electrons regions in the velocity space for electrons located in the position space on the midplane corresponding to the condition $\theta = 0$. Figure reproduced from [Decker 2002, p. 26]

$$\xi \equiv cos\alpha = \frac{p_{\parallel}}{p}, \tag{A.2}$$

with α pitch angle, i.e. the angle between the direction of motion of the considered particle and the direction of the magnetic field, which in the velocity space corresponds to the angle between $v = \sqrt{v_{\parallel}^2 + v_{\perp}^2}$ and $v_{\parallel}$. By p and $p_{\parallel}$, we mean respectively the electron momentum and its component parallel to the magnetic field.
Very often in Fokker-Planck calculations, and especially in the LUKE code, a so-called zero banana width is assumed [Decker 2005b, p. 19]. This means that a trapped electron after reflection returns along the same trajectory to the low-field side. This is an important assumption allowing to treat each flux surface independently and thus decreasing the calculations complexity [Meneghini 2012, p. 201].
The above assumption allows defining the time τ_b spent by a particle in banana motion between two reflections from one magnetic mirror to another and is called **bounce time**. In turns for passing particle, the time τ_t of one complete poloidal circulation is called **transit time** [Decker 2002, pp. 25-27]. The transit time can be defined in the following

way [Schultz 1999, p. 41]:

$$\tau_t \equiv \int_{-\pi}^{\pi} d\theta \frac{r}{|v_\parallel|} \frac{B}{B_\theta}, \tag{A.3}$$

where B - is uniform magnetic field, B_θ - is the poloidal component of uniform magnetic field, $v_\parallel$ - is the electron parallel velocity and θ - is the poloidal angle. The bounce time is defined as:

$$\tau_b \equiv \int_{-\theta_T}^{\theta_T} d\theta \frac{r}{|v_\parallel|} \frac{B}{B_\theta}, \tag{A.4}$$

where θ_T and $-\theta_T$ are poloidal angles in the position space, determining where the magnetic mirrors ("ends of banana" in Fig. A.1) are located.

If there were no collisions and the electromagnetic field would not change, the presented in Fig. A.1 trajectories of particles could not change in time [Donnel 2018, p. 35]. With increased collisionality, the presented in Fig. A.1 trajectories are more frequently interrupted.

Tokamaks today operate in a low-collisionality regime, the so-called banana regime of transport, which in particular means that the average time between two collisions of an electron with other particles is very long in comparison to the bounce time $\tau_b \ll \tau_c$ [Meneghini 2012, p. 201]. This can be expressed by introducing the δ parameter in the following way:

$$\delta = \frac{\tau_b}{\tau_c} << 1. \tag{A.5}$$

This assumption, like the previous zero banana width approximation, has important consequences for the theoretical description of the Fokker-Planck equation implemented in the LUKE code [Schultz 1999, pp. 45-47]. The approximation in Eq. (A.5) is called small drift approximation, because it means that in the time τ_c between two collisions, a trapped particle has plenty of time to perform the bounce motion without any collision.

The above presented two assumptions allow obtaining an important simplification of the Fokker-Planck equation - averaging over particles trajectory, called bounce averaging. The poloidal motion of particles is described by two variables - the effective plasma radius ρ and the poloidal angle θ. The idea of effective plasma radius can be understood better by taking look at the examples of so-called magnetic equilibrium presented in Fig. A.6 and Fig. A.7. By equilibrium, in tokamaks we mean not only the balance between magnetic and plasma pressures, but also the curves obtained by plotting in the poloidal cross-section the contours of constant poloidal magnetic flux. Some example of a single surface of constant poloidal magnetic flux in 3D is presented in Fig. A.5, where magnetic field lines are represented in red.

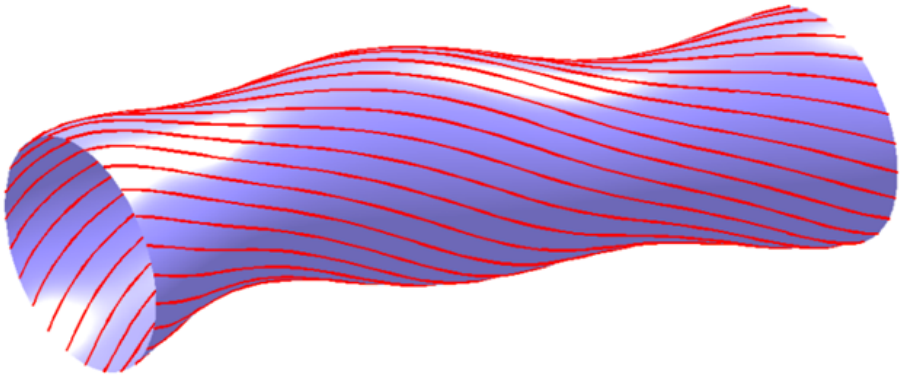

Figure A.5: Part of single constant poloidal magnetic flux surface in a tokamak. Figure reproduced from [CIEMAT 2011]

An example of poloidal cross-section of magnetic flux surfaces for the Tore Supra tokamak is presented in Fig. A.6. In Tore Supra (predecessor of WEST) poloidal magnetic flux surfaces had an almost cylindrical shape. For comparison, an example of magnetic

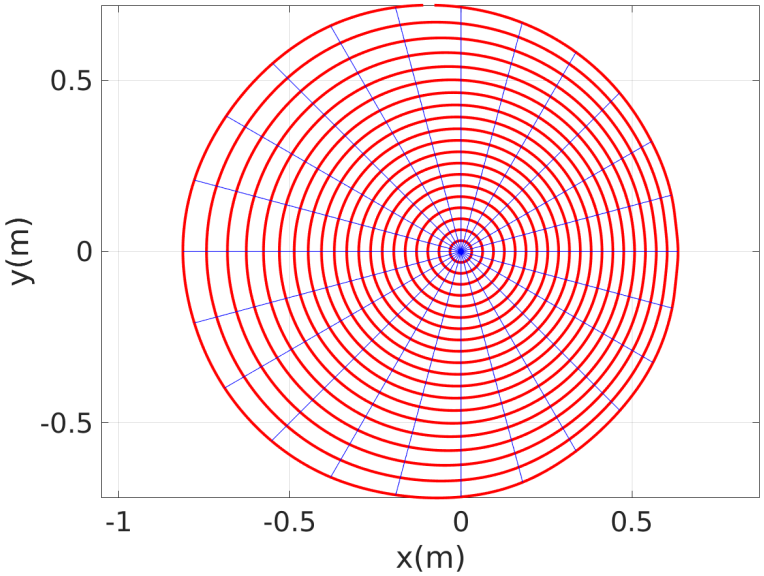

Figure A.6: Magnetic equilibrium in a Tore Supra poloidal cross-section obtained by METIS for the discharge #45525, time t = 27 s.

equilibrium with a D-shape for WEST is depicted in Fig. A.7. In the case of WEST, the cylindrical approximation can not be used anymore. In tokamaks, we consider most often the effective plasma radius ρ instead of the distance r to describe flux surfaces. The effective plasma radius is a quantity which should equal zero in the centre of the magnetic equilibrium and should equal 1 on the last closed flux surface.

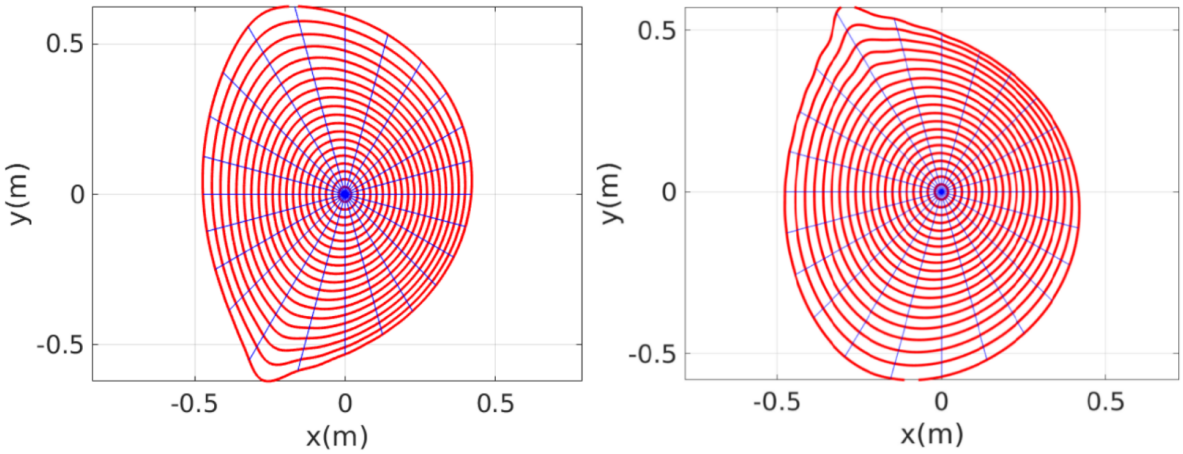

Figure A.7: Two possible configurations of magnetic equilibrium in WEST obtained by the METIS code for discharges #55193, t = 4.5 s (left figure) and #54981, t = 6 s (right figure).

For tokamaks, effective plasma radius can be defined in particular in the following four ways:

1. Geometric effective plasma radius:

$$\rho(\psi_p) = \frac{r(\psi_p, y = 0)}{a_p}, \tag{A.6}$$

where $r(\psi_p, \theta = 0)$ - is the polar radius as defined in Fig. A.2, ψ_p - is the poloidal magnetic flux, a_p - is called plasma radius and is the maximal value of $r(\psi_p, \theta = 0)$.

2. Poloidal effective plasma radius:

$$\rho_p(\psi_p) = \sqrt{\frac{\psi_p}{\psi_{pmax}}}, \tag{A.7}$$

where ψ_{pmax} - poloidal flux on the last closed poloidal flux surface.

3. Toroidal effective plasma radius:

$$\rho_t(\psi_t) = \sqrt{\frac{\psi_t}{\psi_{tmax}}}, \tag{A.8}$$

where ψ_t - is the toroidal magnetic flux and ψ_{tmax} - is the toroidal flux on the last closed toroidal flux surface.

4. Volume effective plasma radius:

$$\rho_V(\psi_p) = \sqrt{\frac{V}{V_{max}}}, \tag{A.9}$$

where V - is the volume of the considered flux tube, V_{max} - is the volume of the last flux tube.

In this work, only the geometrical effective plasma radius was used. LUKE is solving the Fokker-Planck equation by default for 20 points in which magnetic flux contours crosses the positive part of x axis ($\theta = 0$). Then for these 20 points the power absorption and current can be determined.

A.2 One-dimensional approximation

In the theory of the Fokker-Planck equation, it is very important to consider the so-called one-dimensional approximation. This model does not mean considering electrons moving only in one dimension [Vedenov 1967]. The approximation allows calculating the electron velocity distribution function f, using 1D model that provides a solution for a special case of LH waves.
The model assumes that the distribution function is Maxwellian in the direction perpendicular to the magnetic field. This assumption allows writing f as a product of two parts: one part f_m dependent on the perpendicular velocity $v_\perp$ and the second part F dependent on the parallel velocity $v_{||}$:

$$f = f_m(v_\perp)F(\omega), \tag{A.10}$$

where $\omega = \frac{v_{||}}{v_{Te}}$ with v_{Te} the thermal velocity. Then, it is possible to integrate the above equation over perpendicular velocity and obtain [Karney 1979, p. 1819]:

$$\frac{\partial F(\omega)}{\partial \tau} = \frac{\partial}{\partial \omega} D(\omega) \frac{\partial}{\partial \omega} F(\omega) + \frac{2 + Z_i}{2} \frac{\partial}{\partial \omega} [\frac{1}{\omega^3} \frac{\partial}{\partial \omega} + \frac{1}{\omega^2}] F(\omega), \tag{A.11}$$

where D - is the quasilinear diffusion coefficient and Z_i - is ionization level of ions. Normalized time τ is defined as $\tau = \nu_0 t$, where

$$\nu_0 = \frac{\omega_{pe}^4 \ln \Lambda}{2\pi n_0 v_{Te}^3}. \tag{A.12}$$

Eq. (A.11), in the case of lack of electric field and constant wave excitation, has the

steady-state solution:

$$F(\omega) = C \exp[\int_0^{\omega} \frac{-\omega d\omega}{1 + 2\omega^3 D(\omega)/(2 + Z_i)}], \tag{A.13}$$

where C - is a constant. It can be noted that Eq. (A.11) conserves electron density and the electron distribution function has only non-negative values.
One of the most important results obtained using the 1D model is the prediction that high-velocity waves give high current drive efficiency. The model also allows for calculating the current and dissipated power using the obtained formula for F [Fisch 1978]. For $Z = 1$, the calculated current efficiency is 2.5 times smaller than the more precise numerical results [Karney 1979]. Wegrove and Engelmann found a justification of this model in 1984. In 1985, Fuchs et al. obtained a better agreement with numerical results [Fuchs 1985]. It is important to notice that the precise calculation of the current density and dissipated power is not the main goal. The most important is to obtain an accurate estimate of the generated current to applied power ratio, i.e. the current efficiency.
The 1D model gives a precise enough value of the dissipated power, however it is better to calculate the current density using the so-called Fisch-Boozer efficiency formula obtained through another method - Langevin equations. Nevertheless, it is possible to use a 2D model if a higher precision is necessary. There are situations in which the 1D model cannot be used. For example, this model cannot describe the case of EC waves because in their case, waves drive current through the transfer of perpendicular momentum and not parallel like it is assumed in the 1D model. 1D model is not able also to describe the special case of runaway electrons, so-called backward runaway electrons.

A.3 Linearized Fokker-Planck equation

One of the approximations that can be made is a linearization of the collision operator. Firstly, the electron velocity distribution function f can be written in the following way:

$$f = f_m + \widetilde{f}, \tag{A.14}$$

where f_m is the Maxwellian distribution and $\widetilde{f}$ the perturbation from the Maxwellian distribution. Then, the collision operator can be written in the following way:

$$C(f, f) \approx C(f_m, \widetilde{f}) + C(\widetilde{f}, f_m). \tag{A.15}$$

In Eq. (A.15), the collision term of the Maxwellian distribution with itself is zero. Using Eq. (A.14) and Eq. (A.15) for the collision operator, the Fokker-Planck Eq. (3.11) can be written in the following form:

$$\frac{d}{dt}(f_m + \widetilde{f}) = C(f_m, \widetilde{f}) + C(\widetilde{f}, f_m) + C(f, f_i) - \frac{\partial}{\partial v} S_w. \tag{A.16}$$

In order to write the Fokker-Planck equation more compactly, it is possible to use a notation in which $C(\widetilde{f})$ is defined in the following way [Fisch 1987, pp. 184-185]:

$$C(\widetilde{f}) \equiv C(\widetilde{f}, f_m) + C(f_m, \widetilde{f}) + C(\widetilde{f}, f_i). \tag{A.17}$$

The above notation allows writing the Fokker-Planck equation in the following form, after rearranging terms:

$$\frac{d}{dt}\widetilde{f} - C(\widetilde{f}) = -\frac{\partial}{\partial v} S_w - \frac{d}{dt} f_m. \tag{A.18}$$

Next, it is possible to use Eq. (3.18) for the total derivative over time operator, and write

$$(\frac{\partial}{\partial t} + \frac{qE}{m}\frac{\partial}{\partial v})\widetilde{f} - C(\widetilde{f}) = -\frac{\partial}{\partial v} S_w - (\frac{\partial}{\partial t} + \frac{qE}{m}\frac{\partial}{\partial v}) f_m \tag{A.19}$$

and

$$\frac{\partial}{\partial t}\widetilde{f} + \frac{qE}{m}\frac{\partial}{\partial v}\widetilde{f} - C(\widetilde{f}) = -\frac{\partial}{\partial v} S_w - \frac{qE}{m}\frac{\partial}{\partial v} f_m - \frac{\partial}{\partial t} f_m. \tag{A.20}$$

The last term $\frac{\partial}{\partial t} f_m$ is the partial time derivative of Maxwellian distribution which is defined as:

$$f_m \equiv n(\frac{2\pi T}{m})^{-3/2} \exp(-\frac{\varepsilon}{T}), \tag{A.21}$$

where $\varepsilon \equiv \frac{mv^2}{2}$ - is kinetic energy of particle. The assumption of homogeneous plasma provides that spatial derivatives are equal zero ($\frac{\partial}{\partial r} \to 0$), and the partial derivative of f_m with respect to time is equal

$$\frac{\partial f_m}{\partial t} = \frac{\partial n}{\partial t}\frac{\partial f_m}{\partial n} + \frac{\partial T}{\partial t}\frac{\partial f_m}{\partial T} = [\frac{\frac{dn}{dt}}{n} + [\frac{\varepsilon}{T} - \frac{3}{2}]\frac{\frac{dT}{dt}}{T}] f_m. \tag{A.22}$$

Eventually, using the above formula, the linearized Fokker-Planck equation takes the form obtained by Fisch:

$$\frac{\partial}{\partial t}\widetilde{f} + \frac{qE}{m}\frac{\partial}{\partial v}\widetilde{f} - C(\widetilde{f}) = -\frac{\partial}{\partial v} S_w - \frac{qE}{m}\frac{\partial}{\partial v} f_m - [\frac{\frac{dn}{dt}}{n} + [\frac{\varepsilon}{T} - \frac{3}{2}]\frac{\frac{dT}{dt}}{T}] f_m. \tag{A.23}$$

Multiplying the Fokker-Planck equation by the kinetic energy ε and integrating over all velocity space, gives the evolution of temperature:

$$\frac{3}{2}n\frac{\partial T}{\partial t} = \int S_w \partial\varepsilon/\partial v d^3v + EJ. \tag{A.24}$$

The first term on the right hand side of Eq. (A.24) corresponds to heating by the injected waves, and the second term is the Joule heating due to the electric field. The properties of the electron-electron collision operator include conservation of number density, momentum and energy. However, the linearized Fokker-Planck equation allows negative values in the distribution function, in contrast with the original Fokker-Planck equation, in the case of Joule or wave heating.

A.4 High-velocity limit

It is possible to divide the electron distribution function into two parts, a thermal part - slow or thermal electrons and a superthermal part - fast electrons satisfying $v \gg v_T$. The second part is called 'tail', corresponding to a relatively small number of particles with tremendous velocities, up to the limiting speed of light. Collision frequencies ν of the slow and fast electrons are significantly different. In the case of slow electrons, it is $\nu \sim v_T^{-3}$. In the case of fast electrons $\nu \approx constant$.
The following assumption is related to electron velocities, as current drive with fast electrons is considered. Because of that, it is possible to consider only velocities far above the thermal velocity. This assumption is called high-velocity limit and allows simplifying the collision operator to the following form [Fisch 1987, p. 185]:

$$C(f,f) \simeq \Gamma[\frac{1}{v^2}\frac{\partial}{\partial v}(\frac{v_T^2}{v}\frac{\partial}{\partial v} + f) + \frac{1 - v_T^2/2v^2}{2v^3}\frac{\partial}{\partial \mu}(1-\mu^2)\frac{\partial}{\partial \mu}f], \tag{A.25}$$

where

$$\mu \equiv \frac{v_\parallel}{v}, \tag{A.26}$$

$$\Gamma \equiv \frac{nq^4 \ln\Lambda}{4\pi\varepsilon_0^2 m^2}. \tag{A.27}$$

The first term in Eq. A.25 is related to diffusion and deceleration by friction and the second term is related to pitch-angle scattering. It is essential to notice that high-velocity limit does not mean only collisions with fast electrons.
Electron-ion collisions for both, slow and fast electrons, are always in the high-velocity limit because the difference between the mass of any ion and electron is considerable.

Because of that, it is possible to write the collision operator for electron-ion collisions in the following form:

$$C(f, f_i) = \frac{\Gamma Z_i}{2v^3} \frac{\partial}{\partial \mu} (1 - \mu^2) \frac{\partial}{\partial \mu} f. \tag{A.28}$$

The possibility of using the high-velocity limit for solving the Fokker-Planck equation in LUKE is assessed in [Decker 2005b]. The assumption about high-velocity limit does not cause loss of the property of density conservation and keep only non-negative values in the distribution function. It is not possible to use the high-velocity limit Fokker-Planck equation in the case of Spitzer conductivity [Cohen 1950, Spitzer 1953] and current drive with low-phase-velocity waves [Karney 1981].

Appendix B

Screening integrals (Pratt-Tseng atomic model)

B.1 Introduction

In the following Appendix, the solutions of the eight integrals: $\hat{J}^{TP}_{1,2}$, $\hat{J}^{TP}_{1,3}$, $\hat{J}^{TP}_{2,2}$, $\hat{J}^{TP}_{2,3}$, $\hat{J}^{TP}_{3,1}$, $\hat{J}^{TP}_{3,2}$, $\hat{J}^{TP}_{4,2}$,$\hat{J}^{TP}_{4,3}$ are detailed. These integrals take the following general form:

$$\hat{J}^{TP}_{k,l} = \int_0^{2\pi} \frac{(cos\phi)^p \, d\phi}{(acos\phi + b)^n \, (1 + (acos\phi + b)c^{TP})^m}, \tag{B.1}$$

where p, n, m, k, l may have the following values $p = 0, 1$; $n = 1, 2$; $m = 1, 2$; $k = 1, 2, 3, 4$; $l = 2, 3$. In this whole Appendix a and b satisfy the following conditions:

$$\begin{cases} a < 0, \\ b > 0, \\ |b| > |a|. \end{cases} \tag{B.2}$$

The procedure of solving these integrals depends on the value of p. The two cases p = 0 and p = 1 will be considered separately.

B.1.1 Case p = 0

After introducing δ:

$$\delta = \frac{b}{a} < -1, \tag{B.3}$$

the integral takes the following form:

$$\hat{J^{TP}}_{k,l} = \int_0^{2\pi} \frac{d\phi}{(cos\phi + \delta)^n \left(1 + (acos\phi + \delta)\, ac^{TP}\right)^m} \frac{1}{a^n}.$$

In order to solve the integral one can use the tangent half-angle substitution:

$$x = \tan\frac{\phi}{2}, \tag{B.4}$$

$$dx = \frac{1}{2}\left(1 + x^2\right) d\phi, \tag{B.5}$$

$$\cos\phi = \frac{1 - \tan^2\frac{\phi}{2}}{1 + \tan^2\frac{\phi}{2}}. \tag{B.6}$$

After changing variables, the integral takes the form:

$$\begin{aligned} \hat{J}^{TP}_{k,l} &= \int_{-\infty}^{\infty} \frac{\frac{2}{1+x^2}dx}{\left(\frac{1-x^2}{1+x^2} + \delta\right)^n \left(1 + \left(\frac{1-x^2}{1+x^2} + \delta\right) ac^{TP}\right)^m} \frac{1}{a^n} \\ &= \int_{-\infty}^{\infty} \frac{\left(1 + x^2\right)^{m+n-1}}{\left(\delta + 1 + x^2\left(\delta - 1\right)\right)^n \left(1 + x^2 + \left(\delta + 1 + x^2\left(\delta - 1\right)\right) ac^{TP}\right)^m} \frac{2}{a^n}. \end{aligned} \tag{B.7}$$

After the factors have been ordered in relation to the powers of x, the integral takes form:

$$\hat{J^{TP}_{k,l}} = \int_{-\infty}^{\infty} \frac{\left(1 + x^2\right)^{m+n-1}}{\left(\delta + 1 + x^2\left(\delta - 1\right)\right)^n \left(\left(1 + ac^{TP}\left(\delta - 1\right)\right) x^2 + \left(1 + ac^{TP}\left(\delta + 1\right)\right)\right)^m} \frac{2}{a^n}. \tag{B.8}$$

To simplify one can introduce new constants:

$$A_0 = \delta - 1, \tag{B.9}$$

$$B_0 = \delta + 1, \tag{B.10}$$

$$C_0 = 1 + ac^{TP}\left(\delta - 1\right), \tag{B.11}$$

$$D_0 = 1 + ac^{TP}\left(\delta + 1\right). \tag{B.12}$$

Then the integral takes the form:

$$J^{\hat{TP}}{}_{k,l} = \frac{2}{a^n}\int_{-\infty}^{\infty}\frac{(1+x^2)^{m+n-1}\,dx}{(A_0x^2+B_0)^n\,(C_0x^2+D_0)^m}. \tag{B.13}$$

It is possible once again to simplify and reduce the number of constants by introducing A and B constants:

$$A = \frac{B_0}{A_0} = \frac{\delta+1}{\delta-1} > 0, \tag{B.14}$$

$$B = \frac{D_0}{C_0} = \frac{1+ac^{TP}\,(\delta+1)}{1+ac^{TP}\,(\delta-1)} > 0. \tag{B.15}$$

Since the integrated function is symmetrical, the integral can be written with the following limits:

$$J^{\hat{TP}}_{k,l} = \frac{4}{a^n}\frac{1}{A_0^nC_0^m}\int_0^{\infty}\frac{(1+x^2)^{m+n-1}}{(x^2+A)^n\,(x^2+B)^m}dx. \tag{B.16}$$

One can solve the above integral by using the partial fraction decomposition method:

$$\begin{aligned}\frac{(1+x^2)^{m+n-1}}{(x^2+A)^n\,(x^2+B)^m} &= \sum_{j=1}^{n}\frac{T_j}{(x^2+A)^j}+\sum_{j=1}^{m}\frac{T_{j+n}}{(x^2+B)^j}\\ &= \frac{\sum_{j=1}^{n}T_j\,(x^2+A)^{n-j}\,(x^2+B)^m}{(x^2+A)^n\,(x^2+B)^m}\\ &+ \frac{\sum_{j=1}^{m}T_{j+n}\,(x^2+A)^n\,(x^2+B)^{m-j}}{(x^2+A)^n\,(x^2+B)^m},\end{aligned} \tag{B.17}$$

where $T_j \in [1; m+n]$ are coefficients to calculate. We can write:

$$\begin{aligned}\sum_{j=0}^{m+n-1}\begin{pmatrix} m+n-1 \\ j \end{pmatrix}x^{2j} \equiv &\sum_{j=1}^{n}T_j\left(x^2+A\right)^{n-j}\left(x^2+B\right)^m\\ &+\sum_{j=1}^{m}T_{j+n}\left(x^2+A\right)^n\left(x^2+B\right)^{m-j}.\end{aligned} \tag{B.18}$$

Now, based on the above equation it is possible to write a system of m+n equations with m+n unknowns. Solving this system allows obtaining $T_j \in [1; m+n]$ and write:

$$J^{\hat{TP}}{}_{k,l} = \frac{4}{a^n}\frac{1}{A_0^nC_0^m}\left(\sum_{j=1}^{n}T_j\int_0^{\infty}\frac{1}{(x^2+A)^j}dx+\sum_{j=1}^{m}T_{j+n}\int_0^{\infty}\frac{1}{(x^2+B)^j}dx\right), \tag{B.19}$$

where the above integrals have the following solutions:

$$\int_0^\infty \frac{1}{x^2+A}dx = \frac{\pi}{2\sqrt{A}}, \tag{B.20}$$

calculated using the substitution

$$u = \frac{x}{\sqrt{A}}, \tag{B.21}$$

and function $\arctan x$ as the primitive function,

$$\int_0^\infty \frac{1}{(x^2+A)^2}dx = \frac{\pi}{4A^{3/2}}. \tag{B.22}$$

The above integral can be calculated using the reduction formula:

$$\begin{aligned}\int \frac{dx}{(x^2+B)^2} &= \frac{x}{2B(x^2+B)} + \frac{1}{2B}\int \frac{dx}{x^2+B} \\ &= \frac{x}{2B(x^2+B)} + \frac{1}{2\sqrt{B^3}}\arctan\frac{x}{\sqrt{B}},\end{aligned} \tag{B.23}$$

taking the limits of integration from 0 to ∞.

B.1.2 Case p = 1

In this case, the integral can be split into the two following integrals:

$$\begin{aligned}J^{\hat{TP}}{}_{k,l} &= \frac{1}{a}\int_0^{2\pi} \frac{(acos\phi+b)-b}{(acos\phi+b)^n\left(1+(acos\phi+b)\,c^{TP}\right)^m}d\phi \\ &= \frac{1}{a}\int_0^{2\pi} \frac{d\phi}{(acos\phi+b)^{n-1}\left(1+(acos\phi+b)\,c^{TP}\right)^m} \\ &- \frac{b}{a}\int_0^{2\pi} \frac{d\phi}{(acos\phi+b)^n\left(1+(acos\phi+b)\,c^{TP}\right)^m}.\end{aligned} \tag{B.24}$$

These integrals can then be calculated according to the case $p = 0$. Only the case $n-1=0$ requires additional calculations.

B.2 1. Integral $\hat{J}^{TP}_{1,2}$

Integral $\hat{J}^{TP}_{1,2}$ has the following form:

$$\hat{J}^{TP}_{1,2} = \int_0^{2\pi} \frac{d\phi}{(a\cos\phi+b)^2\left(1+(a\cos\phi+b)\,c^{TP}\right)}. \tag{B.25}$$

In this case $p = 0$, $n = 2$ and $m = 1$. Using the procedure derived in the introduction one can obtain:

$$J_{1,2}^{\hat{TP}} = \frac{4}{a^2}\frac{1}{A_0^2 C_0}\int_0^\infty \frac{\left(x^2+1\right)^2}{\left(x^2+A\right)^2\left(x^2+B\right)}dx. \tag{B.26}$$

The partial fraction decomposition method for this integral is as follows:

$$\begin{aligned}
\frac{\left(x^2+1\right)^2}{\left(x^2+A\right)^2\left(x^2+B\right)} &= \frac{T_1}{x^2+A} + \frac{T_2}{\left(x^2+A\right)^2} + \frac{T_3}{x^2+B} \\
&= \frac{T_1\left(AB+(A+B)\,x^2+x^4\right)}{\left(x^2+A\right)^2\left(x^2+B\right)} \\
&+ \frac{T_2\left(B+x^2\right)+T_3\left(A^2+2Ax^2+x^4\right)}{\left(x^2+A\right)^2\left(x^2+B\right)} \\
&= \frac{\left(T_1AB+T_2B+T_3A^2\right)}{\left(x^2+A\right)^2\left(x^2+B\right)} \\
&+ \frac{\left(T_1\left(A+B\right)+T_2+2T_3A\right)x^2}{\left(x^2+A\right)^2\left(x^2+B\right)} \\
&+ \frac{\left(T_1+T_3\right)x^4}{\left(x^2+A\right)^2\left(x^2+B\right)}.
\end{aligned} \tag{B.27}$$

The coefficients before x^4, x^2, x^0 must make the polynomials from numerators of both fractions equal. It allows to write a set of three equations as follows:

$$\begin{cases}
(1') & T_1AB + T_2B + T_3A^2 = 1, \\
(2') & T_1\left(A+B\right) + T_2 + 2T_3A = 2, \\
(3') & T_1 + T_3 = 1,
\end{cases} \tag{B.28}$$

where T_1, T_2, T_3 are the coefficients to be calculated. From the third equation:

$$(3) \Rightarrow T_3 = 1 - T_1. \tag{B.29}$$

Applying Eq. (B.29) in the first equation:

$$(1) \Rightarrow T_2 = \frac{1}{B}\left(1 - T_1AB + \left(T_1 - 1\right)A^2\right), \tag{B.30}$$

$$T_2 = \frac{1}{B}\left(\left(1-A^2\right) + T_1\left(A^2 - AB\right)\right). \tag{B.31}$$

Then from the second equation, it is possible to derive T_1:

$$(2) \Rightarrow BT_1(A+B) + (1-A^2) + T_1(A^2 - AB) + 2\,(1-T_1)\,AB = 2B, \tag{B.32}$$

$$T_1\left(BA + B^2 + A^2 - AB - 2AB\right) = 2B + A^2 - 1 - 2AB, \tag{B.33}$$

$$T_1 = \frac{A^2 - 1 + 2B\,(1-A)}{B^2 - 2AB + A^2} = \frac{A^2 - 1 + 2B(1-A)}{(B-A)^2}. \tag{B.34}$$

So we can write that:

$$\begin{aligned} T_3 &= 1 - T_1 \\ &= \frac{B^2 - 2AB + A^2}{(B-A)^2} - \frac{A^2 - 1 + 2B - 2AB}{(B-A)^2} \\ &= \frac{B^2 + 1 - 2B}{(B-A)^2}, \end{aligned} \tag{B.35}$$

$$T_3 = \frac{B^2 - 2B + 1}{(B-A)^2} = \frac{(B-1)^2}{(B-A)^2}. \tag{B.36}$$

Then it is possible to derive T_2 coefficient:

$$\begin{aligned} T_2 &= \frac{1}{B}\left(\left(1-A^2\right) + \frac{A^2 - 1 + 2B\,(1-A)}{(B-A)^2}\left(A^2 - AB\right)\right) \\ &= \frac{1}{B}\frac{(1-A^2)\,(B-A)^2 + (A^2 - 1 + 2B - 2AB)\,A\,(A-B)}{(B-A)^2} \\ &= \frac{B - A - BA^2 + A^3 - A^3 + A - 2AB + 2A^2B}{B\,(B-A)} \\ &= \frac{B - 2AB + A^2B}{B\,(B-A)}, \end{aligned} \tag{B.37}$$

$$T_2 = \frac{1 - 2A + A^2}{B - A} = \frac{(1-A)^2}{B-A}. \tag{B.38}$$

After having applied the partial fraction decomposition method, one can finally obtain:

$$\begin{aligned}\hat{J}_{1,2}^{TP} &= \frac{4}{a^2}\frac{1}{A_0^2 C_0}\left(T_1\int_0^\infty \frac{dx}{x^2+A} + \right.\\ &+ \left. T_2\int_0^\infty \frac{dx}{(x^2+A)^2} + T_3\int_0^\infty \frac{dx}{x^2+B}\right)\\ &= \frac{4}{a^2}\frac{1}{A_0^2 C_0}\left(T_1\frac{\pi}{2\sqrt{A}} + T_2 I_2 + T_3\frac{\pi}{2\sqrt{B}}\right). \end{aligned} \tag{B.39}$$

B.3 2. Integral $\hat{J}_{1,3}^{TP}$

$\hat{J}_{1,3}^{TP}$ is expressed as follows:

$$\hat{J}_{1,3}^{TP} = \int_0^{2\pi} \frac{d\phi}{(a\cos\phi + b)^2 \left(1 + (a\cos\phi + b)\, c^{TP}\right)^2}. \tag{B.40}$$

In this case $p = 0$, $n = 2$, $m = 2$. Applying the procedure from Introduction, one can obtain that:

$$\hat{J}_{1,3}^{TP} = \frac{4}{a^2}\frac{1}{A_0^2 C_0^2}\int_0^\infty \frac{(1+x^2)^3}{(x^2+A)^2 (x^2+B)^2} dx. \tag{B.41}$$

Using the partial fraction decomposition method we have:

$$\begin{aligned}\frac{(1+x^2)^3}{(x^2+A)^2(x^2+B)^2} &= \frac{T_1}{x^2+A} + \frac{T_2}{(x^2+A)^2} + \frac{T_3}{x^2+B} + \frac{T_4}{(x^2+B)^2}\\ &= \frac{T_1(x^2+A)(x^2+B)^2 + T_2(x^2+B)^2}{(x^4+A)^2(x^2+B)^2}\\ &+ \frac{T_3(x^2+A)^2(x^2+B) + T_4(x^2+A)^2}{(x^4+A)^2(x^2+B)^2}\\ &= \frac{(T_1 AB^2 + T_2 B^2 + T_3 A^2 B + T_4 A^2)}{(x^2+A)^2(x^2+B)^2}\\ &+ \frac{x^2\left(T_1(B^2+2AB) + T_2 2B\right)}{(x^2+A)^2(x^2+B)^2}\\ &+ \frac{x^2\left(T_3(A^2+2AB) + T_4 2A\right)}{(x^2+A)^2(x^2+B)^2}\\ &+ \frac{x^4\left((2B+A)T_1 + T_2 + T_3(2A+B) + T_4\right)}{(x^2+A)^2(x^2+B)^2}\\ &+ \frac{x^6(T_1+T_3)}{(x^2+A)^2(x^2+B)^2}. \end{aligned} \tag{B.42}$$

This leads to the four following equations with unknown coefficients T_1, T_2, T_3, T_4:

$$\begin{cases} (1'') & T_1AB^2 + T_2B^2 + T_3A^2B + T_4A^2 = 1, \\ (2'') & T_1\left(B^2 + 2AB\right) + 2T_2B + T_3\left(A^2 + 2AB\right) + 2T_4A = 3, \\ (3'') & T_1\left(A + 2B\right) + T_2 + T_3\left(B + 2A\right) + T_4 = 3, \\ (4'') & T_1 + T_3 = 1. \end{cases} \tag{B.43}$$

Using the fourth equation one can obtain:

$$(4) \Rightarrow T_3 = 1 - T_1. \tag{B.44}$$

Then it is possible to rewrite equations $(1''), (2'')$ and $(3'')$ in a new form:

$$\begin{cases} (1') & T_1\left(AB^2 - A^2B\right) + T_2B^2 + T_4A^2 = 1 - A^2B, \\ (2') & T_1\left(B^2 + 2AB - A^2 - 2AB\right) + 2T_2B + 2T_4A = 3 - A^2 - 2AB, \\ (3') & T_1\left(A + 2B - B - 2A\right) + T_2 + T_4 = 3 - B - 2A. \end{cases} \tag{B.45}$$

From equation $(3')$ it is possible to derive the T_4 coefficient:

$$(3') \Rightarrow T_4 = 3 - B - 2A - T_2 - T_1(B - A). \tag{B.46}$$

Then after application formula for T_4 one can obtain:

$$\begin{aligned} (2') \quad \Rightarrow \quad & T_1\left(B^2 - A^2\right) + 2T_2B \\ + \quad & 2A\left(3 - B - 2A - T_2 - T_1\left(B - A\right)\right) = 3 - A^2 - 2AB. \end{aligned} \tag{B.47}$$

The above equation allows to derive T_2 coefficient:

$$\begin{aligned} T_1\left(B^2 - A^2 - 2AB + 2A^2\right) + T_2\left(2B - 2A\right) \\ = 3 - A^2 - 2AB - 6A + 2AB + 4A^2, \end{aligned} \tag{B.48}$$

$$T_1\left(B - A\right)^2 + 2T_2\left(B - A\right) = 3\left(1 - 2A + A^2\right), \tag{B.49}$$

$$T_2 = -\frac{1}{2}T_1\left(B - A\right) + \frac{3}{2}\frac{\left(A - 1\right)^2}{B - A}. \tag{B.50}$$

Now it is possible to rewrite equation $(1')$ by substituting T_2:

$$\begin{aligned}(1')\,T_1\left(AB^2-A^2B\right) &+ B^2\left(-\frac{1}{2}T_1\left(B-A\right)+\frac{3}{2}\frac{\left(A-1\right)^2}{B-A}\right)\\ &+ A^2\left(3-B-2A-T_2-T_1\left(B-A\right)\right)\\ &= 1-A^2B. \end{aligned} \tag{B.51}$$

The above equation allows to derive the T_1 coefficient:

$$\begin{aligned}T_1\Big(AB^2-A^2B &- \frac{1}{2}\left(B^2-A^2\right)\left(B-A\right)-A^2\left(B-A\right)\Big)\\ &= 1-A^2B-\frac{3}{2}\left(B^2-A^2\right)\frac{\left(A-1\right)^2}{B-A}\\ &- 3A^2+A^2B+2A^3, \end{aligned} \tag{B.52}$$

$$\begin{aligned}T_1\left(B-A\right)\left(AB-\frac{1}{2}\left(B^2-A^2\right)-A^2\right) &= 1-A^2B-\frac{3}{2}\left(B+A\right)\left(A-1\right)^2\\ &- 3A^2+A^2B+2A^3, \end{aligned} \tag{B.53}$$

$$\begin{aligned}T_1\left(B-A\right)\left(2AB-B^2+A^2-2A^2\right) &= 2-3BA^2+6AB-3B-3A^3\\ &+ 6A^2-3A-6A^2+4A^3, \end{aligned} \tag{B.54}$$

$$-T_1\left(B-A\right)\left(B-A\right)^2 = 2-3A^2B+6AB-3B-3A+A^3, \tag{B.55}$$

$$T_1 = \frac{3A^2B+3B+3A-6AB-A^3-2}{\left(B-A\right)^3}. \tag{B.56}$$

Now it is possible to obtain the full form of T_2 coefficient involving formula for T_1:

$$\begin{aligned} T_2 &= -\frac{1}{2}T_1\left(B-A\right)+\frac{3}{2}\frac{\left(A-1\right)^2}{B-A}= \\ &= \frac{2+A^3+6AB-3A-3B-3A^2B}{2\left(B-A\right)^2}+\frac{3}{2}\frac{\left(A^2-2A+1\right)\left(B-A\right)}{\left(B-A\right)^2} \\ &= \frac{2+A^3+6AB-3A-3B-3A^2B}{2\left(B-A\right)^2} \\ &+ \frac{3A^2B-6AB+3B-3A^3+6A^2-3A}{2\left(B-A\right)^2} \\ &= \frac{2-6A-2A^3+6A^2}{2\left(B-A\right)^2} \\ &= \frac{1-3A+3A^2-A^3}{\left(B-A\right)^2}, \end{aligned} \tag{B.57}$$

$$T_2=\frac{\left(1-A\right)^3}{\left(B-A\right)^2}. \tag{B.58}$$

T_1 coefficient allows also obtaining the full form of the T_3 coefficient:

$$T_3=1-T_1= \tag{B.59}$$

$$=\frac{B^3-3B^2A+3BA^2-A^3-3A^2B-3B-3A+6AB+A^3+2}{\left(B-A\right)^3}, \tag{B.60}$$

$$T_3=\frac{B^3-3AB^2-3B-3A+6AB+2}{\left(B-A\right)^3}. \tag{B.61}$$

And at the end, it is possible to obtain full form of T_4 coefficient:

$$\begin{aligned}
T_4 &= 3 - B - 2A - T_2 - T_1 (B - A) = \\
&= 3 - B - 2A - \frac{(1-A)^3}{(B-A)^2} - \frac{3A^2B + 3B + 3A - 6AB - A^3 - 2}{(B-A)^2} \\
&= \frac{(3 - B - 2A)(B^2 - 2AB + A^2) - (1 - 3A + 3A^2 - A^3)}{(B-A)^2} \\
&+ \frac{-3A^2B - 3B - 3A + 6AB + A^3 + 2}{(B-A)^2} \\
&= \frac{3B^2 - 6AB + 3A^2 - B^3 + 2AB^2 - A^2B - 2AB^2}{(B-A)^2} \\
&+ \frac{4A^2B - 2A^3 - 1 + 3A - 3A^2}{(B-A)^2} \\
&+ \frac{A^3 - 3A^2B - 3B - 3A + 6AB + A^3 + 2}{(B-A)^2} \\
&= \frac{3B^2 - B^3 - 3B + 1}{(B-A)^2} \\
&= \frac{B(3B - B^2 - 3) + 1}{(B-A)^2}, \qquad \text{(B.62)}
\end{aligned}$$

$$T_4 = \frac{3B^2 - B^3 - 3B + 1}{(B-A)^2}. \qquad \text{(B.63)}$$

Finally, the solution of the $\hat{J}^{TP}_{1,3}$ integral is as follows:

$$\hat{J}^{TP}_{1,3} = \frac{2\pi}{a^2} \frac{1}{A_0^2 C_0^2} \left(\frac{T_1}{\sqrt{A}} + \frac{T_2}{2A^{3/2}} + \frac{T_3}{\sqrt{B}} + \frac{T_4}{2B^{3/2}} \right). \qquad \text{(B.64)}$$

B.4 3. Integral $\hat{J}^{TP}_{2,2}$

Integral $\hat{J}^{TP}_{2,2}$ has the following form:

$$\hat{J}^{TP}_{2,2} = \int_0^{2\pi} \frac{d\phi}{(a\cos\phi + b)\left(1 + (a\cos\phi + b)\, c^{TP}\right)}. \qquad \text{(B.65)}$$

In this case $p = 0$, $n = 1$ and $m = 1$. Applying procedure from Introduction one can obtain:

$$\hat{J}^{TP}_{2,2} = \frac{4}{a} \frac{1}{A_0 C_0} \int_0^{\infty} \frac{(1 + x^2)\, dx}{(x^2 + A)(x^2 + B)}. \qquad \text{(B.66)}$$

Partial fraction decomposition is like the following:

$$\begin{aligned}\frac{1+x^2}{(x^2+A)(x^2+B)} &= \frac{T_1}{x^2+A}+\frac{T_2}{x^2+B}\\ &= \frac{T_1(x^2+B)+T_2(x^2+A)}{(x^2+A)(x^2+B)}\\ &= \frac{(T_1B+T_2A)+(T_1+T_2)x^2}{(x^2+A)(x^2+B)}.\end{aligned} \tag{B.67}$$

One can write the fraction in the following form:

$$\frac{1+x^2}{(x^2+A)(x^2+B)} = \frac{(T_1B+T_2A)+(T_1+T_2)x^2}{(x^2+A)(x^2+B)}. \tag{B.68}$$

After comparison of polynomials in numerators, one can write two equations with not known coefficients T_1 and T_2:

$$\begin{cases} T_1B+T_2A=1, \\ T_1+T_2=1. \end{cases} \tag{B.69}$$

Solving this set of equations, it is possible to obtain coefficients T_1 and T_2:

$$T_2 = 1-T_1, \tag{B.70}$$

$$T_1B+(1-T_1)A=1, \tag{B.71}$$

$$T_1 = \frac{1-A}{B-A}, \tag{B.72}$$

$$T_2 = \frac{B-1}{B-A}. \tag{B.73}$$

Then $\hat{J}_{2,2}^{TP}$ integral can be written in the following form:

$$\hat{J}_{2,2}^{TP} = \frac{4}{a}\frac{1}{A_0C_0}\left(\frac{1-A}{B-A}\int_0^\infty \frac{dx}{x^2+A}+\frac{B-1}{B-A}\int_0^\infty \frac{dx}{x^2+B}\right). \tag{B.74}$$

Above integrals were calculated in the introduction. Finally, integral $\hat{J}_{2,2}^{TP}$ has the following solution:

$$\hat{J}_{2,2}^{TP} = \frac{2}{a}\frac{1}{A_0C_0}\frac{1}{B-A}\left((1-A)\frac{\pi}{\sqrt{A}}+(B-1)\frac{\pi}{\sqrt{B}}\right). \tag{B.75}$$

B.5 4. Integral $\hat{J}^{TP}_{2,3}$

The integral $\hat{J}^{TP}_{2,3}$ is like the following:

$$\hat{J}^{TP}_{2,3} = \int_0^{2\pi} \frac{d\phi}{(a\cos\phi + b)\left(1 + (a\cos\phi + b)\, c^{TP}\right)^2}. \tag{B.76}$$

In this case $p = 0$, $n = 1$, $m = 2$. After applying procedure from Introduction one can obtain:

$$\hat{J}^{TP}_{2,3} = \frac{4}{aA_0C_0^2} \int_0^{\infty} \frac{(1+x^2)^2\, dx}{(x^2 + A)\left(x^2 + B\right)^2}. \tag{B.77}$$

Then it is visible that integral $\hat{J}^{TP}_{2,3}$ has a similar form like integral $\hat{J}^{TP}_{1,2}$ by permuting A and B coefficients. Using the expression of $\hat{J}^{TP}_{1,2}$, one can obtain the solution of $\hat{J}^{TP}_{2,3}$:

$$\hat{J}^{TP}_{2,3} = \frac{2\pi}{a} \frac{1}{A_0C_0^2} \left(\frac{T_1}{\sqrt{B}} + \frac{T_2}{2B\sqrt{B}} + \frac{T_3}{\sqrt{A}} \right), \tag{B.78}$$

where coefficients T_1, T_2, T_3 are equal to, respectively

$$T_1 = \frac{B^2 - 1 + 2A\,(1 - B)}{(A - B)^2}, \tag{B.79}$$

$$T_2 = \frac{(1 - B)^2}{A - B}, \tag{B.80}$$

$$T_3 = \frac{(A - 1)^2}{(A - B)^2}. \tag{B.81}$$

B.6 5. Integral $\hat{J}^{TP}_{3,2}$

The integral $\hat{J}^{TP}_{3,2}$ is like the following:

$$\hat{J}^{TP}_{3,2} = \int_0^{2\pi} \frac{\cos\phi d\phi}{(a\cos\phi + b)^2\left(1 + (a\cos\phi + b)\, c^{TP}\right)}. \tag{B.82}$$

In this case $p = 1, n = 2, m = 1$. After applying formula from Introduction:

$$\hat{J}^{TP}_{3,2} = \frac{1}{a}\int_0^{2\pi} \frac{d\phi}{(a\cos\phi + b)\left(1 + (a\cos\phi + b)\, c^{TP}\right)} \tag{B.83}$$

$$-\frac{b}{a}\int_0^{2\pi} \frac{d\phi}{(a\cos\phi + b)^2\left(1 + (a\cos\phi + b)\, c^{TP}\right)}$$

$$= \frac{1}{a}\hat{J}^{TP}_{2,2} - \delta\hat{J}^{TP}_{1,2}. \tag{B.84}$$

B.7 6. Integral $\hat{J}^{TP}_{3,3}$

The integral $\hat{J}^{TP}_{3,2}$ is like the following:

$$\hat{J}^{TP}_{3,3} = \int_0^{2\pi} \frac{\cos\phi d\phi}{(a\cos\phi + b)^2\left(1 + (a\cos\phi + b)\, c^{TP}\right)^2}. \tag{B.85}$$

In this case $p = 1$,$n = 2$, $m = 2$. Applying formula from Introduction:

$$\hat{J}^{TP}_{3,3} = \frac{1}{a}\int_0^{2\pi} \frac{a\cos\phi + b}{(a\cos\phi + b)^2\left(1 + (a\cos\phi + b)\, c^{TP}\right)^2} d\phi \tag{B.86}$$

$$-\frac{b}{a}\int_0^{2\pi} \frac{d\phi}{(a\cos\phi + b)^2\left(1 + (a\cos\phi + b)\, c^{TP}\right)^2}$$

$$= \frac{1}{a}\int_0^{2\pi} \frac{d\phi}{(a\cos\phi + b)\left(1 + (a\cos\phi + b)\, c^{TP}\right)^2} - \frac{b}{a}\hat{J}^{TP}_{1,3}. \tag{B.87}$$

Finally, one can write the solution of integral $\hat{J}^{TP}_{3,3}$ in the following way:

$$\hat{J}^{TP}_{3,3} = \frac{1}{a}\hat{J}^{TP}_{2,3} - \delta\hat{J}^{TP}_{1,3}. \tag{B.88}$$

B.8 7. Integral $\hat{J}^{TP}_{4,2}$

The integral $\hat{J}^{TP}_{4,2}$ is like the following:

$$\hat{J}^{TP}_{4,2} = \int_0^{2\pi} \frac{\cos\phi d\phi}{(a\cos\phi + b)\left(1 + (a\cos\phi + b)\, c^{TP}\right)}. \tag{B.89}$$

In this case $p = 1$, $n = 1$ and $m = 1$. Applying formula from Introduction one can obtain:

$$\begin{aligned}\hat{J}_{4,2}^{TP} &= \frac{1}{a}\int_0^{2\pi}\frac{d\phi}{\left(1+\left(a\cos\phi+b\right)c^{TP}\right)} - \frac{b}{a}\int_0^{2\pi}\frac{d\phi}{\left(a\cos\phi+b\right)\left(1+\left(a\cos\phi+b\right)c^{TP}\right)} \\ &= \frac{1}{a}\int_0^{2\pi}\frac{d\phi}{1+\left(a\cos\phi+b\right)c^{TP}} - \frac{b}{a}\hat{J}_{2,2}^{TP}. \end{aligned} \tag{B.90}$$

After tangent half-angle substitution, the integral takes the form:

$$\begin{aligned}\int_{-\infty}^{\infty}\frac{\frac{2}{1+x^2}dx}{ac^{TP}\left(\frac{1-x^2}{1+x^2}\right)+1+bc^{TP}} &= \int_{-\infty}^{\infty}\frac{2dx}{ac^{TP}\left(1-x^2\right)+\left(1+bc^{TP}\right)\left(1+x^2\right)} \\ &= \int_{-\infty}^{\infty}\frac{2dx}{\left(1+bc-ac\right)x^2+\left(ac+1+bc\right)} \\ &= \frac{2}{ac+1+bc}\sqrt{\frac{ac+bc+1}{-ac+bc+1}}\pi \\ &= \frac{2\pi}{\sqrt{1+c\left(b+a\right)}\sqrt{1+c\left(b-a\right)}}. \end{aligned} \tag{B.91}$$

Returning to $\hat{J}_{4,2}^{TP}$ integral:

$$\hat{J}_{4,2}^{TP} = \frac{\frac{2\pi}{a}}{\sqrt{1+c\left(b+a\right)}\sqrt{1+c\left(b-a\right)}} - \frac{b}{a}\hat{J}_{2,2}^{TP}. \tag{B.92}$$

Using constants C_0 and D_0, it is possible to write the final solution:

$$\hat{J}_{4,2}^{TP} = \frac{2\pi}{a}\frac{1}{\sqrt{C_0 D_0}} - \delta\hat{J}_{2,2}^{TP}. \tag{B.93}$$

B.9 8. Integral $\hat{J}_{4,3}^{TP}$

Integral $\hat{J}_{4,3}^{TP}$ has the following form:

$$\begin{aligned}\hat{J}_{4,3}^{TP} &= \int_0^{2\pi}\frac{\cos\phi d\phi}{\left(a\cos\phi+b\right)\left(1+\left(a\cos\phi+b\right)c^{TP}\right)^2} \\ &= \frac{1}{a}\int_0^{2\pi}\frac{d\phi}{\left(1+\left(a\cos\phi+b\right)c^{TP}\right)^2} \\ &- \frac{b}{a}\int_0^{2\pi}\frac{d\phi}{\left(a\cos\phi+b\right)\left(1+\left(a\cos\phi+b\right)c^{TP}\right)^2}. \end{aligned} \tag{B.94}$$

Now it is possible to use tangent half-angle substitution:

$$\hat{J}_{4,3}^{TP} = \frac{1}{a}\int_{-\infty}^{\infty} \frac{\frac{2}{1+x^2}dx}{\left((1+bc^{TP}) + (ac^{TP})\,\frac{1-x^2}{1+x^2}\right)^2} - \frac{b}{a}\hat{J}_{2,3}^{TP}, \tag{B.95}$$

$$\begin{aligned}
\int_{-\infty}^{\infty} \frac{\frac{2}{1+x^2}dx}{\left((1+bc^{TP}) + (ac^{TP})\,\frac{1-x^2}{1+x^2}\right)^2} &= \int_{-\infty}^{\infty} \frac{2dx\,(1+x^2)}{\left((1+bc)\,(1+x^2) + ac\,(1-x^2)\right)^2} \\
&= \int_{-\infty}^{\infty} \frac{2\,(1+x^2)\,dx}{\left((1+c\,(b-a))\,x^2 + (1+c\,(b+a))\right)} \\
&= 2\int_{-\infty}^{\infty} \frac{(1+x^2)}{(x^2+B)^2}dx\frac{1}{C_0^2}.
\end{aligned} \tag{B.96}$$

Now, the following integral must be calculated:

$$\begin{aligned}
\int_{-\infty}^{\infty} \frac{1+x^2}{(x^2+B)^2}dx &= \int_{-\infty}^{\infty} \frac{x^2+B+1-B}{(x^2+B)^2}dx \\
&= \int_{-\infty}^{\infty} \frac{dx}{x^2+B} + (1-B)\int_{-\infty}^{\infty} \frac{dx}{(x^2+B)^2} \\
&= \frac{\pi}{\sqrt{B}} + (1-B)\,\frac{\pi}{2B^{3/2}}.
\end{aligned} \tag{B.97}$$

Finally, the solution of the integral $\hat{J}_{4,3}^{TP}$ is as follows:

$$\hat{J}_{4,3}^{TP} = \frac{\pi\,(B+1)}{aB^{3/2}}\frac{1}{C_0^2} - \delta\hat{J}_{2,3}^{TP}. \tag{B.98}$$

List of Figures

List of Tables

Bibliography

[Ahn 2016] J. Ahn, X. Garbet, H. Lütjens and R Guirlet. *Dynamics of heavy impurities in non-linear MHD simulations of sawtoothing tokamak plasmas*. Plasma Physics and Controlled Fusion, vol. 58, 2016. https://iopscience.iop.org/article/10.1088/0741-3335/58/12/125009, (accessed 11.07.2021). (Cited in section 1.4.2.)

[Angioni 2012] C. Angioni, F.J. Casson, C. Veth and A.G. Peeters. *Analytic formulae for centrifugal effects on turbulent transport of trace impurities in tokamak plasmas*. Physics of Plasmas, vol. 19, 2012. https://aip.scitation.org/doi/10.1063/1.4773051, (accessed 10.07.2021). (Cited in section 1.4.2.)

[Angioni 2014] C. Angioni and P. Helander. *Neoclassical transport of heavy impurities with poloidally asymmetric density distribution in tokamaks*. Plasma Physics and Controlled Fusion, vol. 56, 2014. https://iopscience.iop.org/article/10.1088/0741-3335/56/12/124001, (accessed 10.07.2021). (Cited in section 1.4.2.)

[Angioni 2017] C. Angioni, M. Sertoli1, R. Bilato, V. Bobkov, A. Loarte, R. Ochoukov, T. Odstrcil, T. Pütterich, J. Stober and The ASDEX Upgrade Team. *A comparison of the impact of central ECRH and central ICRH on the tungsten behaviour in ASDEX Upgrade H-mode plasmas*. Nuclear Fusion, vol. 57, 2017. https://iopscience.iop.org/article/10.1088/1741-4326/aa6453/meta, (accessed 10.07.2021). (Cited in section 1.4.2.)

[Arslanbekov 1995] R. Arslanbekov. *PhD thesis written in English: Etude des electrons rapides a partir du rayonnement X-dur*. 1995. https://inis.iaea.org/collection/NCLCollectionStore/_Public/27/061/27061200.pdf?r=1&r=1, (accessed 09.08.2021). (Cited in section 3.6.)

[Artaud 2018] J.F. Artaud, F. Imbeaux, J. Garcia, G. Giruzzi, T. Aniel, V. Basiuk, A. Bécoulet, C. Bourdelle, Y. Buravand, J. Decker, R. Dumont, L.G. Eriksson,

X. Garbet, R. Guirlet, G.T. Hoang, P. Huynh, E. Joffrin, X. Litaudon, P. Maget, D. Moreau, R. Nouailletas, B. Pégourié, Y. Peysson, M. Schneider, and J. Urban. *Metis: a fast integrated tokamak modelling tool for scenario design*. Nuclear Fusion, vol. 58, no. 10, 2018. https://iopscience.iop.org/article/10.1088/1741-4326/aad5b1/meta, (accessed: 12.07.2021). (Cited in sections (document) and 3.1.)

[Baek 2014] S.G. Baek. *Detection of lower hybrid waves at the plasma edge of a diverted tokamak*. 2014. https://dspace.mit.edu/handle/1721.1/87487, (accessed 18.07.2021). (Cited in section 3.1.)

[Bennett 1934] W.H. Bennett. *Magnetically Self-Focussing Streams*. Physical Review, vol. 45, pages 890–897, 1934. https://journals.aps.org/pr/abstract/10.1103/PhysRev.45.890, (accessed 11.07.2021). (Cited in section 1.2.3.)

[Bielecki 2020] J. Bielecki, M. Scholz and A. Jardin. *KISD lectures on plasma physics and controlled fusion*. 2020. (Cited in sections 1.14 and B.9.)

[Botto 1978] D.J. Botto, J. McEnnan and R.H. Pratt. *Analytic description of photoeffect from atomic ions*. Physical Review A, vol. 18(2), 1978. https://journals.aps.org/pra/abstract/10.1103/PhysRevA.18.580. (Cited in section 4.2.2.)

[BP] BP. *Statistical Review of World Energy*. https://www.bp.com/en/global/corporate/energy-economics/statistical-review-of-world-energy/downloads.html, (accessed 10.07.2021). (Cited in section 1.1.2.)

[Bromberg 1982] J. L. Bromberg. Fusion. science, politics, and the invention of a new energy source. The MIT Press, 1982. https://mitpress.mit.edu/books/fusion, (accessed 15.10.2021). (Cited in section 1.2.3.)

[Burke 2021] D. Burke. 2021. https://en.wikipedia.org/wiki/Safety_factor_(plasma_physics)#/media/File:Toroidal_coord.png, (accessed: 11.07.2021). (Cited in sections 1.12 and B.9.)

[Cardinali 2018] A. Cardinali, C. Castaldo, R. Cesario, L. Amicucci, A. Galli, F. Napoli, L. Panaccione, C. Riccardi, F. Santini, G. Schettini and A. A. Tuccillo. *Radio-frequency current drive for thermonuclear fusion reactors*. Scientific Reports 8, no. 10318, 2018. https://www.nature.com/articles/s41598-018-27996-9, (accessed: 11.07.2021). (Cited in section 2.6.)

[CEA] CEA. *Main parameters of WEST tokamak.* https://westusers.partenaires.cea.fr/group/west/machine-description, (accessed: 01.03.2021). (Cited in sections 1.17, 1.2.6, 1.18, and B.9.)

[Chapman 2010] I.T. Chapman. *Controlling sawtooth oscillations in tokamak plasmas.* Plasma Physics and Controlled Fusion, vol. 53, 2010. https://iopscience.iop.org/article/10.1088/0741-3335/53/1/013001/meta, (accessed 11.07.2021). (Cited in section 1.4.2.)

[Chen 2011] F.F. Chen. *An Indispensable Truth. How Fusion Power Can Save the Planet.* 2011. https://link.springer.com/book/10.1007/978-1-4419-7820-2, (accessed 17.07.2021). (Cited in sections 2.2 and B.9.)

[Chen 2016] F.F. Chen. *Introduction to Plasma Physics and Controlled Fusion.* 2016. https://link.springer.com/book/10.1007/978-3-319-22309-4, (accessed 16.08.2021). (Cited in section 2.4.1.)

[Chen 2019] X. Chen, R. Prater, C. Petty, J. Lohr, D. Su, L. Lao and V. Chan. *Top Launch for Higher Off-axis Electron Cyclotron Current Drive Efficiency.* EPJ Web Conf., 20th Joint Workshop on Electron Cyclotron Emission and Electron Cyclotron Resonance Heating (EC20), vol. 203, 2019. https://www.epj-conferences.org/articles/epjconf/abs/2019/08/epjconf_ec2018_01004/epjconf_ec2018_01004.html, (accessed 11.07.2021). (Cited in sections 1.21 and B.9.)

[CIEMAT 2009] CIEMAT. *Toroidal system of coordinates.* 2009. http://fusionwiki.ciemat.es/wiki/Toroidal_coordinates, (accessed 17.07.2021). (Cited in sections A.2 and B.9.)

[CIEMAT 2011] CIEMAT. *Flux tube.* 2011. http://fusionwiki.ciemat.es/wiki/Flux_tube, (accessed 19.07.2021). (Cited in sections A.5 and B.9.)

[Claessens 2020] M. Claessens. Iter: The giant fusion reactor: Bringing a sun to earth. Springer, 2020. https://www.springer.com/gp/book/9783030275808, (accessed 10.07.2021). (Cited in sections 1.2 and B.9.)

[Coda 2008] S. Coda, O. Sauter, M.A. Henderson and T.P. Goodman. *Full Bootstrap Discharge Sustainment in Steady State in the TCV Tokamak.* Proceedings of the 22nd IAEA Fusion Energy Conference, 2008. https://infoscience.epfl.ch/record/128501, (accessed 10.08.2021). (Cited in section 2.2.)

[Cohen 1950] R. S. Cohen, Jr. L. Spitzer and P. McR. Routly. *The Electrical Conductivity of an Ionized Gas.* Physical Review, vol. 80, no. 2, pages 230–238, 1950. https://journals.aps.org/pr/abstract/10.1103/PhysRev.80.230, (accessed: 12.07.2021). (Cited in section A.4.)

[Decker 2002] J. Decker. *Master thesis: Synergism of Radio-Frequency Current Drive with the Bootstrap Current.* 2002. https://dspace.mit.edu/bitstream/handle/1721.1/87209/51176004-MIT.pdf?sequence=2&isAllowed=y, (accessed 10.07.2021). (Cited in sections 3.5, A.4, A.1, and B.9.)

[Decker 2005a] J. Decker. *PhD thesis: Electron Bernstein Wave Current Drive Modeling in Toroidal Plasma Confinement.* 2005. https://dspace.mit.edu/handle/1721.1/33937, (accessed 10.07.2021). (Cited in sections 2.4.1 and 3.5.)

[Decker 2005b] J. Decker and Y. Peysson. *DKE: a fast numerical solver for the 3-D relativistic bounce-averaged electron Drift Kinetic Equation.* MIT Plasma Science and Fusion Center, 2005. https://dspace.mit.edu/handle/1721.1/93267?show=full, (accessed: 12.07.2021). (Cited in sections (document), 3.1, 3.5, A.1, and A.4.)

[Decker 2014] J. Decker, Y. Peysson, J.-F. Artaud, E. Nilsson, A. Ekedahl, M. Goniche, J. Hillairet and D. Mazon. *Damping of lower hybrid waves in large spectral gap configurations.* Physics of Plasmas, vol. 21, 2014. https://aip.scitation.org/doi/abs/10.1063/1.4894749?journalCode=php, (accessed 10.07.2021). (Cited in sections 2.4.4, 3.4, 3.4, 3.4, 5.4.2, and B.9.)

[Donnel 2018] P. Donnel. *PhD thesis: Impurity transport in tokamak plasmas: gyrokinetic study of neoclassical and turbulent transport.* 2018. https://www.researchgate.net/publication/329861142_Impurity_transport_in_tokamak_plasmas_gyrokinetic_study_of_neoclassical_and_turbulent_transport, (accessed 11.07.2021). (Cited in sections 1.4.2, A.1, A.1, and B.9.)

[Donnel 2019] P. Donnel, X. Garbet, Y. Sarazin, Y. Asahi, F. Wilczynski, E. Caschera, G. Dif-Pradalier, P. Ghendrih and C. Gillot. *Turbulent generation of poloidal asymmetries of the electric potential in a tokamak.* Plasma Physics and Controlled Fusion, vol. 61, 2019. https://iopscience.iop.org/article/10.1088/1361-6587/aae4fe, (accessed 10.07.2021). (Cited in section 1.4.2.)

[Ekedahl 2010] A. Ekedahl, L. Delpech, M. Goniche, D. Guilhem, J. Hillairet, M. Preynas, P.K. Sharma, J. Achard, Y.S. Bae, X. Bai, C. Balorin, Y. Baranov, V. Basiuk, A. Bécoulet, J. Belo, G. Berger-By, S. Brémond, C. Castaldo, S. Ceccuzzi, R. Cesario, E. Corbel, X. Courtois, J. Decker, E. Delmas, X. Ding, D. Douai, C. Goletto, J.P. Gunn, P. Hertout, G.T. Hoang, F. Imbeaux, K.K. Kirov, X. Litaudon, R. Magne, J. Mailloux, D. Mazon, F. Mirizzi, P. Mollard, P. Moreau, T. Oosako, V. Petrzilka, Y. Peysson, S. Poli, M. Prou, F. Saint-Laurent, F. Samaille and B. Saoutic. *Validation of the ITER-relevant passive-active-multijunction LHCD launcher on long pulses in Tore Supra.* Nuclear Fusion, vol. 50, 2010. https://iopscience.iop.org/article/10.1088/0029-5515/50/11/112002/meta, (accessed 12.07.2021). (Cited in sections 3.4 and B.9.)

[Faust 2016] I.C. Faust. *Quantification of Lower Hybrid wave absorption in the edge of the Alcator C-Mod tokamak.* 2016. https://dspace.mit.edu/handle/1721.1/107282, (accessed 18.07.2021). (Cited in section 3.1.)

[Fermi 1928] E. Fermi. *Eine statistische Methode zur Bestimmung einiger Eigenschaften des Atoms und ihre Anwendung auf die Theorie des periodischen Systems der Elemente.* Zeitschrift für Physik, vol. 48, 1928. https://link.springer.com/article/10.1007/BF01351576, (accessed 27.10.2021). (Cited in section 4.2.1.)

[Fisch 1978] N. J. Fisch. *Confining a Tokamak Plasma with rf-Driven Currents.* Physical Review Letters, vol. 41, no. 13, pages 873–876, 1978. https://journals.aps.org/prl/abstract/10.1103/PhysRevLett.41.873, (accessed: 12.07.2021). (Cited in sections 1.3.1, 3.5, and A.2.)

[Fisch 1987] N. J. Fisch. *Theory of current drive in plasmas.* Reviews of Modern Physics, vol. 59, no. 1, pages 175–234, 1987. https://journals.aps.org/rmp/abstract/10.1103/RevModPhys.59.175, (accessed: 12.07.2021). (Cited in sections 1.3.1, 2.1, 2.3, 2.3, 3.5, A.3, and A.4.)

[Freidberg 2007] J. P. Freidberg. *Plasma Physics and Fusion Energy.* Cambridge University Press, 2007. https://www.cambridge.org/core/books/plasma-physics-and-fusion-energy/CD7B530D2889F70446F34E14EE0EF703, (accessed: 12.07.2021). (Cited in sections 1.2.3, 1.2.5, 2.1, 2.1, 2.2, 2.5, 2.6, 2.7, 2.4.4, and B.9.)

[Frisch 2019] M. J. Frisch, G. W. Trucks, H. B. Schlegel, G. E. Scuseria, M. A. Robb, J. R. Cheeseman, G. Scalmani, V. Barone, G. A. Petersson, H. Nakatsuji, X. Li, M. Caricato, A. V. Marenich, J. Bloino, B. G. Janesko, R. Gomperts, B. Mennucci, H. P.

Hratchian, J. V. Ortiz, A. F. Izmaylov, J. L. Sonnenberg, D. Williams-Young, F. Ding, F. Lipparini, F. Egidi, J. Goings, B. Peng, A. Petrone, T. Henderson, D. Ranasinghe, V. G. Zakrzewski, J. Gao, N. Rega, G. Zheng, W. Liang, M. Hada, M. Ehara, K. Toyota, R. Fukuda, J. Hasegawa, M. Ishida, T. Nakajima, Y. Honda, O. Kitao, H. Nakai, T. Vreven, K. Throssell, J. A. Montgomery Jr., J. E. Peralta, F. Ogliaro, M. J. Bearpark, J. J. Heyd, E. N. Brothers, K. N. Kudin, V. N. Staroverov, T. A. Keith, R. Kobayashi, J. Normand, K. Raghavachari, A. P. Rendell, J. C. Burant, S. S. Iyengar, J. Tomasi, M. Cossi, J. M. Millam, M. Klene, C. Adamo, R. Cammi, J. W. Ochterski, R. L. Martin, K. Morokuma, O. Farkas, J. B. Foresman and D. J. Fox. *Gaussian 16, Revision C.01.* 2019. Gaussian Inc. Wallingford CT, https://gaussian.com/, (accessed 20.10.2021). (Cited in section 4.2.3.)

[Fuchs 1985] V. Fuchs, R. A. Cairns, M. M. Shoucri, K. Hizanidis and A. Bers. *A one dimensional model for lower hybrid current drive including perpendicular dynamics.* The Physics of Fluids, vol. 28, no. 12, pages 3619–3628, 1985. https://aip.scitation.org/doi/10.1063/1.865318, (accessed: 12.07.2021). (Cited in section A.2.)

[Février 2016] O. Février, P. Maget, H. Lütjens, J. F. Luciani, J. Decker, G. Giruzzi, M. Reich, P. Beyer, E. Lazzaro, S. Nowak and the ASDEX Upgrade team. *First principles fluid modelling of magnetic island stabilization by electron cyclotron current drive (ECCD).* Plasma Physics and Controlled Fusion, vol. 58, 2016. https://iopscience.iop.org/article/10.1088/0741-3335/58/4/045015/meta. (Cited in section 2.4.2.)

[Garcia 2008] J. Garcia, G. Giruzzi, J. F. Artaud, V. Basiuk, J. Decker, F. Imbeaux, Y. Peysson and M. Schneider. *Integrated modeling of ITER steady-state scenarios.* Plasma Physics and Controlled Fusion, vol. 50, 2008. https://iopscience.iop.org/article/10.1088/0741-3335/50/12/124032, (accessed 04.10.2021). (Cited in section 2.6.)

[Gell 1984] Y. Gell and R. Nakach. *Stochastic generation of currents by lower-hybrid waves.* Physics Letters A, vol. 101, no. 4, pages 209–213, 1984. https://www.sciencedirect.com/science/article/abs/pii/0375960184903815, (accessed: 12.07.2021). (Cited in section 3.5.)

[Gell 1985] Y. Gell and R. Nakach. *Employment of plasma beat waves in stochastic current drive.* Physical Review A, vol. 31, no. 6, pages 3846–3856,

1985. https://journals.aps.org/pra/abstract/10.1103/PhysRevA.31.3846, (accessed: 12.07.2021). (Cited in section 3.5.)

[Ghendrih 2015] P. Ghendrih, E. Tsitrone, C. Bourdelle, S. Brémond, J. Bucalossi, Y. Corre, A. Ekedahl, G. Giruzzi, R. Guirlet, P. Maget, Y. Marandet, M. Missirlian, P. Moreau, E. Nardon and B. Pégourié. *The WEST research plan*. 2015. http://irfm.cea.fr/Images/astImg/693/WEST-research-plan-v1_2015-02.pdf, (accessed: 11.07.2021). (Cited in section 1.2.6.)

[Gil 2009] C. Gil, C. De Michelis, D. Elbeze, C. Fenzi, J. P. Gunn, F. Imbeaux, Ph. Lotte, D.Mazon, O. Meyer, M. Missirlian, Ph. Moreau, R. Reichle, R. Sabot, F. Saint-Laurent, J.-L. Segui, A. Simonin, J.-M. Travere, J.-C. Vallet and Tore Supra Team. *Diagnostic Systems on Tore Supra*. Fusion Science and Technology, vol. 56, pages 1219–1252, 2009. https://www.tandfonline.com/doi/abs/10.13182/FST09-A9175, (accessed 15.07.2021). (Cited in sections 5.2 and 5.2.)

[Granetz 2014] R. S. Granetz, B. Esposito, J. H. Kim, R. Koslowski, M. Lehnen, J. R. Martin-Solis, C. Paz-Soldan, T. Rhee, J. C. Wesley, L. Zeng and ITPA MHD Group. *An ITPA joint experiment to study runaway electron generation and suppression*. Physics of Plasmas, vol. 21, 2014. https://doi.org/10.1063/1.4886802, (accessed 15.10.2021). (Cited in section 1.3.2.)

[GUS 2020] GUS. 2020. https://stat.gov.pl/en/topics/environment-energy/energy/energy-efficiency-in-poland-2008-2018,5,16.html, (accessed 10.07.2021). (Cited in sections 1.1 and B.9.)

[Hambling 2016] D. Hambling and R. Webb. *Fired Up*. New Scientist, vol. 229, pages 34–37, 2016. https://www.sciencedirect.com/science/article/abs/pii/S0262407916302317, (accessed: 11.07.2021). (Cited in sections 1.3 and B.9.)

[Harvey 1981] R.W. Harvey, K.D. Marx and M.G. Mccoy. *Non-linear Fokker-Planck studies of RF current drive efficiency*. Nuclear Fusion, vol. 21, no. 2, pages 153–157, 1981. https://iopscience.iop.org/article/10.1088/0029-5515/21/2/003, (accessed: 12.07.2021). (Cited in section 3.5.)

[Harvey 1989] R. W. Harvey, M. G. McCoy and G. D. Kerbel. *Power Dependence of Electron-Cyclotron Current Drive for Low- and High-Field Absorption in Tokamaks*. Physical Review Letters, vol. 62, no. 3, pages 426–429, 1989. https://journals.aps.org/prl/abstract/10.1103/PhysRevLett.62.426, (accessed: 11.07.2021). (Cited in section 2.4.2.)

[Hesslow 2017] L. Hesslow, O. Embréus, A. Stahl, T. C. DuBois, G. Papp, S. L. Newton and T. Fülöp. *Effect of Partially Screened Nuclei on Fast-Electron Dynamics*. Physical Review Letters, vol. 118, no. 25, 2017. https://journals.aps.org/prl/abstract/10.1103/PhysRevLett.118.255001, (accessed: 12.07.2021). (Cited in sections (document), 3.5, 4.3, 4.3, 4.8, and B.9.)

[Hillairet 2010] J. Hillairet, D. Voyer, A. Ekedahl, M. Goniche, M. Kazda, O. Meneghini, D. Milanesio and M. Preynas. *ALOHA: an Advanced LOwer Hybrid Antenna coupling code*. Nuclear Fusion, vol. 50, no. 12, 2010. https://iopscience.iop.org/article/10.1088/0029-5515/50/12/125010/meta, (accessed: 12.07.2021). (Cited in sections (document), 3.2, 3.2, and B.9.)

[Hillairet 2015] J. Hillairet, J. Kim, N. Faure, J. Achard, Y. S. Bae, J. M. Bernard, L. Delpech, M. Goniche, S. Larroque, R. Magne, L. Marfisi, S. Park, S. Poli, N. Dechambre and K. Vulliez. *Design and tests of 500 kW RF windows for the ITER LHCD system*. Fusion Engineering and Design, vol. 94, pages 22–30, 2015. https://www.sciencedirect.com/science/article/abs/pii/S0920379615001568, (accessed: 12.07.2021). (Cited in section 2.1.)

[IAEA] IAEA. *Enabling Technology for Fusion: IAEA Forum Pushes Forward Advanced Mock-ups*. https://www.iaea.org/newscenter/news/enabling-technology-for-fusion-iaea-forum-pushes-forward-advanced-mock-ups, (accessed 11.07.2021). (Cited in sections 1.23 and B.9.)

[Ismailov 2016] R. E. Ismailov, P. B. Aleynikov and S. V. Konovalov. *Dreicer mechanism of runaway electron generation in presence of high-Z impurities*. 2016. Proceeding article of 43rd EPS Conference on Plasma Physics. European Physical Society. http://ocs.ciemat.es/EPS2016PAP/pdf/P2.022.pdf, (accessed 15.10.2021). (Cited in section 1.3.2.)

[ITER] ITER. https://www.iter.org/sci/BeyondITER, (accessed 11.07.2021). (Cited in section 1.2.5.)

[ITER Organization 1999] ITER Organization. *ITER Physics Basis, Chapter 6: Plasma auxiliary heating and current drive*. 1999. https://iopscience.iop.org/article/10.1088/0029-5515/40/7/512, (accessed: 11.07.2021). (Cited in section 2.4.3.)

[ITER Organization 2018] ITER Organization. *ITER Research Plan within the Staged Approach (Level III – Provisional Version)*. 2018. https:

//www.iter.org/doc/www/content/com/Lists/ITER%20Technical%20Reports/Attachments/9/ITER_Research_Plan_within_the_Staged_Approach_levIII_provversion.pdf, (accessed: 12.07.2021). (Cited in sections 1.1.3, 2.1, and 2.6.)

[Ivanova-Stanik 2020] I. Ivanova-Stanik. *Numerical Studies of Impurity Transport in JET ILW Discharges*. 2020. https://www.ncbj.gov.pl/en/dokument/numerical-studies-impurity-transport-jet-ilw-discharges, (accessed 11.07.2021). (Cited in sections 1.4 and 1.4.2.)

[Jardin 2017] A. Jardin. *PhD thesis: Soft X-ray measurements for impurity transport studies in tokamak plasmas*. 2017. https://www.researchgate.net/publication/322991697_Soft_X-ray_measurements_for_impurity_transport_studies_in_tokamak_plasmas, (accessed 11.07.2021). (Cited in sections 1.26 and B.9.)

[Jardin 2020a] A. Jardin, J. Bielecki, K. Król, Y. Peysson, D. Mazon, D. Dworak and M. Scholz. *Study of the mutual dependence between Lower Hybrid current drive and heavy impurity transport in tokamak plasmas. Part 1. Preparatory work and theoretical background*. 2020. https://www.ifj.edu.pl/badania/publikacje/raporty/2020/2105.pdf, (accessed 10.07.2021). (Cited in sections 4, 4.2.1, 4.2, 4.4, 4.9, 6, and B.9.)

[Jardin 2020b] A. Jardin, J. Bielecki, D. Mazon, J. Dankowski, K. Król, Y. Peysson and M. Scholz. *Synthetic X-ray Tomography Diagnostics for Tokamak Plasmas*. Journal of Fusion Energy, vol. 39, 2020. https://link.springer.com/article/10.1007/s10894-020-00250-9, (accessed 28.10.2021). (Cited in section 5.3.)

[Jardin 2021] A. Jardin, D. Mazon, F. Jaulmes, R. Bilato, C. Angioni, K. Król, D. Colette, G. Vogel, ASDEX Upgrade Team, TCV Team and EUROfusion MST1 Team. *Investigations of the impact of heating schemes and poloidal asymmetries on the heavy impurity transport in AUG and TCV*. Proceedings of the 47th EPS Conference on Plasma Physics, 2021. http://ocs.ciemat.es/EPS2021PAP/pdf/P3.1065.pdf, (accessed 28.10.2021). (Cited in section 1.4.2.)

[Karney 1979] C.F.F. Karney and N.J. Fisch. *Numerical studies of current generation by radio-frequency traveling waves*. Physics of Fluids, vol. 22, no. 9, pages 1817–1824, 1979. https://aip.scitation.org/doi/10.1063/1.862787, (accessed: 12.07.2021). (Cited in sections A.2 and A.2.)

[Karney 1981] C.F.F. Karney and N.J. Fisch. *Currents driven by electron cyclotron waves.* Nuclear Fusion, vol. 21, no. 12, pages 1549–1557, 1981. https://iopscience.iop.org/article/10.1088/0029-5515/21/12/004, (accessed: 12.07.2021). (Cited in section A.4.)

[Karney 1986] C.F.F. Karney and N.J. Fisch. *Fokker-Planck and quasilinear codes.* The Physics of Fluids, vol. 29, no. 180, 1986. https://arxiv.org/pdf/physics/0501066.pdf, (accessed: 11.07.2021). (Cited in section 3.5.)

[Kessel 2007] C.E. Kessel, G. Giruzzi, A.C.C. Sips, R.V. Budny, J.F. Artaud, V. Basiuk, F. Imbeaux, E. Joffrin, M. Schneider, M. Murakami, T. Luce, Holger St John, T. Oikawa, N. Hayashi, T. Takizuka, T. Ozeki, Y.-S. Na, J.M. Park, J. Garcia and A.A. Tucillo. *Simulation of the hybrid and steady state advanced operating modes in ITER.* Nuclear Fusion, vol. 47, no. 9, pages 1274–1284, 2007. https://iopscience.iop.org/article/10.1088/0029-5515/47/9/026, (accessed: 12.07.2021). (Cited in section 2.6.)

[Kirillov 1975] V. D. Kirillov, B.A. Trubnikov and S.A. Trushin. *Role of impurities in anomalous plasma resistance.* Fizika Plazmy, 1 :218 – 237, Mar - Apr, 1975. The article is probably not available online. (Cited in section 4.2.1.)

[Klima 1973] R. Klima. *Nonlinear dragging of particles during high-frequency heating.* Plasma Physics, vol. 15, no. 10, pages 1031–1038, 1973. https://iopscience.iop.org/article/10.1088/0032-1028/15/10/008/meta, (accessed: 12.07.2021). (Cited in section 3.5.)

[Klima 1979] R. Klima and A.V. Longinov. *Excitation of a steady-state current in a toroidal plasma by broad-spectrum waves.* Fizika Plazmy, vol. 5, pages 496–500, 1979. (Cited in section 3.5.)

[Koch 1959] H.W. Koch and J. W. Motz. *Bremsstrahlung cross-section formulas and related data.* Reviews of Modern Physics, vol. 31(4), 1959. https://journals.aps.org/rmp/abstract/10.1103/RevModPhys.31.920. (Cited in section 4.4.)

[Król 2020] K. Król. *Screening effect of partially ionized high-Z impurities in relativistic electron Fokker-Planck calculations and runaway electron dynamics Part 1 – Preliminary work towards statistical study of partial screening effect in WEST tokamak discharges.* IFJ Report No. 2103/AP, 2020. https://www.ifj.edu.pl/

badania/publikacje/raporty/2020/2103.pdf, (accessed 21.10.2021). (Cited in sections 4 and 6.)

[Król 2021] K. Król, Y. Peysson, D. Mazon, M. Scholz, A. Jardin, J. Bielecki, D. Dworak, J. F. Artaud, J. Hillairet, J. Morales, L. Fleury, J. Decker and M. Goniche. *Impact of partial screening effect on fast electron dynamics in WEST tokamak plasmas with high Z impurities*. 2021. http://ocs.ciemat.es/EPS2021PAP/pdf/P2.1072.pdf, (accessed 04.10.2021). (Cited in sections 5.1 and 6.)

[Köhn 2014] C. Köhn and U. Ebert. *Angular distribution of bremsstrahlung photons and of positrons for calculations of terrestrial gamma-ray flashes and positron beams*. Atmospheric Research, vol. 135-136, 2014. https://www.sciencedirect.com/science/article/pii/S0169809513000963?via%3Dihub. (Cited in section 4.4.)

[Lamoureux 1997] M. Lamoureux and N. Avdonina. *Bremsstrahlung in hot plasmas with partially ionized atoms*. Physical Review E, vol. 55, 1997. https://journals.aps.org/pre/abstract/10.1103/PhysRevE.55.912, (accessed 20.10.2021). (Cited in section 4.2.2.)

[Landau 1936] L.D. Landau. *The Transport Equation in the Case of Coulomb Interactions*. Phys. Z. Sowjet, vol. 10, no. 154, 1936. https://www.sciencedirect.com/science/article/pii/B9780080105864500298?via%3Dihub, (accessed: 11.07.2021). (Cited in section 3.5.)

[Lau 2013] C. Lau. *Effects of RF power on SOL density profiles and RF coupling on the Alcator C-Mod tokamak*. 2013. https://dspace.mit.edu/handle/1721.1/83824, (accessed 18.07.2021). (Cited in section 3.1.)

[Lawson 1957] J. D. Lawson. *Some Criteria for a Power Producing Thermonuclear Reactor*. Proceedings of the Physical Society. Section B, vol. 70, 1957. https://iopscience.iop.org/article/10.1088/0370-1301/70/1/303/pdf, (accessed 15.10.2021). (Cited in section 1.2.2.)

[Liptac 2006] J.E. Liptac. *PhD thesis: Lower hybrid modeling and experiments on Alcator C-Mod*. 2006. https://dspace.mit.edu/handle/1721.1/41281, (accessed 12.07.2021). (Cited in sections 3.1 and 3.3.)

[Litaudon 2006] X. Litaudon. *Internal transport barriers: critical physics issues?* Plasma Physics and Controlled Fusion, vol. 48, 2006. https://iopscience.iop.org/article/10.1088/0741-3335/48/5A/S01, (accessed 04.10.2021). (Cited in section 2.6.)

[Loarte] A. Loarte. https://www.ugent.be/ea/appliedphysics/en/research/fusion/research/data-analysis.htm, (accessed: 11.07.2021). (Cited in sections 2, 4, and B.9.)

[LUKE 2019] LUKE. *LUKE manual*. 2019. https://westusers.partenaires.cea.fr/group/west/manual5, (accessed: 15.09.2021). (Cited in section 5.4.1.)

[Lundqvist 1983] S. Lundqvist and N.H. March. Theory of the inhomogeneous electron gas. Springer, 1983. https://www.springer.com/gp/book/9780306412073, (accessed 20.10.2021). (Cited in section 4.2.1.)

[Martín-Solís 2010] J. R. Martín-Solís, R. Sánchez and B. Esposito. *Experimental Observation of Increased Threshold Electric Field for Runaway Generation due to Synchrotron Radiation Losses in the FTU Tokamak*. Physical Review Letters, vol. 105, 2010. https://journals.aps.org/prl/abstract/10.1103/PhysRevLett.105.185002, (accessed 15.10.2021). (Cited in section 1.3.2.)

[Matthews 2005] G.F. Matthews. *Material migration in divertor tokamaks*. Journal of Nuclear Materials, vol. 337-339, 2005. https://www.sciencedirect.com/science/article/abs/pii/S0022311504008426, (accessed 11.07.2021). (Cited in sections 1.24 and B.9.)

[Mazon 2012] D. Mazon, D. Vezinet, D. Pacella, D. Moreau, L. Gabelieri, A. Romano, P. Malard, J. Mlynar, R. Masset and P. Lotte. *Soft x-ray tomography for real-time applications: present status at Tore Supra and possible future developments*. Review of Scientific Instruments, vol. 83, 2012. https://doi.org/10.1063/1.4730044, (accessed 28.10.2021). (Cited in section 5.3.)

[Mazon 2016] D. Mazon, C. Fenzi and R. Sabot. *As hot as it gets*. Nature Physics, vol. 12, pages 14–17, 2016. https://www.nature.com/articles/nphys3625?WT.feed_name=subjects_plasma-physics, (accessed 11.07.2021). (Cited in sections 1.15 and B.9.)

[Mazon 2021] D. Mazon, M. Chernyshova, A. Jardin, Y. Peysson, K. Król, P. Malard, T. Czarski, A. Wojeński, K. Malinowski, D. Colette, K.T. Poźniak, G. Kasprowicz, W. Zabołotny, R.D. Krawczyk, P. Kolasiński, M. Gąska, P. Linczuk, J. Bielecki, M. Scholz, D. Dworak and WEST Team. *First GEM Measurements at WEST and perspectives for fast electrons and heavy impurities transport studies in tokamaks, Proceeding article of ECPD 2021 Conference*. 2021. Link to associated poster (proceeding article submitted but not published yet): https:

//www.clpu.es/ECPD2021-Poster%20Sessions_02, (accessed 04.10.2021). (Cited in sections 5.4.5 and 6.)

[McCracken 2012] McCracken. Fusion: The energy of the universe. Academic Press, 2012. https://www.elsevier.com/books/fusion/mccracken/978-0-12-384656-3, (accessed: 11.07.2021). (Cited in sections 1.5, 1.2.3, 1.10, 1.11, 1.25, 1.4.2, and B.9.)

[Meneghini 2012] O. Meneghini. *Full-wave modeling of lower hybrid waves on Alcator C-Mod.* 2012. https://dspace.mit.edu/handle/1721.1/76501, (accessed 18.07.2021). (Cited in sections 2.4.1, 3.1, 3.3, A.1, and A.1.)

[Mlynář 2016] J. Mlynář. *Presentation: Tokamak Physics.* 2016. https://slideplayer.com/slide/8348990/, (accessed 12.07.2021). (Cited in sections 2.3 and B.9.)

[Montgomery 1964] D.C. Montgomery and D.A. Tidman. *Plasma Kinetic Theory.* McGraw-Hill, New York, 1964. (Cited in section 3.5.)

[Mouhot 2010] C. Mouhot and C. Villani. *Landau damping.* Journal of Mathematical Physics, vol. 51, 2010. https://aip.scitation.org/doi/10.1063/1.3285283, (accessed 16.07.2021). (Cited in section 2.4.1.)

[Mouhot 2011] C. Mouhot and C. Villani. *On Landau damping.* Acta Mathematica, vol. 207, pages 29–201, 2011. https://projecteuclid.org/journals/acta-mathematica/volume-207/issue-1/On-Landau-damping/10.1007/s11511-011-0068-9.full, (accessed 16.07.2021). (Cited in section 2.4.1.)

[Moynihan 2015] M. Moynihan. 2015. https://en.wikipedia.org/wiki/Pinch_(plasma_physics)#/media/File:Plasma_Pinch_Mechanism.png, (accessed: 11.07.2021). (Cited in sections 1.6 and B.9.)

[Mumgaard 2015] R.T. Mumgaard. *Lower Hybrid Current Drive on Alcator C-Mod: Measurements with an Upgraded MSE Diagnostic and Comparisons to Simulation.* 2015. https://dspace.mit.edu/handle/1721.1/103661, (accessed 18.07.2021). (Cited in section 3.1.)

[Nilsson 2012] E. Nilsson. *Master thesis: Modelling of Lower Hybrid Current Drive in the Tore Supra Tokamak.* 2012. https://odr.chalmers.se/handle/20.500.12380/179211, (accessed 10.07.2021). (Cited in sections 2.8, 3.1, 3.1, 3.5, 3.10, 3.6, 3.12, 5.2, and B.9.)

[Nilsson 2013] E. Nilsson, J. Decker, Y. Peysson, J.-F. Artaud, A. Ekedahl, J. Hillairet, T. Aniel, V. Basiuk, M. Goniche and F. Imbeaux. *Comparative modelling of lower hybrid current drive with two launcher designs in the Tore Supra tokamak.* Nuclear Fusion, vol. 53, 2013. https://iopscience.iop.org/article/10.1088/0029-5515/53/8/083018, (accessed 10.07.2021). (Cited in sections 3.1, 3.3, 3.2, 3.10, and B.9.)

[Nilsson 2014] E. Nilsson. *Bachelor thesis: Lower hybrid current drive in the Tore Supra tokamak.* 2014. https://research.chalmers.se/en/publication/204407, (accessed 10.07.2021). (Cited in section 3.1.)

[Nilsson 2015] E. Nilsson. *PhD thesis: Dynamics of runaway electrons in tokamak plasmas.* 2015. https://pastel.archives-ouvertes.fr/tel-01212017, (accessed 07.04.2021). (Cited in sections 1.3.2, 1.22, 1.3.2, and B.9.)

[Ohkawa 1970] T. Ohkawa. *New methods of driving plasma current in fusion devices.* Nuclear Fusion, vol. 10, pages 185–188, 1970. https://iopscience.iop.org/article/10.1088/0029-5515/10/2/012, (accessed 11.07.2021). (Cited in sections 1.3.1 and 2.1.)

[Oliphant 1934] M.L.E. Oliphant, P. Harteck and E. Rutherford. *Transmutation Effects Observed with Heavy Hydrogen.* Proceedings of the Royal Society, vol. 144 (853), pages 692–703, 1934. https://royalsocietypublishing.org/doi/10.1098/rspa.1934.0077, (accessed: 11.07.2021). (Cited in section 1.2.3.)

[Paoletti 1999] F. Paoletti, A. Cardinali, S. Bernabei, A. Post-Zwicker, W. Tighe and S. Von Goeler. *Experimental and theoretical investigation of local synergy between ion Bernstein and lower hybrid waves in the Princeton Beta Experiment—Modified.* Physics of Plasmas, vol. 6, no. 3, pages 863–872, 1999. https://aip.scitation.org/doi/10.1063/1.873350, (accessed: 11.07.2021). (Cited in section 2.7.)

[Parail 2002] V.V. Parail. *Energy and particle transport in plasmas with transport barriers.* Plasma Physics and Controlled Fusion, vol. 44, pages A63–A85, 2002. https://iopscience.iop.org/article/10.1088/0741-3335/44/5A/304, (accessed 11.07.2021). (Cited in sections 1.4.2, 1.27, and B.9.)

[Paz-Soldan 2014] C. Paz-Soldan, N. W. Eidietis, R. Granetz, E. M. Hollmann, R. A. Moyer, J. C. Wesley, J. Zhang, M. E. Austin, N. A. Crocker, A. Wingen and Y. Zhu. *Growth and decay of runaway electrons above the critical electric*

field under quiescent conditions. Physics of Plasmas, vol. 21, 2014. https://aip.scitation.org/doi/abs/10.1063/1.4866912, (accessed 15.10.2021). (Cited in section 1.3.2.)

[Peeters 2013] A.G. Peeters. 2013. https://www.ipp.mpg.de/2058230/Peeters.pdf, (accessed 11.07.2021). (Cited in sections 1.19, 1.20, and B.9.)

[Petty 2001] C.C. Petty, F.W. Baity, J.S. de Grassie, T.K. Mau, R.I. Pinsker, M.Porkolab and R. Prater. *Fast wave current drive at high ion cyclotron harmonics on DIII-D.* Plasma Physics and Controlled Fusion, vol. 43, no. 12, pages 1747–1758, 2001. https://iopscience.iop.org/article/10.1088/0741-3335/43/12/308, (accessed: 11.07.2021). (Cited in section 2.4.3.)

[Petty 2002] C.C. Petty, R. Prater, J. Lohr, T.C. Luce, W.R. Fox, R.W. Harvey, J.E. Kinsey, L.L. Lao and M.A. Makowski. *Detailed measurements of the electron cyclotron current drive efficiency on DIII-D.* Nuclear Fusion, vol. 42, no. 12, pages 1366–1375, 2002. https://iopscience.iop.org/article/10.1088/0029-5515/42/12/303, (accessed: 11.07.2021). (Cited in section 2.4.2.)

[Peysson 1993] Y. Peysson, P. Froissard and C. Pocheau. *Study of radiation scattering in the hard X ray energy range by a tokamak inner wall.* Nuclear Fusion, vol. 33, 1993. https://iopscience.iop.org/article/10.1088/0029-5515/33/8/I04, (accessed 07.08.2021). (Cited in sections 3.6 and 3.6.)

[Peysson 1999] Y. Peysson. *Status of Lower Hybrid Current Drive.* AIP Conference Proceedings, vol. 485, no. 1, pages 183–192, 1999. https://aip.scitation.org/doi/10.1063/1.59729, (accessed: 12.07.2021). (Cited in section 2.1.)

[Peysson 2004] Y. Peysson, J. Decker, A. Bers, R. Harvey and A. Ram. *Advanced 3-D electron kinetic calculations for the current drive problem in magnetically confined thermonuclear plasmas.* 2004. https://hal.archives-ouvertes.fr/ICPP2004/hal-00002036, (accessed 10.07.2021). (Cited in sections 3.5 and 3.5.)

[Peysson 2007] Y. Peysson and J. Decker. *Advanced Lower Hybrid Current Drive Modeling.* AIP Conference Proceedings, vol. 933, 2007. https://aip.scitation.org/doi/abs/10.1063/1.2800496, (accessed 26.07.2021). (Cited in section 3.1.)

[Peysson 2008a] Y. Peysson and J. Decker. *Documentation of C3PO code: C3PO, a ray-tracing code for arbitrary axisymmetric magnetic equilibrium.* 2008. Text

is available as an attachment to C3PO code and can be found in directory: YOUR_LUKE_DIRECTORY/Project_DKE/Modules/C3PO/Doc (status as at 26.07.2021). (Cited in sections 3.3 and 3.3.)

[Peysson 2008b] Y. Peysson and J. Decker. *Fast electron bremsstrahlung in axisymmetric magnetic configuration.* Physics of Plasmas, vol. 15, no. 9, 2008. https://aip.scitation.org/doi/10.1063/1.2981391, (accessed: 12.07.2021). (Cited in sections (document), 3.1, 3.6, 3.6, and 3.6.)

[Peysson 2010] Y. Peysson, L. Morini and J. Decker. *The wave kinetic equation.* 2010. Text is available as an attachment to C3PO code and can be found in directory: YOUR_LUKE_DIRECTORY/Project_DKE/Modules/C3PO/Doc. (Cited in section 3.3.)

[Peysson 2012] Y. Peysson, J. Decker and L. Morini. *A versatile ray-tracing code for studying rf wave propagation in toroidal magnetized plasmas.* Plasma Physics and Controlled Fusion, vol. 54, no. 4, 2012. https://iopscience.iop.org/article/10.1088/0741-3335/54/4/045003, (accessed: 12.07.2021). (Cited in sections (document) and 3.3.)

[Peysson 2014] Y. Peysson and J. Decker. *Numerical Simulations of the Radio-Frequency–driven Toroidal Current in Tokamaks.* Fusion Science and Technology, vol. 65, no. 1, pages 22–42, 2014. https://www.tandfonline.com/doi/abs/10.13182/FST13-643, (accessed: 12.07.2021). (Cited in sections (document), 3.1, 3.3, and 3.5.)

[Peysson 2019] Y. Peysson, A. Jardin and K. Krol. *Screening effect of partially ionized high-Z impurities in relativistic linearized bounce-averaged electron Fokker-Planck calculations for RF current drive and runaway electron dynamics.* 2019. Internal notes. (Cited in sections 4, 4.2.1, and 4.2.2.)

[Peysson 2020] Y. Peysson, D. Mazon, J.-F. Artaud, A. Ekedahl, L. Delpech, J. Hillairet, T. Hoang, X. L. Zou, WEST Team, X. Y. Bai, Y. P. Zhang, HL-2A Team, K. Krol, J. Bielecki, A. Jardin, M. Scholz, D. Dworak and J. Decker. *Lower Hybrid Current Drive in High Aspect Ratio Tokamaks.* 2020. https://link.springer.com/article/10.1007%2Fs10894-020-00266-1, (accessed 03.10.2021). (Cited in sections 2.4.4, 3.4, and 5.4.2.)

[Peysson 2021a] Y. Peysson, D.Mazon, J. F. Artaud, A. Ekedahl, J.Hillairet, A. Jardin, K. Król, J. Bielecki, D. Dworak, M. Scholz, J. Decker and WEST Team. *First prin-*

ciples modeling of fast electron physics - SLUKE : a new framework for automatic LUKE modeling. 2021. International Conference on Diagnostics for Fusion Reactors (ICFRD), Varenna, Italy, 2021, https://agenda.infn.it/event/20740/contributions/142140/, (accessed 15.10.2021). (Cited in section 6.)

[Peysson 2021b] Y. Peysson, D. Mazon, A. Jardin, K. Król, J. Bielecki, D.Dworak, M. Scholz, O. Embreus, L. Hesslow, T. Fülop, M. Hoppe, J. Decker and WEST TEAM. *Effect of partially ionized high-Z atoms on fast dynamics electron tokamak plasmas.* 2021. https://conferences.iaea.org/event/214/contributions/17186/, (accessed 10.07.2021). (Cited in sections 4.3, 4.5, 4.6, 4.7, 4.10, 6, and B.9.)

[Pitts 2006] R. Pitts, R. Buttery and S. Pinches. *Fusion: the way ahead.* Physics World, vol. 19, no. 3, 2006. https://iopscience.iop.org/article/10.1088/2058-7058/19/3/35, (accessed: 11.07.2021). (Cited in sections 1.13 and B.9.)

[Pitts 2007] R.A. Pitts. 2007. https://crppwww.epfl.ch/~pitts/pitts/pitts_varenna_27_09_2007.pdf, (accessed: 03.03.2021). (Cited in sections 1.16 and B.9.)

[Pitts 2019] R.A. Pitts, X. Bonnin, F. Escourbiac, H. Frerichs, J.P. Gunn, T. Hirai, A.S. Kukushkin, E. Kaveeva, M.A. Miller, D. Moulton, V. Rozhansky, I. Senichenkov, E. Sytova, O. Schmitz, P.C. Stangeby, G. De Temmerman, I. Veselova and S. Wiesen. *Physics basis for the first ITER tungsten divertor.* Nuclear Materials and Energy, vol. 20, 2019. https://www.sciencedirect.com/science/article/pii/S2352179119300237, (accessed 11.07.2021). (Cited in section 1.4.1.)

[Poli 2012] F.M. Poli, C.E. Kessel, M.S. Chance, S.C. Jardin and J. Manickam. *Ideal MHD stability and performance of ITER steady-state scenarios with ITBs.* Nuclear Fusion, vol. 52, no. 6, 2012. https://iopscience.iop.org/article/10.1088/0029-5515/52/6/063027/meta, (accessed: 12.07.2021). (Cited in section 2.6.)

[Pratt 1972] R. H. Pratt and H. K. Tseng. *Behavior of Electron Wave Functions near the Atomic Nucleus and Normalization Screening Theory in the Atomic Photoeffect.* Physical Review A, vol. 5, 1972. https://journals.aps.org/pra/abstract/10.1103/PhysRevA.5.1063, (accessed 20.10.2021). (Cited in section 4.2.2.)

[Preynas 2011] M. Preynas, A. Ekedahl, N. Fedorczak, M. Goniche, D. Guilhem, J.P. Gunn, J. Hillairet, X. Litaudon, J. Achard, G. Berger-By, J. Belo, E. Corbel,

L. Delpech, T. Ohsako and M. Prou. *Coupling characteristics of the ITER-relevant lower hybrid antenna in Tore Supra: experiments and modelling*. 2011. https://iopscience.iop.org/article/10.1088/0029-5515/51/2/023001, (accessed 14.07.2021). (Cited in sections 2.9, 2.10, and B.9.)

[Preynas 2012] M. Preynas. *PhD theis written in English: Etude du couplage linéaire et non-linéaire de l'onde hybride basse aux plasmas de tokamaks*. 2012. (The text of the thesis is not available online.). (Cited in sections 5.2 and 5.2.)

[Pütterich 2010] T. Pütterich, R. Neu, R. Dux, A.D. Whiteford, M.G. O'Mullane, H.P. Summers and the ASDEX Upgrade Team. *Calculation and experimental test of the cooling factor of tungsten*. Nuclear Fusion, vol. 50, no. 2, 2010. https://iopscience.iop.org/article/10.1088/0029-5515/50/2/025012, (accessed: 12.07.2021). (Cited in sections (document), 1.4.3, 1.28, and B.9.)

[Pütterich 2019] T. Pütterich. *Determination of the tolerable impurity concentrations in a fusion reactor using a consistent set of cooling factors*. Nuclear Fusion, vol. 59, 2019. https://iopscience.iop.org/article/10.1088/1741-4326/ab0384, (accessed 11.07.2021). (Cited in sections 1.29 and B.9.)

[Ramponi 2007] G. Ramponi, D. Farina, M.A. Henderson, E. Poli, G. Saibene and H. Zohm. *ITER ECRH-ECCD System Capabilities for Extended Physics Applications*. Fusion Science and Technology, vol. 52, no. 2, pages 193–201, 2007. https://www.tandfonline.com/doi/abs/10.13182/FST07-A1498, (accessed: 11.07.2021). (Cited in section 2.4.2.)

[Reux 2015] C. Reux, V. Plyusnin, B. Alper, D. Alves, B. Bazylev, E. Belonohy, A. Boboc, S. Brezinsek, I. Coffey, J. Decker, P. Drewelow, S. Devaux, P.C. de Vries, A. Fil, S. Gerasimov, L. Giacomelli, S. Jachmich, E.M. Khilkevitch, V. Kiptily, R. Koslowski, U. Kruezi, M. Lehnen, I. Lupelli, P.J. Lomas, A. Manzanares, A. Martin De Aguilera, G.F. Matthews, J. Mlynář, E. Nardon, E. Nilsson, C. Perez von Thun, V. Riccardo, F. Saint-Laurent, A.E. Shevelev, G. Sips, C. Sozzi and JET contributors. *Runaway electron beam generation and mitigation during disruptions at JET-ILW*. Nuclear Fusion, vol. 55, 2015. https://iopscience.iop.org/article/10.1088/0029-5515/55/9/093013, (accessed 15.10.2021). (Cited in sections 1.3.2 and 1.3.2.)

[RICE] RICE. https://cnx.org/contents/pZH6GMP0@1.409:lO_vrGwv@3/Nuclear-Binding-Energy, (accessed: 11.07.2021). (Cited in sections 1.2.1, 1.4, and B.9.)

[Ritchie 1] H. Ritchie. 1. https://ourworldindata.org/energy-mix, (accessed 10.07.2021). (Cited in section 1.1.1.)

[Ritchie 2] H. Ritchie. 2. https://ourworldindata.org/how-long-before-we-run-out-of-fossil-fuels, (accessed 10.07.2021). (Cited in section 1.1.2.)

[Rosenbluth 1956] M. N. Rosenbluth, W. M. MacDonald and D. L. Judd. *Fokker-Planck Equation for an Inverse-Square Force*. Physical Review, vol. 107, 1956. https://journals.aps.org/pr/abstract/10.1103/PhysRev.107.1, (accessed 21.10.2021). (Cited in section 4.1.)

[Sauter 2000] O. Sauter, M.A. Henderson, F. Hofmann, T. Goodman, S. Alberti, C. Angioni, K. Appert, R. Behn, P. Blanchard, P. Bosshard, R. Chavan, S. Coda, B.P. Duval, D. Fasel, A. Favre, I. Furno, P. Gorgerat, J.-P. Hogge, P.-F. Isoz, B. Joye, P. Lavanchy, J.B. Lister, X. Llobet, J.-C. Magnin, P. Mandrin, A. Manini, B. Marlétaz, P. Marmillod, Y. Martin, J.-M. Mayor, A.A. Martynov, J. Mlynar, J.-M. Moret, C. Nieswand, P. Nikkola, P. Paris, A. Perez, Z.A. Pietrzyk, R.A. Pitts, A. Pochelon, G. Pochon, A. Refke, H. Reimerdes, J. Rommers, E. Scavino, G. Tonetti, M.Q. Tran, F. Troyon and H. Weisen. *Steady-State Fully Non-inductive Current Driven by Electron Cyclotron Waves in a Magnetically Confined Plasma*. Physical Review Letters, vol. 84, no. 15, pages 3322–3325, 2000. https://journals.aps.org/prl/abstract/10.1103/PhysRevLett.84.3322, (accessed: 11.07.2021). (Cited in section 2.4.2.)

[Schmidt 2011] A.E.W. Schmidt. *Measurements and Modeling of Lower Hybrid Driven Fast Electrons on Alcator C-Mod*. 2011. https://dspace.mit.edu/handle/1721.1/68879, (accessed 18.07.2021). (Cited in sections 3.1 and 3.6.)

[Scholz 2019] M. Scholz, K. Król, A. Kulińska, L. Karpiński, A. Wójcik-Gargula and M. Fitta. *On the Possibility of Initiating the Proton–Boron Nuclear Fusion Reaction in the Plasma-Focus Device*. Journal of Fusion Energy, vol. 38, 2019. https://link.springer.com/article/10.1007/s10894-019-00225-5, (accessed 28.10.2021). (Cited in section 1.1.3.)

[Schultz 1999] S.D. Schultz. *Lower Hybrid and Electron Cyclotron Current Drive With Bootstrap Current in Tokamaks, PhD thesis*. 1999. https://dspace.mit.edu/handle/1721.1/85353, (accessed 18.07.2021). (Cited in sections 3.1, 3.5, 3.5, A.1, and A.1.)

[Shafranov 2001] V. D. Shafranov. *The initial period in the history of nuclear fusion research at the Kurchatov Institute*. Uspekhi Fizicheskikh Nauk, vol. 171, 2001. https://fire.pppl.gov/rf_shafranov.pdf, (accessed 15.10.2021). (Cited in section 1.2.3.)

[Shutterstock] Shutterstock. https://www.shutterstock.com/, (accessed: 26.02.2021). (Cited in sections 1.8 and B.9.)

[Spitzer 1953] L. Spitzer and R. Härm. *Transport Phenomena in a Completely Ionized Gas*. Physical Review, vol. 89, no. 5, pages 977–981, 1953. https://journals.aps.org/pr/abstract/10.1103/PhysRev.89.977, (accessed: 12.07.2021). (Cited in section A.4.)

[Stahl 2015] A. Stahl, E. Hirvijoki, J. Decker, O. Embréus and T. Fülöp. *Effective Critical Electric Field for Runaway-Electron Generation*. Physical Review Letters, vol. 114, 2015. https://journals.aps.org/prl/abstract/10.1103/PhysRevLett.114.115002, (accessed 15.10.2021). (Cited in section 1.3.2.)

[Swanson 2003] D. G. Swanson. *Plasma Waves, 2nd Edition*. 2003. https://www.routledge.com/Plasma-Waves/Swanson/p/book/9780750309271, (accessed 13.07.2021). (Cited in section 2.4.1.)

[Vedenov 1967] A.A. Vedenov. *Theory of weakly turbulent plasma*. Reviews of Plasma Physics, vol. 3, pages 229–276, 1967. https://link.springer.com/chapter/10.1007/978-1-4615-7799-7_3, (accessed: 12.07.2021). (Cited in section A.2.)

[Vries 2012] P. C. Vries, G. Arnoux, A. Huber, J. Flanagan, M. Lehnen, V. Riccardo, C. Reux, S. Jachmich, C. Lowry, G. Calabro, D. Frigione, M. Tsalas, N. Hartmann, S. Brezinsek, M. Clever, D. Douai, M. Groth, T. C. Hender, E. Hodille, E. Joffrin, U. Kruezi, G. F. Matthews, J. Morris, R. Neu, V. Philipps, G. Sergienko, M. Sertoli and JET EFDA contributors. *The impact of the ITER-like wall at JET on disruptions*. Plasma Physics and Controlled Fusion, vol. 54, no. 12, 2012. https://iopscience.iop.org/article/10.1088/0741-3335/54/12/124032, (accessed: 11.07.2021). (Cited in sections 1, 3, and B.9.)

[Wagner 1982] F. Wagner. *Regime of Improved Confinement and High Beta in Neutral-Beam-Heated Divertor Discharges of the ASDEX Tokamak*. Physical Review, vol. 49, pages 1408–1412, 1982. https://journals.aps.org/prl/abstract/10.1103/PhysRevLett.49.1408, (accessed 11.07.2021). (Cited in section 1.2.5.)

[Wagner 2010] F. Wagner, A. Becoulet, R. Budny, V. Erckmann, D. Farina, G. Giruzzi, Y. Kamada, A. Kaye, F. Koechl, K. Lackner, N. Marushchenko, M. Murakami, T. Oikawa, V. Parail, J.M. Park, G. Ramponi, O. Sauter, D. Stork, P.R. Thomas, Q.M. Tran, D. Ward, H. Zohm and C Zucca. *On the heating mix of ITER.* Plasma Physics and Controlled Fusion, vol. 52, no. 12, 2010. https://iopscience.iop.org/article/10.1088/0741-3335/52/12/124044/meta, (accessed: 12.07.2021). (Cited in section 2.6.)

[Walkowiak 2021] J. Walkowiak, A. Jardin, J. Bielecki, Y. Peysson, D. Mazon, D. Dworak, K. Krol and M. Scholz. *Approximate atomic models for fast computation of the Fokker-Planck equation in fusion plasmas with high-Z impurities and suprathermal electrons.* 2021. To be submitted to Physics of Plasmas in October 2021. (Cited in section 6.)

[Wallace 2010] G.M. Wallace. *PhD thesis: Behavior of Lower Hybrid Waves in the Scrape Off Layer of a Diverted Tokamak.* 2010. https://dspace.mit.edu/handle/1721.1/57694, (accessed 18.07.2021). (Cited in sections 3.1 and A.1.)

[Weinberg 1961] S. Weinberg. *Eikonal Method in Magnetohydrodynamics.* The Physical Review, vol. 126, 1961. https://journals.aps.org/pr/abstract/10.1103/PhysRev.126.1899, (accessed 23.07.2021). (Cited in sections 3.3 and 3.3.)

[Wesson 2004] J. Wesson. Tokamaks. Clarendon Press - Oxford, 2004. (Cited in sections 1.2.3, 1.2.3, 1.2.5, 2.1, 2.3, 2.4.4, and 2.4.4.)

[Westerhof 2010] E. Westerhof. *Non-inductive current drive.* Fusion Science and Technology, vol. 57, no. 2T, pages 222–229, 2010. https://core.ac.uk/download/pdf/35070401.pdf, (accessed: 12.07.2021). (Cited in sections 2.1, 2.1, 2.1, 2.4, 2.3, 2.4.3, 2.4.4, 3.4, and B.9.)

[Wolf 2002] R.C. Wolf. *Internal transport barriers in tokamak plasmas.* Plasma Physics and Controlled Fusion, vol. 45, 2002. https://iopscience.iop.org/article/10.1088/0741-3335/45/1/201, (accessed 10.07.2021). (Cited in section 1.4.2.)

[Woods 2006] L. C. Woods. Theory of tokamak transport. new aspects for nuclear fusion reactor design. Wiley-VCH, 2006. https://onlinelibrary.wiley.com/doi/book/10.1002/3527607978, (accessed 15.10.2021). (Cited in section 1.2.5.)

[Wort 1971] D.J.H. Wort. *The peristaltic Tokamak.* Plasma Physics, vol. 13, no. 3, pages 258–262, 1971. https://iopscience.iop.org/article/10.1088/0032-1028/13/3/008, (accessed: 12.07.2021). (Cited in sections 1.3.1, 2.1, and 3.5.)

[Xue 2020] L. Xue, J. Garcia, G.Y. Zheng, G.T. Hoang, J.F. Artaud, X.R. Duan, J.X. Li, G. Giruzzi, X.L. Zou, W. Pan, J.H. Zhang, M. Huang, H.L. Wei, X.Y. Bai, X.Q. Ji, X.M. Song, S. Wang, X. Song, M. Xue, W.Y. Huang and the HL-2M team. *Integrated plasma scenario analysis for the HL-2M tokamak*. Nuclear Fusion, vol. 60, 2020. https://iopscience.iop.org/article/10.1088/1741-4326/ab4c65/meta, (accessed 15.10.2021). (Cited in section 1.2.5.)

[Young 2020] H.D. Young and R.A. Freedman. University physics with modern physics. Pearson Education, 2020. https://www.pearson.com/uk/educators/higher-education-educators/program/Young-University-Physics-with-Modern-Physics-Global-Edition-//15th-Edition/PGM2741904.html, (accessed: 11.07.2021). (Cited in sections 1.7, 1.9, 1.2.3, and B.9.)

Streszczenie

Na drodze do energii termojądrowej, tokamaki stanowią obecnie najbardziej obiecującą metodę przeprowadzenia kontrolowanej reakcji termojądrowej. Aby uniknąć problemu retencji trytu, jaki ma miejsce w przypadku ścian tokamaka wykonanych z komponentów węglowych, divertor Międzynarodowego Eksperymentalnego Reaktora Termojądrowego (ITER) będzie wykonany z wolframu (W). W związku z tym małe stężenia domieszek wolframu będą obecne w plazmie ITER-a. Niewielkie stężenia wolframu są wystarczające, aby znacząco wpłynąć na działanie tokamaka, a mogą nawet prowadzić do zakończenia wyładowania plazmowego. W szczególności krytycznym zagadnieniem, które musi być zbadane, jest wpływ domieszek o wysokiej liczbie atomowej Z na dynamikę szybkich (supratermalnych) elektronów. Zagadnienie to jest ważne z ze względu na dwa aspekty. Po pierwsze konieczne jest rozwijanie metod tłumienia wiązek elektronów uciekających w plazmie po zerwaniu sznura plazmowego. Po drugie domieszki wolframowe mają negatywny wpływ na efektywność generowania prądu szybkich elektronów w plazmie tokamakowej. Jak dotąd, główny nacisk kładziono na badania dotyczące domieszek o niskiej liczbie atomowej Z, takich jak węgiel, azot czy argon. Jednak obecnie konieczne jest rozszerzenie metod badania dynamiki szybkich elektronów na cięższe domieszki, takie jak krypton, molibden czy wolfram. W związku z tym niezbędne jest uwzględnienie efektu częściowego ekranowania podczas oddziaływania pomiędzy jonami domieszek a szybkimi elektronami w plazmie. Cel ten został osiągnięty poprzez konsekwentne włączenie teorii częściowego ekranowania do obliczeń kinetycznych. Wykorzystany w pracy łańcuch kodów numerycznych C3PO/LUKE/R5-X2 jest standardowym narzędziem do modelowania LHCD w tokamaku Tore Supra, ostatnio zmodernizowanym do tokamaka WEST. W przedstawionej pracy szczególny nacisk został położony na konsekwencje obecności nie w pełni zjonizowanych domieszek o wysokiej liczbie atomowej Z na generowanie przepływu prądu za pomocą fal LH oraz intensywność promieniowania hamowania emitowanego przez szybkie elektrony dla przypadku tokamaka WEST.

Abstract

On the road to fusion energy, tokamaks currently represent the most promising method to confine the thermonuclear plasma. To avoid the tritium retention issue experienced with carbon walls, the divertor of the International Thermonuclear Experimental Reactor (ITER) will be made of tungsten (W). However, this means that small concentrations of tungsten impurities will be present in the ITER plasma. They are sufficient to significantly affect the operation of the tokamak, sometimes even leading to the termination of the plasma discharge. In particular, a critical issue that needs to be investigated is the effect of high-Z impurities on the dynamics of fast (suprathermal) electrons. This issue arises when considering either the mitigation of a runaway electron beam in a post-disruptive plasma or a suprathermal electron population generated with a current drive method, using, e.g. Lower Hybrid (LH) waves. So far, the main focus has been put on relatively low-Z impurities such as carbon, nitrogen or argon. However, it is now necessary to extend the methods of studying the dynamics of fast electrons to heavier impurities such as krypton, molybdenum or tungsten. Consequently, it is necessary to consider the partial screening effect during the interaction between impurity ions and fast electrons in a plasma. This goal has been achieved by consistently incorporating the partial screening theory into kinetic calculations. The chain of numerical codes C3PO/LUKE/R5-X2 used for this purpose is the standard tool for modelling LH current drive on the Tore Supra tokamak, recently upgraded to the WEST - W environment in a steady-state tokamak. A particular emphasis is placed on the consequences of high-Z non-fully ionized impurities on LH current drive and the fast electron bremsstrahlung intensity on WEST.